On the Climate-Agriculture-Water Nexus at the Regional Scale

by

Catherine A. Nikiel

Submitted to the Department of Civil and Environmental Engineering
in partial fulfillment of the requirements for the degree of

Doctor of Philosophy in Civil and Environmental Engineering

at the

MASSACHUSETTS INSTITUTE OF TECHNOLOGY

February 2022

Author .....
Department of Civil and Environmental Engineering
November 19, 2021

Certified by .....
Elfatih A. B. Eltahir
H. M. King Bhumibol Professor of Hydrology and Climate
Thesis Supervisor

Accepted by .....
Colette L. Heald
Professor of Civil and Environmental Engineering
Chair, Graduate Program Committee

On the Climate-Agriculture-Water Nexus at the Regional Scale

by

Catherine A. Nikiel

Submitted to the Department of Civil and Environmental Engineering
on November 19, 2021, in partial fulfillment of the
requirements for the degree of
Doctor of Philosophy in Civil and Environmental Engineering

Abstract

Development of large-scale agriculture is one of the most significant anthropogenic global change processes during the 20^{th} century. In this thesis, connections between climate, agriculture, and water availability are investigated, using examples from Egypt and the Central United States.

Agriculture reflects and impacts water availability at local, regional, and global scales. A bottom-up, reconstruction of agricultural water consumption in Egypt illustrates how this process is driven by socioeconomic trends and constrained by ecological limits. This analysis shows that Egypt is currently withdrawing most of the Nile's annual flow, 61.5 km^3, and in the coming few years will be importing that same volume as virtual water, to satisfy the growing population and economy.

Agricultural land-use change in the Central U.S. is found to be the dominant factor in shaping regional climate during the 20^{th} century. Agricultural development (expansion, intensification, irrigation) accounts for observed July-August temperature decreases (0.2-0.3 °C) from 1920-1949 to 1970-1999 and about 30% of precipitation increases (0.2 to 0.3 mm/day). These agriculturally driven cooling and wetting trends in the historical period have led to a modification of summer (May-August) water availability (represented through Precipitation-Evapotranspiration (P-E)) with increases of about 17 mm from 1915-1944 to 1975-2004, and significant increases in summer relative humidity and rainfall over a highly productive region spanning Iowa, Illinois, Indiana, and Ohio.

In the future, projected climate change will impact the same agricultural systems significantly, requiring adaptation of existing drainage infrastructure to manage projected excess springtime soil moisture, and development of supplemental irrigation systems to manage the drier summers. Temperature increases, consistent with global warming, and associated reductions in summer relative humidity are shown in multi-model ensembles of CMIP5 and CMIP6 to lead to summer drying: a P-E reduction of 12 mm and 36 mm respectively.

Finally, this thesis investigates impacts of agriculture on the climatology of heat waves in the Central U.S. Non-irrigated (irrigated) agriculture has increased June-

September average daily maximum wet-bulb temperatures by 0.3 (0.7) °C in the historical period. In the future, irrigated agricultural areas will be 0.9 °C hotter than without irrigation. These enhancements of heat stress will exacerbate projected impacts of climate change.

Thesis Supervisor: Elfatih A. B. Eltahir
Title: H. M. King Bhumibol Professor of Hydrology and Climate

Acknowledgments

I cannot express enough gratitude for the people in my life who have supported me to this point. Thank you to my advisor, Dr. Elfatih Eltahir and my entire committee – Jonathan Winter, Earle Williams, and Charles Harvey for their insights, guidance, and support. To my parents, Krystyna and Leszek Nikiel, for their unfailing support and love and for always being willing to talk. To my dear friends, Myrna G., Emma C., and Clare J., who were with me mostly from afar, and to Emily P., my best friend, my housemate, and a source of joy and sanity as we weathered the pandemic together. Thank you to the communities I have been a part of at MIT, particularly MITSO and the pit orchestra for MTG, as well as the warm and welcoming Parsons Lab community. Finally, Thank you to group members past and present – to Yeon-Woo C., Patric R., Suchul K., Alexandre T., Gin K. Mohamed S., Hamed I. Mariam A., Mekki S., Noriko E., Tim A., Natalie W., Ross A., and Nabil M. – for their input, generous teaching, and company.

Contents

List of Figures

List of Tables

Chapter 1

Introduction

The development of agriculture has been heralded as the beginning of modern civilizations; It allowed humans to settle and develop the connections and complexity of modern society [137]. Before the Industrial Revolution, agriculture was arguably the most important imprint of humans on the environment, with large swaths of land being converted to pasture and cropland. With the development of new agricultural technologies like fertilizers, new breeds of crop varieties, the mechanization of farm work, and the implementation of irrigation, the 20th century saw the advent of green revolutions across several continents [85]; In 1850 there were 580 million hectares of cropland globally, which nearly tripled to 1.58 billion in 2016 (Fig. 1-1) [216]. At the same time, cropland became even more productive. Global average wheat yields more than tripled from 1961 to 2018 from 1.09 to 3.42 tonnes per hectare, and maize yields saw a similar scale of increase from 1.94 to 5.92 tonnes per hectare [215]; these increases in yield and production were necessary to meet the needs of a rapidly growing and globalizing population, which totaled 3.09 billion in 1961 and 7.63 billion in 2018 [220]. However, growth has been uneven across regions and remains vulnerable in the face of climate change and further population growth [208].

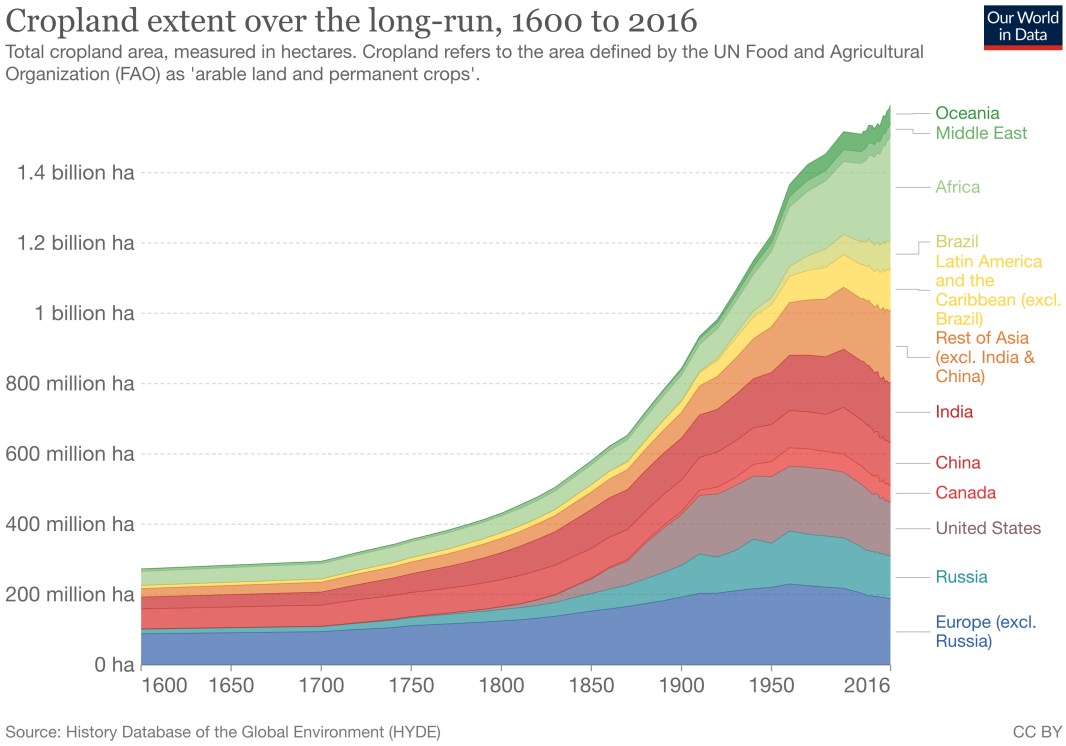

Figure 1-1: Cropland extent over the long-run, 1600-2016. (Source: History Database of the Global Environment. Downloaded from Our World in Data) [216]

If we acknowledge that agriculture has had a significant impact on the environment, then it stands to reason that it must be integrated into our understanding of the earth system as a whole. This includes robust representation in hydroclimate analysis. This thesis aims to explore the connections between agriculture, water and the climate system and show the explicit impact that agricultural development has had on both water and climate in the past and into the future.

Adding to the complexity of these connections is the understanding that they are not uni-directional (Fig. 1-2). Water impacts agriculture through its dependence on water availability for growth, but the expansion and intensification of agricultural production places new stresses on often limited water systems that must be shared with other use sectors (Chapter 2). Climate impacts the suitability of agriculture through temperature and precipitation amounts, but land use and land cover (LULC) change is shown to modify the regional climate in an area and adjust both temperature and precipitation (Chapters 3-5). Water and climate are linked through the cycle of evapotranspiration and precipitation, but these connections are also affected by climate change, which modifies the location, magnitude and intensity of these components of the water cycle (Chapters 4-5).

These connections between agriculture, climate, and water are seen especially starkly in two places: the Central United States and Egypt. In both places, agricultural development has driven cropland expansion and the intensification of agriculture to boost production significantly over the 20th Century. In the Central U.S., the expansion of agriculture has been dependent on management of the yearly water cycle, and has in turn had a measurable impact on that cycle itself. In Egypt, agricultural development is the key determinant behind water availability.

In this thesis, we will explore the connection between climate, agriculture, and water in these two regions through a set of connected studies. This thesis is a collection of peer reviewed and published papers as well as additional research that is being prepared for publication. Papers either published or in review are noted at the beginning of the relevant chapters, as well as other publications and presentations made about the work to the scientific community. More in depth background and

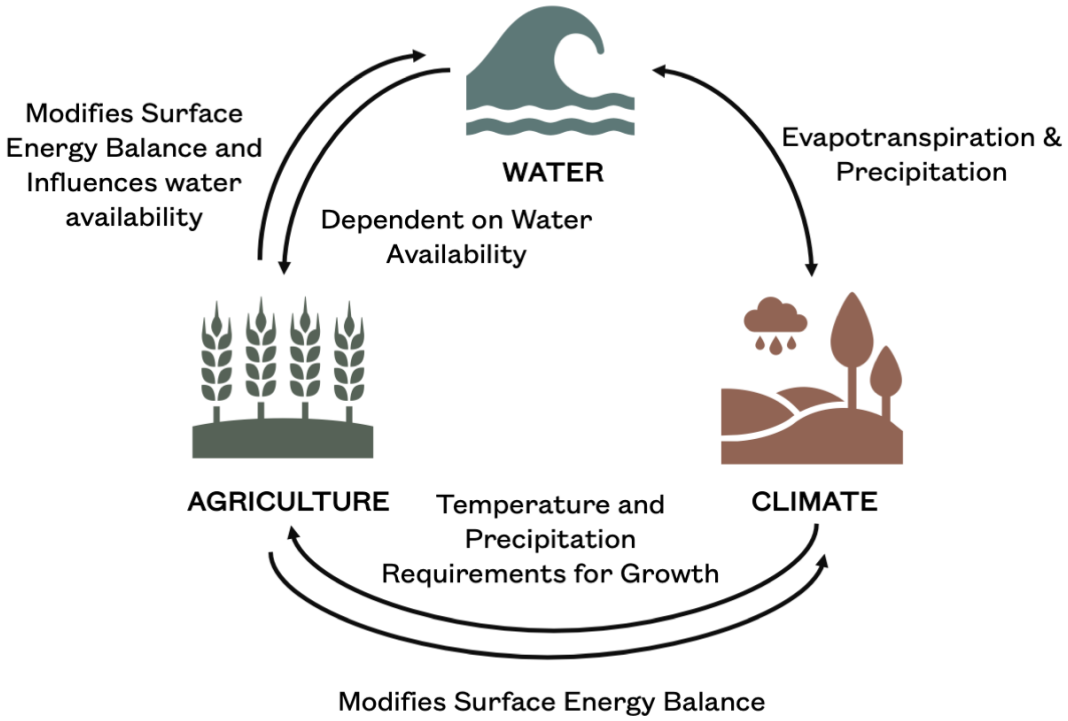

Figure 1-2: The Climate-Agriculture-Water Nexus

literature review on the individual topics is included at the beginning of each chapter.

Chapter 2 focuses on how intense agricultural development can be the primary determinant behind water availability in a region. We focus on Egypt's Nile Delta because it is a highly productive system that is severely water limited and development has brought it to the ecological carrying capacity of the system within the last few decades. The study aims to determine when Egypt will begin to import more virtual water in the form of agricultural products than it uses annually from the Nile. To do this, this study provides a highly detailed annual bottom-up reconstruction of water use in the country from 1961-2017, and pairs it with an in depth analysis of supply changes, socio-economic drivers of demand, and measures that Egypt has taken to manage its resources over the last sixty-years. The main results of the chapter are as follows:

1. By constructing an independent annual 60-year, bottom-up analysis of water supply and demand in Egypt, we show the direct connection between water demand and socio-economic growth and use these demand relationships to project

for future virtual water demand.

2. Supply and demand analysis is paired with incremental analysis of adaptation measures taken in order to manage water needs, showing how resource limits are addressed through social, economic, political, and environmental management decisions.

3. We show that under nominal population and economic growth rates, Egypt has reached the carrying capacity of the Nile, and will import as much water as it withdraws from the Nile in roughly 2022.

Chapter 3 investigates the impact that agricultural development in the Midwest and Great Plains of the United States has had on the historical summer climate. We ask how agricultural development – expansion, intensification, and irrigation – has contributed to observed (historical) changes in mean July-August temperature and precipitation. This work contributes novel work to the topic of agricultural impact on regional climate, the importance of agricultural yield intensification, and the causes of the regional "Warming Hole" phenomena [194]. The main results of the chapter are as follow:

1. Agricultural development played a greater role in historical regional climate change in this region in the summer than greenhouse gas increases.

2. While agriculture is a key driver of observed changes, SST teleconnections, particularly in the North Atlantic and Tropical Pacific also drove a significant portion of observed changes.

3. Full consideration of all three LULC components and their competing effects are necessary to fully understand climate impacts.

Chapter 4 investigates the impact of climate change on the hydrology of summer agriculture in the American Midwest, with a particular focus on the core Cornbelt states of Iowa, Illinois, Indiana and Ohio. The research aims to answer how the balance of growing season (May-August) precipitation-evapotranspiration (P-E) has

changed in this Cornbelt region, a highly managed and productive agricultural area, and how it will be impacted by future climate change. This work contributes to the literature on the historical and future seasonal cycle of P-E using the most recently available global climate model simulations, and also ties historical and future changes directly to agricultural development and the management and drainage of wetland areas. The main results of the chapter are as follow:

1. Using multi-model ensembles of CMIP5 and CMIP6 models, analysis shows an intensification of the seasonal cycle of P-E in the Cornbelt, with P-E become more positive in the spring, and more negative in the summer.

2. In comparison to the wetting of P-E in this region in the historical period (shown through gridded and in-situ observations), the future changes are of similar magnitude but opposite direction. Rather than pushing the region into a novel climate state, future drying will revert the seasonal cycle to an earlier normal.

3. The projected drying of P-E in the May-August season will occur in an area that is a drained natural wetland, with little existing supplemental irrigation. Therefore, this area has ample room for climate adaptation.

Chapter 5 builds on the connections between agriculture and hydroclimate that have been explored in Chapters 3 and 4 and connects them to a pressing issue of public health – humid heat. This chapter aims to answer how agricultural development and other climate forcings have impacted the climatology of extreme summer wet-bulb temperature in the Central U.S. as well as the intensity, duration, and frequency of discrete humid heat wave events. We connect our modeling results to a mechanistic understanding of how agriculture is linked to wet-bulb temperatures and show how historical and future changes in wet-bulb occurrence relate to public health impacts. The main results of this chapter are as follow:

1. Agricultural development in the 20th century has contributed to increased daily maximum wet-bulb temperatures, and the inclusion of agricultural development

in models is necessary to approach the historical pattern of wet-bulb. Areas of irrigated agriculture will contribute to an even further enhanced wet-bulb temperature increase in the future.

2. Regions of elevated and extreme wet-bulb temperatures will expand in the Central U.S. under climate change in the 21st century, exposing larger portions of the population to dangerous conditions.

3. Accurate representation of the Great Lakes surface temperatures is crucial to future wet-bulb projections and accurate representation of the historical temperature and moisture patterns of the area. Varying levels of projected warming in the Great Lakes strongly influence future wet-bulb temperature, and can even be linked to modeled heat wave events tied to the Great Lakes themselves.

4. Extreme heat wave events will become more frequent, longer lasting, and more intense in 2070-2099 under the RCP8.5 warming scenario. Agricultural development has made these events more frequent and longer lasting in the historical period and will continue to do so in the future.

Chapter 2

Past and Future Trends of Egypt's Agricultural Water Consumption and its Sources

Relevant Papers and Presentations

Nikiel C. A. and Eltahir, E. A. B. (2021). Past and future trends of Egypt's water consumption and its sources. Nature Communications. 12, 4508 [181]

Nikiel, C.A. and Elfatih A.B. Eltahir (2019). Agricultural Technology in the Nile Basin: Current Use and Potential Expansion. In Eltahir, Elfatih A.B, Ed. Stephanie McPherson, *A Path Forward for Sharing the Nile Water: Sustainable, Smart, Equitable, Incremental* (pp. 100-135). Cambridge, MA. [179]

2.1 Introduction

"The Egypt to which the Hellenes come in ships is a land which has been won by the Egyptians as an addition, and that it is a gift of the

[Nile]." (Herodotus Book 2:5) [105]

Water availability is crucial to the continued growth and development of communities, both demographically and socioeconomically. It supports population growth through direct consumption, and allows the growth of industry and agricultural production. In arid areas such as North Africa and the Middle East, where agriculture is reliant largely on man made systems of irrigation, and where population is increasing rapidly, understanding water management is increasingly important. Egypt, one of the largest and most economically prosperous countries in Africa, is an agricultural powerhouse, but also in a precarious position of water scarcity. Almost all of the water needed for life is supplied by the Nile River [70], a relatively fixed supply dictated by both nature and a water use agreement negotiated with Sudan in 1959 [257]. The Egyptian water use system is a case study of a loop in perfect but precarious balance, in danger from the larger threat of climate change, pressures of growing neighbors, and their own development success.

Following expansion of the Sahara Desert, thousands of years ago, and migration of native populations to shelter in the Nile Valley, an intimate relationship developed between an emerging Egypt and the Nile. This connection has manifested in historical, political, ecological, and hydrological dimensions. However, Egypt's fast-growing population and developing economy have strained already scarce water resources through dietary changes and municipal and industrial consumption. Egypt is facing external pressures on perceived water rights, limited national water resource availability, and a struggle to fashion a sustainable development vision for its future. The current policies regarding irrigation in the New Lands at the edges of the Nile Delta, the current rate of water reuse, and the level of success achieved in reducing fertility rates will not be enough to close the demand gap in the future [68].

Egypt's population has been growing rapidly in recent decades, at a rate of 2.1% annually from 1989 to 2018 [259], following a similar trajectory of world population growth (Fig. 2-1). This added population places pressure on limited water resources,

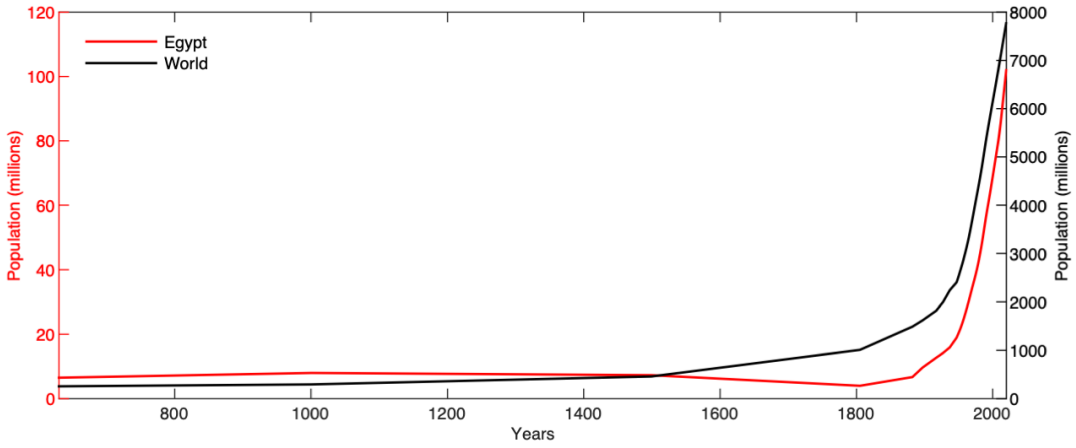

Figure 2-1: Egyptian population (millions) [red line] and world population (millions) [black line] from 1 - 2020 C.E. [259] (Data Source: Table B.1.4)

both through direct consumption and through increased demand for food and other products. In 2017, the total renewable water resource per capita was 628 m^3/yr, already below the level for water scarcity according to the Falkenmark Index [62] [69]. This pressure due to population growth, while straightforward, is essential to include while drawing the picture of historical and future demand for water, as Egypt faces increasing scarcity of natural resources.

Egypt has also experienced rapid economic growth since the mid 1950's (Fig. 2-2a). From 1989 to 2018, the Egyptian GDP grew at 4.4% annually, while GDP per capita grew at 2.3% annually over the same period [65]. This growth has been concurrent with an increase in water consumption for both municipal and agricultural purposes and an increase in both domestic production and imports of agricultural commodities. As GDP has grown, the diet of Egyptians has changed dramatically; increasing trade connections with other food producers have increased availability of some goods, particularly animal products (Fig. 2-2b). The average per capita supply of proteins from animal origins increased by 39% from 18 g/cap/day in 1999-2001 to 25 g/cap/day in 2011-2013 [66]. At the same time, the prevalence of undernourishment dropped by 0.7% to 4.5% [66]. Egypt currently ranks among the top countries globally in the daily per capita caloric supply (3,522 kcal/capita/day), just behind the United States [219]. These trends are projected to continue, especially in meat

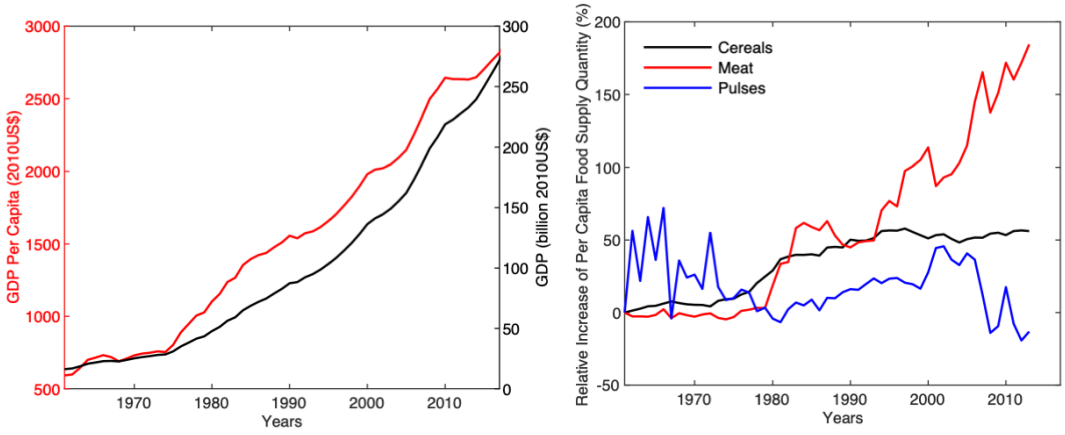

Figure 2-2: a) Gross Domestic Product (Constant 2010 $US) [black line] and GDP per Capita [red line] in Egypt [65] (Data Source: Table B.1.6) b) Relative change in per capita food supply (kg/capita/year) relative to 1961 for meat [red line], cereals [black line], and pulses (beans, chickpeas, lentils) [blue line]. 1961 values for meat, cereal, and pulses are 10.71, 161.43, and 6.5 kg/capita/yr respectively [66] (Data Source: Table B.1.10)

consumption which has a strong relationship with GDP per capita [214]. The projected consumption of red meat in 2030 is 1,581,000 tonnes up from 2001-2017 average of 1,136,050 tonnes; the projected consumption of white meat is 1,681,000 tonnes up from 2011-2017 average of 1,054,740 tonnes [6]. However, calories coming from meat are still a small percentage of overall daily caloric intake, increasing from 2.4% to 3.5% from 1961 to 2013 [64].

At the same time, water supply from the Nile, which accounts for 98% of renewable water resources in Egypt, has remained relatively steady (Fig. 2-3) [70]. While detailed flow records do not exist prior to the installation of modern gauging systems (circa mid to late 1800's), the Nile's floods have been monitored and recorded for millennia. Records of flood heights from the Rhoda Nilometer show these levels remained relatively constant over the 800-year record [26] [97]. Geologic research has suggested "very little downcutting [in the riverbed has occurred] in Nubia since [the time of the New Kingdom some 3000 years ago]" suggesting that flood heights across the full 700-year record are directly comparable [225]. In the modern record, flows recorded at Aswan and Dongola have been slightly decreasing, as a result of increased withdrawal of natural flows upstream from Sudan's annual withdrawal of 4 km^3 in

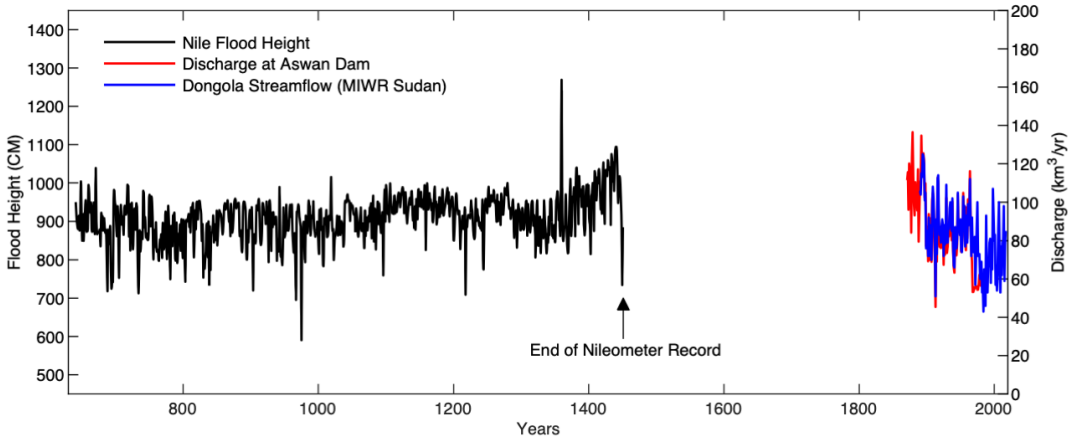

Figure 2-3: Qualitative comparison of stable Nile Flood heights (CM) from 641 to 1451 [black line - left axis] [26] and decreasing modern yearly average discharge from Aswan Dam (km^3/yr) [red line - right axis] and flow at Dongola (km^3/yr) [blue line - right axis] [265] [59] (Data Source: Table B.1.14 & B.1.20). Note that the reader should not interpret a 1:1 correlation between the y-axes, and that the two separate groupings of data have been presented together to reflect that there has been little change in the Nile based on geologic survey [225]

1959 to current withdrawals of 13-16.7 km^3 [265] [59] [189] [227] [257] [277].

This work identifies and quantifies actions that Egypt has taken over the past six decades to manage internal pressures on water resources. A detailed, long term picture of the changes in water demand and water use is constructed and used as a foundation to project demand on water out to 2035, and further to propose solutions that can be explored towards more efficient water use. While much past work [4] [182] [13] [176], including governmental literature, has presented snapshots in time of water use and virtual water trade in Egypt, this analysis uses water and crop data to quantitatively describe in significant detail water use in Egypt, over a period of six decades. The key innovations of this study are in the detailed year-by-year reconstruction of trends in water use down to the individual crop level, the improved understanding of the factors that drive these trends, and the use of this context to project water demand into the near future based on empirical demand relationships. The detailed diagnosis of water use in Egypt facilitates identification of opportunities for water saving, water reuse, and improved water use efficiency in general.

2.2 Background

2.2.1 Water in Egypt: Historical and Future

This chapter focuses on historical and future trends in Egyptian water management: First, in the historical period, Egypt has managed water supply and demand through five avenues (Fig. 2-4 & 2-5): improving water infrastructure and management by building the High Aswan Dam; increasing in-country agricultural production through harvested area expansion and improving crop yields; expansion of water reuse; reducing population growth rate; and increasing import of agricultural products - especially staples such as wheat and maize. Extensive data sets are integrated to rigorously document this historical adaptation process.

Second, future population and economic growth will increase water demand dramatically and require Egypt to rely more heavily on virtual water imports, at a higher annual growth rate than has been seen in the past. The concept of virtual water, coined in the 1990's by Dr. Tony Allan, was first applied to the Middle East and North Africa as a region that addressed water scarcity with importation [8]. This analysis show through a novel bottom-up reconstruction of water-use that Egypt's demand for water passed the carrying capacity of the Nile in the late 1970's and was importing the use equivalent of at least 40 km^3 of virtual water in the late 2010's. Assuming persistence of the recent socioeconomic trends, we project that Egypt will import 61.5 km^3/yr during this decade of the 2020s. At that point Egypt will be importing more virtual water from abroad than they have been withdrawing from the Nile internally on average for the past 30 years. A comprehensive analysis framework is shown in the data and methodology and results sections for reconstruction of past water uses and projection of future water demand leading to these conclusions.

2.2.2 Egypt's Response to Increasing Water Demands

Rapid changes in demographic and economic factors in Egypt have spurred equally large responses in an attempt to control and manage water supply and demand.

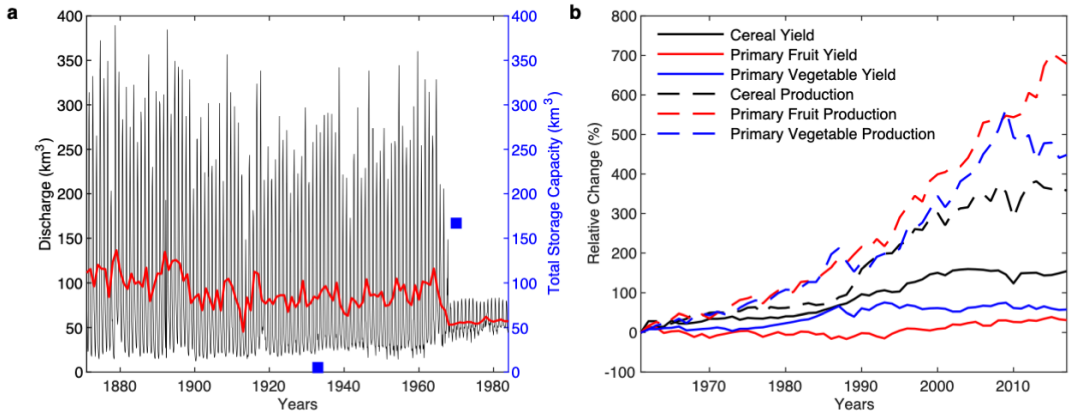

Figure 2-4: a. Flow of the Nile at Aswan (km^3) in monthly [black line] and yearly [red line] averages [265] (Table B.1.20). Blue squares represent the total storage capacity (km^3) and marks the construction of the Aswan and High Aswan Dams [70] (Table B.1.19). b. Relative (%) change in production (harvested tonnes) [dotted lines] and yield (production/area) [solid lines] of cereal [black], primary fruit [red], and primary vegetable [blue] crop groupings. 1961 production values are 5.0, 1.9, and 2.8 million tonnes respectively, and 1961 yield values are 29,057, 169,113, and 152,611 hg/ha respectively (Table B.1.7).

Egypt's effort in the areas of controlling variability in the Nile water supply, agricultural productivity, water reuse, fertility rates, and food imports have been substantial. However, future pressures will require Egypt to intensify some of these measures and adopt new approaches.

Much of the work done by Egypt can be viewed as a transition through several water states. As seen in Fig. 2-3, the Nile river was largely uncontrolled for most of its history, with natural flood cycles characterizing the flow. Agriculture, and Egyptian life in general was guided by the seasonal flood and drought cycles of the river and water still flowed freely into the Mediterranean Sea. This began to change in earnest when Egypt built the High Aswan Dam from 1960-1970; this curtailed the flow of the river, and the resulting reservoir with a total design capacity of 160 km^3 reduced interannual variability of flow, providing a steady and controlled supply of water to farms, which could now control the application of irrigation to fields while minimizing losses to the Mediterranean (Fig. 2-4a) [73]. These decades also saw the advent of major use treaties; through the 1959 Water Agreement between Sudan and Egypt, Egypt would be allocated 55.5 km^3 of the Nile water annually while Sudan

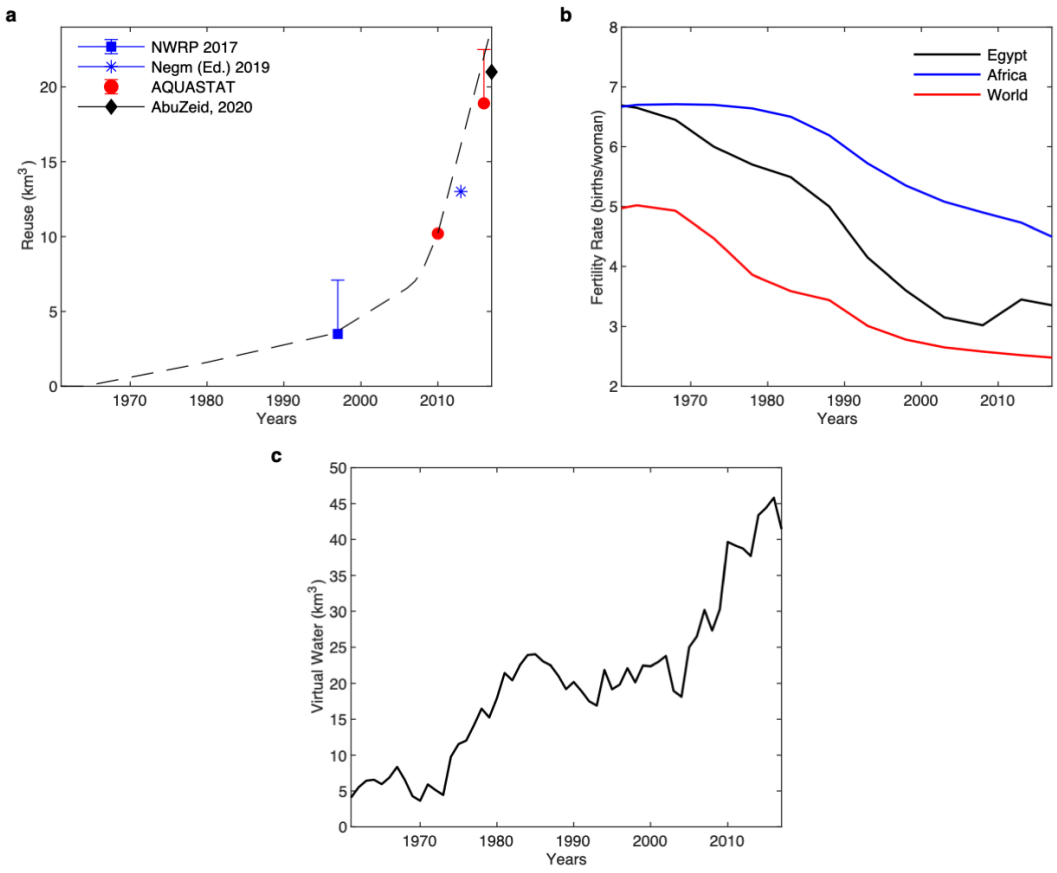

Figure 2-5: a. Estimated water available for reuse from direct agricultural drainage reuse, Nile Delta and Valley groundwater, and treated wastewater reuse (km^3). The error bars shown account for estimates of wastewater reuse in the absence of data for those years [182] [176] [4] [226]. Sources for individual components in Fig. C-9. The black dotted line shows the reuse timeseries used in analysis. b. Total Fertility Rate (births/woman) plotted for Egypt [black line], Africa on average [blue line], and the world on average [red line] [258] (Table B.1.5). c. Virtual water imports (km^3) of agricultural goods (primary and secondary crops and animal products) scaled to Egypt use equivalent (Table B.1.1) (Table B.1.2) (Table B.1.3) (Table B.1.11).

was allocated 18.5 km^3 [257]. When the treaty was established, Egypt was consuming 48 km^3 according to the agreement.

In the 1980's Egypt began to experience an agricultural boom. This was achieved partly through expansion of agricultural area, especially on the edges of the Delta (dubbed the "New Lands"), and partly through yield increases in virtually every major crop (Fig. 2-4b). Egypt ranks among the highest yield producers of many crops including wheat, maize, rice and cotton [215]. While this increased water demand, a concurrent push to increase the reuse of water – from direct agricultural drainage, groundwater pumping, and wastewater reuse – made up for some of the increased consumption (Fig. 2-5a).

At the same time, Egypt begun a push towards reducing population growth, and reduced its total fertility rate by nearly half in thirty years, down to a rate of 3 births per woman in the late 2000's (Fig. 2-5b) [258]. This decrease has been much steeper than the fertility rate drops in Africa as a whole and on par with global fertility rate reductions.

Even with these adaptation measures, Egypt's demand continued to rise at a time when it was at full utilization of available natural water resources. Consequently, the 1970's were also the beginning of increases in agricultural imports, viewed here through the lens of their virtual water equivalent (Fig. 2-5c). The import rate increased dramatically after 2000, and the cereal import dependency ratio has increased from 34% to 42% from 1999-2001 to 2011-2013 [75] (Fig. 2-6). The bulk of agricultural imports consist of wheat and maize (Fig. 2-7).

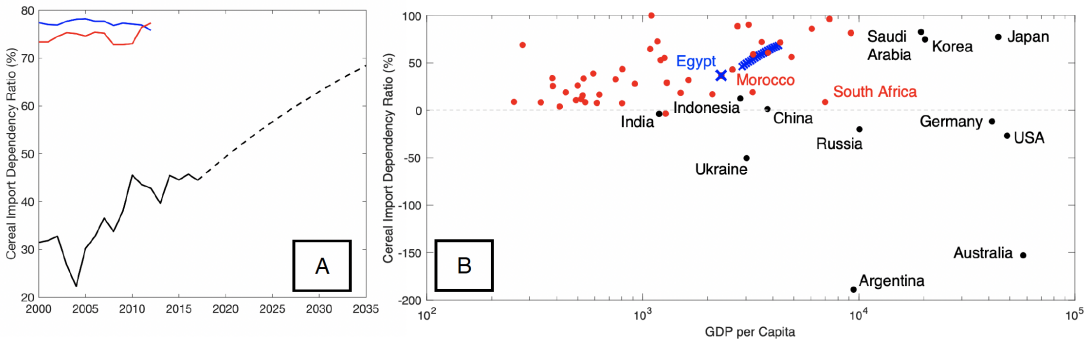

Figure 2-6: a) Cereal Import Dependency Ratio (%) using FAO data (2000-2017) and projected data for maize, wheat, rice, barley, and sorghum in the nominal scenario (2.3% GDP per capita growth and 1.7% population growth) (2017-2035) [black]. This is compared to the historical ratio for Japan [blue] and S. Korea [red] [75]. (b) 2003-2012 Avg. Cereal Import Dependency Ratio (%) vs. 2003-2012 Avg. GDP per Capita. African countries [red] and other select countries important for import and export relationships [black], Projected ratio for Egypt [blue x] in the nominal scenario (2018-2035). (Table B.1.6)(Table B.1.12)

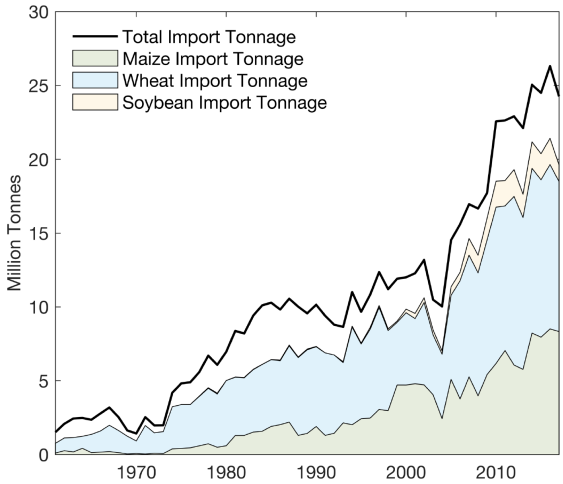

Figure 2-7: Total import tonnage (million tonnes) and breakdowns of maize, wheat, and soybean imports (million tonnes). (Table B.1.11)

2.3 Data and Methodology

2.3.1 Data

All data sources used can be found in Appendix B (Table B.1). Agricultural and trade data used in this study come from the Food and Agriculture Organization of the United Nations and is augmented by population and economic data from the World Bank and United Nations Population Division of the Department of Economic and Social Affairs. Water use numbers for available years are obtained from AQUASTAT, a division of the FAO.

The bottom-up analysis focuses on a group of crops that are selected with the goal of including the most significant water consumers. The primary agricultural crops considered in the analysis are wheat, maize, rice, seed cotton, sugarcane, sugar beet, banana, barley, broad beans, berseem, grape, groundnut, olive, onion, orange, potato, sorghum, tomato, dry beans, chickpea, lentils, green beans, lemons and limes, apples, mango, dates, watermelon, tea, sunflower seeds, garlic, strawberry, artichoke, cabbage, carrots & turnips, cauliflower & broccoli, chili pepper (green), cucumber, eggplant, melons, nectarines & peaches, pumpkins & squash, sweet potato, tangerine, vegetables fresh and leguminous (n.e.s.), and soybean. The grouping Fruits & Vegetables include Banana, Orange, Tomato, Potato, Onion, Olive, Lemons & Limes, Apple, Watermelon, Mango, Strawberry, Artichoke, Cabbage, Carrots & Turnips, Cauliflower & Broccoli, Green Chili Peppers, Cucumber, Eggplant, Melons, Peaches & Nectarine, Pumpkin & Squash, Sweet Potato, Tangerine, and other Vegetables Fresh & Leguminous n.e.s. Production, imports and exports focused on the primary commodity (i.e. no juices and processed forms) except when noted below. Secondary crops include cottonseed oil, maize oil, palm oil, raw sugar, molasses, cotton lint, cottonseed cake, sunflower seed cake, and soybean cake. Animal Products include beef, buffalo, sheep, chicken, milk (dried, whole fresh, whole skim), butter (cow & buffalo), eggs (hen in shell) and cheese (buffalo, whole cow, skim cow).

Per capita demand relationships developed for the period 1975-2014 with GDP per capita can be seen in Appendix C (Fig. C-1) for each individual crop. Only

primary products are considered in production (in country) water use numbers for the historical period to avoid double counting of feed and meat products. In the demand model used to project both future demand and create the historical hindcast, primary product demand is taken as the production and import quantity less the export quantity. Several of the crop products considered are traded primarily in their secondary form. When considering crop production, sugarcane, sugar beet and seed cotton were used. The secondary products sugar (raw equivalent), molasses, and cotton lint were used in terms of trade demand (imports minus exports). Therefore, products that are primarily exported are already accounted for in the production of the primary crop. Additionally, some crops have demand relationships that are heavily influenced by policy decisions – berseem, cotton, and sugarcane – and use a time-based relationship rather than one based on GDP per capita. All estimates of crop water consumption (historical production, historical imports, historical hindcast, and future projections) are scaled by irrigation application efficiency in order to simulate the Egypt equivalent use needed in order to meet the demand for those crops. Therefore, empirical and model-based estimates are consistent.

FAO data were available from 1961-2013 for most commodities, and available to 2017 in many cases. In the event that data were not available for the full period, the nearest recorded value to that date were used, and extrapolated outwards to ensure full period coverage for analysis. 2013 values were extrapolated to 2017 for cottonseed cake, soybean cake, sunflower seed cake, and artichoke imports. Berseem area, yield, and production values for 1978 are used for 1961-1977 and 2007 values are used for 2008-2017. Strawberry area, yield, and production values for 1980 are used for 1961-1979. Soybean area, yield, and production values for 1972 are used for 1961-1971. Sugar beet area and yield for 1979 were used for 1961-1978. Sunflower seed area, yield, and production values for 1971 were used for 1961-1970, and sunflower cake data from 1995 was used from 1961-1994. 2014 data were expanded to 2017 for Buffalo butter, Cow Butter production, buffalo cheese, skim cow cheese, whole cow cheese production, skim cow milk production and eggs (hen in shell). Import and Export data for skim cow milk were filled with zeros prior to 1994. Finally large

amounts of missing import data were replaced with zeros: pre-2000 for cabbages, all data except 2014/2016 for carrots and turnips, pre-1996 and post 2014 for cauliflower and broccoli, everywhere except 2013-2016 for chili peppers (green), pre-1993 for garlic, 1961-1999 for strawberries, pre-1997 and post-2013 for cucumber, everywhere except 2015 for eggplant, pre-2005 for melons, in 2014 and 2016 for sweet potato and tangerine and in 2016-2017 for fresh vegetables (n.e.s.). For 2014-2017, food supply data were filled in using the New Food Balances data where available. This may cause slight inconsistencies due to differences in classification or calculation method. Beyond this extrapolation of data to ensure consistent availability of data between commodities, all publicly available data were integrated into the analysis, including FAO estimates. No data were removed due to flagging by the FAO as being an estimation or reconstruction based on a secondary source. Production, yield, and harvested area data for primary crops can be seen in Fig. C-2 & C-3.

Overall water use numbers for Egypt have low independence between sources and are often available for only a handful of years in the last several decades. Most of the official numbers provided are dictated by the bounds established in the 1959 agreement between Egypt and Sudan where the former was allocated 55.5 km^3/yr and the latter was allocated 18.5km^3/yr [257]. According to flow measurements at Dongola, near the Sudan-Egypt border, the 30-yr average flow (1988-2017) was 74.7 km^3/yr [59]. All sources of water except desalination are included in this analysis. Municipal use, industrial use, and reuse values are interpolated and extrapolated from available data and literature values (Fig. C-9). So far, the increase in per capita water usage seems to have tracked closely with increases in per capita GDP. This growth may have also been driven by the increase in city population. The percentage of the population living in cities remained stable from 42.8% in 1995 to 42.7% in 2017 (United Nations), however, because of the increase in population this means that in 2017, roughly 14.5 million more people lived in urban areas compared to 1995. We do assume though that per capita municipal consumption will remain constant in the future at roughly 112 m^3/capita/year (305.4 liters/capita/day) [72] and project municipal water demand for a range of population projections (Fig. 2-8).

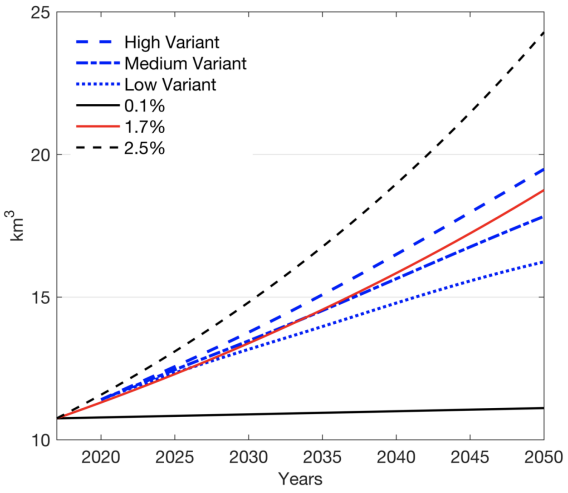

Figure 2-8: Municipal water use projections (km^3) based on population projections in Figure 2-11b. (Table B.1.4)(Table B.1.16)

Crop ET requirement numbers were taken from a single source for consistency and because they were specific to Egypt and the use of irrigated water [162] [164]. For commodities that are traded in substantial amounts but not grown in Egypt (e.g. tea), a blue water number taking into account the source of the imports was used [165]. This study is concerned with irrigated water from the Nile and therefore uses only blue water numbers, which refer to the amount of surface and groundwater consumed [162]. In general, the numbers align with the water requirement numbers collected from the FAO which are given in terms of irrigation requirement [63]. Differences likely arise because FAO numbers are non-region or cultivar specific. In country water consumption numbers is used for all crops and animal products, even when exploring virtual water and trade, as we are interested in the magnitude of water that trade replaces and what would otherwise be in-country production and consumption of water. Berseem water use numbers are not available from the same source and are taken from a study on evapotranspiration needs of berseem in northern India, a location at roughly the same latitude and average PET during the growing season [256]. This number is taken as the 2007-2011 average and scaled in the same manner as other crop water requirements discussed below.

In order to determine the water use requirements of different crops through time,

this analysis understands that water application is a factor in determining yield. However, yield growth is also influenced by fertilizer application, climate, seed variety, soil salinity, and other management and ecological characteristics. In order to develop a realistic water requirement function, a 1996-2005 average crop ET water requirement is taken from the literature [162] and combined with the available FAO data on production, area harvested, and yield. Two scenarios for Nile water consumption for historical crop production were devised, both based on the literature value for crop specific, Egypt specific water consumption and the 1996-2005 averages of production and harvested area. The first is an estimate using a constant m^3/ha for each crop, and the second uses a constant m^3/tonne value. These estimates, scaled for irrigation application efficiency, can be seen as the blue and red lines in Fig. C-7. In order to account for factors such as increasing yield and increasing water application, as well as the other yield influencing factors above, we settle on a m^3/tonne water consumption requirement that equates to the average of these two estimates. This can be seen as the black line in Fig. C-7. It is important to note that all crops are assumed to receive exactly their water requirement in any given year. Per tonne water requirements for secondary commodities remain constant due to the absence of comparable yield and area data and use the 1996-2005 average water requirement throughout.

There are three main areas of input uncertainty in the agricultural analysis: crop water consumption numbers, the accuracy of agricultural commodity data (production, yield, area harvested etc.), and availability of water use data. Mekonnen and Hoekstra (2010) list a number of uncertainties in their calculation of the water consumption numbers including the lack of crop specific irrigation data, the low spatial resolution of crop growth seasons and fertilizer application, the actual level of irrigation supplied, and the effect of factors other than water stress on crop yield [161]. Despite these uncertainties, most of the crops fall within the range of FAO water requirements. FAOSTAT does not release official measures of uncertainty or error for their data as it is aggregated by the individual countries. However, in some cases official data are supplemented with estimates or aggregate data from other sources. All available data from FAOSTAT were used in the analysis, and missing data were

filled in as noted. Only in the calculation of trade value/quantity was the data limited to official numbers only. Finally, only a few data points were available for the construction of time series of municipal and industrial use and reuse. Interpolation was used between the available data, and for reuse, error bounds were added in Fig. 2-5a where data for a component were missing or inconsistent across sources. The largest component of uncertainty in the historical reconstruction of water use was the scaling of crop water consumption requirement through time and a visual comparison of several analysis options is available in Fig. C-7. Additionally, this analysis included most of the main players, but there are some commodities and products not included and the analysis focuses on the production and trade of the primary commodity except where noted.

2.3.2 Terminology

In this study water use is used to define the water taken from the Nile. Total Use is defined as the water withdrawn for industrial, municipal, and agricultural purposes. This use is added to reuse in order to determine the total demand for water in the country. In the case of agricultural use, crop water consumption is scaled by irrigation application efficiency, and then reuse is accounted for. Water consumption is based solely on the crop ET water requirement numbers taken from the literature. This definition of total Nile water use aligns with the AQUASTAT definition of freshwater withdrawal, which is the total withdrawal less desalination, direct use of treated municipal wastewater, and direct use of agricultural drainage water. This estimate counts subsequent pumping of local groundwater recharge as a reuse component, which is not the case in the AQUASTAT totals.

2.4 Results

2.4.1 Reconstruction of Historical Nile Water Use

This study applies a bottom up, individual crop-based estimate of agricultural water consumption and virtual water trade, using the assumptions covered above. This empirical reconstruction of water use is completely independent from official use estimates, and depends only on agricultural data, the physiologically based estimates of water requirement, and an estimation of irrigation application efficiency based on the use of different irrigation technologies. A comparison to AQUASTAT agricultural withdrawal figures adjusted with reuse estimates can be seen in Fig. C-7.

Adjustments must be made to account for system losses between withdrawal of water from the Nile and field application, known as irrigation application efficiency (water use efficiency at the field scale). This irrigation application efficiency is calculated using proportions of irrigation type and the attributed efficiencies of the technologies [27]. The curve of irrigation application efficiency moves from roughly 61% in the 1960's to 66% in the mid 2010's and can be seen in Fig. C-6. This loss rate is consistent with figures given in the literature [3]. As seen by these low efficiencies, and the small progress made in improving them in the last 50 years, the main true loss in the system is soil evaporation at the field scale.

Here we dissect water demand in Egypt, from in-country production and trade, and identify which crops dominate in-country water use over time (Fig. 2-9a). This analysis is made possible by the extensive and influential work in water footprint accounting for agriculture at the global and regional scale [167] [166]. Figure 2-9b shows the agricultural use estimates combined with other water demands (municipal, industrial, reuse), compared to the available Nile water flow into Egypt which encompasses all water not consumed upstream. Two major conclusions about Egypt's water demand are clear from this comparison.

First, Egypt began fully utilizing available local water resources in the late 1970's and has only met total water demand through increasing virtual water imports (dark grey shading) and increasing reuse (light red shading). Increases in irrigation ap-

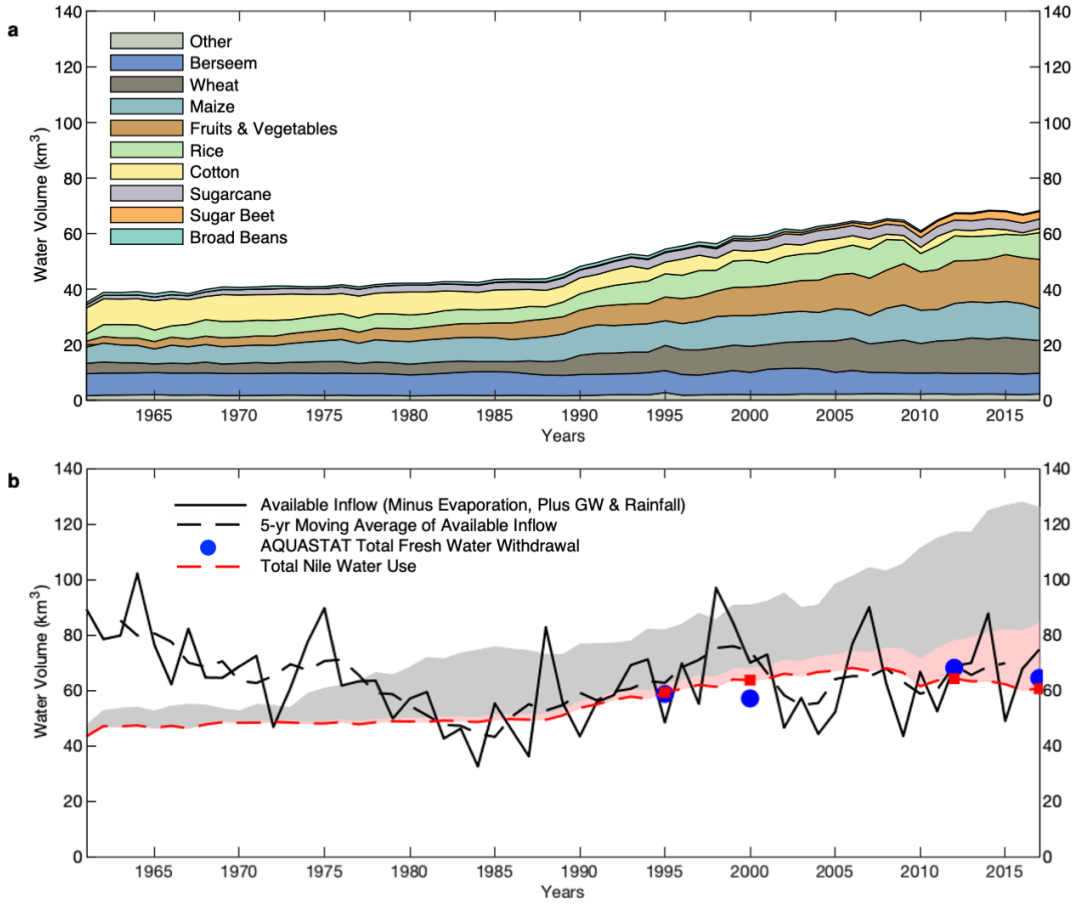

Figure 2-9: a. Historical water application in Egypt for agriculture broken down by crop (Table B.1.1) (Table B.1.2) (Table B.1.7) b. Historical total Nile water use (km^3) (agriculture + municipal + industrial - reuse) [red dotted line] compared to available supply [black lines]. Red squares mark values for 1995, 2000, 2012, and 2017. This is the flow at Dongola station adjusted by evaporation at Lake Nasser and from other surface water bodies (estimated at 10 km^3 and 2 km^3 respectively) [68], with added rainfall and primary groundwater abstraction (1.5 km^3 and 0.5 km^3 respectively) [2] [70]. Storage change in Lake Nasser is not considered in this availability estimate. These are compared to the AQUASTAT numbers for freshwater withdrawal in Egypt [blue dots] [164] (Table B.1.16). Dark Grey shading represents the amount of Virtual Water Import (km^3) (shown in Fig. 2-5c), and light red shading shows the amount of drainage, wastewater reuse and GW reuse (km^3) (shown in Fig. 2-5a). These shaded areas represent the additional demand met by these sources, and not a range of values.

plication efficiency, and to a greater extent water reuse, have improved the water productivity of major crops and allowed Egypt to survive on a relatively constant Nile water use in the past two decades (Fig. C-4 & C-5).

Second, even after accounting for reuse utilization in Egypt (Fig. 2-5a) this analysis shows that Egypt's direct consumption of the Nile water is roughly 61.5 km^3 on average from 1988 to 2017 (Fig. 2-9b). This aligns closely with water accounting in the literature for the modern period [4]. Adding the environmental flow to the Mediterranean of about 2-4 km^3 [89], Egypt utilizes 8.0 to 10.0 km^3 more than the share of 55.5 km^3 allocated through the 1959 Nile Agreement between Egypt and Sudan [257]. This additional water comes partially from Sudan's unconsumed share of 1.8-5.5 km^3 out of the 18.5 km^3 enumerated in the 1959 Agreement [182], and partially from increases in the Nile flow of about 5-6 km^3 [59] [238] [3]. An accounting of Sudan's historical use of the Nile water is beyond the scope of this Egypt-centric study but is reported to be 13-16.7 km^3/yr [189] [227] [277]. Much of the increased water demand in Egypt has been met by virtual water imports, which reached 40 km^3 in the 2010's (Fig. 2-5c), a figure supported by other studies that quantified historical virtual water trade [3] [4] [188].

Virtual water import is calculated identically to in-country use which is detailed in the data and methodology section. A comparison of the Egyptian Nile water system for 1988-1995 and 2010-2017 is presented in Figure 2-10 to further document the evolving dynamics of water supply and demand in Egypt. This schematic relies on several independent sources of data where each flux is uncertain, and hence it does not necessarily satisfy strict water balance. A notable feature is the difference in evaporation from Lake Nasser between the two periods which arises from a 1000 km^2 difference in lake area (roughly 30%). (Table B.1.15, Table B.1.17)

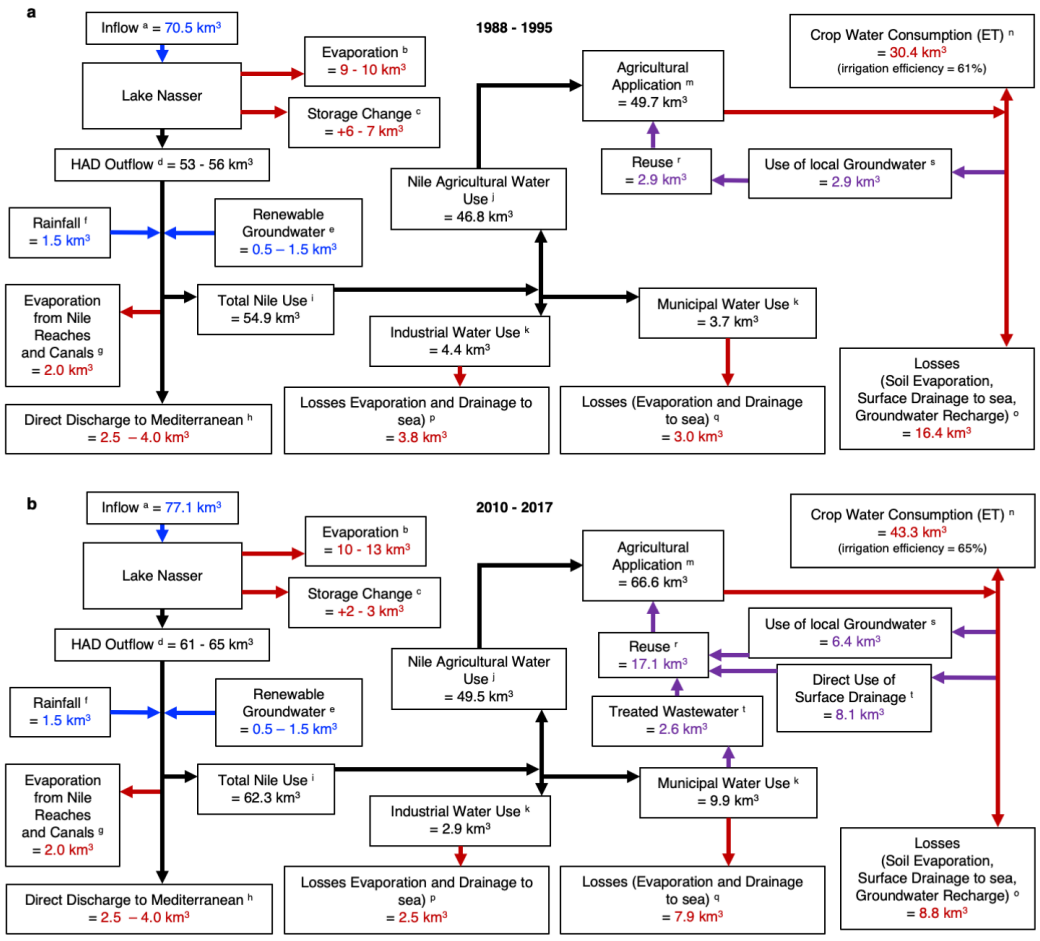

Figure 2-10: a. Egyptian Nile water system 1988-1995 average annual fluxes (km^3/yr). Red values are sinks, blue are sources, and purple indicates reuse. b. Same as panel a but for the period 2010-2017. A figure for the average fluxes from 1988 – 2017 can be seen in Fig. C-13. [a] Average annual inflow at Dongola. (Table B.1.14) [b] Average annual Evaporation from Lake Nasser, 10 km^3 from literature [68] and outer bound calculated using Lake Nasser height (Table B.1.17), Height-Volume equation (Table B.1.15), and CRUTS4.04 Potential Evapotranspiration (Table B.1.13) [c] Average annual storage change calculated using Lake Nasser height (Table B.1.17 and, Height-Volume equation (Table B.1.15) [d] Average annual outflow calculated through water balance of (a) – (b) – (c). Range of values reflect uncertainty in Lake Nasser balance components. [e] AQUASTAT [70] [f] [2] [g] Calculated through estimation of surface area and evaporation rate. Confirmed in [176] [4] [h] [89] [i] Calculated through methodology described in Methods. [j] (m) – (r) [k] AQUASTAT Database [72] (See Fig. C-9) [m] (n) * Irrigation Application Efficiency (See Fig. C-6) [n] Calculated from production and water consumption data as described in Methods. [o] (m) – (n) – (t) – (u) [p] (k) * 0.86. Loss rate from [188] [q] (l) * 0.80. Loss rate from [188] [r] (s) + (t) + (u). See Fig. C-9. [s] [226] [69] [171] [148] [t]. AQUASTAT Database [72]. (Table B.1.16)

2.4.2 Projections of Future Water Demand

Future projections for water demand are made starting in 2017 and shown in this study until 2035. The main assumption in the projections is that all additional demand, which is driven by population increase and GDP per capita increase, will need to be satisfied through imports as Egypt is at its in-country production limit already.

There are two drivers of growth: population increase adds a full person's worth of demand, and economic growth adds marginal demand to existing populations. The range of population projections considered in the future scenarios span from 0.1% to 2.5% annual growth and encompass the range of growth scenarios given by the United Nations [259], and the 30-yr historical rate falls in this range as well. Similarly, the economic range of scenarios considered was 0.1% to 4.5% annual growth, which also contained the historical 30-yr growth rate. In order to present a single likely scenario to focus on when interpreting the projections, a nominal scenario is highlighted. This scenario reflects 2.3% GDP per capita growth to match the last 30 years, and 1.7% population growth to match the UN Medium Variant Projection by 2035 [259] (Fig. 2-11).

In order to anchor the future projection and also make it compatible with the hindcast reconstruction, all future values were calculated as additional values versus 2017 levels. Extrapolation of future demand for water is done through a historical linear regression of GDP per capita and demand or trade demand depending on the commodity from 1975-2014. No upper limit is imposed on the estimates of demand. Berseem, seed cotton, and sugarcane per capita demand is held constant in the future to account for demand changes that are policy rather than growth driven, and to avoid combining an increased demand for meat from out of country and forage crops. The total tonnage demand of these crops will still increase due to population growth. As with historical imports, the water value given is in terms of an Egypt equivalent use by scaling with irrigation application efficiency.

Future projections include water demand coming from agricultural goods, as well

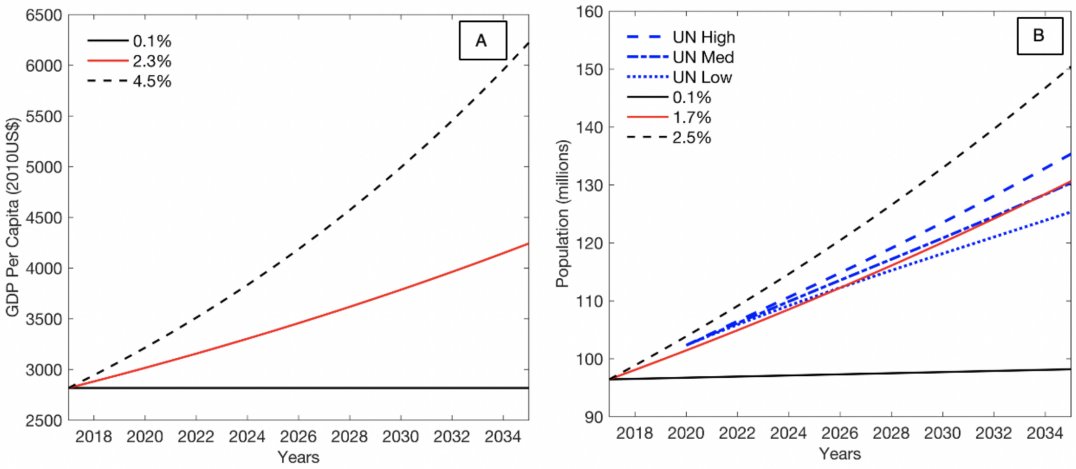

Figure 2-11: (a) High and low projections of GDP per capita (2010US$) growth (%) used in the study (black) along with the projection that follows the past 30-yr average growth (red) used as the nominal scenario. (b) High and low projections of population (millions) used in the study (black) alongside the high, medium, and low variant UN population projections (blue). Also plotted is the projection that follows the UN Medium projection scenario (red) and is used as the nominal scenario. (Table B.1.6)(Table B.1.4)

as from increased municipal use. Industrial use and reuse were not extrapolated and were held at 2017 levels, since they are influenced more strongly by policy and other drivers than just population and GDP growth. To maintain the scaling performed in the historical analysis, future water requirement numbers for individual commodities are the 2012-2017 average water requirement values.

Historical analysis has shown that Egypt is fully utilizing the available resources of the Nile River and yet is facing increasing internal and external pressures that will raise water demand and decrease availability of water. As detailed in the data and methodology section we develop an empirical model of historical and future water demand in Egypt with population growth and economic growth as inputs. Assuming a range of economic and population scenarios (Fig. 2-11), and the empirical relationships between demand for crops and economic growth (Fig. C-1), we project future water demand for Egypt.

In keeping with this discussion about Egypt's characterization as the gift of the Nile, this study projects when Egypt's imports of virtual water will reach 61.5 km^3

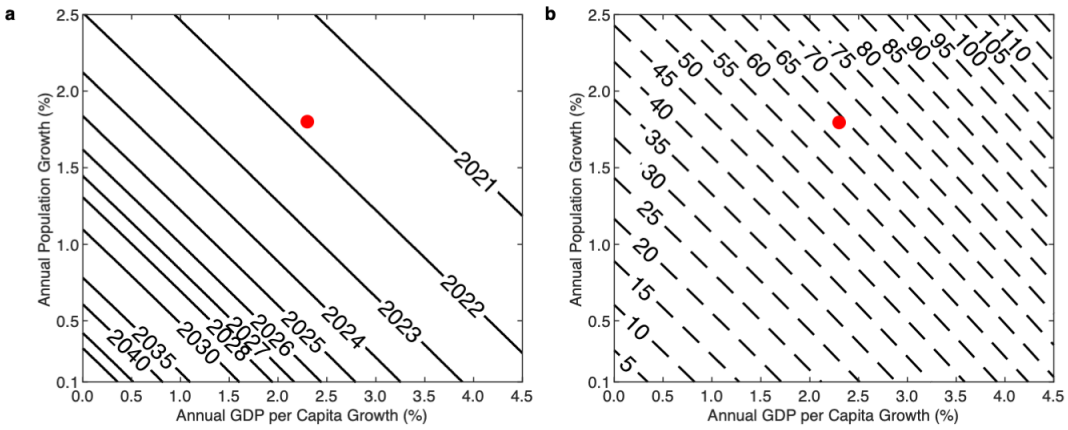

Figure 2-12: a. Projected Year that Virtual Water Imports will Reach 61.5 km^3 with population increase and GDP per capita increase. Future increases in demand are added to the Hindcast (model) estimate of total demand minus total estimated Nile use. The red dot marks the nominal scenario of 1.7% population growth and 2.3% GDP per capita growth. b. Additional virtual water (km^3) needed in 2030 to satisfy increased demand (i.e. projected virtual water Imports in 2030 values minus 2017 virtual water import amount). The red dot marks the nominal scenario of 1.7% population growth and 2.3% GDP per capita growth.

(the thirty-year average Nile water use for all purposes, accounting for both reuse and application losses), driven by an increase in demand that must be met externally (Fig. 2-12a). For scenarios that assume population and economic growth rates close to the growth rates over the past thirty years, this important benchmark will be reached in this decade of the 2020s.

By 2030 the projected trend corresponds to a significant increase in virtual water imports in most population and economic growth scenarios (Fig. 2-12b). To visualize this process along one growth trajectory, we show the projected virtual water imports for a nominal scenario with a GDP per capita growth rate that matches the 1988-2017 average (2.3%) and a population growth rate that matches the UN Medium Variant population projection in 2035 (1.7%) (Fig. 2-13). This is paired with increased demand in the municipal sector, which will need to be met by reallocating internal resources. The rate of increase of virtual water goes up over time (dashed black line) due to the compounding nature of the population and economic growths, as more people enjoy higher consumption rates per capita.

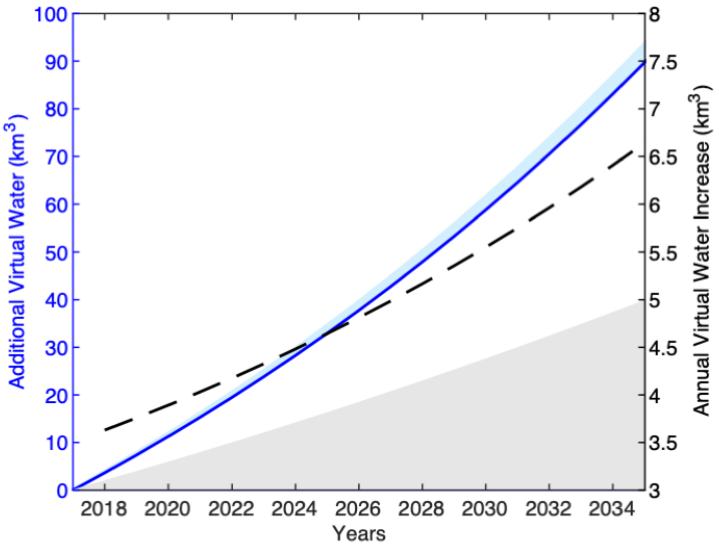

Figure 2-13: Additional Virtual Water Demand (km^3) [blue line] and Annual Increase Rate (km^3) [black dotted line] for a nominal growth scenario (1.7% population growth, 2.3% GDP per capita growth) versus 2017 levels. Light blue shading represents the increased municipal water demand. Grey shading represents the additional virtual water imports in a 0% GDP growth, 1.7% population growth scenario.

We apply the same demand relationships described in the data and methodology section to hindcast the historical water demand using data on population and GDP per capita data. As expected, the hindcasted water demand is close to the sum of the in-country Nile water use (which also accounts for municipal and industrial use and the water reclaimed from reuse) and virtual water import, which together meet the historical demand (Fig. 2-14). The future projection is less linear than the historical hindcast, mainly because the hindcast accounts for increasing reuse, which bends the demand curve downwards at an increasing rate in the early 2000's. The future projection assumes the rate of reuse to be constant post-2017. This is further evidence of the importance of improving irrigation application efficiency.

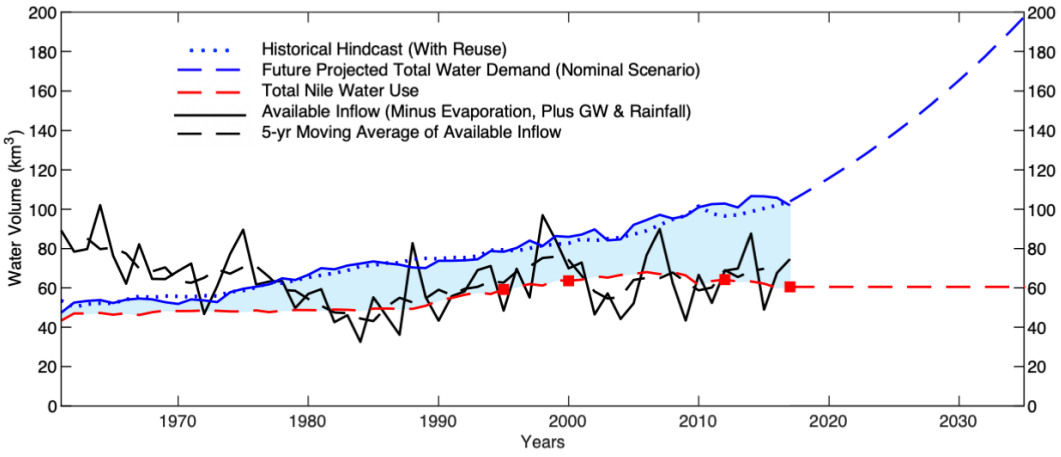

Figure 2-14: Historical (1961-2017) hindcast of total water use paired with the nominal projections of total water needed in Figure 2-13. The blue dotted line shows the total hindcasted water use (km^3/yr), including efficiency scaled total agricultural demand, municipal use and industrial use, and reuse. This is compared to the sum of historical virtual water imports (km^3/yr) [blue shading] and the total Nile use estimate (km^3/yr) [red dashed line] and is shown as the solid blue line. Future projections are divided between in-country consumption (km^3/yr) [red dashed line] and increased virtual water demand (km^3/yr) [blue dashed line]. Red squares mark total Nile use estimate for 1995, 2000, 2012, and 2017.

2.5 Policies to Meet Future Water Demand and Calculation of a Virtual Water Trade Balance (VWTB)

We have shown through the reconstruction that Egypt has taken several measures to manage historical water demand and increase available supply. However, the country is increasingly constrained by its ecological bounds. Throughout the last several decades it has increased land productivity and water productivity, decreased human fertility rates, and increased trade in order to meet demand. However, these measures have only kept Egypt at the edge of satisfying water demand. Egypt reached full utilization of the Nile in the 1970's and has been cutting and compensating ever since. The reconstruction of past water uses and adaptations allows an identification of avenues for management changes that grow out of historical successes and failures. In order to underscore major principles underlying proposed policies, we recommend the consideration of a hybrid of policies that we have grouped under two conceptual

umbrellas:

1. **Water Value Appreciation (WVA)** strategies revolve around recognizing and leveraging the true value of water as a limited resource through a robust water pricing system, improving irrigation application efficiency at the field scale, and adjusting cropping patterns to emphasize ecological suitability and water use efficiency.

2. **Water Share Amplification (WSA)** strategies focus on maximizing per capita water share through an approach of smart and efficient management of agricultural import and export (virtual water trade), applicable to arid countries in general, that amplifies Egypt's share of natural water resources. Part of this efficient trade balance includes sourcing meat from neighboring countries and strengthening inter-basin ties with Sudan and Ethiopia.

We also propose further focus on reduction of population growth rate as a means of reducing strain on already scarce per capita water supplies. These proposed measures will help balance the supply of water and Egypt's growing demand and are discussed further below.

Egypt must place more concrete value on water in the future. Despite Egypt's status as a water scarce nation, there has been a disconnect between this scarcity of water and its price. Water tariffs for residential customers are among the lowest in the world (between \$0.03 and \$0.12 per m^3 in 2017) and are slightly higher for industrial and commercial customers [84]. More problematic is that farmers are not charged for irrigation water [40]. This does not encourage water use efficiency, and actually incentivizes waste, as increased application of water is often thought to boost crop productivity all else being equal. Water pricing for farmers should be tied to either the marginal cost of increasing water supplies or to the cost of increasing water use efficiency though others have noted the obstacles to increasing this efficiency [141].

One of the main changes in attitude that must occur is shifting value from land to water. Land in Egypt is plentiful, and water is not; previous policies were designed as if the opposite is true. From 1980 to 2000, Egypt dramatically increased its crop

yields through the use of more water and the adoption of agricultural technologies such as fertilizer (Fig. 2-4b; Fig. C-2; Fig. C-3) [110]. This effort was focused on land productivity (tonnes per unit area), a resource that is much less constrained than water. Water productivity (tonnes/m^3) did not improve as drastically until the more recent aggressive implementation of reuse technologies (Fig. 2-5a; Fig. C-4; Fig. C-5). Even now, though yields of maize are as high or higher than much of the world, their local water consumption requirement is up to 200 m^3/tonne higher than in the countries where Egypt imports maize from [163]. Egypt has improved their water reuse – from groundwater, wastewater, and direct drainage reuse – but has made comparatively little progress in irrigation application efficiency at the field scale, where the true loss occurs through soil evaporation. This rate of soil evaporation is higher for low-efficiency technologies that do not target the plant specifically and deliver controlled amounts of water that can be fully utilized for transpiration [27]. Reducing conveyance and application losses are key in increasing water productivity in agriculture [188] [247] however there are policy challenges in incentivizing change and ensuring that savings in one sector do not incentivize waste in another [86].

More efficient application necessarily reduces the amount of available reuse. Additionally, attempted increase in reuse in areas such as local groundwater use may lead to unsustainable practices of over pumping. Egypt has made great strides in exploiting available sources of reuse, so much that in 2017 they captured and reused as much as the applied agricultural water that did not go to plant evapotranspiration (Fig. C-12). Fig. 2-10 shows that municipal and industrial uses are still a viable target for loss reduction, as Omar and Moussa (2016) cite the respective loss rates of these systems at 80% and 86% [188].

Reducing loss in these systems is also important as population growth will create increased demand. Measures need to be taken in order to maximize the available water on a per capita basis. This can take many forms; first Egypt needs to strive further to reduce fertility rates and slow population growth. Although fertility rates have fallen below the average fertility in Africa (3.3 versus 4.4 births per woman in 2018, see Fig. 2-5b) they are still well above the global average of 2.5 [258].

Subsequently, selection of crops that are ecologically suited and easily irrigated using high efficiency measures should be a key goal for future agricultural policy. For example, the expansion of olives is an option as a crop that is well suited to the regional climate and to the use of drip irrigation methods. This expansion is already planned for Egypt, and their efficiency under drip irrigation suggests a promising role in Egypt's export portfolio [96] [175].

The projections of future demand presented here show that Egypt will also need to rely more on trade, both from outside the Nile basin and from basin trading partners [12]. There is resistance to increasing imports of food products – especially staple goods such as wheat – due to national security concerns, as well as the importance of agriculture in the labor sector [282]. The 2012-2017 FAO Country Programming Framework (CPF) proposes ambitious targets to increase self-sufficiency by 2030 [67]. However, food security priorities are best coordinated with efforts to decrease water demand in order to increase overall resilience. This is especially important in light of difficulties imposed by the COVID-19 pandemic. Currently 69% of Egypt's main import, wheat, comes from Russia, and roughly 90% from Russia and former Soviet Republics [80]. As exporters of staple products, such as Russia, cut back in light of their own production concerns during the coronavirus pandemic [213], Egypt needs to re-examine their relationships and dependencies. Future import policies need to ensure that Egypt is not totally dependent on one import or export crop, and not dependent on one country for buying or selling goods.

One opportunity for Egypt to increase their imports of virtual water while saving water internally is through the import of meat from neighboring countries, particularly Sudan. In 2007-2011 Egypt withdrew an average of 7.4 km^3 of water from the Nile for in-country production of berseem, also known as Egyptian clover, which is a major feed crop. In total, feed crops consumed in 2010 had a consumptive demand of 15 km^3 (Fig. C-10). At the same time their import of red meat (beef and buffalo) has not increased substantially despite an increasing appetite (Fig. C-10). On average in 1998-2004, Egypt imported the equivalent of 18.3 Mm^3 of virtual water in sheep from Sudan, although livestock movement across the Egypt-Sudan border is

often under-documented [289]. Sudan currently raises livestock almost entirely under rain-fed, nomadic conditions although this could change with future irrigation development [71]. Reducing cultivated area of berseem and importing meat instead would save water, free up land, and increase inter-basin ties that could encourage greater cooperation down the road on water and economic issues. However, there are caveats to this approach, as berseem has long been used as a rotation crop with other cereals to preserve and renew soil quality [53].

2.5.1 Virtual Water Trade Balance

We investigate the Virtual Water Trade Balance (VWTB) as a concept of maximizing the water available to a country, both in terms of water productivity and in terms of market value. Using the trade relationships between crops, we can quantify the impact of shifting production away from water intensive but relatively cheap-to-import goods like grains, and instead focus on high value crops like fruits and vegetables that have lower water consumption requirements or are better candidates for higher efficiency irrigation technologies.

In order to develop this policy proposal, a tabulation of the tradeoffs between crops was necessary. A calculation of overall VWTB for exports and imports can be found in Table B.2 and uses data from FAO for 2007-2011. In order to avoid inconsistencies in reporting over such a short period, only years with official data were used in the calculation of trade value and quantity. A crop-by-crop comparison table can be found in Table B.5, and was calculated using the following formula:

VWTB = (tonnes of Crop A purchased using 1 km^3 of water to grow and sell crop B) / (tonnes of crop A grown with 1 km^3 of water)

In a hypothetical trade transaction in which all the revenue from exporting crop B is used to import crop A, VWTB is calculated as the ratio of the virtual water volume imported and embodied in crop A per unit volume of virtual water exported and embodied in crop B. Simply, the VWTB number given is a measure of units of virtual water imported for each unit of water exported.

The VWTB for Egypt overall is currently 2.31 (Table B.2). Meaning that they are

making 2.31 times more revenue than they are spending, per unit of consumed water traded, or in other terms each unit volume of virtual water exported facilitates 2.31 units of virtual water imports. Using a set of water share amplification metrics calculated for current crops produced and traded we develop a policy proposal presented in Table B.6. Additional considerations of irrigation method may make some crops more advantageous, but only if irrigation systems are well maintained and operated to reduce losses.

Regarding the suite of policy umbrellas proposed above, no single solution will be able to compensate for all additional needs. Measures must work to mitigate internal demand (water pricing, reduced fertility rates, and optimized cropping patterns), increase internal supply (through improving irrigation application efficiency at the field scale), as well as leverage Egypt's advantages to form stronger ties with neighbors and the global market.

2.6 Discussion & Conclusions

Egypt's responses to increasing water demand in the past have demonstrated the severity of the water scarcity situation, and historical adaptations to rising demand on water will need to continue and strengthen. Efforts targeting an increase in productivity of agriculture should pivot to recognizing and leveraging the true value of water as a limited resource through a robust water pricing system [254]. As virtual water imports increase, smart management of agricultural export and import portfolios can leverage Egypt's high agricultural yields and amplify their share of natural water resources through the export of high value, high water efficiency crops (fruits and vegetables) and the import of low value, low water efficiency crops (grains). Inter-basin connectivity will be key in the future and using these relationships to import water-intensive commodities like meat can allow allocation of water elsewhere [289]. Finally, studies have shown that a high rate of population growth is one of the most important factors in worsening future water deficits [3], and further reducing rates of growth through proven methods like healthcare expansion and education [179] will

slow decreases in per capita water share, a key metric of water scarcity.

Increased industrial demand for water will come with economic growth and diversification, and tourism and urbanization will drive municipal demand. As Egypt's neighbors grow alongside Egypt, they have already begun to exert new pressures. This is especially important with the imminent completion and filling of the Grand Ethiopian Renaissance Dam (GERD). The effect of the GERD was not quantitatively included in this analysis, but is acknowledged as an additional potential stressor, especially with regards to increased upstream withdrawals [277] [18].

Demand and supply of water will also be affected by climate change, although we do not analyze those changes in this study. At a large scale, while climate change will result in small increases in the mean flow of the river, it will increase inter-annual variability of flow and increase the need for additional storage [238]. Sea level rise and saltwater intrusion are already a threat to freshwater resources in the Nile Delta and will further affect the potability of water for agricultural and municipal purposes [104] [1]. Increased temperatures will affect both agricultural productivity and crop suitability, and also increase rates of evaporation from surface water and the field [99]. Optimizing ecological suitability and irrigation systems is crucial for being able to adapt to future changes more easily.

In the framing of this study, we posed the question of whether Egypt will continue to be the gift of the Nile. Historically and culturally the two are synonymous, and Egypt was, is, and will continue to be dependent on the resources the Nile provides. However, historical reconstruction and future projections show that the level of dependence has been and must continue to change. In the near future, Egypt will be dependent on external virtual water to the same level as its level of dependence on the River, and policies and attitudes will need to reflect and adapt to this new reality. Through the reconstruction of Egypt's water demand we have shown here that Egypt is approaching a threshold between the Nile as a dominant force in sustaining Egypt's growth and existence, and a new paradigm characterized by an equally important role for basin and global interconnection and cooperation.

The results presented here illustrate that the future of water in Egypt is just

as reliant on external cooperation with its neighbors as it is on its own ability to optimally manage internal demand and use of water. Adaptations are ultimately in Egypt's best interest, as they allow for continued growth and prosperity with more careful management of resources. Egypt has the chance to be an example for other developing water scarce nations, and a leader in the Nile Basin. If changes are not made it will soon serve as an ecological cautionary tale with implications for the entire region.

Chapter 3

Summer Climate Change in the Midwest and Great Plains due to Agricultural Development during the Twentieth Century

Relevant Papers and Presentations

Nikiel, C.A. and E.A. Eltahir, 2019: Summer Climate Change in the Midwest and Great Plains due to Agricultural Development during the Twentieth Century. *J. Climate*, 32, 5583-5599, https://doi.org/10.1175/JCLI-D-19-0096. [180]

Nikiel, C.A. and Elfatih A.B. Eltahir (2018). Regional Climate Change in the Central United States due to Agricultural Development during the 20th Century. Presented at the American Geophysical Union (AGU) Fall Meeting, Washington, D.C. December 2018.

3.1 Introduction

The Midwest and Great Plains of the United States contain some of the most productive and expansive areas of agricultural land in the country as well as sizable proportions of the population. This area, colloquially known as the Cornbelt, is one of the highest yielding global agricultural areas for maize [20] and the United States is a leading exporter of soybeans and corn [240, 241]. Additionally, urban centers such as Chicago, Illinois, Indianapolis, Indiana, and Columbus, Ohio are in the top 20 most populous cities in the United States [260].

While definitions of the Midwest and Great Plains differ, this study focuses on states that encompass the areas of highest agricultural development and production — North Dakota, South Dakota, Nebraska, Kansas, Minnesota, Wisconsin, Missouri, Michigan, Iowa, Illinois, Indiana, and Ohio. Agricultural development has dominated land use change in this region during the 20th century and is an increasingly important area of focus for climate studies [203, 202]. Cropland areas are particularly sensitive to drought and other extreme conditions, and the economic importance of this region makes understanding regional and local climate impacts here a particular concern. Assessments have noted that damages to agriculture in these regions from drought, floods, and extreme heat are among the biggest threats in a changing climate [263].

While crops are impacted by climate change, large scale agricultural land use has been shown to have climate feed-backs. Several studies suggest that rapidly changing land use conditions in the 20th century may have partially masked the signal of greenhouse gas (GHG) triggered climate change in this region [24, 131]. In the exploration of the climate-agriculture-water nexus in this thesis, we approach this topic with an understanding that agriculture impacts the other two factors as it is itself impacted by them.

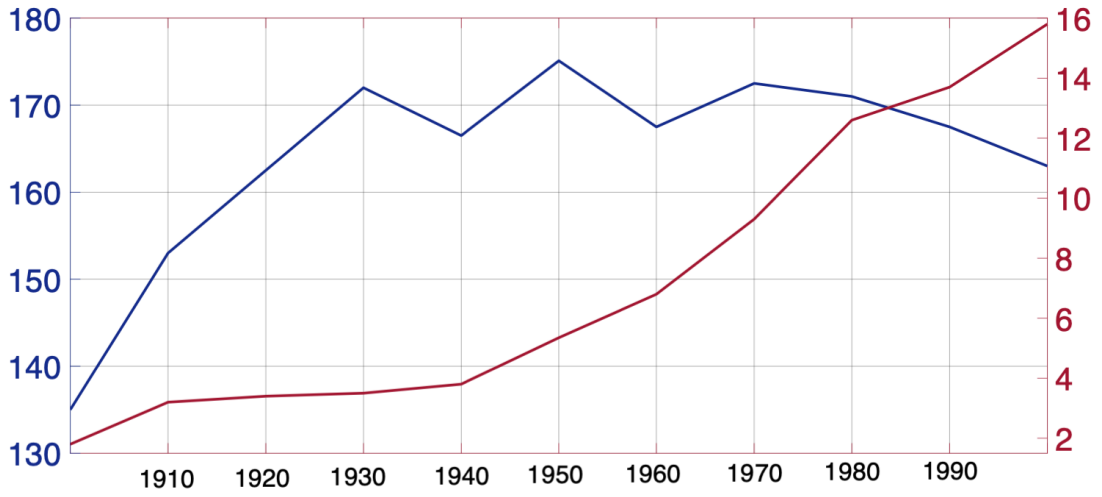

Figure 3-1: Million hectares of irrigated [red] (HID [239]) and non-irrigated [blue] (LUHv1 [33]) cropland in the model domain area (30-51N,71-112W) from 1900-2000

3.2 Background

Cropland expansion and redistribution has been widespread in the Central United States in the 19th and 20th centuries. Cropland areas have largely disappeared in the East while they have replaced open grassland in the Great Plains up through Canada. Small fluctuations occurred throughout the 20th Century but the majority of changes in cropland distribution happened prior to the 1940's (Fig. 3-1).

Another major agricultural change has been an increase in yield. Corn has seen an average yield increase, weighted by annual state production total, in the Midwest of 370% from 1900 to 2016, with almost all the increase occurring after 1935 [262] (Fig. 3-2). Soybean has seen a weighted average yield increase of 400% from 1924 to 2016 (Fig. 3-3). This increase in yield is attributed partially to management improvements like mechanization, fertilizer, and new varieties [56] and partially to more favorable growing conditions [130] [224].

While the larger trends in both of these crops are positive and linear, the time series are marked by a large inter-annual yield variability, and clearly show losses attributed to major seasonal events such as drought in 1988 and floods in 1993. [20]. Studies have attributed regional summer cooling over agricultural areas in the Midwest to this agricultural intensification [172, 9].

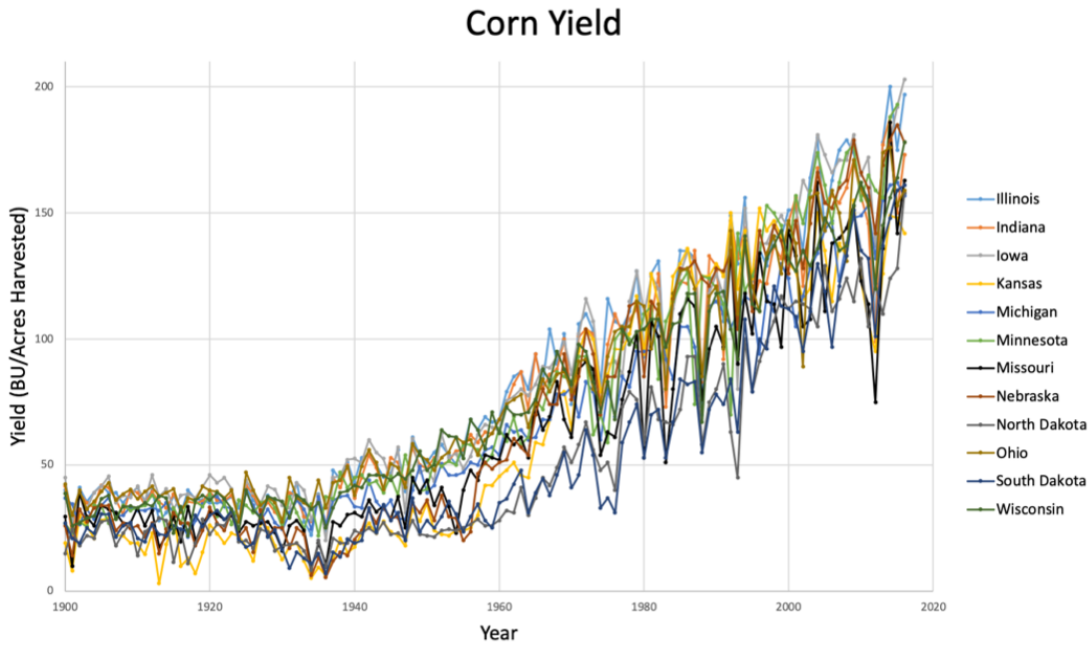

Figure 3-2: Yield of Corn (BU/Acre) in Midwestern States from 1900-2016 take from USDA NASS Survey Statistics ([262]).

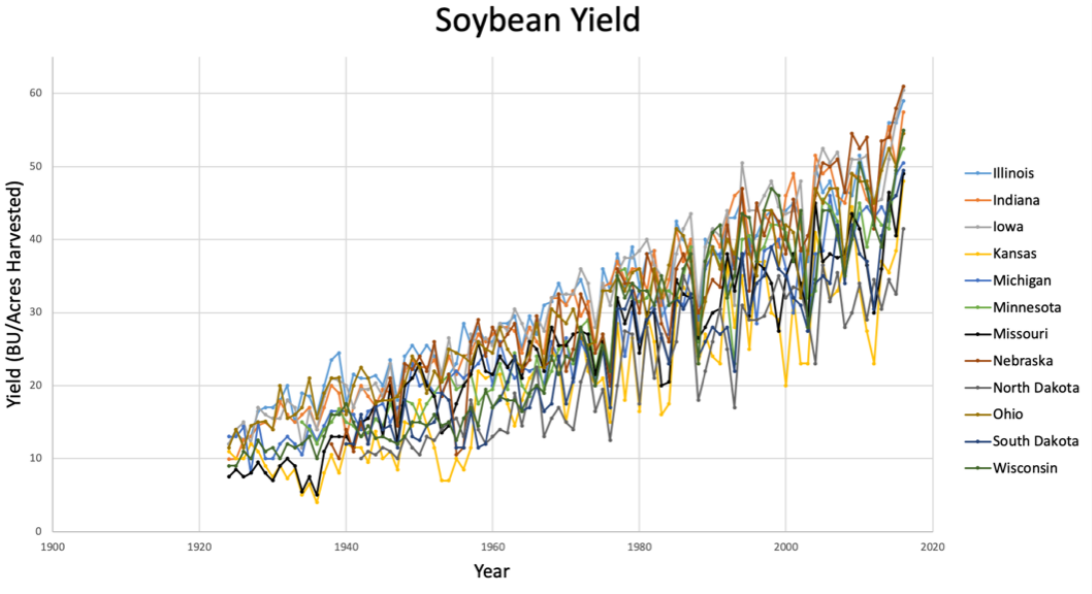

Figure 3-3: Yield of Soybean (BU/Acre) in Midwestern States from 1900-2016 take from USDA NASS Survey Statistics ([262]).

Finally, irrigation began to increase in the Midwest and Great Plains around the same time as the uptick in yields and comprises the third main component of agricultural development that will be modeled [239]. Three large irrigated areas in Eastern Nebraska, the southern Mississippi River Valley and the Texas Panhandle are all included in the modeling domain despite their exclusion from the immediate region of interest. Eltahir (1998) proposed a connection between soil moisture increases and energy balance changes that are also applicable in irrigated areas [58]. Studies have shown that evapotranspiration and latent heat flux, a measure of the turbulent transport of moisture away from the surface and into the atmosphere, are increased over irrigated areas [58, 5, 190, 92, 142, 206, 113, 36]. Conversely, sensible heat flux, the complementary component of turbulent heat transfer away from the surface, is reduced as a result. This increase in latent heat flux is accompanied by surface cooling in irrigated areas [131, 113, 206, 172, 125, 144].

Additionally, it has been proposed that irrigation increases precipitation downwind of the irrigated area even when precipitation is suppressed directly over irrigation [44, 142, 113, 119, 121, 10, 11, 145]. These effects are tied to an alteration of the large-scale circulation, atmospheric moisture content, and moist static energy [192, 131, 121, 10, 11, 36, 88, 145] that also correspond with decreases in planetary boundary layer (PBL) height. However, the competing effects on convective potential directly over irrigated areas due to modification of energy and moisture fluxes still leave uncertainty as to their impact on preciptiation [125, 92, 206, 119, 121, 145]. Additionally, several studies have noted that circulations induced by cooling over irrigated areas can either augment or counter existing atmospheric patterns such as the Lower Level Jet (LLJ) [113] or monsoonal circulation, [121] and influence the overall pattern of moisture advection and precipitation.

A study of the effects of agricultural development in this region of the United States is justified due to the anomalous observed changes in summer temperature and precipitation that have occurred in this area in the latter half of the 20th Century — dubbed the "Warming Hole" [194]. Although the position, intensity and proposed causes of the warming hole differ depending on the framing of the study,

multiple recent studies have shown the presence of a summer warming hole (Fig. 3-4) centered in the Central United States and stretching into Canada and have proposed agricultural land use change as a cause [195, 198, 154, 9]. Douglas (2016) identified a Region of Significant Change (ROSC) (39-48° N and 100-82° W) and showed that a comparison of 1920-1949 to 1970-1999 climatologies highlighted a period of significant change, corresponding both with irrigation expansion and yield increases [54]. Observed changes in temperature [172], precipitation [9], and humidity [28] in this region have been attributed to agricultural land use changes. The U.S. warming hole is a rare, but not unique, phenomena. Central and Eastern China has also experienced a similar cooling and wetting over the same period (see Sup. Fig. 3-4 in Alter et al. (2018) [9]) and Zhang et al. (2016) identified a late century warming hole through an analysis of summer maximum and minimum temperature ratios [290].

Natural internal variability can also influence regional climate on decadal and centennial scales. Sea surface temperature has been a well documented forcing of seasonal precipitation and temperature changes in the United States [263]. In general, drought conditions and warmer summertime temperatures in Central North America are connected to a cold Pacific ocean and a warm Atlantic ocean [252, 232, 234, 231, 267, 76, 222, 268, 38, 233, 266, 52, 124] with many studies emphasizing either the role of the Pacific [232, 7, 128, 231, 76, 268, 159, 30, 124] or the Atlantic [60, 127, 133, 273, 274, 177]. In particular the correlation to the North Atlantic is strong for the analysis regions in this study (Table 3.1). A further study of SST teleconnections and the connection to patterns like the Great Plains Lower Level Jet can be found in the Appendix.

Fig. 3-5 shows the Pearson correlation coefficient between grid cell time series of July-August averaged precipitation and the area averaged North Atlantic SST in the same months. The observed changes in precipitation in the CRU data are also shown for comparison. The pattern of correlation closely matches the observed changes and are consistent with the changes that might be expected as the North Atlantic transitioned from a very warm period in 1920-1949 to a very cool period in 1970-1999 (Fig. 3-6).

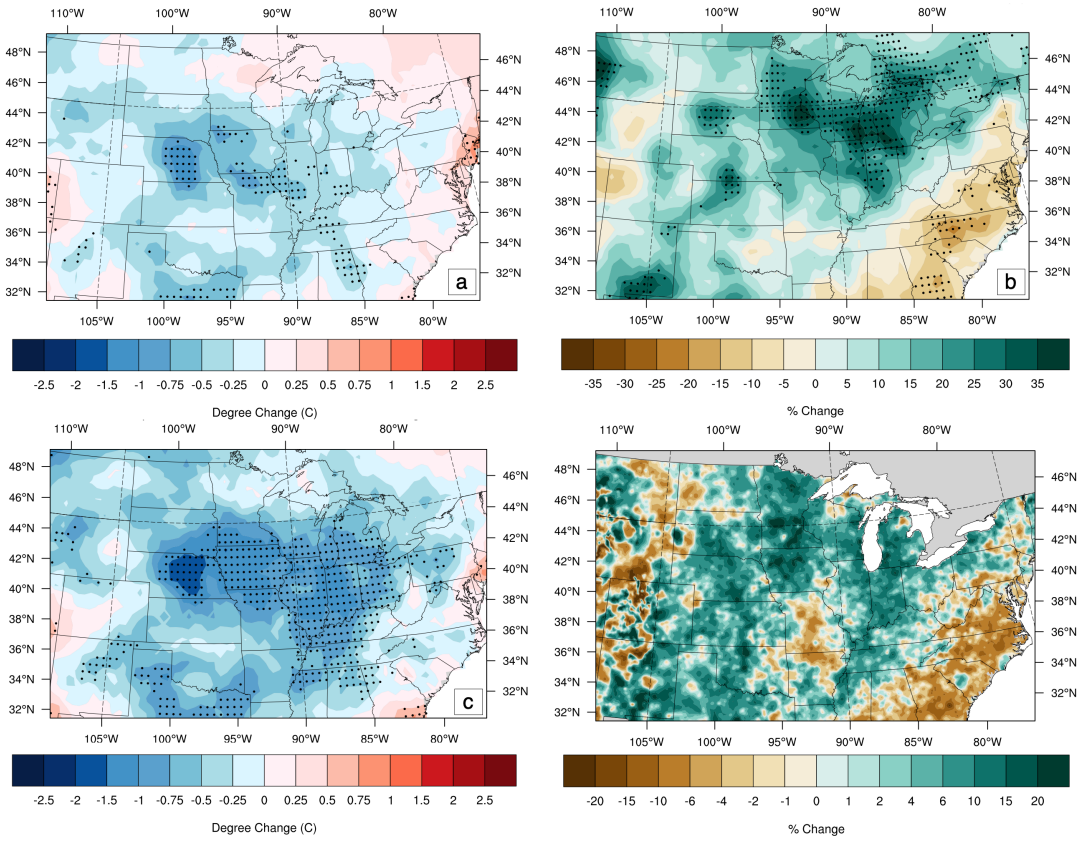

Figure 3-4: Observed changes in (a) mean surface temperature (degrees C) (CRUTS4.01), (b) precipitation (%) (CRUTS4.01), (c) maximum surface temperature (degrees C) (CRUTS4.02), and (d) evapotranspiration (%) ([140]). Change shown is the difference between July-August monthly average from 1920-1949 to 1970–1999. Stippling shows a significant change between the two periods according to a Kolmogorov–Smirnov test at the 5% significance level.

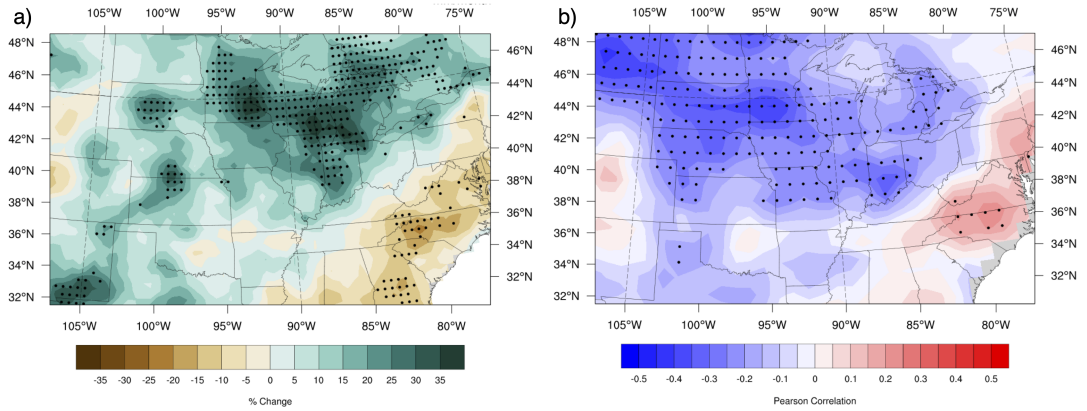

Figure 3-5: Comparison of a) July-August average precipitation changes (%) in the CRU data from 1920-1949 to 1970-1999 and b) Pearson correlation coefficient between detrended and standardized grid point anomaly timeseries of CRU data and area averaged, standardized, detrended North Atlantic SST temperature anomalies (degrees C) (37-53°N, 303-317°E). The region is the same as that described in Donat et al. (2016) [52]

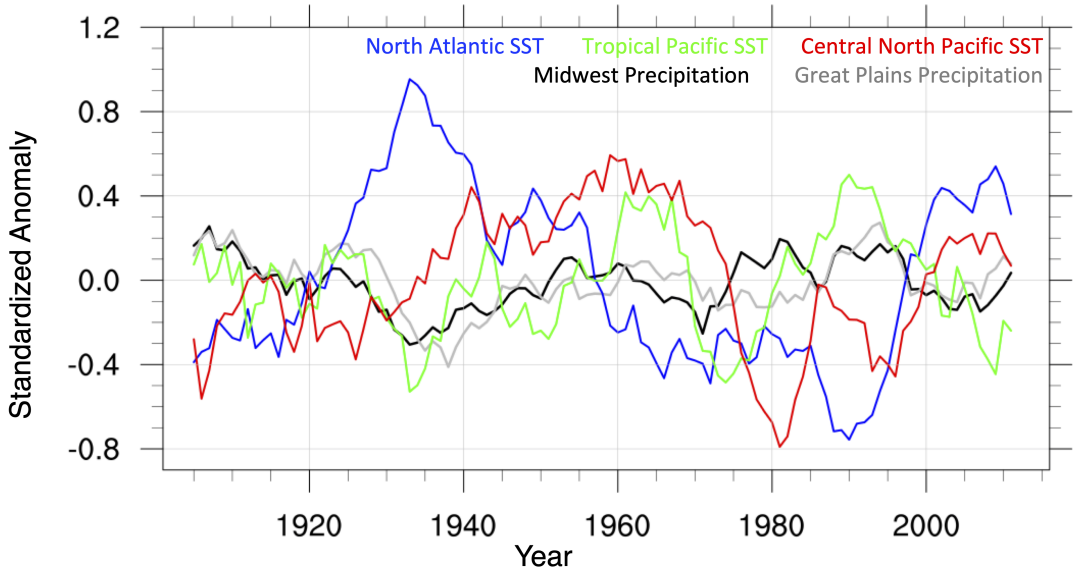

Figure 3-6: Timeseries of area averaged, standardized, detrended SST anomalies (degrees C) for North Atlantic (37-53°N, 303-317°E) (blue), Tropical Pacific (1S-9N, 197-209E) (green) and Central North Pacific (29-35°N, 179-195°E) (red) and observed precipitation anomalies (mm/day) (CRU) in the Midwest (38-48°N, 82-109°W) (black) and Great Plains (33-48°N, 95-109°W) (grey). Baseline period used for anomalies is 1981-2010.

Table 3.1: Pearson correlation coefficients between July-August area averaged, standardized, de-trended anomalies of CRU temperature and precipitation and the following SST time series. *indicates significance at p = 0.05 and **indicates significance at p = 0.01. T = Temperature and P = Precipitation.

	Midwest T	*G. Plains T*	*Midwest P*	*G. Plains P*
North Atlantic (*Donat et al.*, 2016)	0.31**	0.34**	-0.43**	-0.20*
Tropical Pacific (*Mei et al.*, 2011)	-0.20*	-0.18	0.29**	0.24**
Central North Pacific (*Mei et al.*, 2011)	0.25**	0.16	-0.25**	-0.15

3.3 Data

The experiments conducted in this study are made possible through the use of several newly developed data sets, allowing for a more in-depth picture of the changes that have occurred in this region over the course of the entire 20th century. The reanalysis data set used here to provide lateral boundaries and initial conditions for the historical runs is CERA-20C, developed by the European Centre for Medium-Range Weather Forecasts (ECMWF) [57]. CERA-20C is the newest generation product developed through the ERA-CLIM2 project developed on 91 atmospheric model levels and with a land resolution of 125 km with 4 soil layers and an ocean grid resolution of 110 km with 42 levels [57]. This coupled ocean-atmosphere product assimilates sea surface pressure from the International Surface Pressure Databank (ISPD) and the International Comprehensive Ocean-Atmosphere Data Set (ICOADS) as well as marine winds from ICOADS; CERA-20C also uses ocean temperature and salinity profiles from HADISST2 [134]. The simulations are run with ensemble member 5 from the 10-member product. This ensemble member was chosen because it exhibits less of a warm bias in the early centuries than the other members in the region of interest.

However, caution must be used in interpretation of early century simulations as there is evidence that the reanalysis data is less reliable. There is a wide spread in

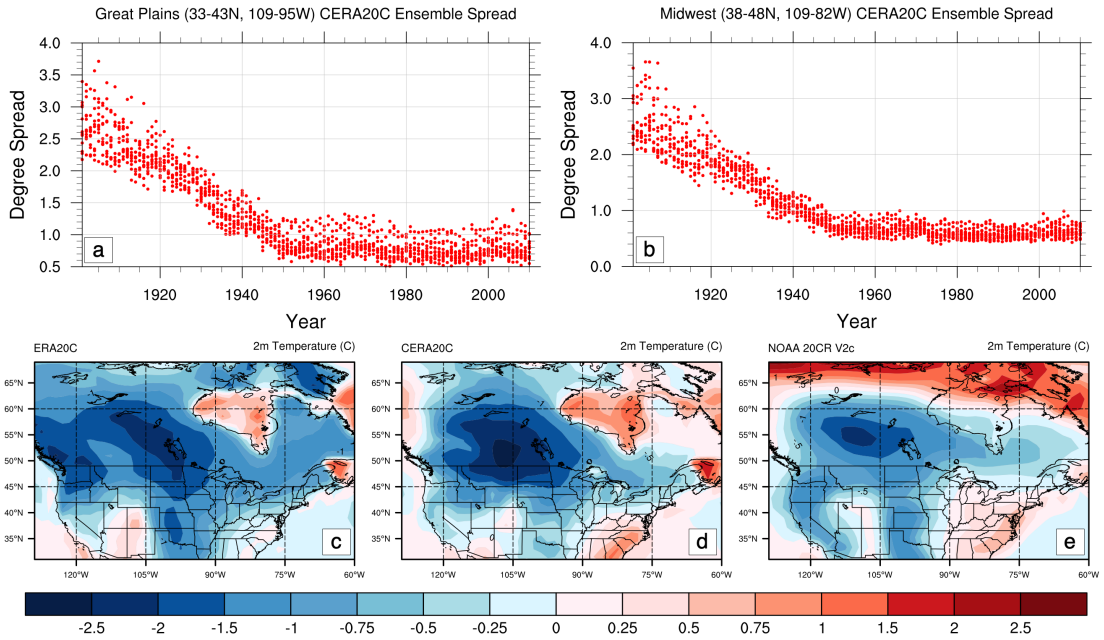

Figure 3-7: (a) CERA-20C ensemble spread in temperatures (K) averaged over the Great Plains. (b) As in (a), but for the Midwest. (c) July–August average temperature change (°C) from 1920–1949 to 1970–1999 in ERA-20C 2-m temperature (ECMWF). (d) As in (c), but for CERA-20C. (e) As in (c), but for NOAA 20CR V2c.

the 10-member ensemble of CERA-20C, although this stabilizes in the mid-century (Fig. 3-7 a,b). More evidence for reanalysis shortcomings is seen in an intense cooling feature in Canada that does not exist in the observations (Fig. 3-7 c,d,e). This anomalous cooling is present in CERA-20C and another ECMWF product, ERA-20C [204], as well as NOAA 20CR V2c developed by the National Oceanic and Atmospheric Administration (NOAA) in collaboration with the Cooperative Institute for Research in Environmental Sciences (CIRES) [35]. Analysis methodology was chosen with these potential problems in mind, and an attempt was made to minimize their impacts on the results. Although anomalous boundary condition features will show in results that present a single simulation, results that show the changes due to vegetation and GHG are free of boundary condition error because all simulations are conducted with the same set of boundary conditions. This cooling feature provides further justification for the use of ensemble 5 from the 10-member CERA20C reanalysis product, as the cooling is less intense and widespread than in some of the other ensemble members.

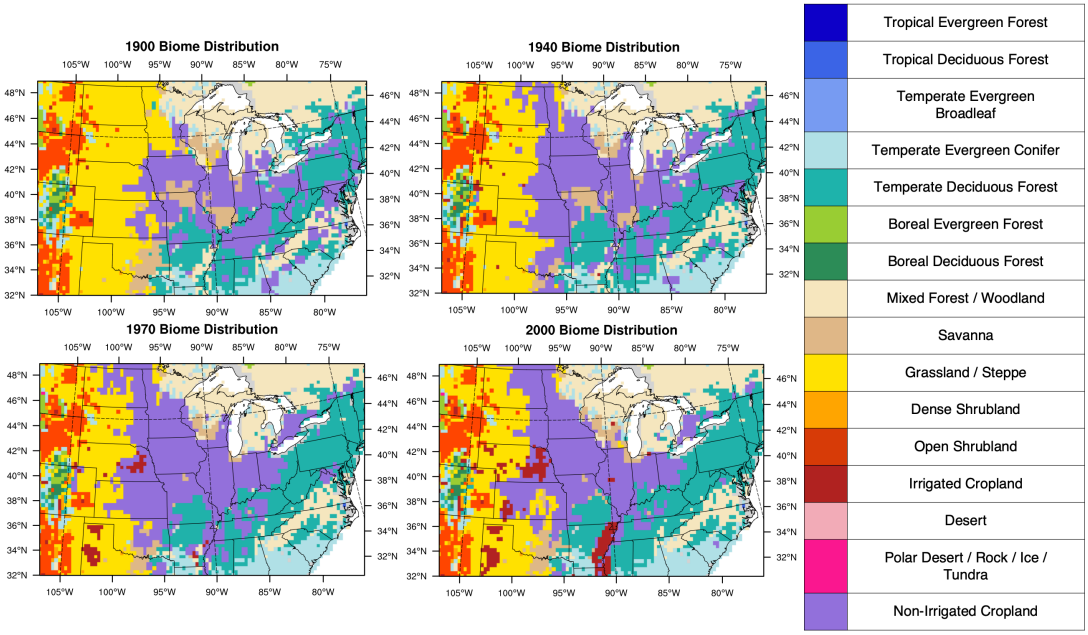

Figure 3-8: Biome distribution maps used as land surface input for select years.

Land surface boundary conditions are compiled from three separate data sources: 1) A 5-minute resolution potential vegetation dataset [207] 2) the Harmonized Global Land Use Dataset 1500-2100 (LUHv1) for cropland designation at 0.5-degree resolution [118, 33] and 3) The Historic Irrigation Dataset (HID) at 5-minute resolution [239]. A composite land surface dataset was then developed for each decade (Fig. 3-8). With a 50% threshold for cropland and a 25% threshold for irrigation. More information on composition of land use data can be found in [178].

To determine agricultural intensification, data on acres harvested, acres planted and yield for corn were obtained from the U.S. Department of Agriculture's (USDA) National Agricultural Statistics Service (NASS) [262]. Yield can be translated to net primary production (NPP) through an inventory-based method that has been used widely [205, 107, 275, 169, 15, 139, 123]. This yield increase was then designated within the model by a modification of the net crop photosynthesis rate, as net primary production is a measure of the amount of carbon fixed into new biomass in vegetation and can broadly be described as the difference between photosynthetic production and respiration [221]. NPP rates in the model were tuned to a corn equivalent NPP derived from a reconstructed 1992 NPP spatial map developed by Prince et al. (2001)

[205]. In the model cropland has the physiological characteristics of a C_4 pathway crop and therefore all values were determined as corn NPP equivalent for consistency. More information on representing agricultural intensification can be found in Nikiel (2018) [178].

Observed temperature and precipitation data come from the Climatic Research Unit Time Series (CRUTS4.01) developed by the University of East Anglia which spans 1901-2016 at 0.5° (latitude) x 0.5° (longitude) resolution [93]. Historical trends in evapotranspiration data are taken from the Livneh daily CONUS near-surface gridded meteorological and derived hydro-meteorological data provided by the NOAA-OAR-ESRL PSD, Boulder, Colorado, USA, from their Web site at https://www.esrl.noaa.gov/psd/, which are available from January 1915 to December 2011 at 1/16° (latitude) x 1/16° (longitude) resolution [140]. SST observations are taken from the Extended Reconstructed Sea Surface Temperatures Version 5 (ERSSTv5) [112]. In this study, the SST regions used are the North Atlantic (37-53° N, 303-317° E closely matching Donat et al. (2016) [52]), Tropical Pacific (1S-9° N, 197-209° E) and Central North Pacific (29-35° N, 179-195° E) where the latter two are roughly derived from regions used in Mei et al. (2011) [159].

The ocean boundary conditions are set using the Hadley Centre Sea Ice and Sea Surface Temperature Data Set (HADISSTv1.1) provided by the Met Office Hadley Centre in collaboration with the National Oceanography Centre, Southampton and the Lamont-Doherty Earth Observatory of Columbia University [212]. Finally, GHG concentrations were designated annually for CO2, CH4, N2O, CFC-11, and CFC-12 using the concentrations approved for use in the CMIP5 project and in preparation for the Intergovernmental Panel on Climate Change (IPCC) Annual Report 5 (2013) [160].

3.4 Methodology

The simulations for this study were performed using the MIT Regional Climate Model (MRCM). MRCM is an updated version of the Regional Climate Model Version 3

Table 3.2: Description of Simulation Experiments

	Boundary Conditions	*GHG*	*Vegetation*
nV-nG	Evolving	Static	Static
nV-G	Evolving	Evolving (annual)	Static
V-G	Evolving	Evolving (annual)	Evolving (decadal)

(RegCM3) climate model, originally developed at the National Center for Atmospheric Research (NCAR) and maintained by the International Center for Theoretical Physics (ICTP). The model has been further modified by the Eltahir research group to improve representations of albedo, dust emissions, cloud and convection schemes, and boundary layer dynamics [152, 153, 83, 81, 82]. MRCM is composed of an atmospheric circulation model coupled with a land surface model. The present setup uses the Grell Cumulus Scheme with the Arakawa and Schubert convective closure assumption [14, 87]. This combination has been shown as the most appropriate in previous studies of the Midwestern United States [278, 279, 280]. A vital development for MRCM was the replacement of the original land surface model, the Biosphere-Atmosphere Transfer Scheme (BATS), with the Integrated BIosphere Simulator (IBIS) [278]. Several studies have noted the suitability of RegCM3 [51, 131, 48], and of a coupled RegCM3-IBIS framework, for regional climate modeling in the Central United States [279, 280].

A 3-member ensemble per experiment set of simulations is presented here. All simulations are run on a domain centered at 40.5° N and 91.5° W with a 30-km grid spacing, and 122 zonal points, 80 meridional points and 18 vertical sigma levels. The outer 9 grid cells are not included in analysis in order to avoid any boundary effects. The CERA-20C simulations are run as three ensembles initiated at January 1-3, 1901 through December 31, 2005. Each set is composed of three simulations: 1) No vegetation development and no GHG increases (nV-nG), 2) No vegetation development with realistic GHG increases (nV-G), and 3) Vegetation development and realistic GHG increases (V-G) (Table 3.2).

The simulations with no vegetation development and no GHG were run with 1900

conditions for those parameters respectively. The V-G simulation in each of the sets is run in decadal segments (except the first simulation which is run from 1901 to 1905) with the land use map being updated to reflect cropland and irrigation expansion in the 10 years surrounding 1900, 1910, 1920, etc. The decadal runs were run with one extra year at the beginning of each of the decadal simulations – starting January 1-3 depending on the ensemble – which was not used in the post-processing and the construction of the full time-series.

Soil moisture conditions are equilibrated for the region with long term offline simulations of IBIS, and no longer spin up time was needed to establish equilibrium. Irrigation was initially introduced into MRCM for testing land-atmosphere processes in semi-arid regions, and the original irrigation scheme was set to return the root zone soil moisture at every time step to the weighted average root zone field capacity in each of the four top layers that make up the root zone (0-100 cm) [151]. The same irrigation setup was later used to investigate the effects on precipitation in the Gezira region in East Africa and in West Africa in conjunction with the West African monsoon [119, 121, 11]. In the current setup, the model is slightly modified in order to more realistically represent irrigation in the region. Rather than replenishing the root zone constantly, irrigation is applied when a threshold of 75% of average root zone relative field capacity is reached. Additionally, irrigation is restricted from July to September rather than May to September, which aligns with a restriction on crop growth before July.

The analysis is performed for two main regions, the Great Plains (33-43° N, 95-109° W) and the Midwest (38-48° N, 82-109° W) (Shown in dashed lines in Figure 3-9). The ROSC identified by Douglas (2016) [54] is mostly included within these two regions, but the distinction is made between these two analysis regions in order to be mindful of differences in seasonal precipitation climatology, SST teleconnection influences, and differing components of agricultural development. The time periods of comparison are 1920-1949 (early period) and 1970-1999 (late period) which are consistent with Douglas (2016) and Alter et al. (2018) [54] [9]. Additionally, all averages are shown for July-August, the period of maximum crop growth and irrigation impacts. This

time period also overlaps with previous studies and allows for comparison [5, 190, 44, 9]. Where appropriate, area averaged changes are accompanied by a description of significance from the results of Kolmogorov-Smirnov two sample test (K-S test) at a 95% confidence level (N = 30) [102, 237].

3.5 Results and Comparison to Observations

3.5.1 Temperature

In the observational data, temperatures decreased an average of 0.31° C (0.16° C) in the Great Plains (Midwest) between the early and late period, with isolated cooling in the Midwest of 1-1.5° C (Fig. 3-9a). These areas of cooling are surrounded by warming along the East coast and into the Northeast and Canada, as well as in the West.

While differences exist in the spatial distribution of temperature changes and the magnitude of peak cooling and warming, cooling occurs in both observations and simulations through the Central Great Plains and Midwest. Overall, agricultural development led to widespread cooling throughout the domain, particularly in areas that are irrigated or intensified over the simulation period (Fig. 3-9c). Pockets of heating are seen in the East, due to the reduction of cropland in the land use data-set, and the reversion to forest type biomes present in the potential vegetation dataset. Whether this reforestation actually occurred is beyond the scope of this study and is a limitation of the development of the land use dataset. GHG lead to overall warming in the domain with patches of cooling (Fig. 3-9d). The magnitude of this change is much smaller than the change due to the vegetation or the background conditions.

In order to estimate the impact of SST, a multi-linear regression was conducted at every grid point between the three SST regions identified earlier and CRU observational data. The time series were detrended as before. The SST impact on temperature is shown to be weaker than vegetation, and also concentrated in the Northwest of the domain, not aligned with the major agricultural areas, and offset

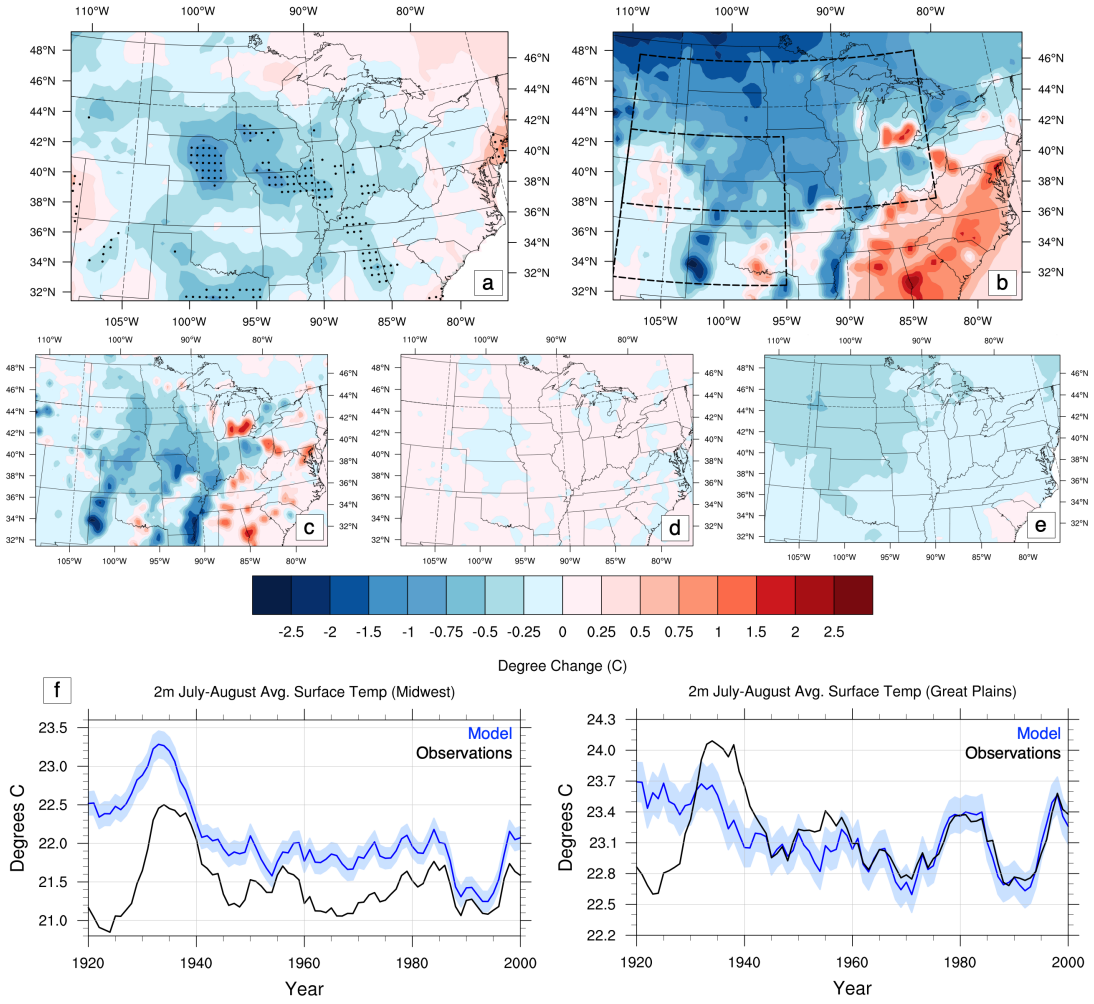

Figure 3-9: (a) July–August mean surface temperature change (° C) from 1920–49 to 1970–99 in observation (CRUTS4.01) data, (b) change in V-G simulation, (c) change due to vegetation in simulations, (d) change due to GHG in simulations, and (e) estimates of temperature change attributed to SST in the North Atlantic (378–53°N, 3038–317°E), tropical Pacific (1°S–9°N, 197–209°E), and central North Pacific (29–35°N, 179–195°E) using a multilinear regression to observed CRU temperature. (f) Time series of area-averaged temperature in the model ensemble (blue) with shading representing the standard deviation of the three-run ensemble. CRU data are shown in black

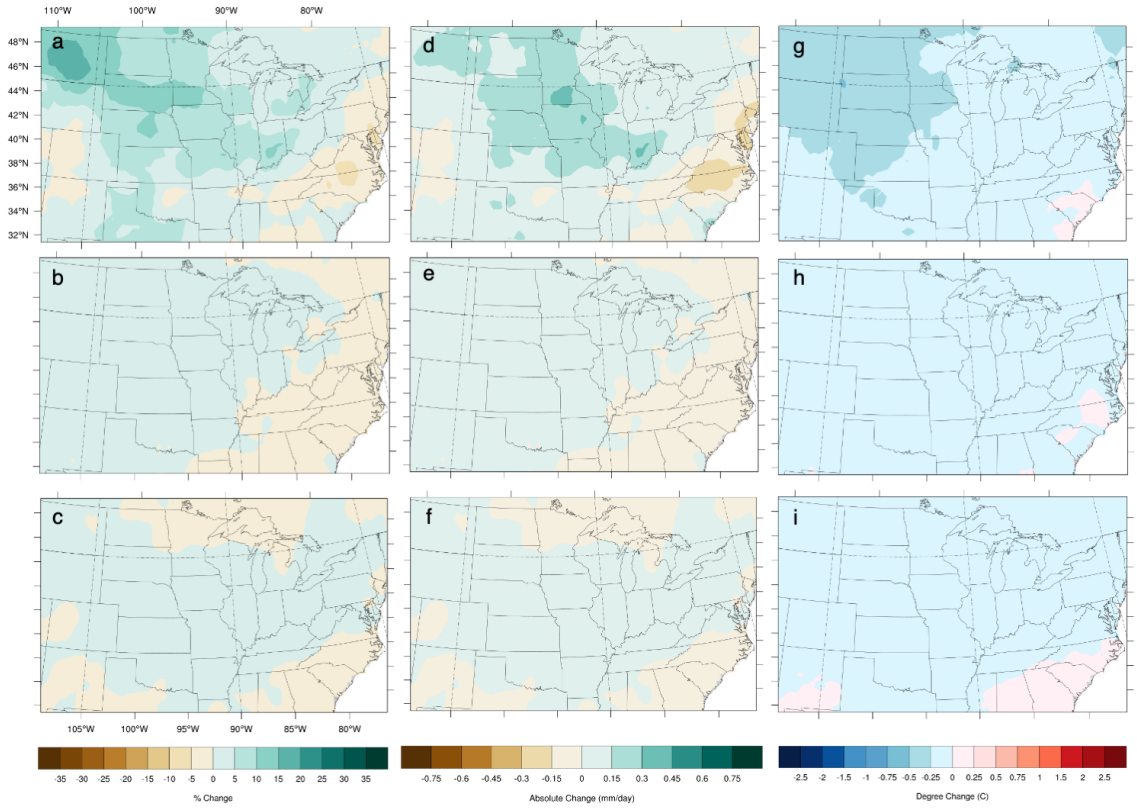

Figure 3-10: a-c) July-August percent precipitation change (%) from 1920-1940 to 1970-1999 attributed to changes in the North Atlantic (37-53°N, 303-317°E) (top), Tropical Pacific (1S- 9°N, 197-209°E) (middle), and Central North Pacific (29-35°N, 179-195°E) (bottom) d-f) same as (a-c) except for absolute precipitation change (mm/day). g-i) same as (a-c) except for absolute temperature change (degrees Celsius).

from the observed pattern of change (Fig. 3-9e). Impacts of the individual SST regions calculated using linear regression can be seen in Figure 3-10, and it can be seen that the North Atlantic contributes most to the estimated change.

The largest deviations in the cooling pattern are due to the influence of the boundary conditions and associated errors (Fig. 3-11). The abnormal cooling in the Northwest of the domain and heating along the East coast in this component has a strong influence on the overall change, compared to the impact of vegetation and GHG in these areas. The simulations have more skill in matching the observed temperatures in the two regions after 1950, especially in the Great Plains (Fig. 3-9f), and this again points to the increased reliability of boundary conditions post-1950.

The area averaged changes in temperature attributed to agricultural development (expansion of cropland, development of irrigation, and intensification) in the Great Plains (Midwest) is -0.32 (-0.24) °C; the change attributed to GHG is 0.02°C in both regions. The vegetation impact is shown to have an order of magnitude more impact than GHG on these regions. The temperature effect due to vegetation is higher in the Great Plains likely due to the enhanced evaporative cooling in irrigated areas. Averaging over grid cells that are designated as non-irrigated (irrigated) cropland in the 2000 land use map, the average temperature change associated with the agricultural development is a cooling of 0.6°C (1.5°C). The average irrigated cooling compares well to the July irrigation mean cooling of 1.4°C in Adegoke et al. (2003) [5], while Lobell et al. (2009) [143] found an irrigation cooling of 0-10°C with roughly 5°C in July-August in Nebraska. Alter et al. (2018) found a cooling of 1°C in intensified cropland areas [9]. The average cooling from vegetation and heating from GHG in these regions was able to collectively approximate the observed cooling.

The "residual" change in these regions is found to be small, and on the order of the impact from GHG between the early and late periods. This suggests that the bulk of the surface cooling in mean July-August temperatures between these two periods in these regions can be attributed to agricultural development, and that natural variability likely played a minimal role in creating the spatial pattern of the temperature change between these two periods. Although this period corresponds with a mid century hiatus in global surface temperature trends from the 1940s to 1970s [91], the pattern of regional cooling investigated here is distinct and is coincident with increased precipitation as described below.

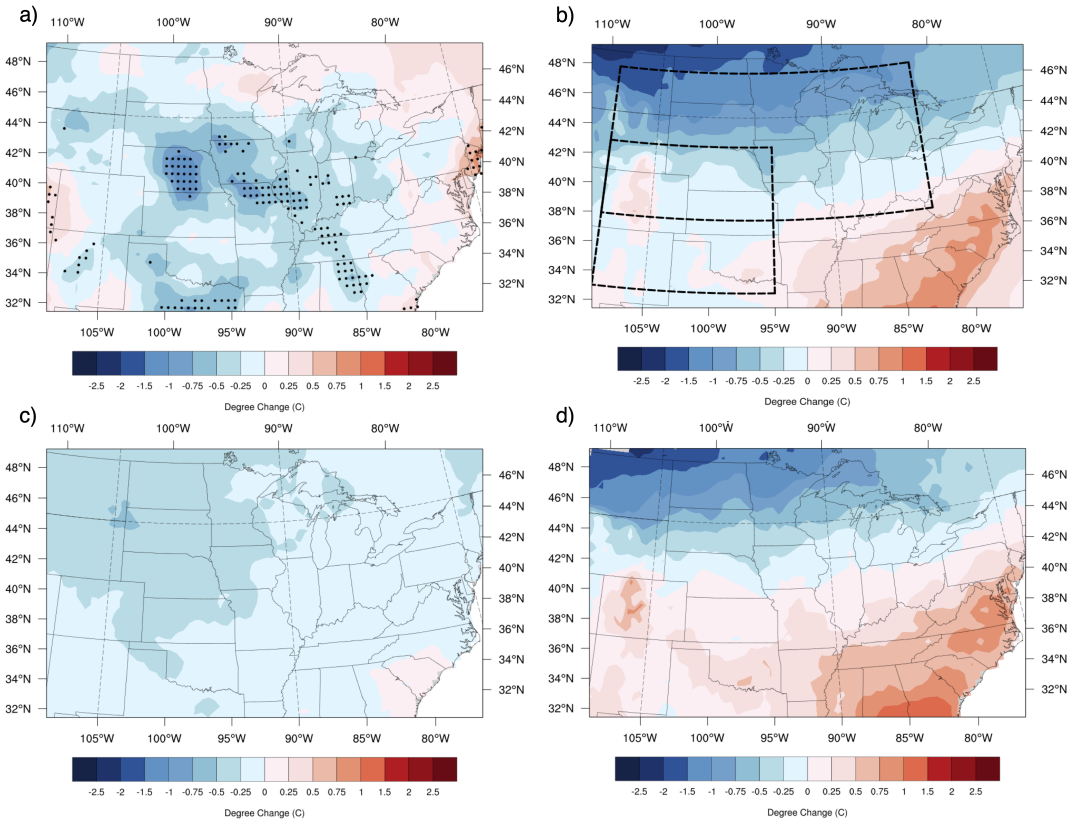

Figure 3-11: Absolute July-August temperature change (degrees C) from 1920- 1940 to 1970-1999 shown in a) CRU data b) MRCM nV-nG simulations i.e. the change attributed to residual forcings (not vegetation or greenhouse gas concentrations). c) Estimates of combined temperature change attributed to SST in the North Atlantic (37-53°N, 303-317°E), Tropical Pacific (1°S-9°N, 197-209°E), and Central North Pacific (29-35°N, 179-195°E) using a multilinear regression to observed CRU temperature d) An estimation of boundary errors, made by removing SST influence in (c) from changes seen in the nV-nG simulation.

3.5.2 Precipitation

In the observational data, precipitation increased an average of 0.18 mm/day (0.34 mm/day) in the Great Plains (Midwest) between the early and late period, which amounts to an increase of 9% (16%), with isolated increases in the Midwest of 30% (Fig. 3-12a). The increase in precipitation that occurs in the Central United States contrasts with the drying that occurs to the east of the Appalachian Mountains.

A dominant pattern of precipitation changes — a dry-wet-dry banding moving from the northwest to the southeast — is captured in the simulations as well as the observations (Fig. 3-12a-b). However, the strongest precipitation feature in the observations — wetting in Great Plains and particularly in the Midwest — is not present as a distinct feature in the simulations though both show an average increase in precipitation in this area. The increases in precipitation due to vegetation resembles the pattern of increase seen in the observations (Fig. 3-12c).

GHG do not cause a distinct pattern of precipitation change (Fig. 3-12d) and the precipitation increases caused by vegetation are similar in spatial pattern but do not match the intensity of observed change. While changes broadly occur in areas of agriculture development there does not seem to be a distinct pattern of change associated with irrigation specifically. There is an increase in precipitation of 4.3% and 5.2% in non-irrigated and irrigated areas respectively. Alter et al. (2018) found an increase in July-August rainfall of 0.15-0.45 mm/day (5-15%) due to intensification over large areas the Great Plains with isolated increases of 0.6 mm/day (20%) [9]. Lo and Famiglietti (2013) found an increase in summer rainfall of 15% in their study of irrigation impacts in the California Central Valley [142]. The decrease in precipitation percentage in the West is attributed to the residual forcing (Fig. 3-13) although the strong magnitude is likely due to a decrease in an already dry area.

The area averaged changes in precipitation attributed to agricultural development (expansion of cropland, development of irrigation, and intensification) in the Great Plains (Midwest) is 0.08 (0.06) mm/day; the change attributed to GHG is 0.03 mm/day in both regions. Precipitation change due to vegetation changes in the sim-

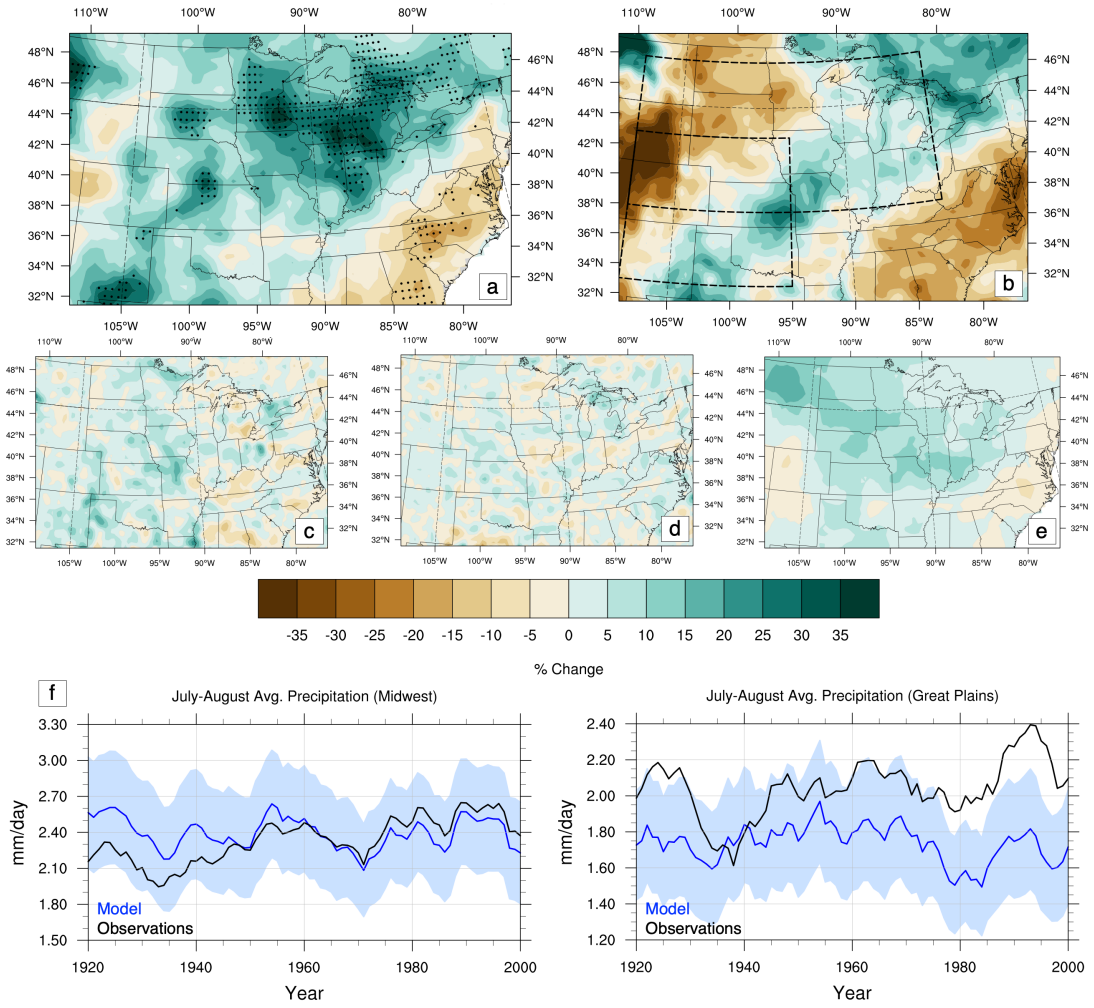

Figure 3-12: (a) July–August mean precipitation change (%) from 1920–49 to 1970–99 in observation (CRUTS4.01) data, (b) change in V-G simulation, (c) change due to vegetation in simulations, (d) change due to GHG in simulations, and (e) estimates of precipitation change attributed to SST in the North Atlantic (37–53°N, 303–317°E), tropical Pacific (1°S–9°N, 197–209°E), and central North Pacific (29–35°N, 179–195°E) using a multilinear regression to observed CRU precipitation. (f) Time series of area averaged precipitation in the model ensemble (blue) with shading representing the standard deviation of the three-run ensemble. CRU data are shown in black.

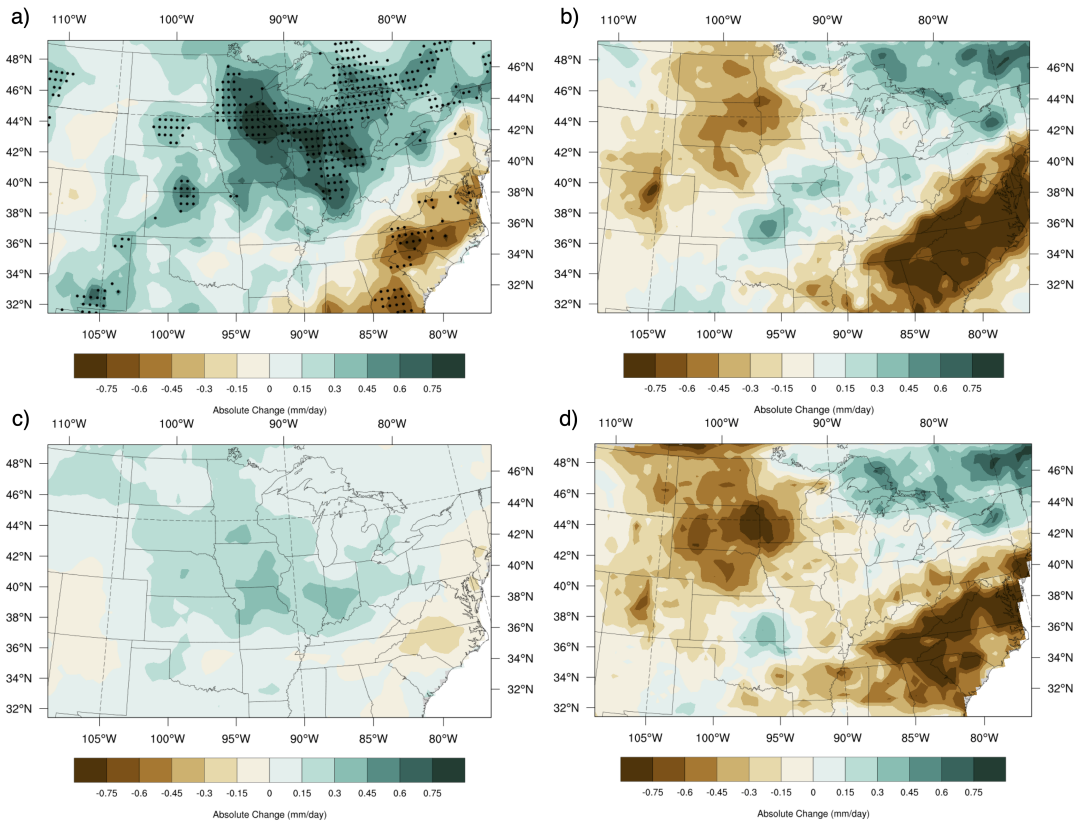

Figure 3-13: Absolute July-August precipitation change (mm/day) from 1920-1949 to 1970-1999 shown in a) CRU data b) MRCM nV-nG simulations i.e. the change attributed to residual forcings (not vegetation or greenhouse gas concentrations). c) Estimates of combined precipitation change attributed to SST in the North Atlantic (37-53°N, 303-317°E), Tropical Pacific (1°S-9°N, 197-209°E), and Central North Pacific (29-35°N, 179-195°E) using a multilinear regression to observed CRU precipitation d) An estimation of boundary errors, made by removing SST influence in (c) from changes seen in the nV-nG simulation.

ulations is therefore roughly double the impact from GHG. However, unlike in the temperature results, the "residual" change in these regions is not negligible, especially in the Midwest where nearly 75% of the observed change is not explained by either vegetation or GHG increases in the model simulations. This suggests that one or more additional forcings contributed to the July-August average precipitation changes over this area between the early and late period. However, the patterns of precipitation change in the full simulations were shown to resemble the observed change. Therefore, it is reasonable to explore the influence of natural variability on this pattern. This variability in the form of SST forced precipitation change estimates was calculated in the same way as for temperature, and the result is an increase centered in the area of agricultural change, with corresponding drying in the East (Fig. 3-12e). The coherency and strength of the estimated change attributed to SST is greater than the simulation based impacts of vegetation and GHG. Impacts of the individual SST regions calculated using linear regression can be seen in Figure 3-10, and it can be seen that the North Atlantic contributes most to the modeled change.

3.5.3 Evapotranspiration

Evapotranspiration does not have a long-term observational analogue. However, comparisons to independent reconstructions of evapotranspiration change in the region show that the spatial pattern of vegetation induced evapotranspiration changes in MRCM simulations closely match the pattern in the independent data set developed using the variable infiltration capacity (VIC) model [140]. Increases in evapotranspiration occur throughout much of the agricultural area and correspond well to modeled changes, and decreases in evapotranspiration in the Northwest, Missouri and Arkansas are also captured (Fig. 3-14).

The model and observations also compare well in the absolute daily July-August average value in the two regions (Fig. 3-14f), especially in the Midwest. This adds confidence to the selection of vegetation parameters that are used to represent the intensification of agricultural productivity. Further exploration of evapotranspiration rates and related impacts on water availability and energy partitioning are explored

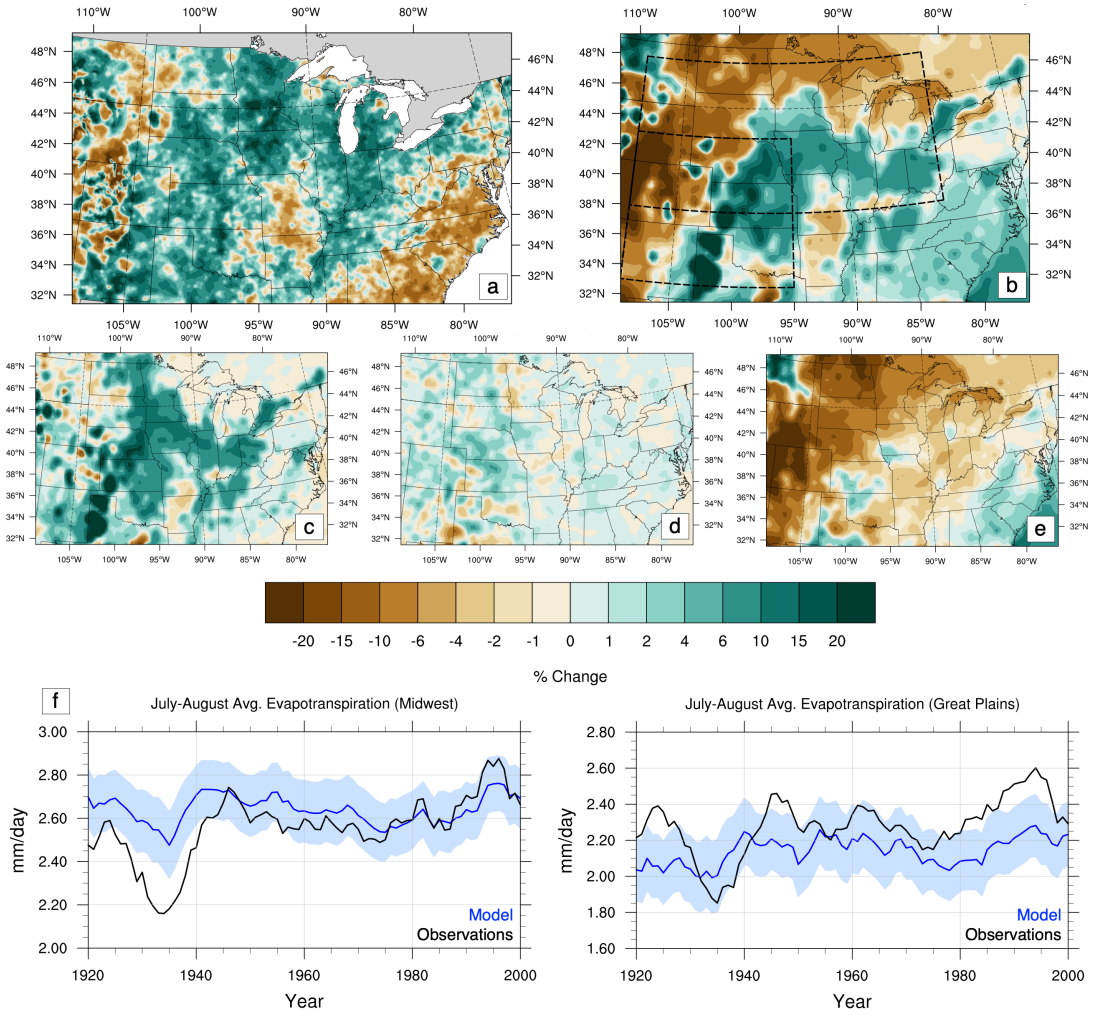

Figure 3-14: (a) July–August mean evapotranspiration change (%) from 1920–1949 to 1970–1999 in VIC data ([140]), (b) change in V-G simulation, (c) change due to vegetation in simulations, (d) change due to GHG in simulations, and (e) "residual" change in simulations due to natural variability, boundary condition errors, and other non-explicitly defined forcings. (f) Time series of area-averaged evapotranspiration in the model ensemble (blue) with shading representing the standard deviation of the three-run ensemble. VIC data are shown in black.

Table 3.3: Description of Agricultural Component Experiments

	Bound. Cond.	*GHG*	*Land Use*	*Intensified*
PD	1982-2005 (CERA-20C)	Evolving (Ann.)	2000	No
FD	1982-2005 (CERA-20C)	Evolving (Ann.)	2000	Yes
PDplus	1982-2005 (CERA-20C)	Evolving (Ann.)	1900	No

in Chapters 4 and 5.

3.6 Decomposition of Agricultural Development Components

In order to further understand the impact of the three-component agricultural development in this region, shorter sensitivity experiments were conducted where the changes were broken down into the intensification of agriculture and the expansion of both irrigated and non-irrigated cropland. These experiments are conducted with CERA-20C but are performed from 1982-2005, and all comparisons are made with simulations run during this period, removing any influence from changing boundary conditions. Unlike the other simulation results shown in this chapter, these short-term simulations are composed of a single run, not a 3-member ensemble. Setup, land use and parameters for each of the simulations are described in Table 3.3.

Intensification of agriculture creates a more cohesive regional impact with a decrease in temperature and an increase in precipitation and evapotranspiration (Fig. 3-15a,c,e). Alternatively, expansion causes a widespread decrease in precipitation and evapotranspiration, and a mixed temperature impact over agricultural areas (Fig. 3-15b,d,f). The decreases seen are not surprising, as Sterling et al. (2012) showed that agricultural areas have a higher evapotranspiration rate than grasslands when irrigated and a lower evapotranspiration rate otherwise [246]. Expansion can also be framed here as redistribution of agriculture into the area of interest, as cropland is eliminated east of the Appalachians and develops in the west. The competing effects of land use change shown here support an argument for careful inclusion of all components of land-use change.

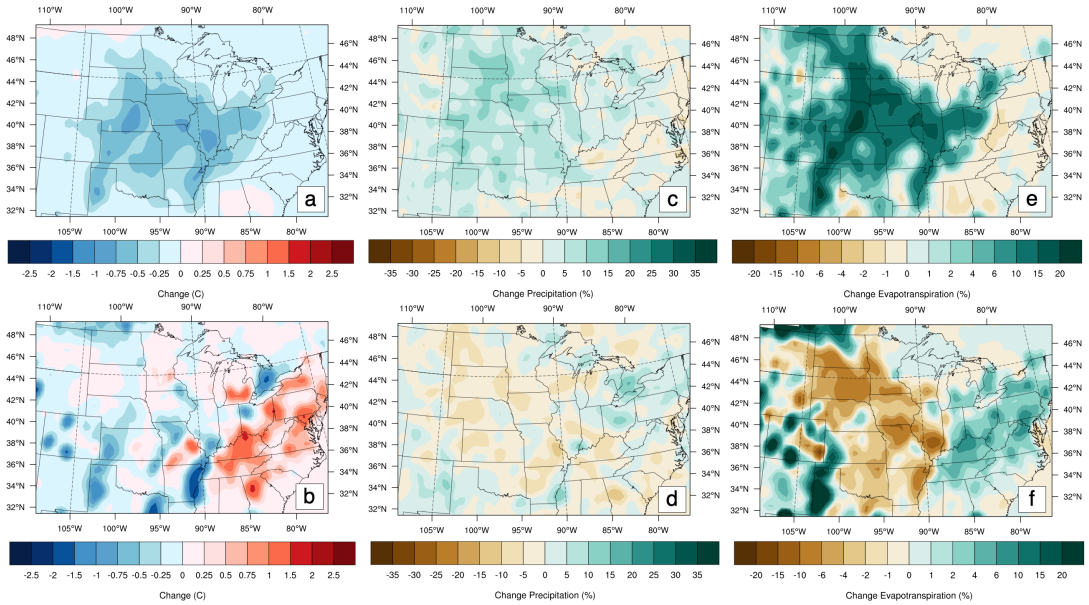

Figure 3-15: July–August average temperature changes (C) in the MRCM short-term simulations (1982–2005) due to (a) intensification of agricultural land only and (b) the expansion of irrigated and non-irrigated cropland with consistent productivity. (c),(d) As in (a),(b), but for precipitation (%). (e),(f) As in (a),(b), but for evapotranspiration (%). Data are plotted using a 9-point smoothing function.

3.7 Discussion and Conclusions

In Nikiel (2018), work was presented on expanding the MIT Regional Climate Model (MRCM) simulation time period capability in order to capture the full 20th century, as well as on developing a methodology to capture the full extent of agricultural change within the capabilities of the Integrated Biosphere Simulation (IBIS) land use model [178]. This chapter builds on this work substantially and includes a further investigation of the natural variability and SST teleconnections at play in this region, updates in simulation and analysis region and methodology, and a decomposition of the competing effects of land use change components. Additionally, this analysis includes changes in evapotranspiration in the region, a variable strongly tied to agricultural development and summer moisture availability that will be explored more in depth in Chapter 4.

This study introduces several novel results to the existing literature on the impacts of agricultural development on climate in the Midwest [255, 48, 10, 172, 9]. First,

this study presents the consideration of continuous expansion and intensification of agriculture throughout the 20th century, rather than a simple sensitivity study within a single time period. Additionally, all three elements of agricultural development - expansion, irrigation, and yield increases - are included rather than a subset, and are allowed to evolve concurrently through time using recent, long term land use data and reanalysis. Extensive installation of drainage tiles during the late 1800s and early 1900s in the states included in our Midwest region is not discussed here for several reasons. Firstly, drainage is intended to moderate spring soil moisture peaks and, as will be discussed in Chapter 4, the connection to changes in July-August is complex. Additionally, it is likely that the reduction in spring soil moisture excess is not enough to move the evaporation regime from energy-limited to water limited and therefore is unlikely to have an effect on the partitioning of latent and sensible heat fluxes.

Through careful inclusion of all major components of agricultural development that influence energy and water budget partitioning, this study was able to model the influence of these land use changes on the regional climate of the Midwest and Great Plains during the 20th Century. Vegetation changes had a substantial impact on temperature in the region, with strong cooling in agreement with observed change, especially given the relatively weak historical GHG effect. Precipitation variability and change during the period are more complex, and influences from vegetation and GHG are not enough to explain observed precipitation changes. In particular for precipitation, both agricultural intensification and expansion play distinct and occasionally opposing effects on shaping the pattern of changes in this region. The coherent cooling and wetting effect of intensification is modified by shifting land use patterns and the drying that accompanies them. These compounding effects show the importance of carefully considering and including all relevant details of land use forcings.

It is important to consider the areal extent of agriculture and its productivity separately within the climate system for two reasons. First, as shown in the sensitivity studies, they have, at times, opposing effects and modify the energy and water budgets to different degrees. Second, in the course of the 20th century, and likely in the

future, these changes have had different development arcs. While expansion and redistribution of cropland areas was dominant in the early part of the century and continued more modestly in later decades, intensification began in the 1930's and 40's in the US and has seen a consistent rise. Future population growth and food demand increase pressure to maintain and improve productivity even while cropland area itself is shrinking [263, 210]. As the balance of land use components changes in the future, so will their effects on regional climate. Areas that have seen significant agricultural development in the 20th century may stabilize in the 21st, allowing GHG and other anthropogenic factors to drive future changes in a way that breaks from historical trends. Therefore, it is important to carefully consider each component as well as a holistic view to understand the breakdown of effects as well as realistically depict changes in model simulations.

Although the results here show that land use change has shaped the regional climate changes in this region over the last century, natural internal variability is shown to be influential. Literature has highlighted the strong impact of natural variability in North America [47] and in the occurrence of the warming hole itself [16]. An understanding of the importance of these natural variations has been taken into consideration in the multiple member design of this study, and the consideration of non-anthropogenic forcings on the observed changes. The decadal variability of SST patterns, particularly in the Atlantic, seem to have played a role in precipitation changes, with supporting influences from the Tropical Pacific and the Central North Pacific. The mechanism for this change is probably the strengthening and westward expansion of the North Atlantic Subtropical High (NASH) [268, 111], which is explored further in the supplementary material for this chapter.

By combining the three major forcings considered here — agricultural development, GHG, and SST patterns — a superposition of simulation results and observation based estimates is able to reproduce, to a large degree, the pattern of precipitation and temperature changes that occurred in the Central United States during the 20th century (Fig. 3-16).

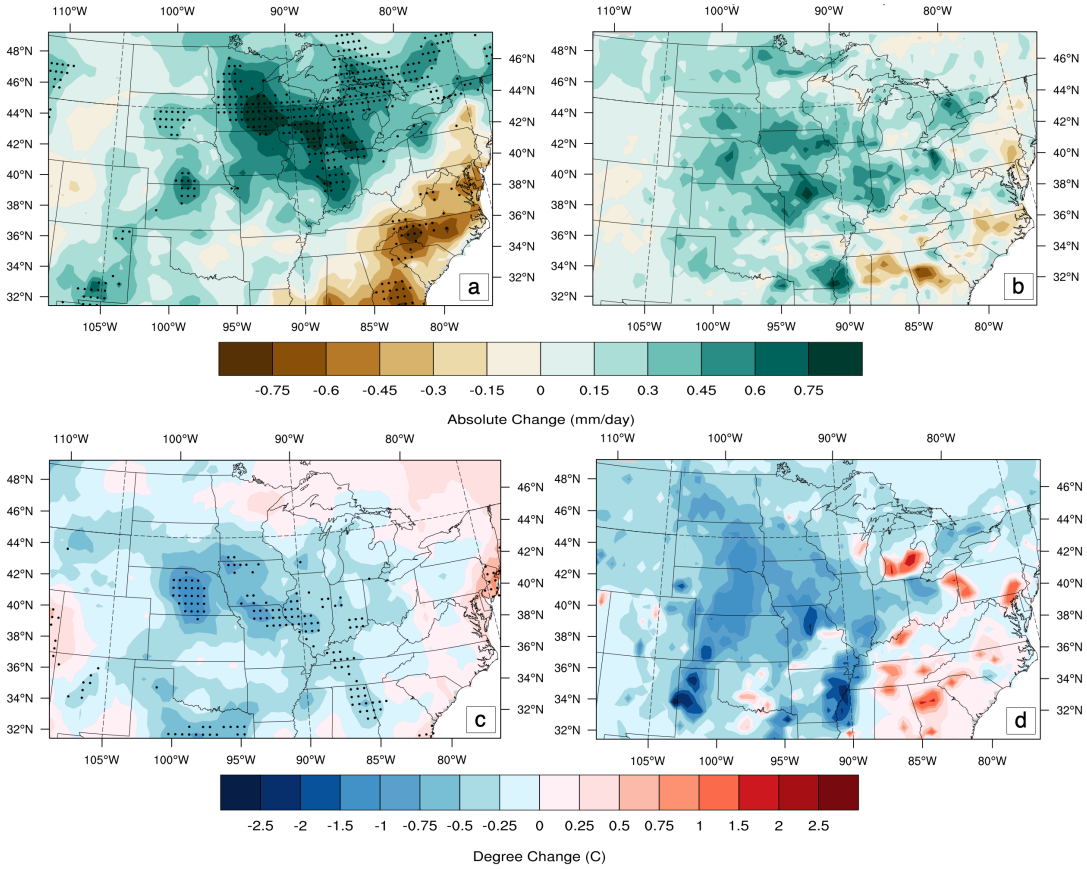

Figure 3-16: (a) Observed July–August precipitation change (mm/day) from 1920–1949 to 1970–1999 in CRU data. (b) Composite precipitation change in the same period from simulated vegetation and GHG impacts as well as estimated SST influence (individual components shown in Figs. 3-12c–e). (c) Observed July–August temperature change (°C) from 1920–1949 to 1970–1999 in CRU data. (d) Composite temperature change in the same period from simulated vegetation and GHG impacts as well as estimated SST influence (individual components shown in Figs. 3-9c–e).

Chapter 4

Impact of Climate Change on the Hydrology of Summer Agriculture in the American Midwest

Relevant Papers and Presentations

Nikiel, C.A. and Elfatih A.B. Eltahir (2021). Impact of Climate Change on the Hydrology of Summer Agriculture in the American Midwest. In preparation for submission to Journal of Climate.

4.1 Introduction and Background

The United States is a vital supplier of corn and soybean to the world, producing upwards of 30% of the total market in both summer crops [155] [240] [241], with an agricultural product market value of over $76 billion dollars in 2007 [98]. Much of the production of these crops is in an area known as the "Cornbelt" that spans the Midwestern United States, and is centered over Iowa, Illinois, Indiana, and Ohio (Fig. 4-1a) [271]. As seen in Chapter 3, yields in this region have increased dramatically over the 20th century, up to 400% (Fig. 3-2 and 3-3), and the production in this region

is of national and international importance (Fig. 4-1b) [262]. Climate studies focused on this region are important because changes in the mean climate and variability of the region in the long-term may affect the yield potential of crops, and conditions that have been favorable for yield increases may disappear [197]. Even in the very short term, increased temperatures and depressed precipitation can severely impact the health of a season's harvest [74]. For example, the drought of 1988 resulted in a 30% reduction in grain yields [98]. Understanding the conditions that have supported this agricultural production in the past — and how they may change in the future — is important given increasing global demand for food and feed.

Despite its position as an agricultural powerhouse today, the Cornbelt region in its pre-developed state was not a prime candidate for intense cultivation. Historically an ecologically rich swampland, this region was an attractive source for lumber for the eastern seaboard markets of the colonies and early America especially after the completion of the Erie Canal in 1825 [41]. In 1849, the passage of the first Swamplands Act turned over wetland areas to states into order to reclaim them for useful purposes, since they were viewed largely as areas that spread disease [156]. This reclamation took off dramatically when drainage tiles became mass produced and more easily accessible, and the newly drained land became some of the most productive in the country [156]. Today, roughly 95% of wetland areas in the Cornbelt have been drained for both animal pasture and crop agriculture with most of this drainage occurring pre-1930 [156] [242]. Connection to the east coast of the United States through the Great Lakes and an expanding railroad network made the area economically favorable for large scale commercial production [114]. To this day, a substantial amount of the Cornbelt is drained annually (Fig. 4-1c, Fig. E-1) [264].

The natural hydrology of the area is characterized by a fall, winter, and spring where precipitation exceeds evapotranspiration and creates a peak in soil moisture in the late spring (Fig. 4-2a-b); very wet springs can cause significant delays in planting, early crop losses, and long-term yield impacts [287]. This spring peak necessitates the extensive drainage of the area, and during spring the combined effect of natural drainage and artificial drainage contributes to stream flow, but more importantly,

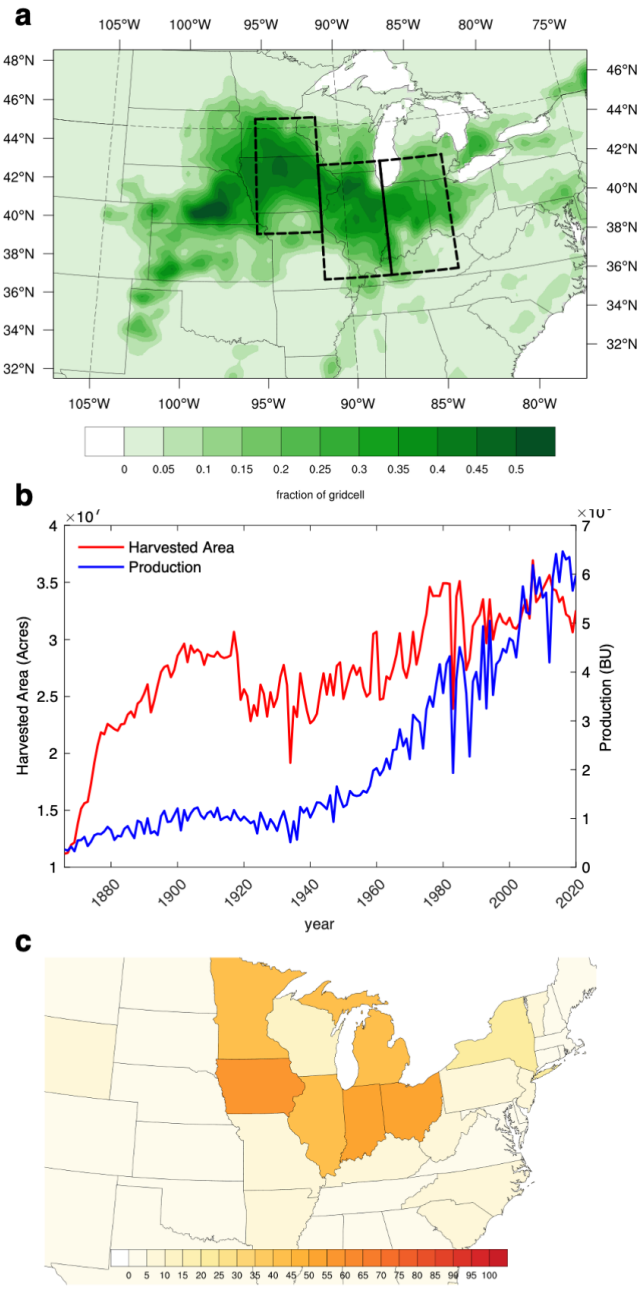

Figure 4-1: a) 1975-2004 average fraction of grid cell (0.25x0.25 degree) used to grow C4 pathway annual crops [117]. Black boxes show analysis regions, 1-3 from left to right. Region 1 (264.5-268.5°E,39.5-45.5°N), Region 2 (268.5-272.5°E,37.0-43.0°N), and Region 3 (272.5-276.5°E,37.0-43.0°N). The full area is referred to here as the Heartland b) Total harvested area (Acres) [red] and total production (Bushels) [blue] of grain corn in Iowa, Illinois, Indiana, and Ohio from 1866-2020. [262] c) Percentage of acres of harvested cropland drained by subsurface tiles in 2017 [261].

constrains the peak and variability of soil moisture. This is seen through the higher correlation between total spring (JFMAM) precipitation and peak streamflow in Illinois during the same period ($R^2 = 0.53$), versus the relationship between precipitation and peak soil moisture in JFMAM ($R^2 = 0.19$) (Fig. 4-2c). Additionally, peak soil moisture in the spring from 1984-2018 varied roughly half as much as summer minimum soil moisture from June-September (JJASO) illustrating the management of spring moisture in this region (Fig. 4-2d). After its peak in April to May, root layer soil moisture declines throughout the summer when evapotranspiration exceeds precipitation until it reaches a minimum in August-September (Fig. 4-2b).

There is disagreement in the literature on the trajectory of summer moisture supply in the Midwestern United States under climate change, with some earlier modeling literature pointing to drying of soil moisture due to increased temperatures that can even counteract increased precipitation in other seasons [276] [49] [36]. However, it has been shown that these findings are sensitive to model choice and land use parameterization [281] [280] [235]. Using a complex land surface scheme rather than a bucket model, Seneviratne et al. (2002) showed that increases in summer drying were moderate and compensated for by increases in precipitation in the spring [235]. Winter and Eltahir (2012) similarly found that increases in summer dryness from increases in evapotranspiration were counteracted by increases in precipitation in their regional climate model experiments [280]. Patricola and Cook (2013) in their two-part study, also show increases in spring (MAM) precipitation and decreases in the summer (JJA) that are comparable [201] [200]. The question is whether these seasonal changes can compensate for one another in the drained system, and, if not, if future changes pose a dire risk in the context of historical trends.

This study focuses on the changes in climate in the Midwest in summer, May-August (MJJA), and the resultant precipitation minus evapotranspiration (P-E) for several reasons. First, this switch in P-E regimes is a defining trait of summer hydrology in the region and dry extremes in late summer can pose significant problems during the most critical part of grain filling and yield development for summer crops like corn [245]. While there are pockets of irrigation in the region (Fig. 4-3) most of

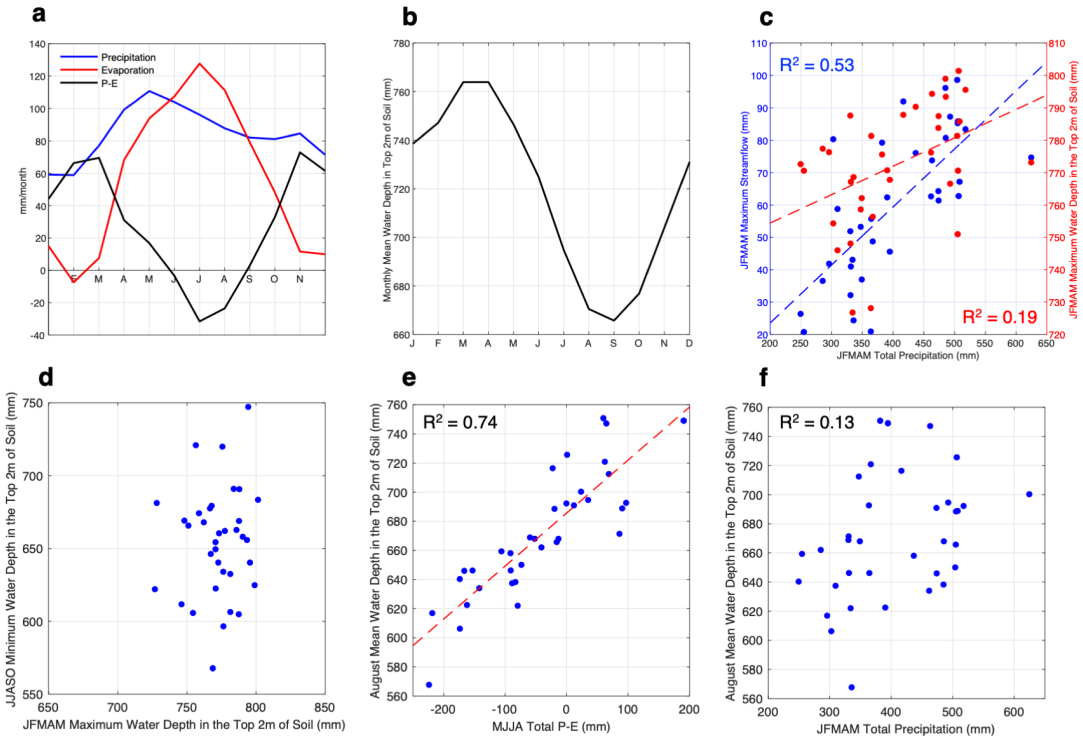

Figure 4-2: a) 1984-2018 average climatology of precipitation (mm/month) [blue], evaporation (mm/month) [red], and Precipitation-Evapotranspiration (mm/month) [black] for Illinois [46]. b) 1984-2018 average climatology of water depth in the top 2m of Soil (mm) [46] c) 1984-2018 average January-May total precipitation (mm) versus January-May maximum streamflow in Illinois (mm) [blue] with linear trend and January-May total precipitation (mm) versus January-May maximum water depth in the top 2m of soil (mm) [red] with linear trend [46] d) 1984-2018 average January-May maximum water depth in the top 2m of soil (mm) versus June-October minimum water depth in the top 2m of soil (mm) [46] e) 1984-2018 average August mean water depth in the first 2m of soil (mm) versus MJJA total Precipitation-Evaporation (mm) plotted with linear trend line [red] [46] f) 1984-2018 average January-May total precipitation (mm) versus August mean water depth in the top 2m of soil (mm) [46]

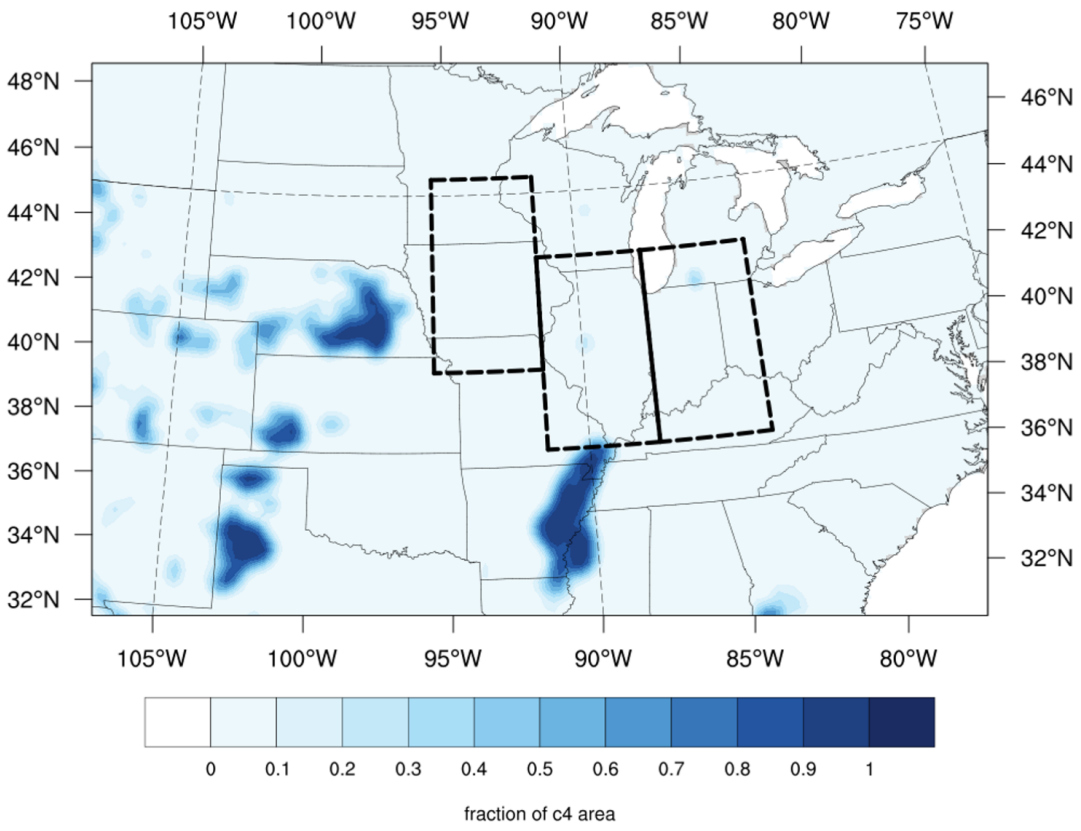

Figure 4-3: 1975-2004 average fraction of C4 pathway annual cropland grid cell (0.25x0.25 degree) that is irrigated [117]. Black boxes show analysis regions, 1-3 from left to right, where Region 1 (264.5-268.5E,39.5-45.5N), Region 2 (268.5-272.5E,37.0-43.0N) and Region 3 (272.5-276.5E,37.0-43.0N). The full area is referred to here as the Heartland.

the Cornbelt is rainfed. In 2007 only roughly 1.7% of cropland in Illinois was irrigated [174].

Second, because of the nature of artificial drainage in the study region, spring metrics like precipitation and soil moisture are more decoupled from summer responses like soil moisture minimum than they might be in other more natural systems. As mentioned before, previous studies have shown that increases in precipitation in the winter and spring could potentially alleviate summer drying. However, this is only the case if the soil is not completely saturated at its peak even under the current precipitation levels. For most years, soil moisture is close to saturation by the end of the spring [287], and further wetting is avoided in large part due to the exten-

sive drainage network described above. In fact, while in-situ data from Illinois show that January-May Total Precipitation has shown a positive trend of 2.00 mm/year (p-value = 0.18) from 1984-2018, peak soil moisture values during the same period have decreased by 0.5 mm/yr (p-value = 0.095) (Fig. 4-4). While changes in spring conditions may set up different starting conditions for summer drying, the metric that is crucial to agriculture is the P-E deficit that occurs in the summer. Summer P-E has a strong correlation to August mean water depth in the upper 2m of soil (R^2 = 0.74) (Fig. 4-2e), while spring precipitation has a substantially weaker correlation (R^2 = 0.13) (Fig. 4-2f).

4.2 Methodology and Data

Data from the Coupled Model Intercomparison Project 5 and 6 (CMIP5/CMIP6) multi-model ensembles were obtained from the Centre for Environmental Data Analysis (CEDA) Archive through http://esgf-index1.ceda.ac.uk. We acknowledge the World Climate Research Programme, which, through its Working Group on Coupled Modelling, coordinated and promoted both CMIP5 and CMIP6. We thank the climate modeling groups (Listed in Table A-1 and Table A-2) for producing and making available their model output, the Earth System Grid Federation (ESGF) for archiving the data and providing access, and the multiple funding agencies who support CMIP5, CMIP6 and ESGF. For CMIP5 the U.S. Department of Energy's Program for Climate Model Diagnosis and Intercomparison provides coordinating support and led development of software infrastructure in partnership with the Global Organization for Earth System Science Portals.

This study uses a combination of CMIP5 and CMIP6 simulations with available historical and rcp85/ssp585 runs with evapotranspiration (evspsbl) and precipitation (pr) output provided at monthly timescales. All ensembles with a complete time period and scenario availability are used. A complete list of models and number of ensembles used can be found in Appendix A (Table A-1 and Table A-2). Changes from the historical period (1975-2004) to the future period (2070-2099) for precipitation,

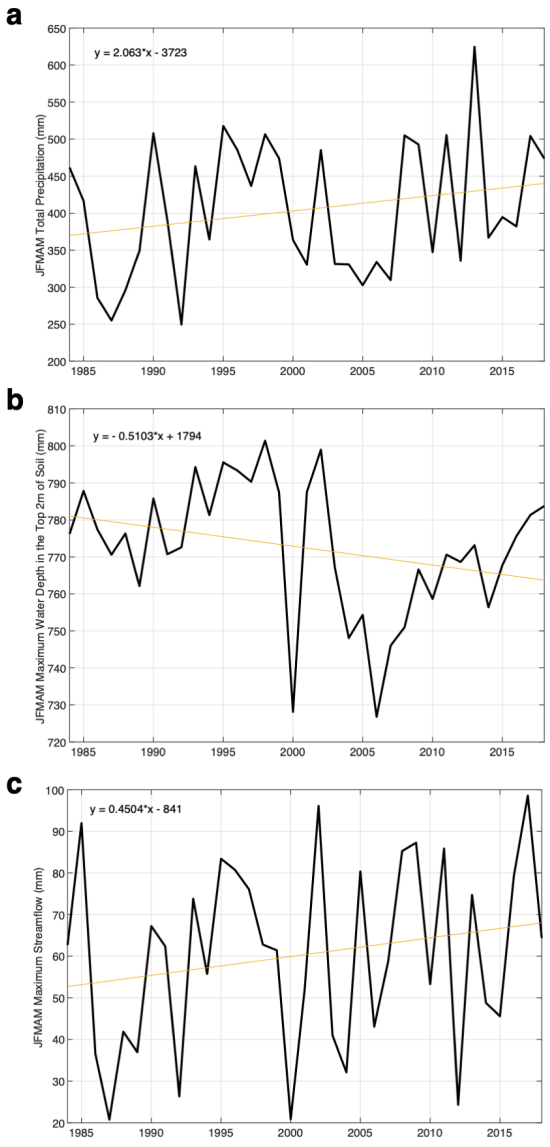

Figure 4-4: a) 1984-2018 January-May maximum water depth in the top 2m of soil (mm) in ISWS data averaged over stations in Illinois [46]. Linear trend and equation in yellow. b) 1984-2018 January-May total precipitation (mm) in ISWS Data averaged over stations in Illinois. Linear trend and equation shown by yellow line. c) 1984-2018 January-May maximum streamflow (mm) in ISWS sata averaged over stations in Illinois. Linear trend and equation in yellow.

evapotranspiration, and P-E are calculated for each ensemble individually, after which ensemble averages are made among multiple ensemble models. The multi model mean is calculated from the model ensemble means in order not to weigh multi-ensemble models more heavily. Future scenarios taken from CMIP5 and CMIP6 may differ slightly between the two ensembles due just to the scenario applied as forcing. CMIP5 utilizes the relative concentration pathways alone while CMIP6 incorporates a measure of societal change known as the Shared Socioeconomic Pathway. RCP85 in CMIP5 and SSP585 in CMIP6 are considered analogous but differences may exist [191].

Observations were taken from Livneh daily CONUS near-surface gridded meteorological and derived hydrometeorological data generated using the Variable Infiltration Capacity VIC hydrologic model v.4.1.2.c which was driven with the companion meteorological data and available from 1915-2012 at 1/16-degree resolution. Livneh data were provided by the NOAA/OAR/ESRL PSL, Boulder, Colorado, USA, from their Web site at https://psl.noaa.gov/data/gridded/data.livneh.html [140].

While the Livneh et al. (2013) data used here for observational comparison include the caveat that they should not be used for trend analysis, we cautiously use them here for three reasons. First, the area of interest in this study has one of the most long-term, dense networks of observational stations in the North American continent. Second, this analysis relies mainly on the trend in the latter part of the 20th century when gaps in data availability are expected to be less common. Third, we compare the trends shown in the data to trends in other observational data sources.

Precipitation data for comparison were taken from CRUTS4.01 [94], produced by CRU at the University of East Anglia and funded by the UK National Centre for Atmospheric Science (NCAS), a NERC collaborative centre. Potential Evapotranspiration Data were taken from CRUTS4.04 [95]. Data are available to download at http://dx.doi.org/10.5285/58a8802721c94c66ae45c3baa4d814d0. In-situ observational data for Illinois from 1984-2018 were obtained from the Water and Atmospheric Resources Monitoring Program (WARM) [46]. The hydrologic and meteorological data used in this study are publicly available from the Illinois State

Water Survey (ISWS) Water and Atmospheric Resources Monitoring (WARM) Program (https://www.isws.illinois.edu/warm/datatype.asp) and U.S. Geological Survey (USGS) Water Data for the Nation (https://waterdata.usgs.gov/nwis), for which the authors are thankful. Data were processed and provided to the authors by Pat J.-F. Yeh. Total precipitation is averaged from 117 ISWS stations throughout the state. Soil moisture data are measured at 19 Illinois Climate Network (ICN) stations across 11 layers down to 2m [108]. Sixteen of the nineteen stations that had data available as far back as 1984 are used, with two stations at Dixon Springs. Runoff was calculated using area-weighted streamflow from gages at the Illinois River at Valley City, the Rock River near Joslin, and the Kaskaskia River near Venedy. Their combined drainage area covers approximately two thirds of Illinois [287]. Evaporation values used are calculated through atmospheric water balance, which is shown in Yeh et al. (1998) to correspond well to soil water balance methods [287].

Cropland and Irrigation area were obtained from LUHv2 and available to download at http://luh.umd.edu/ [117]. Crop Yield and Acreage data are obtained from Crop Surveys from the USDA National Agricultural Statistics Service (https://quickstats.nass.usda.gov/) [262].

To show the full range of P-E summer totals in all of the component models in the CMIP5 and CMIP6 ensembles, bias correction was performed on the May-August total P-E values at each grid cell in the regridded 0.5-degree GCM ensembles. We utilize a Gaussian distribution and quantile mapping to align the GCM to observed data. A Gaussian is appropriate for P-E since it has a relatively normal distribution in its original form.

Note the differences in the composition of the methods of analysis will cause differences in the averages presented between periods. The averages in Table 4.1 provide the most complete version of the ensemble change for the un-bias corrected P-E data. The historical timeseries for CMIP5 omit two models because of data limitations (not available prior to 1950) and the histograms as mentioned above use the bias corrected data.

Table 4.1: Area average precipitation (mm/MJJA), evapotranspiration (mm/MJJA), and Precipitation-Evapotranspiration (mm/MJJA) of MJJA Total Observations [140] and Multi-Model-Means of the GCM modeling groups (mm/MJJA) for the historical period (1975-2004) and the future period (2070-2099) under RCP8.5. Region 1 (264.5-268.5°E,39.5-45.5°N), Region 2 (268.5-272.5°E,37.0-43.0°N), and Region 3 (272.5-276.5°E,37.0-43.0°N). Heartland is the average of the three individual regions.

	Hist. E	Future E	Δ E	Hist. P	Future P	Δ P	Hist. P-E	Future P-E	Δ P-E
Reg. 1 Obs.	459.5 (0.9/yr)			440.7 (1.9/yr)			-18.6 (0.86/yr)		
Reg. 1 CMIP5	428.7	440.8	12.1	399.7	400.8	1.1	-29.2	-40.5	-11.3
Reg. 1 CMIP6	426.4	445.9	19.6	376.8	359.4	-17.4	-49.6	-86.5	-36.9
Reg. 2 Obs.	462.0 (0.93/yr)			413.3 (1.9/yr)			-48.7 (0.97/yr)		
Reg. 2 CMIP5	467.4	481.7	14.3	426.2	430.7	4.5	-41.4	-51.5	-10.2
Reg. 2 CMIP6	450.2	480.4	30.2	395.4	389.0	-6.5	-54.7	-91.4	-36.7
Reg. 3 Obs.	452.7 (1.05/yr)			423.9 (1.6/yr)			-28.8 (0.48/yr)		
Reg. 3 CMIP5	473.3	496.3	23.0	450.6	457.2	6.6	-22.9	-39.6	-16.7
Reg. 3 CMIP6	455.8	495.9	40.1	422.1	428.0	6.0	-33.7	-67.9	-34.1
Heart. Obs.	458.1 (0.96/yr)			426.0 (1.8/yr)			-32.0 (0.77/yr)		
Heart. CMIP5	456.4	472.9	16.5	425.5	429.6	4.1	-31.2	-43.9	-12.7
Heart. CMIP6	444.1	474.1	30.0	398.1	392.1	-6.0	-46.0	-81.9	-35.9

4.3 Results

We examine May-August monthly average precipitation, evapotranspiration, and P-E from observational data [140] and from an ensemble of models for CMIP5 (Table A-1) [249] and CMIP6 individually (Table A-2) [61]. All GCMs are regridded to 0.5 by 0.5 degrees for comparison and combination, and all available ensembles with both historical and RCP 8.5 data were used in this analysis. The study area is defined as the Heartland and this region is shown in Figure 4-1a and all subsequent figures. We have chosen this area consisting of three equally sized subregions as the core of agricultural productivity in the Cornbelt. All analysis is performed from the historical period (1975-2004) to the future period (2070-2099) under RCP8.5 emissions projections. P-E is analyzed primarily over the summer months as the deficit over this period determines agricultural success, but some analysis is presented for the full seasonal cycle.

4.3.1 Historical Climate and Trends

The Heartland study region experienced a total of about 458 mm of evapotranspiration and 426 mm of precipitation in May-August on average from 1975-2004. This region has relatively high levels of both variables in the summer compared to the rest of the Central and Eastern United States, but the differences between the two amounts still marks the Heartland out as a region with large negative P-E in the U.S., particularly in Northern Illinois (Fig. 4-5).

In the historical period, evapotranspiration has been increasing in the observations but has been outpaced by increases in precipitation in the area of interest (Fig. 4-6a,i) (Fig. E-2) and these changes can be attributed in part to agricultural development as shown in Chapter 3. This increase in evapotranspiration results in to an increase in vapor pressure (Fig. 4-6b) and through a concurrent constant temperature trend (Fig. 4-6e), an increase in relative humidity (Fig. 4-6g). This increase in relative humidity is correlated with an increase in precipitation over the region (Fig. 4-6i). Both the observations and the GCMs show a mostly negative P-E (average of -32 mm in

observations) in the Cornbelt region during May-August, the core of the agricultural period (Fig. 4-5c and E-3a-b). This P-E deficit has the highest magnitude in Illinois in the observations and in Illinois and Iowa in the GCMs.

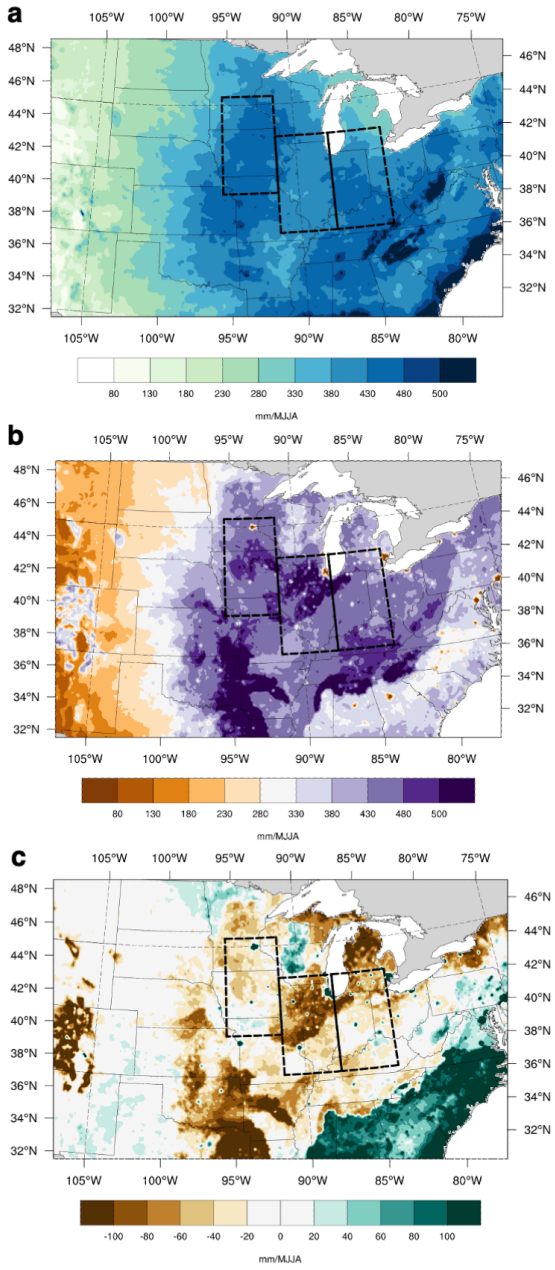

Figure 4-5: a) 1975-2004 average May-August total precipitation (mm) [140] b) 1975-2004 average May-August total evapotranspiration (mm) [140] c) 1975-2004 average May-August total Precipitation-Evapotranspiration (mm) [140]

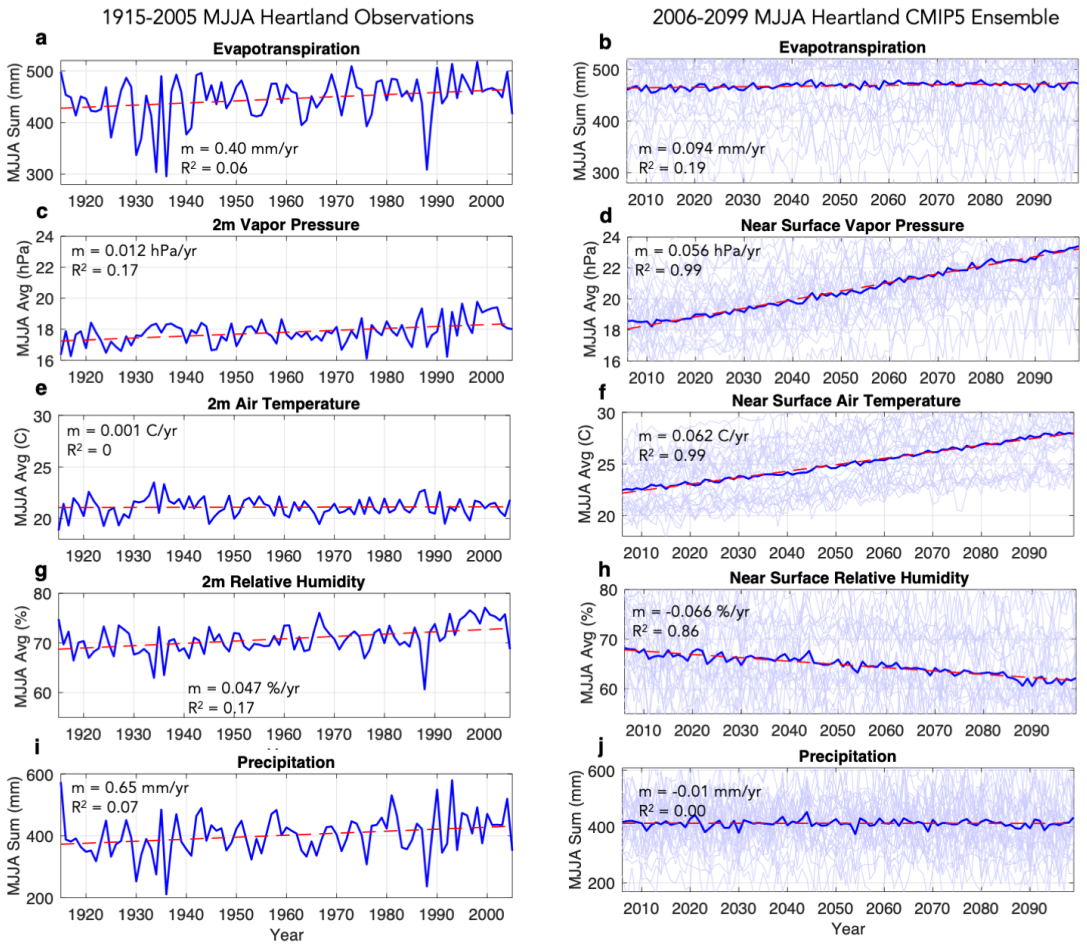

Figure 4-6: a) 1915-2005 timeseries of MJJA total heartland average evapotranspiration (mm) [140] b) 2006-2099 timeseries of MJJA total heartland average evapotranspiration (mm) from CMIP5 Multi Model Ensemble c) 1915-2005 timeseries of MJJA total heartland average 2m vapor pressure (hPa) (CRUTS4.05) d) 2006-2099 timeseries of MJJA total heartland average near surface vapor pressure (hPa) from CMIP5 Multi Model Ensemble e) 1915-2005 timeseries of MJJA total heartland average 2m air temperature (C) (CRUTS4.05) f) 2006-2099 timeseries of MJJA total heartland average near surface air temperature (C) from CMIP5 Multi Model Ensemble g) 1915-2005 timeseries of MJJA total heartland average 2m relative humidity (%) (CRUTS4.05) h) 2006-2099 timeseries of MJJA total heartland average near surface relative humidity (%) from CMIP5 Multi Model Ensemble i) 1915-2005 timeseries of MJJA total heartland average precipitation (mm) [140] j) 2006-2099 timeseries of MJJA total heartland average precipitation (mm) from CMIP5 Multi Model Ensemble. Used all models listed in Table A-1 except for CMCC-CM, FGOALS-g2, FIO-ESM, GISS-E2-H, GISS-E2-R, HadGEM2-CC, HadGEM2-ES Ensemble 1, IPSL-CM5A-LR Ensemble 4, MPI-ESM-LR, MPI-ESM-MR due to data availability.

While the observational data shows increasing historical trends in P-E in this region due to this balance between increasing precipitation and evapotranspiration, both the CMIP5 and CMIP6 suite of models show drying over this historical period, and indeed over the entire 20th century (Figs. 4-8 and 4-9). In fact, the models in CMIP5 and CMIP6 show a wide range in trends in precipitation and evapotranspiration in the region over the historical period, often showing a negative trend in precipitation (Fig. 4-7). However, it should be noted that models may expect to have contrasting trends in a region and period where climate change forcing has been mild, and where Chapter 3 has shown that internal variability played a role in changing variables like precipitation. Another explanation for this mismatch is a failure to fully represent agricultural intensification in the 20th century, a factor that has significantly influenced the historical regional hydrology [180] [9]. Additionally, the included models have a wide range of Land Use and Land Cover representations as well as representation of the Great Lakes [132] [45].

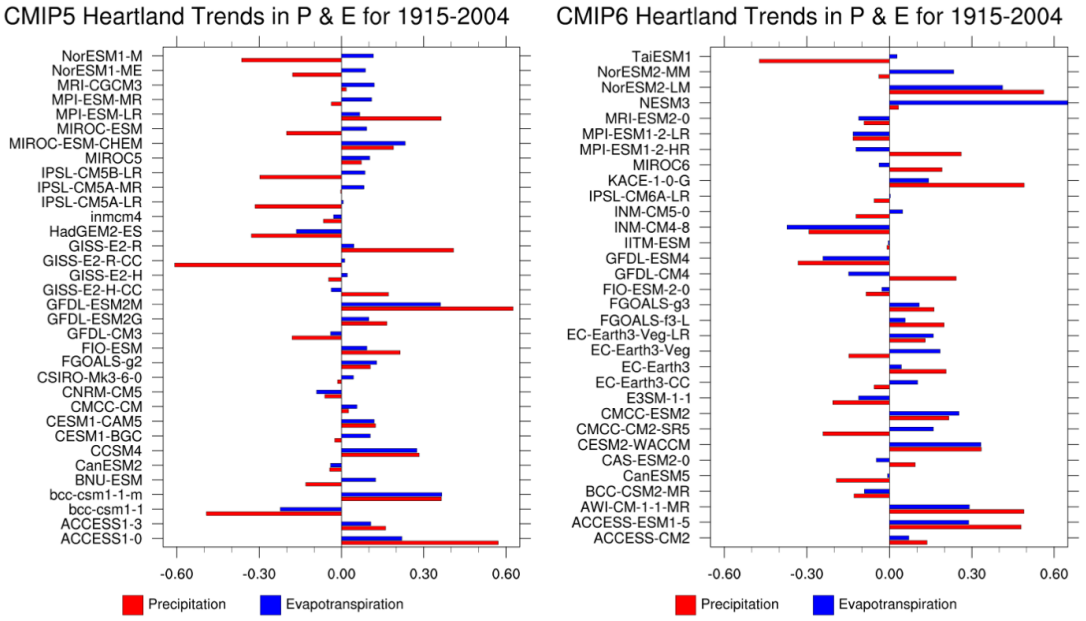

Figure 4-7: Historical (1915-2004) trends in total May-August precipitation (mm/yr) and evapotranspiration (mm/yr) in the ensemble mean CMIP5 and CMIP6 GCMs

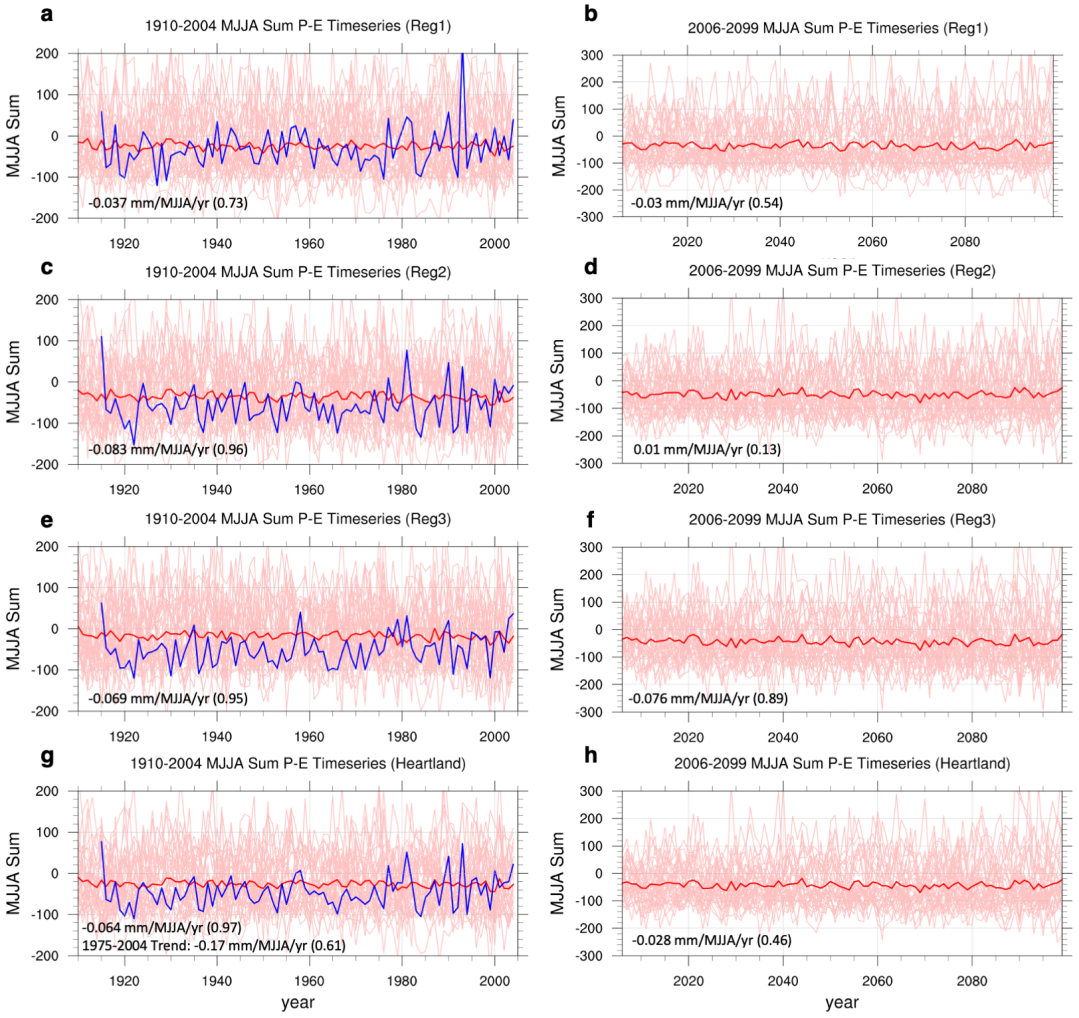

Figure 4-8: Total MJJA P-E timeseries in CMIP5 for Region 1 (264.5-268.5°E,39.5-45.5°N) for a) Historical (1910-2004) b) Future (2006-2099) under RCP8.5 with all individual models [pink], the multi-model-mean [red] and the observations [blue] [140]. c-d) Region 2 (268.5-272.5°E,37.0-43.0°N) e-f) Region 3 (272.5-276.5°E,37.0-43.0°N) g-h) Heartland (average of regions 1-3). Note that the historical multi-model-mean does not include HadGEM2-CC and CESM1-WACCM since these models' historical record begins post 1950.

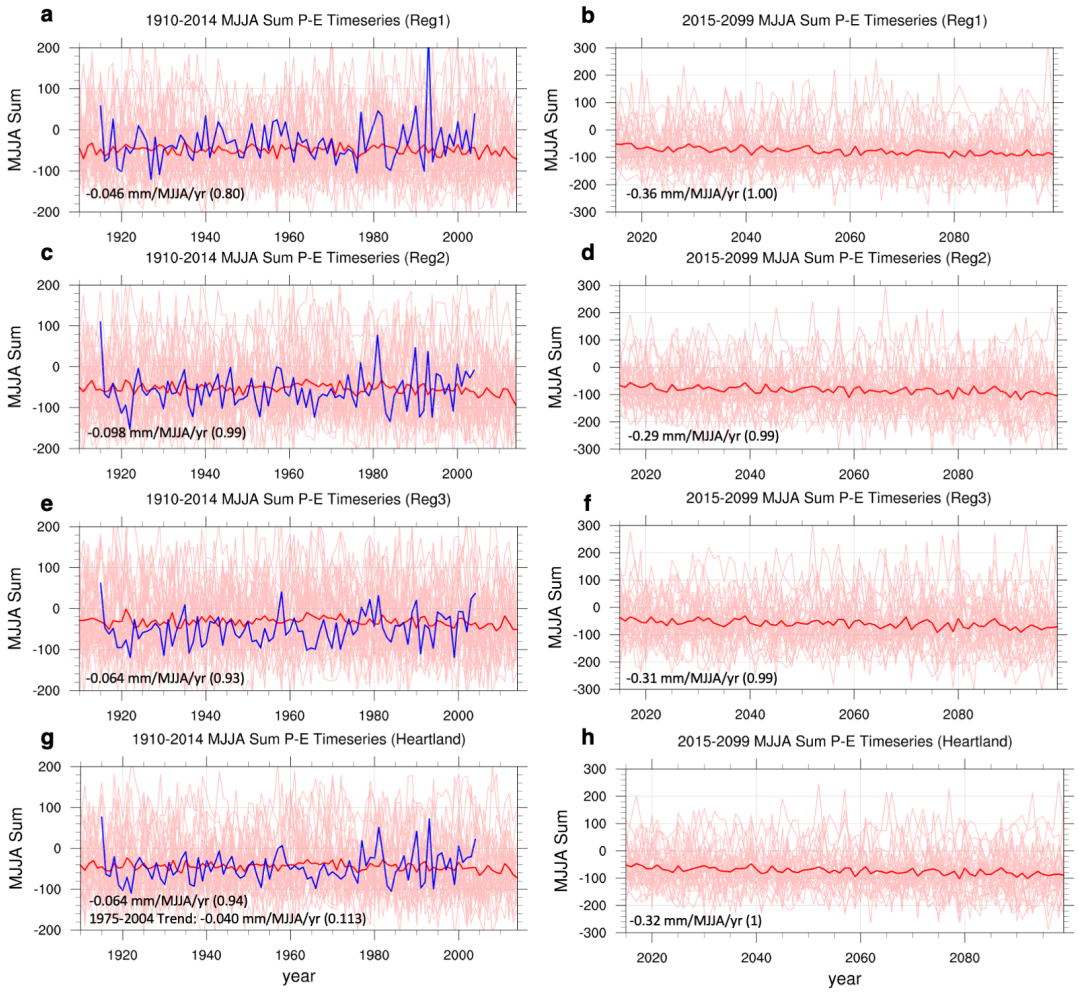

Figure 4-9: Total MJJA P-E timeseries in CMIP6 for Region 1 (264.5-268.5°E,39.5-45.5°N) for a) Historical (1910-2014) b) Future (2015-2099) under RCP8.5 with all individual models [pink], the multi-model-mean [red] and the observations [blue] [140]. c-d) Region 2 (268.5-272.5°E,37.0-43.0°N) e-f) Region 3 (272.5-276.5°E,37.0-43.0°N) g-h) Heartland (average of regions 1-3).

The positive trend in P-E in gridded observational data is corroborated by trends in May-August total change in terrestrial water storage, calculated from data from 19 Illinois Climate Network weather stations maintained by Illinois State Water Survey (ISWS), Water and Atmospheric Resources Monitoring (WARM) Program (2018) and 11 USGS stream gauges [46]. (Fig. 4-10). The change in terrestrial water storage (TWSC) is the sum of the change in soil moisture storage and groundwater storage.

Yeh and Wu (2018) found a significant positive trend in both precipitation and evaporation for the period 1992-2013 using these same data, with precipitation increases outpacing evaporation [288]. Basso et al. (2021) showed that contrasting changes in minimum and maximum temperatures, increased humidity, and increased precipitation over the historical period have led to reductions in vapor pressure deficit and have likely reduced crop water deficits in the historical period [19]. This reduction in vapor pressure deficit has been related to a decrease in potential evapotranspiration, but the impact on actual evapotranspiration was not investigated.

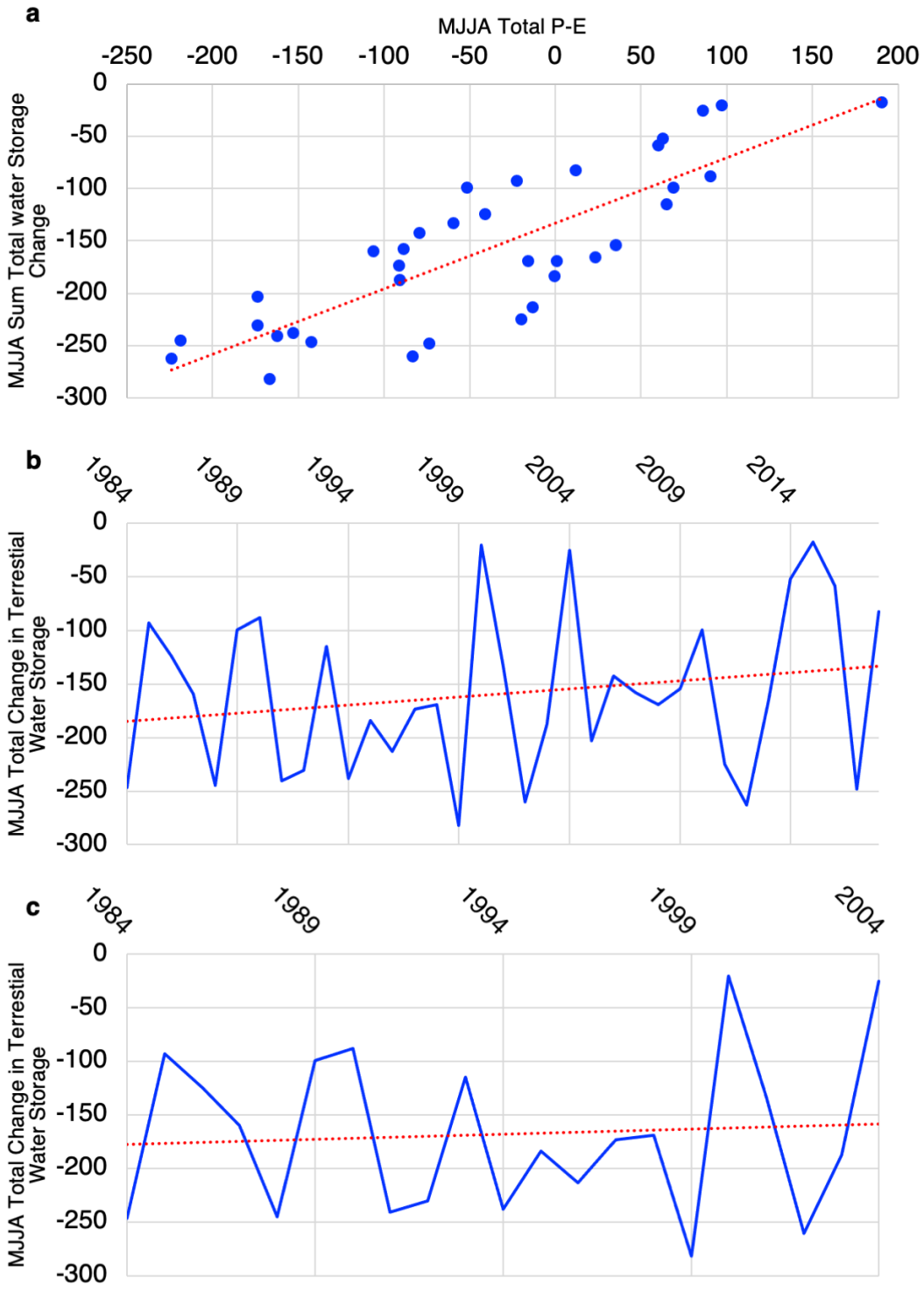

Figure 4-10: Comparison of ISWS data a) MJJA total P-E (mm) versus MJJA sum total water storage change (TWSC) (mm) ($R^2 = 0.6831$) b) MJJA total water storage change (mm) from 1984-2018 (trend = 1.5 mm/MJJA/yr) c) MJJA total water storage change (mm) from 1984-2004 (trend = 0.96 mm/MJJA/yr) [46]

4.3.2 Future Climate and Trends

In the future period, models predict that summer P-E will decrease across the region due to a larger and spatially consistent increase in evapotranspiration (Fig. 4-12) as compared to a mixed change in precipitation (Fig. 4-13) with the Heartland in the transition zone (Fig. 4-15c-d). In precipitation, the models disagree in the direction of future trends, though they are more consistent in the positive trend of evapotranspiration (Fig. 4-11). The CMIP5 multi-model ensemble projects a decrease in P-E from -31.2 mm in the historical period to -43.9 mm in the future; similarly, the CMIP6 multi-model ensemble projects a respective decrease from -46.0 mm to -81.9 mm (Table 4.1).

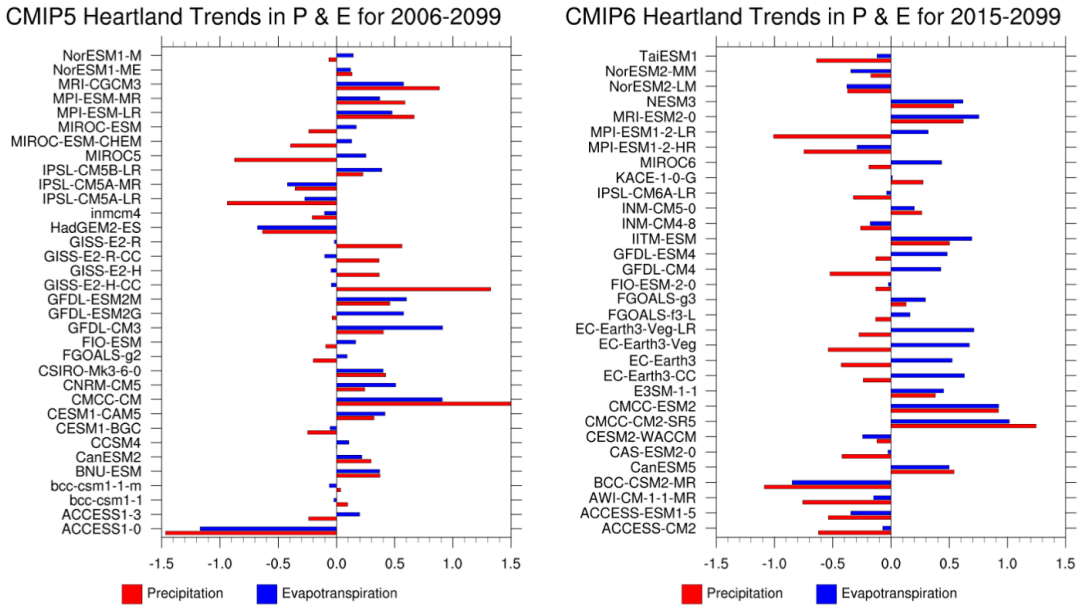

Figure 4-11: Future (2006-2099 & 2015-2099) trends in total May-August precipitation (mm/yr) and evapotranspiration (mm/yr) in the ensemble mean CMIP5 and CMIP6 GCMs

CMIP6 predicts a decrease in precipitation across this region in contrast to a relatively stable summer precipitation total in CMIP5. The center of the evapotranspiration increase in both model groups is over the Great Lakes region. Histograms of summer P-E occurrence averaged over the Heartland in CMIP5, and CMIP6 show that the mean shifts towards drying in the future under RCP8.5 in contrast to the wetting that occurred in the 20th century in observations (Fig. 4-15e-g). Note that

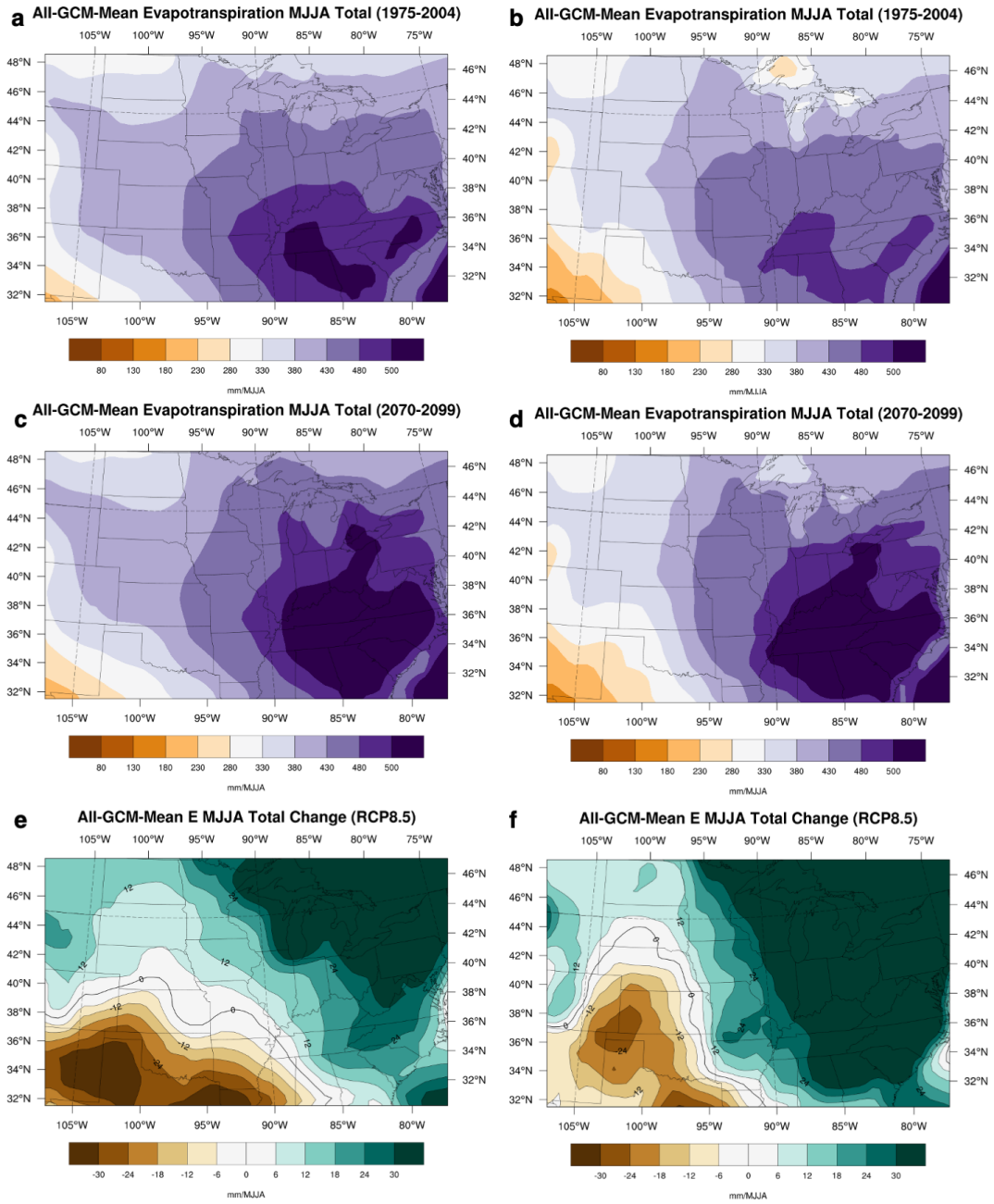

Figure 4-12: Average MJJA total Multi-Model-Mean evapotranspiration (mm/yr) for a) Historical period (1975-2004) in CMIP5 b) Historical period (1975-2004) in CMIP6 c) Future period (2070-2099) under RCP8.5 in CMIP5 d) Future period (2070-2099) under RCP8.5 in CMIP6 e) Change in historical to future period under RCP8.5 in CMIP5 f) Change in historical to future period under RCP8.5 in CMIP6.

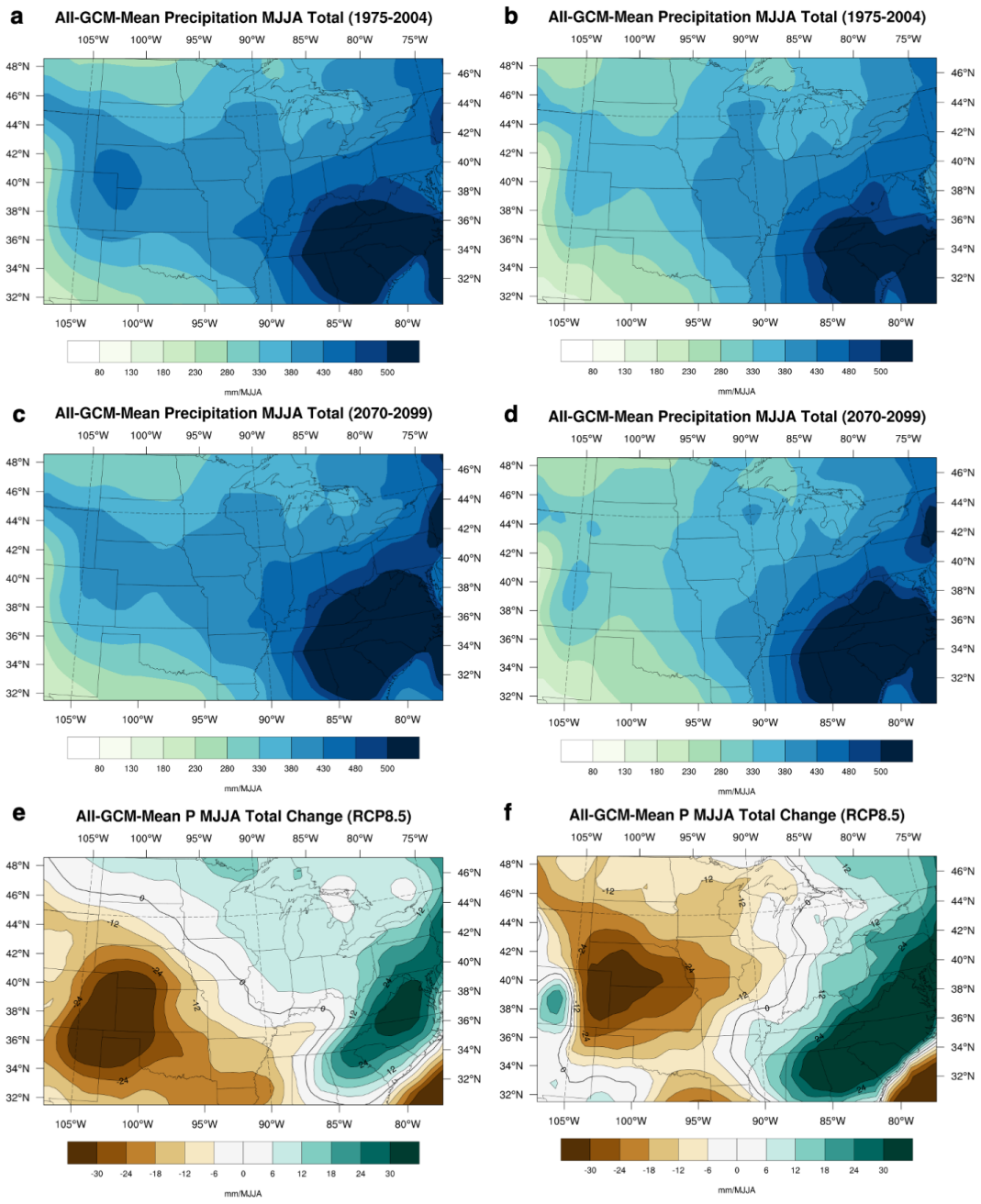

Figure 4-13: Average MJJA total Multi-Model-Mean precipitation (mm/yr) for a) Historical period (1975-2004) in CMIP5 b) Historical period (1975-2004) in CMIP6 c) Future period (2070-2099) under RCP8.5 in CMIP5 d) Future period (2070-2099) under RCP8.5 in CMIP6 e) Change in historical to future period under RCP8.5 in CMIP5 f) Change in historical to future period under RCP8.5 in CMIP6

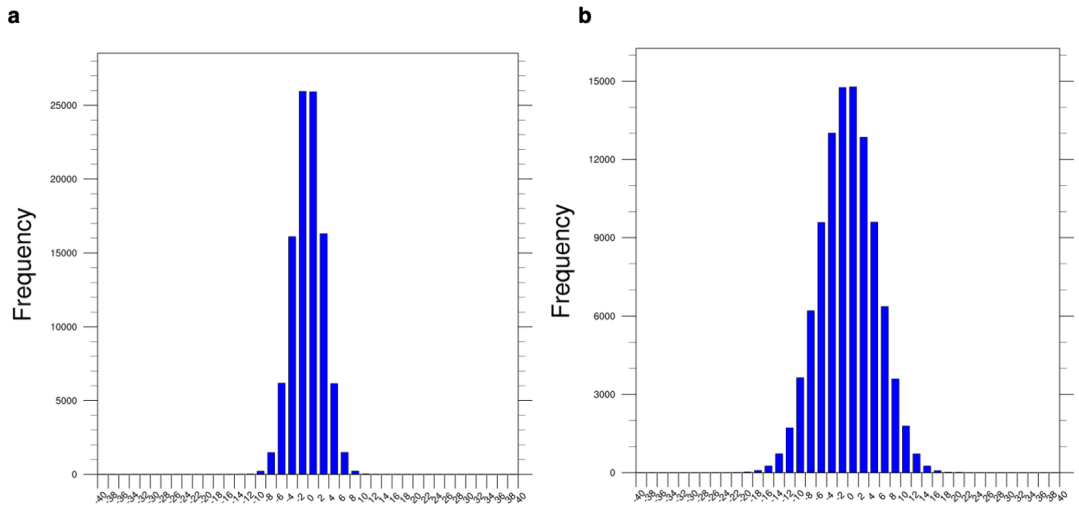

Figure 4-14: Sample distribution of historical (1975-2004) to future (2070-2099) May-August total P-E (mm/yr) changes in a) CMIP5 and b) CMIP6 performed through bootstrapping of 30-yr averages with replacement within individual ensembles.

the GCM data in the histograms has been bias corrected using quantile mapping as described in the methods. The same trends in near surface variables in the CMIP5 multi model ensemble relate the changes in evapotranspiration and precipitation, this time driven by 21st century climate changes. As before, increases in evapotranspiration and near surface vapor pressure are positively correlated (Fig. 4-6b,d). However the strong 21st century warming in the region (Fig. 4-6f) leads to a resulting decrease in relative humidity (Fig. 4-6h), and a stable or decreasing precipitation over the region (Fig. 4-6j). In order to show significance of future P-E changes in CMIP5 and CMIP6 multi-model ensembles, a bootstrapping procedure was performed for each ensemble with historical to future P-E changes being simulated by random sampling of 30-years with replacement for each period out of the total 60 years in each ensemble (1975-2004 & 2070-2099). This sampling and change calculation was performed 100,000 times and the results of the multi-model mean P-E changes are shown in Fig. 4-14.

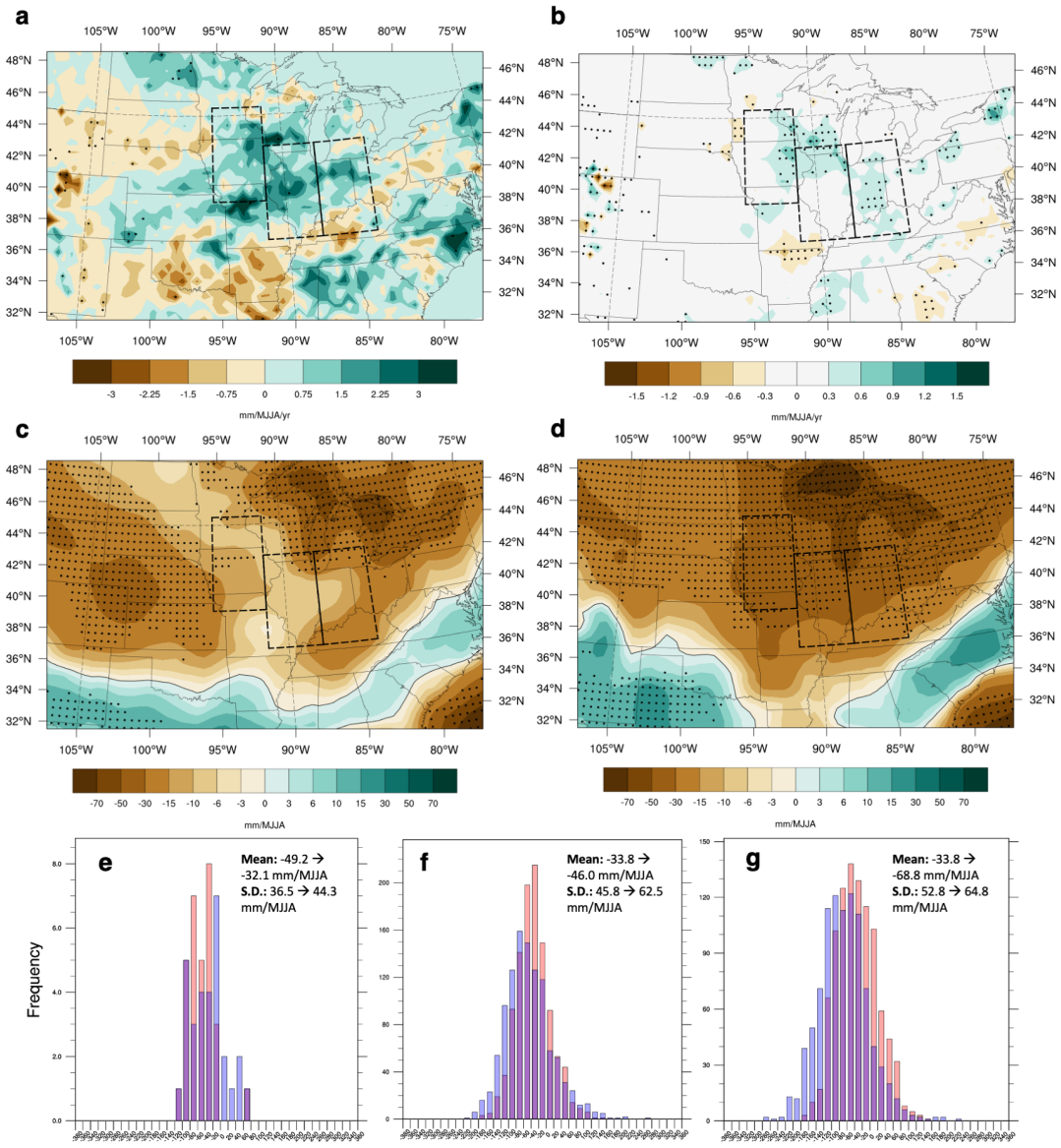

Figure 4-15: a) 1975-2004 Theil-Sen trend in May-August total precipitation-evapotranspiration (mm/yr) regridded to 0.5 x 0.5 degree. Stippling indicates p-value less than 0.05 according to Mann-Kendall significance test [140] b) Same as (a) but for 1915-2010 c) CMIP5 Multi Model Mean of 1975-2004 average to 2070-2099 average of May-August total Precipitation-Evapotranspiration (mm) under RCP8.5. Zero contour shown as black dotted line. Stippling shows grid cells where at least 75% of models agree on the direction of change. d) Same as (c) but for CMIP6 e) Frequency of Heartland average May-August total P-E (mm/yr) in the observations in early period (1915-1944) [red] and late period (1975-2004) [blue] f) Frequency of Heartland average May-August total P-E in all CMIP5 models in historical period (1975-2004) [red] and under RCP8.5 (2070-2099) [blue] g) same as (f) except for CMIP6.

4.3.3 Seasonality and Inter-annual Variability of Climate Changes

Two additional factors that must be considered are changes in the interannual variability of P-E and the timing of the P-E changes across the summer months. Figs. 4-15f-g both show an increase in the standard deviation of P-E summer totals, with CMIP5 showing a larger change in standard deviation relative to the change in mean than in CMIP6 (CMIP5: 16.7 mm/MJJA change in standard deviation for a 12.2 mm/MJJA change in the mean, and CMIP6: 12.0 mm/MJJA change in standard deviation for a 25.0 mm/MJJA change in the mean respectively). Practically, this means that the Heartland region will see generally drier summers, with more summers even drier than what is seen now but will still experience some of the same wet extremes that the region currently deals with. This is reflected in Fig. 4-16 where the 10th percentile of total MJJA P-E shows a drying in both CMIP5 and CMIP6 but the 90th percentile shows little change or a slight drying depending on the model ensemble.

A second factor that must be considered is the timing of the projected P-E changes. The motivation for this study period and region is the existence of highly productive and important summer agriculture, with growth concentrated in May-August. While average rainfalls are important in the long run to sustain stable agriculture, yields each year can often come down to a few weeks of abnormally dry or wet conditions [245].

As seen above, increased variability in P-E in the future increases the chance of an abnormally wet or dry summer but the finer timing of this is important. Drying in spring when soil is wettest could be beneficial for planting. Drying concentrated in the late summer when soil moisture is depleted could be disastrous. While July and August have higher P-E deficits, the drying is spread over the entire summer (Fig. 4-17). Presented climatologies (Fig. 4-18) also show that spring precipitation is projected to increase, although due to factors discussed previously, it is unclear how much additional spring wetting would serve to offset summer moisture divergence. The opposite trends in P-E between seasons shows the amplification of the seasonality

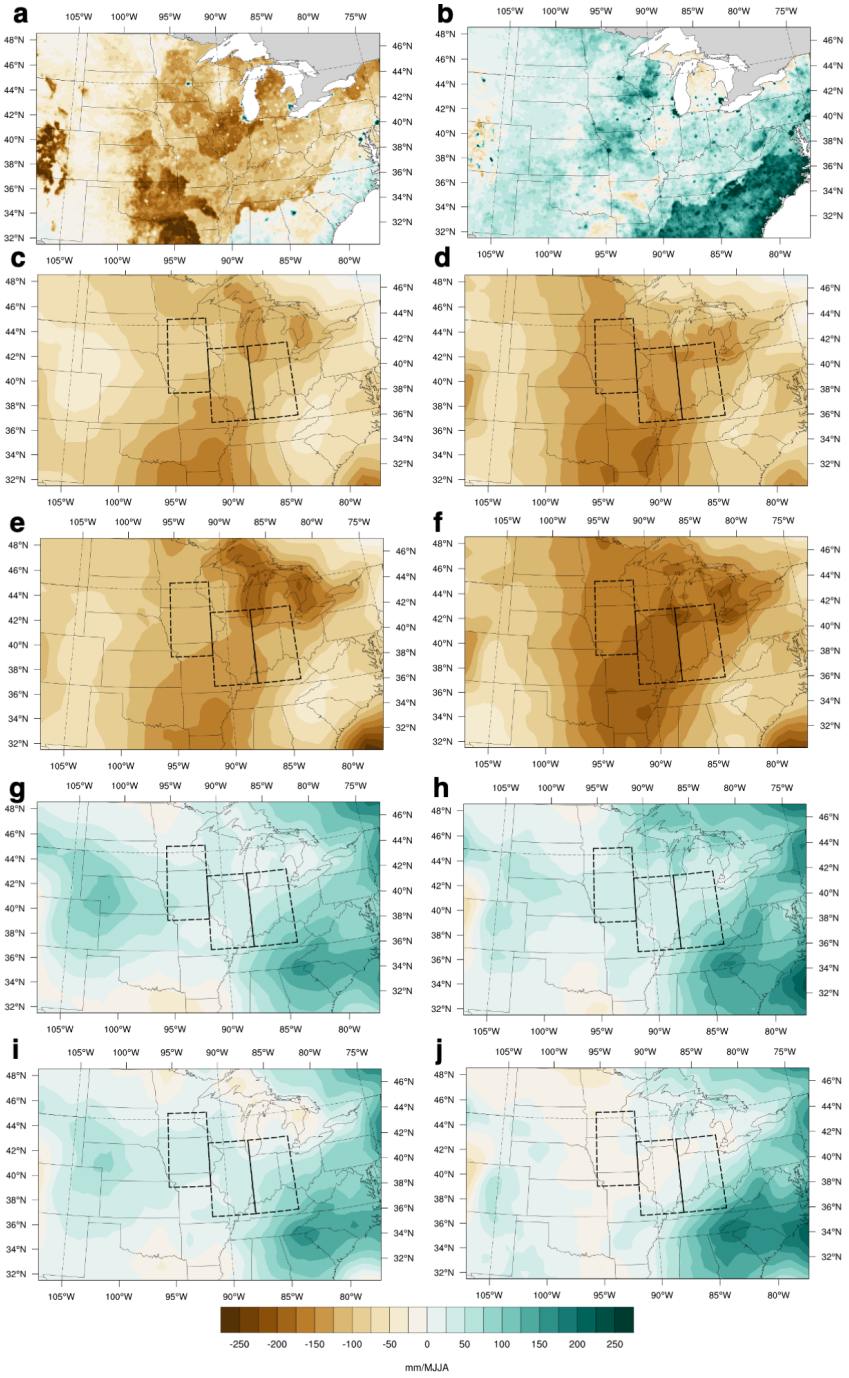

Figure 4-16: a) CMIP5 Multi Model Mean 10th percentile of 1975-2004 MJJA total Precipitation-Evapotranspiration (mm/MJJA) b) Same as (a) but for CMIP6 c) Same as (a) but for 2070-2099 RCP8.5 d) Same as (c) but for CMIP6. e) CMIP5 Multi Model Mean 90th percentile of 1975-2004 MJJA total Precipitation-Evapotranspiration (mm/MJJA) f) Same as (e) but for CMIP6 g) Same as (e) but for 2070-2099 RCP8.5 h) Same as (g) but for CMIP6.

in soil moisture in this region, with springs getting wetter and summers getting drier.

4.4 Discussion & Conclusions

In the historical period (1975-2004), in an era and location where land use change (particularly agricultural intensification) was the dominant impact on regional climate [180] [9], precipitation and evapotranspiration increased with the former dominating moisture availability. Climate changes in this region in the future (2070-2099) will cause summer evapotranspiration to increase dramatically, paired with increased temperatures, while precipitation remains constant or decreases.

Taken in isolation, the summer drying projected in the future might seem uncompromisingly negative in its impact. However, this drying should be compared to wetting in the late 20th century. Bias corrected data show that the decrease in P-E in the RCP8.5 scenario under CMIP5 is equivalent in magnitude to the increase in the historical period in the observations, essentially resetting the region to an earlier climate state. The decrease in P-E projected over the course of the 21st century in CMIP5 and CMIP6 is 12.7 mm and 35.9 mm respectively. This compares to an increase in the observed P-E from 1915-1944 to 1975-2004 of 17.1 mm (from -49.2 mm to -32.1 mm) (Table 4.1, Fig. 4-15e). Considering this — and the generally wet history of the hydrology in this area — it can be deduced that the drying projected in the 21st century may not be significant enough to severely impact crop growth. However, it is also true that the recent wetter decades have contributed to yield growth and current production levels, which did not exist under historically drier conditions [197]. Additionally, the models' failure to capture historical trends found in observations and their general inability to replicate wider regional climate phenomena like the warming hole [133] [157] means that their future projections for moisture availability should be considered uncertain. Additionally, results in Chapter 3 showed that precipitation in this region in the historical period has been influenced strongly by internal variability in the past and which may be reversed in the future.

While acceleration of the hydrologic cycle is a broadly recognized but regionally

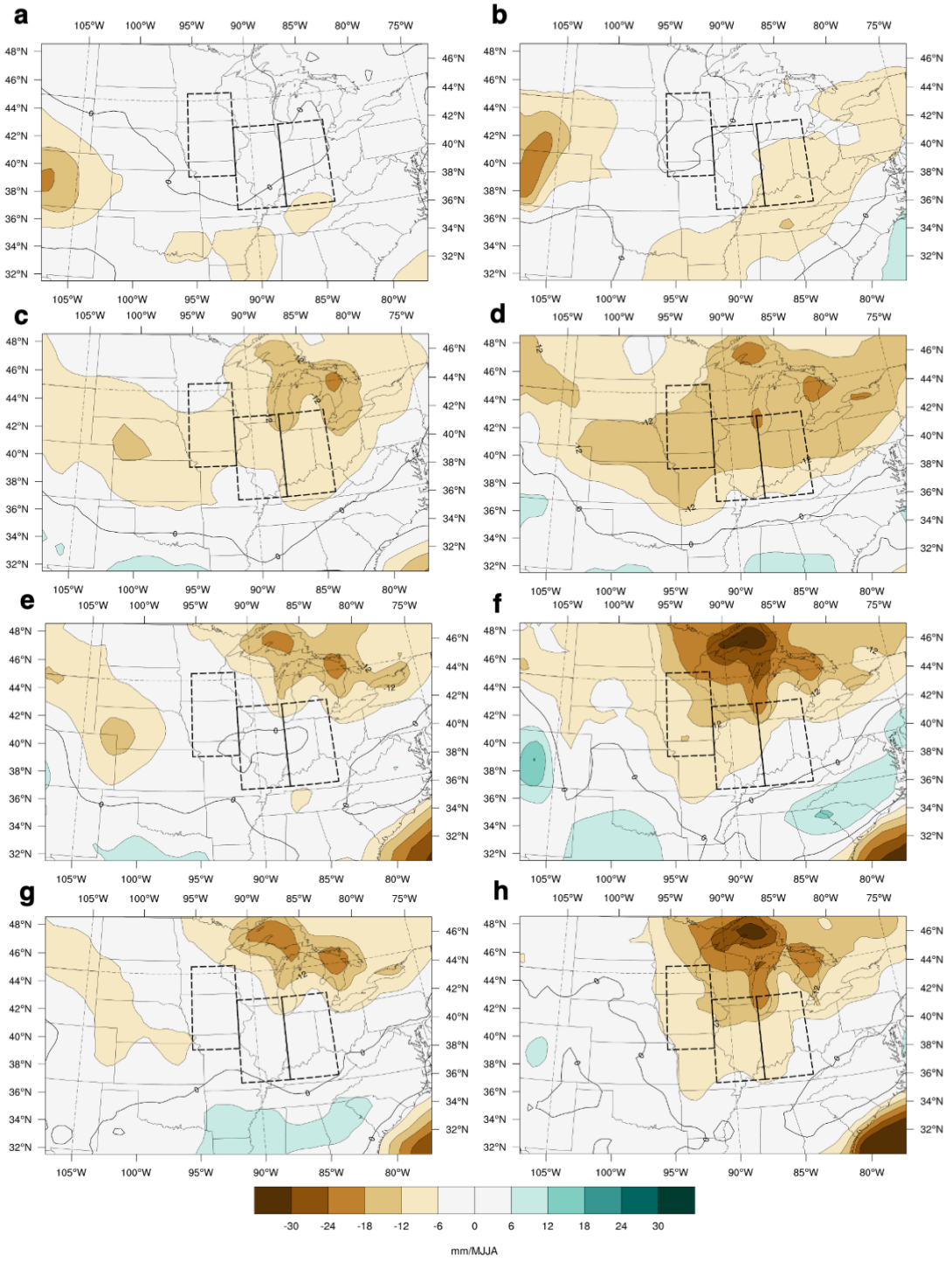

Figure 4-17: Multi-Model-Mean average 1975-2004 to 2070-2099 change in monthly P-E (mm/MJJA) under RCP8.5 for: a) May in CMIP5 b) May in CMIP6 c) June in CMIP5 d) June in CMIP6 e) July in CMIP5 f) July in CMIP6 g) August in CMIP6 h) August in CMIP6

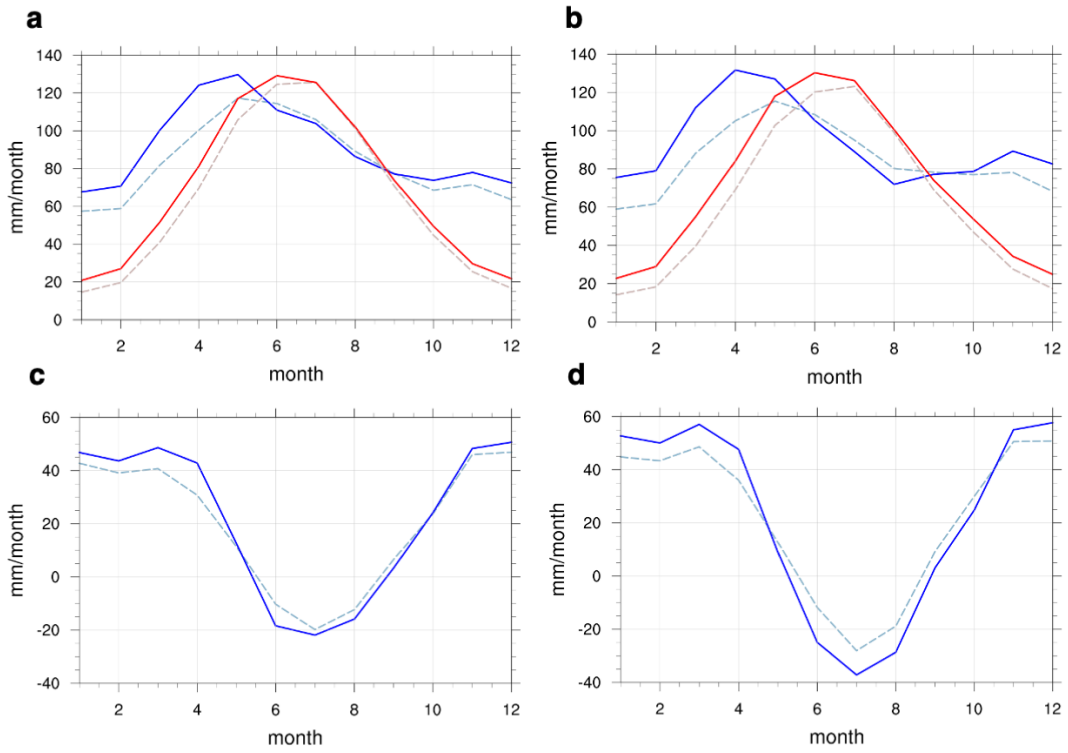

Figure 4-18: a) Change in climatology of precipitation (mm/month) [blue] and evapotranspiration (mm/month) [red] from the historical period (1975-2004) [light dashed line] to future (2070-2099) [dark solid line] averaged over the Heartland Region in CMIP5. b) Same as (a) but for CMIP6 c) Change in climatology of P-E (mm/month) from the historical period [light dashed line] to future [dark solid line] averaged over the Heartland region in CMIP5 d) same as (c) except for CMIP6.

varying impact of climate change [288] [116] [187] we highlight the contrasting impacts of climate change and land use change on changes in soil moisture seasonality, explored through the balance of precipitation and evapotranspiration. In the past, agricultural development has contributed to intensification of the hydrologic cycle (increases in both precipitation and evapotranspiration). In the future under climate change, this intensification of the hydrologic cycle will not occur in all seasons (general increase in evapotranspiration and decrease in precipitation in summer), but the balance between the two will contribute to an enhancement in the seasonality of soil moisture, with springs getting wetter and summers getting drier.

The P-E drying that will occur in the Cornbelt in the future is imposed over a period of wetting for a region that was historically wetlands, and that relies on a widespread network of subsurface drainage to deal with waterlogged soils. While drying may make some supplemental irrigation necessary in dry pockets like northern Illinois, this will be in a system largely without agricultural water stress. In years where demands on the Cambrian-Ordovician aquifer (located largely under Iowa, Illinois, Wisconsin, and Minnesota) from municipal and industrial uses cause strains on water supply, alternative farm scale measures may become necessary in adaptation to increasingly lopsided seasonal water availability. Conversely, drying may also make late spring and early summer drainage less crucial in areas of Indiana and Ohio. The existence of extensive artificial drainage systems will likely mute the impact of the projected spring wetting due to climate change, and the recent wetting trend in summer P-E due to land use change and natural variability will likely mute the projected drying during summer. However, in both cases an expansion of drainage and supplementary irrigation respectively may be necessary in some sub-regions in some years. Climate change will always call for adaptation. But the heterogeneous pairing between historical and future trends shown here are further proof that climate change adaptation must be both local and context-dependent.

Chapter 5

Impact of Agricultural Development and Climate Change on the Severity of Heatwaves in the Central U.S.

5.1 Introduction

Heat waves are the most deadly natural hazard in the United States, killing more people annually on average than floods, tornadoes, or extreme cold (Fig. 5-1). They are an insidious danger because they are difficult to categorize, pose uneven risks to different demographics and socioeconomic populations, and because heat related deaths are not always accurately recorded and often attributed to preexisting health disorders [183] [146]. Drawing a direct causal link between heat incidence and all resulting mortalities is difficult, due in part to incomplete reporting, changing definitions, and co-morbid conditions, as well as the fact that future human adaptations to rising temperatures cannot be easily predicted [146] [193].

In a warming climate, where annual mean temperatures are projected to rise roughly 4°C in the Central U.S. by the late 21st century under RCP8.5 [101], heat waves are projected to get more frequent, longer lasting, and more intense. The National Oceanic and Atmospheric Administration's National Weather Service defines

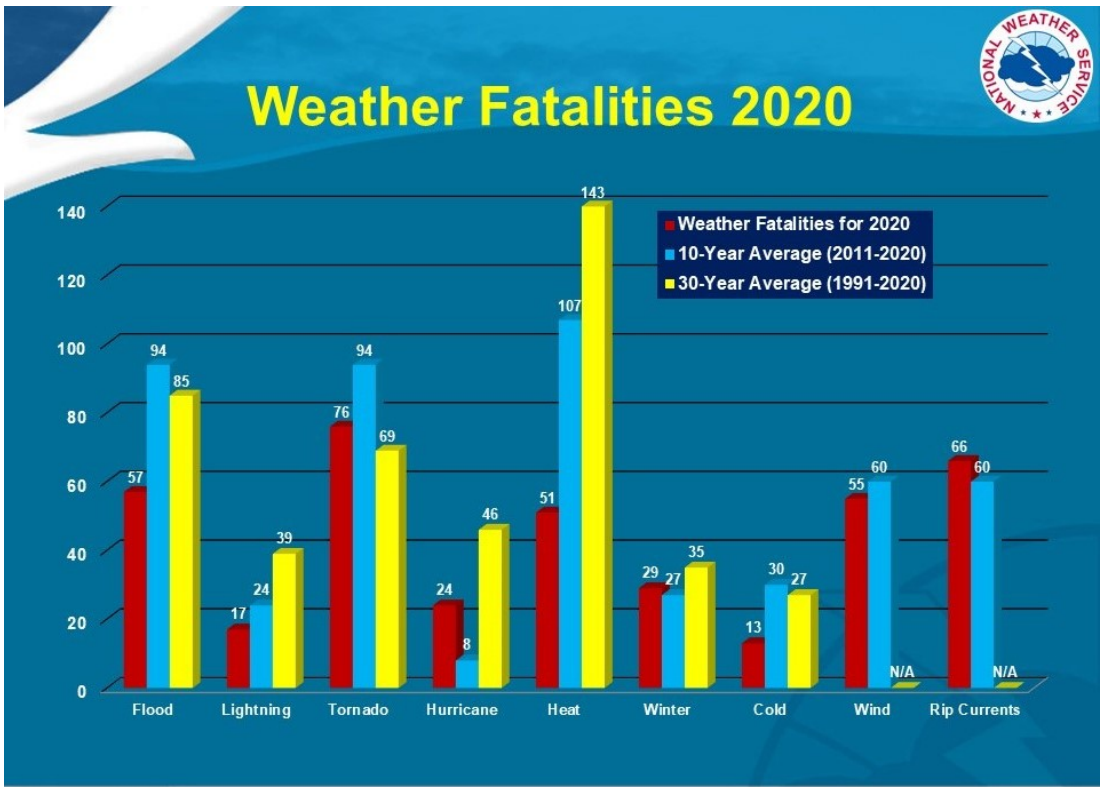

Figure 5-1: Weather fatalities by cause for 2020, 2011-2020 average, and 1991-2020 average. The U.S. Natural Hazard Statistics provide statistical information on fatalities, injuries and damages caused by weather related hazards. These statistics are compiled by the Office of Services and the National Climatic Data Center from information contained in Storm Data, a report comprising data from NWS forecast offices in the 50 states, Puerto Rico, Guam and the Virgin Islands. The Centers for Disease Control and Prevention is the official government source of cause of death in the United States, including weather-related fatalities.

a heat wave as "a period of abnormally and uncomfortably hot and humid weather" typically lasting two or more days [184]. This generalized definition creates issues when trying to define heat waves for the purpose of scientific study and for emergency response planning across different regions. Consequently, studies apply variable statistical definitions and methodologies of analysis to heat wave events, making quantitative comparison of results more difficult [217] [250] [78]. Despite this, various individual studies have predicted an increase in the intensity, frequency, and duration of heat waves across the world with climate change [158] [250] [78] [50] [49] [17] [223] [170].

While many early, and some current, studies have looked solely at dry-bulb temperature changes with climate change [138] [250] [158], recent studies have begun to incorporate humidity as a variable of concern and show predicted increases in the frequency, intensity and duration of humid heat events [78] [50] [223] [170] [230] [270] [209] [129] [173]. While heat index is a more robust metric for analysis than dry-bulb temperature, recent work on wet-bulb temperatures (TW) show that this is an even more comprehensive indicator of truly dangerous heat incidence [236] [193] [122]. The metric has previously been adopted for use in industrial and military sectors where workers are more likely to spend long periods of the day outside in potentially dangerous conditions [55] [196].

Wet-bulb temperature is a useful metric for studying dangerous heat occurrence because it has both a physical, empirically demonstrated connection to atmospheric energy balance, and also a set of thresholds directly related to human health. Eltahir, 1998 showed the mechanistic connection between soil moisture, moist static energy, and wet-bulb temperature which can be seen in the figure below (Fig. 5-2) [58].

The study ties elevated soil moisture conditions to ultimate increases in moist static energy and wet-bulb temperature through a decrease in the Bowen Ratio (ratio of sensible to latent heat flux), increases of atmospheric water vapor, increases in net radiation at the surface, and decreases in planetary boundary layer depth [58]. Agriculture, particularly highly productive agriculture and irrigation, modifies these elements in a very similar way to increased soil moisture. Agricultural develop-

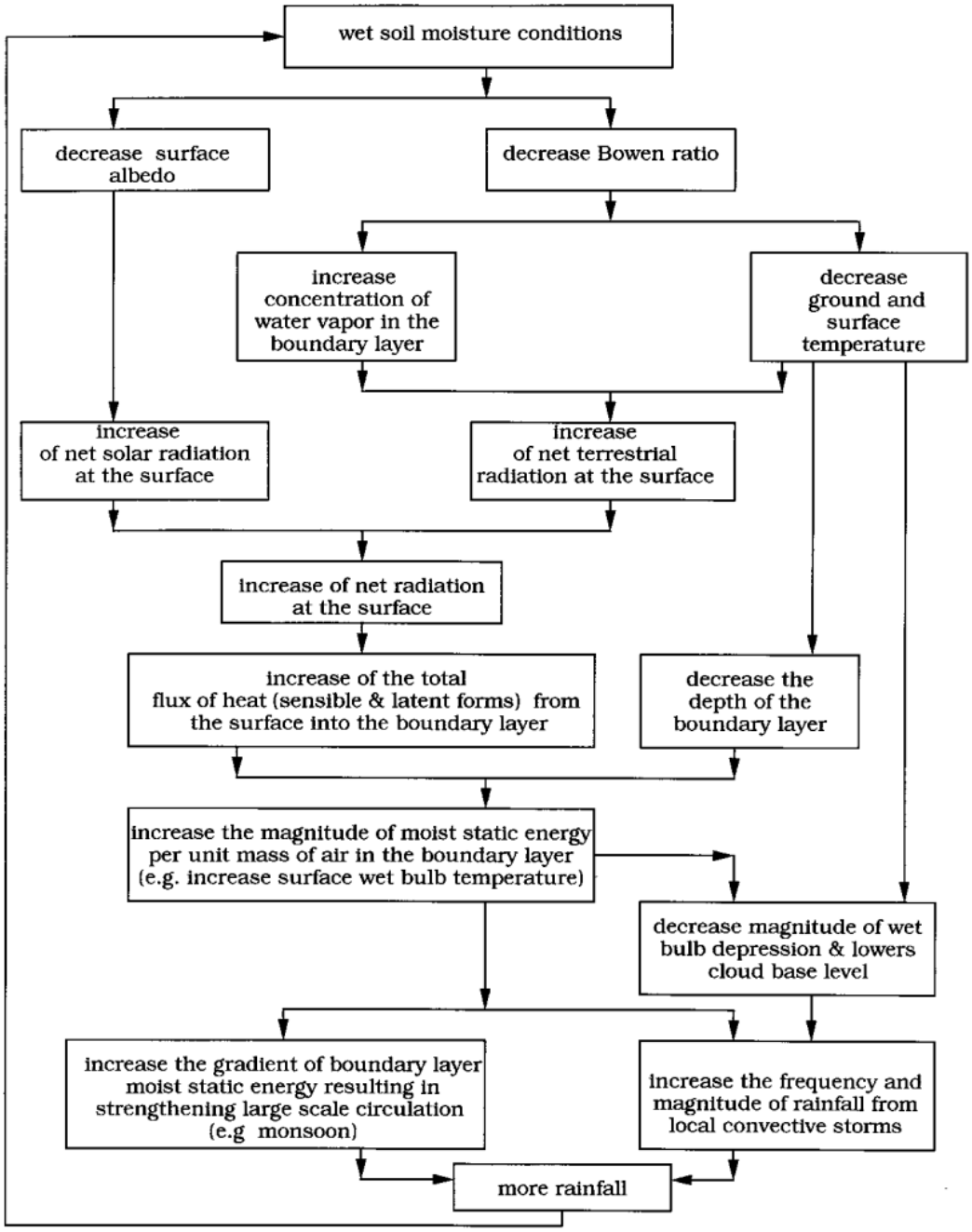

Figure 5-2: The proposed hypothesis for relating soil moisture conditions and subsequent rainfall processes. (Source: Eltahir (1998(Figure 2 [58]). Used with Permission.

ment on the whole increases evapotranspiration (and therefore latent heat flux) and atmospheric water content, as we showed in Chapters 3 & 4 (Fig. 4-6). In turn, decreased surface temperatures (decrease in sensible heat flux) result in a lowering of the planetary boundary layer. The described modifications tend to increase net radiation. Moist Static Energy (MSE), a measure of the total energy in the atmospheric boundary layer, is a function of both the total heat flux into the atmosphere and the depth of the planetary boundary layer which are oppositely trending with respect to agricultural development ([58] Equation 5):

$$MSE = g * z + c_p * T + L * q \tag{5.1}$$

$$MSE_{max} = MSE_{min} + g\frac{F}{\Delta P} \tag{5.2}$$

Where g is gravitational acceleration, z is elevation, cp is the specific heat capacity, T is temperature, L is the latent heat of vaporization, q is water vapor mixing ratio, F is the total heat flux at daily timescales, and ΔP is the afternoon boundary layer depth. MSE minimum is the moist static energy in the early morning when it is at its lowest. Eltahir, 1998 shows that wet-bulb temperature follows the same relationship as MSE in relation to soil moisture and net radiation changes [58]. Wet-bulb temperature, the temperature that a parcel attains when water is evaporated into it until saturation at constant pressure, can be related to MSE by the following formulation ([218] Equation 2.30):

$$\frac{T - T_w}{w_s(p, T_w) - w} = \frac{L}{c_p} \tag{5.3}$$

Where T is dry-bulb temperature, w is the mixing ratio, and the dependence of L on temperature is neglected. While wet-bulb temperature has this mechanistic con-

nection to energy partitioning and moist static energy, it can also be tied easily to health risk. Under well ventilated conditions, the human skin temperature approaches the magnitude of wet-bulb temperature, and studies have shown that fatal wet-bulb temperature is roughly 35 °C, at which point the body can no longer maintain thermal homeostasis by cooling itself through evaporation (sweating) [236]. However, by translating National Weather Service charts of Heat Index Health Risk to wet-bulb temperature, we can see that dangerous conditions exist at much lower thresholds, with wet-bulb temperatures as low as 25°C being dangerous for health depending on humidity levels (Fig. 5-3).

The danger of elevated but not outright deadly humid heat levels can be shown well through the July 12-16, 1995 heat wave event that killed upwards of 1000 people in and around the city of Chicago [183]. By plotting the hourly wetbulb temperatures for the event using ERA5 reanalysis data [106] (Fig. 5-4) we can see that wetbulb temperatures reached 26-27 degrees Celsius in the Chicago area, and exceeded 30 degrees in the larger region for brief periods of time, though temperatures never reached the outright deadly 35 degree threshold. The 1995 event shows some key characteristics of humid heat events that will be central to our analysis. First, it was a multi-day event, spanning July 12-16 (Fig. 5-4). While day-time wet-bulb temperature was high during the event, it was also notable for dangerously high night-time temperatures. Nighttime heat is a risk factor for heat related mortality because it prevents the body from recovering from daytime heat stress [22].

Wet-bulb temperature is therefore a meaningful metric for heat stress studies. Several studies have already recorded increases in humid heat metrics in the historical period in the United States [248] [244]. Studies of high wet-bulb temperature areas in Southwest Asia, South Asia, and the North China Plain have shown that these hot-spot regions will see increased risk of deadly events with climate change [193] [122] [126]. Several studies have looked at how humid heat waves will change globally in the future [77] [223] [170] but they have not translated their analysis to a regional level in the United States or assessed the specific characteristics of these future heat waves and the mechanisms through which their occurrence will be modified. Recently, studies

NOAA NWS Heat Index

Temperature

Relative Humidity (%)	°C	26.7	27.8	28.9	30.0	31.1	32.2	33.3	34.4	35.6	36.7	37.8	38.9	40.0	41.1
	°F	80	82	84	86	88	90	92	94	96	98	100	102	104	106
	50	81	83	85	88	91	95	99	103	108	113	118	124	131	137
	55	81	84	86	89	93	97	101	106	112	117	124	130	137	145
	60	82	84	88	91	95	100	105	110	116	123	129	137	145	153
	65	82	85	89	93	98	103	108	114	121	128	136	144	153	162
	70	83	86	90	95	100	106	112	119	126	134	143	152	161	172
	75	84	88	92	97	103	109	116	124	132	141	150	160	171	182
	80	84	89	94	100	106	113	121	129	138	148	158	169	181	193

Caution | Extreme Caution | Danger | Extreme Danger

Equivalent Wetbulb

Temperature

Relative Humidity (%)	°C	26.7	27.8	28.9	30.0	31.1	32.2	33.3	34.4	35.6	36.7	37.8	38.9	40.0	41.1
	°F	80	82	84	86	88	90	92	94	96	98	100	102	104	106
	50	18.8	19.7	20.6	21.5	22.4	23.3	24.2	25.2	26.1	27.1	28.0	29.0	29.9	30.9
	55	19.7	20.6	21.5	22.5	23.4	24.3	25.3	26.3	27.2	28.2	29.2	30.2	31.1	32.1
	60	20.5	21.4	22.4	23.3	24.3	25.3	26.3	27.3	28.3	29.3	30.3	31.3	32.3	33.2
	65	21.3	22.3	23.2	24.2	25.2	26.2	27.3	28.3	29.3	30.3	31.3	32.3	33.3	34.3
	70	22.1	23.0	24.0	25.1	26.1	27.2	28.2	29.2	30.3	31.3	32.3	33.4	34.4	35.4
	75	22.8	23.8	24.8	25.9	27.0	28.0	29.1	30.1	31.2	32.2	33.3	34.3	35.4	36.4
	80	23.5	24.6	25.6	26.7	27.8	28.9	30.0	31.0	32.1	33.1	34.2	35.3	36.3	37.4

Caution | Extreme Caution | Danger | Extreme Danger

Figure 5-3: Conversion tables between Heat Index (top) (Source: NOAA National Weather Service Heat Safety Tools [185]) and wet-bulb temperature (bottom). Colors indicate heat stress risk levels. (Figure adapted from [122])

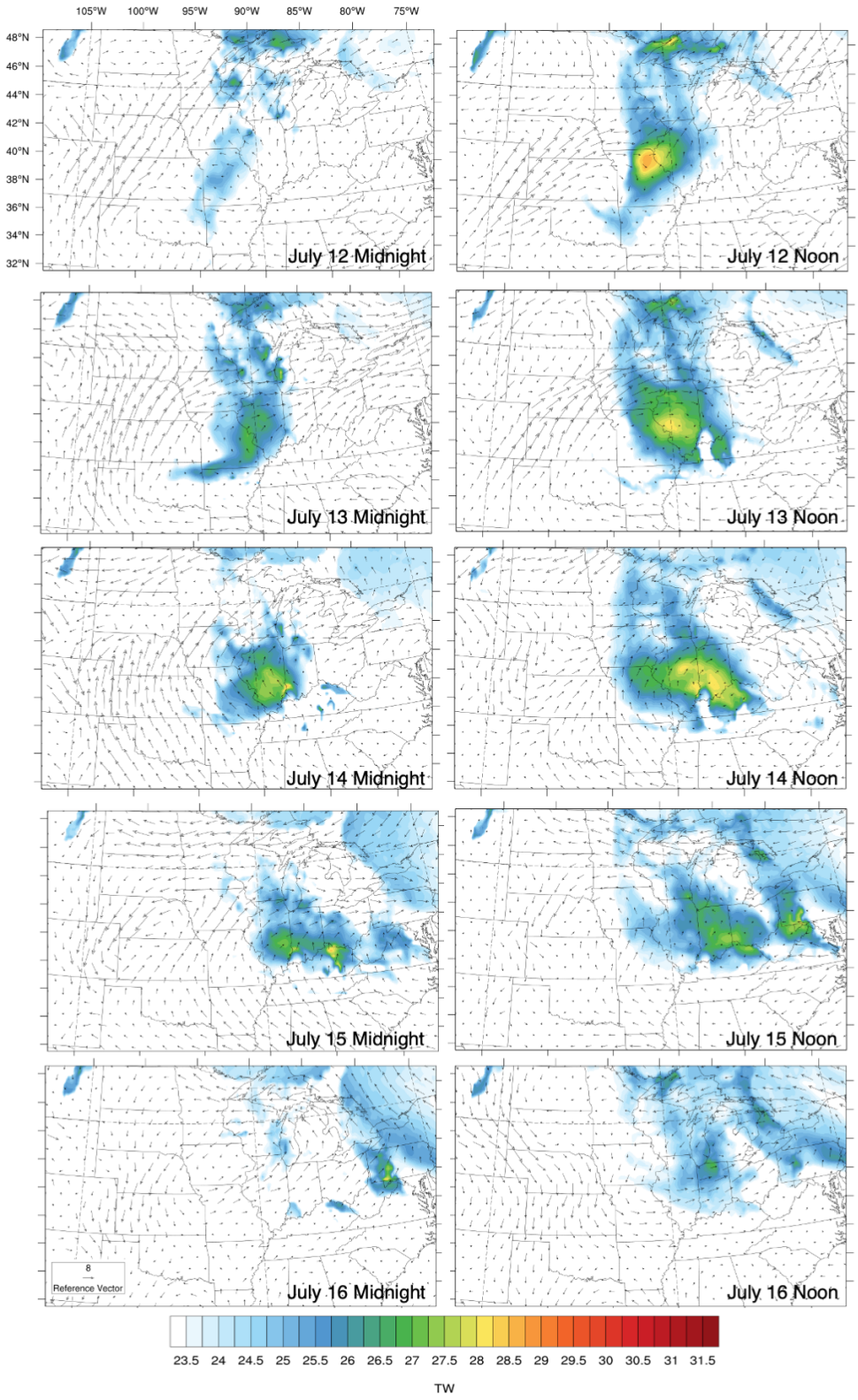

Figure 5-4: 6hr running mean of hourly wet-bulb temperature (degrees C) calculated from ERA5 reanalysis for noon and midnight of July 12-16, 1995. Vectors show 850 mb wind anomaly relative to 1979-2004 hourly climatology

have looked at humid heat at the regional scale [269] [211] [230] and have focused particularly on the dominance of moisture versus temperature departures in these extreme events using observational data. Lutsko, 2021 analyzed patterns of apparent temperature, another humidity inclusive metric, and found that patterns of change were largely guided by patterns of specific humidity rather than temperature [147]. Similarly, Schoof et al. (2019) found that future extreme heat events are likely to be dominated by high humidity [230].

Studies that have examined the physical mechanisms behind humid heat have not done so with a robust inclusion of the impacts of agricultural development, and have relied on station observation data rather than utilizing global or regional modeling simulations [211]. Kang and Eltahir (2018) looked at the impacts of irrigation development on the North China plain and showed that irrigation increase historical extreme daily maximum wet-bulb temperature by 0.5 °C under historical conditions and by 1.0 °C under the RCP8.5 climate change scenario, an amplification that was theorized to be due to water vapor feedback [126]. A study by Mishra et al. (2020) looked at the impact of irrigation in India and found similar amplification of moist heat stress driven largely by decreases in the planetary boundary layer depth [168]. Krakauer et al. (2020) found that irrigation increased the occurrence of high percentile wet-bulb temperatures and the occurrence of dangerous wet-bulb temperature days [129]. However, none of these studies considered agricultural expansion or intensification in their work.

5.2 Background

In the U.S. maximum wet-bulb temperatures occur in a corridor along the Mississippi River from the Gulf Coast to the Great Lakes as well as some elevated temperatures along the Atlantic coast (Fig. 5-5b). Historically, wet-bulb temperature has been more elevated near the Gulf of Mexico, a function of generally higher summer temperature and humidity that we will explore later in a comparison of regional distributions of daily maximum wet-bulb temperature. However, we look at the Midwest

here for two reasons. First, as the focus of this thesis is the Climate-Agriculture-Water Nexus, we are interested in the impact of agricultural areas which are largely in the Midwestern U.S. rather than along the Gulf Coast. Second, the Midwest ends up being a transition zone in terms of wet-bulb temperature extremes. While these areas are not generally exposed to dangerous wet-bulb temperature conditions in the historical period, they will be far more likely to experience them at the end of the 21st century according to our modeling projections as will be shown in the results section. Therefore, populations that may have only rarely experienced dangerous wet-bulb temperature conditions in past will experience them with increasing regularity.

Despite being in a generally cooler area, the Midwest is no stranger to humid heat stress events. High wet-bulb temperature maximum events stretch up through the Mississippi Valley and are associated with increased mortality risk, especially during certain standout years (1995) relative to what would be expected from the pattern of maximum temperatures alone (Fig. 5-5) [183]. In these figures of extreme wet-bulb temperatures the Midwest emerges as a hot spot for high wet-bulb events.

In this study, we examine the impact that historical agricultural development has had on the historical pattern of extreme wet-bulb temperature. Future projections then show the impacts of climate change and further intensification of wet-bulb temperature in irrigated areas. The impact of climate change on wet-bulb temperature in the immediate Great Lakes region is also shown, with a discussion of how modeling choices and prescription of lake surface temperatures are important for accurate forecasting.

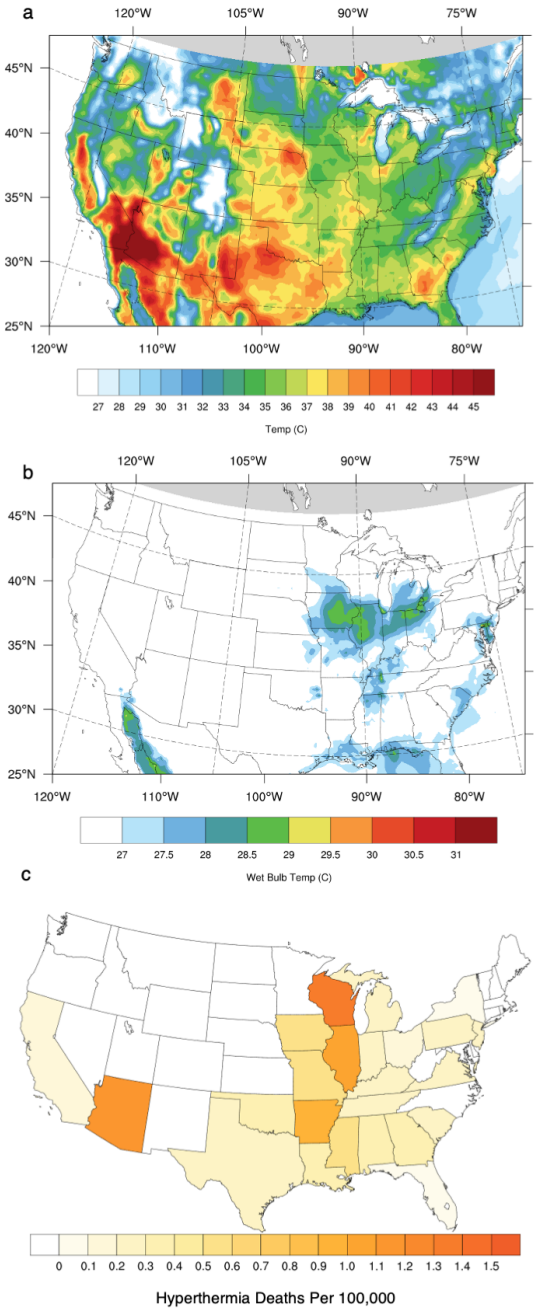

Figure 5-5: Maximum 6hr running mean 2m Temperature (degrees C) in 1995 in ERA5 (left). Maximum 6hr running mean 2m wet-bulb temperature (degrees C) in 1995 in ERA5 (middle). Hyperthermia death rate per 100,000 people for 1995 (right). Data obtained from CDC Wonder Database Compressed Mortality File [32]

5.3 Data and Methodology

In order to provide the most accurate boundary conditions for the regional climate modeling simulations, comparison to observed metrics was performed for a group of models. The set of models considered was taken from Maloney et al. (2014), a large modeling study of North American climate change impacts, with the addition of GFDL-ESM2G of IPSL-CM5A-MR which were available but not included in their study [150]. Comparisons were made with either ERA-Interim Reanalysis data or CRUTS4.01 gridded observations where available for June-September 1979-2004 averages of 2m temperature, precipitation, near surface relative humidity, average wet-bulb temperature, average daily maximum wet-bulb temperature, period maximum daily maximum wet-bulb temperature, and 95th percentile daily maximum wet-bulb temperature. Wet-bulb temperatures in the reanalysis and GCM data were calculated according to the formulation in Davies-Jones, 2008 [42]. June-September was chosen as the analysis season because it contains nearly all the extreme wet-bulb temperature days, and captures the seasonal wet-bulb temperature climatology maximum.

Visual comparison to reanalysis and observation patterns was used in addition to comparisons of pattern correlation and normalized root mean squared error. No three models performed consistently well across all three metrics, but ultimately CCSM4, CNRM-CM5, and HadGEM2-ES were chosen for their scores as well as their compatibility with the regional model. The first realization is used for HadGEM2-ES and CNRM-CM5 and the sixth realization for CCSM4. More information about these three models can be found in Table A-1. Ultimately, most analysis is presented here for CCSM4, as it retains the smallest bias in extreme wet-bulb temperature (Fig. 5-8), and most closely matches historical heat wave event statistics with ERA5. Further comparison to simulated results in the historical period is performed with ERA5, the newest generation analysis available from the European Centre for Medium Range Weather Forecasting (ECMWF), for 1975-2005 [106]. ECMWF notes that the years 1975-1978 are experimental, but we include them here in-order to have full over-

lap with our 30-yr simulation period. While ERA-Interim continues to be a reliable reanalysis data-set, we use ERA5 for further comparison as the newest generation product from ECMWF, and one where the full 1975-2004 period was available.

Several adjustments were made to the original MRCM configuration used for the simulations presented in Chapter 3 of this thesis in order to accurately represent wet-bulb temperature, particularly in the extremes (Fig. 5-6). Improvements were made to surface level zonal wind (ibisdrv.f) in accordance with simulations performed for a previous heat wave study in East Asia [126]. Adjustments were also made to calculation and smoothing of wet-bulb temperatures within the model (canopy.f) in order to prevent erroneous extreme values in accordance with code utilized in a previous heat wave study in South Asia [122]. Additional updates were also added to convection and cloud parameters (condtq.f and cldfrac.f) [120].

In order to fully investigate the impacts of both agricultural development and climate change on the evolution of wet-bulb temperatures, a set of greenhouse gas forcing and land use simulations were performed (Table 5.1). Four simulations were performed for each GCM, two in the historical period (1975-2004) and two in the future period (2070-2099) under RCP8.5 forcing. One of each time period was run with a 1900 land use map while the other was run with a 2000 land use map. These land use setups involved the use of a 1900 and 2000 cropland and irrigated area map respectively (Fig. 3-8), and a photosynthesis (ancr) modification factor of 0.49 and 2.11 respectively in order to represent yield intensification. The simulations will from here on be referenced by their forcing GCM and land use e.g. CCSM4-2000. More discussion of the meaning and development of this factor is found in Chapter 3 and in Nikiel and Eltahir (2019) [180]. A description of MRCM, the regional climate model used in these dynamical down-scaling experiments can also be found in Chapter 3.

Bias correction is performed on the wet-bulb temperature results using a comparison to ERA5. The procedure follows the bias correction performed in previous studies conducted with MRCM [126]. Wet-bulb temperature is simulated in the model at an hourly timescale and processed to a 6hr running mean. The daily maximum is then calculated. ERA5 wet-bulb temperature is produced, also at the 1hr timescale, and

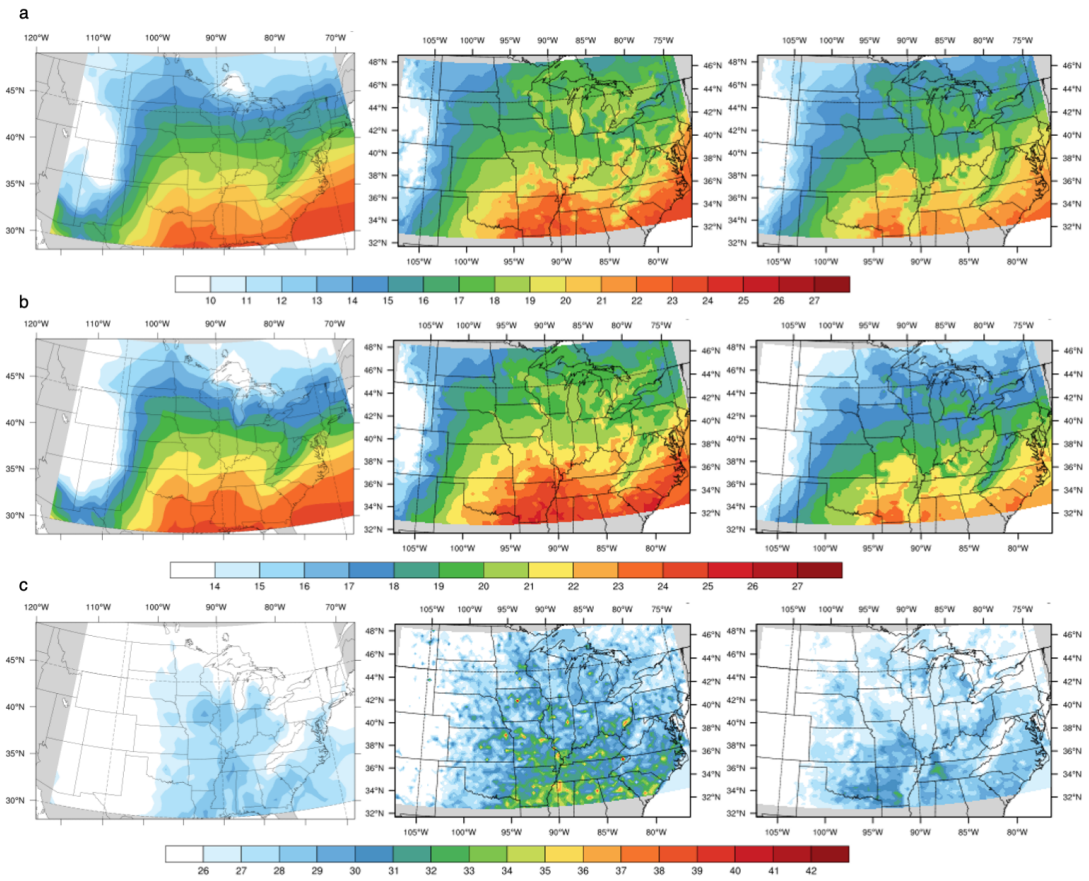

Figure 5-6: a) 6 hr moving mean June-September wet-bulb temperature (degrees C) average (1993-1997) in ERA-Interim (left), original code (middle), modified code (right). b) same as (a) but for average daily maximum wet-bulb temperature (degrees C) c) same as (a) but for maximum daily maximum wet-bulb temperature (degrees C)

Table 5.1: Set of Simulations Performed for Heat Wave Analysis

Simulation Name	*Forcing*	*Time Period*	*Land Use*	*ancr*
ERAI-2000	ERA-Interim	1975-2004	2000	2.11
ERAI-1900	ERA-Interim	1975-2004	1900	0.49
CCSM4-2000	CCSM4	1975-2004 & 2070-2099	2000	2.11
CCSM4-1900	CCSM4	1975-2004 & 2070-2099	1900	0.49
CNRM-2000	CNRM-CM5	1975-2004 & 2070-2099	2000	2.11
CNRM-1900	CNRM-CM5	1975-2004 & 2070-2099	1900	0.49
Had-2000	HadGEM2-ES	1975-2004 & 2070-2099	2000	2.11
Had-1900	HadGEM2-ES	1975-2004 & 2070-2099	1900	0.49

processed the same way, and then ERA5 is regridded to the MRCM grid for comparison. Both sets of daily maximum wet-bulb temperature are then used to calculate mean daily maximum climatologies over 1975-2004, and a 30-day moving mean is calculated from this climatology. The magnitude of the bias for each GCM is individually calculated by subtracting the GCM climatology from the ERA5 mean climatology for each day at each grid point. This bias is then added to the 6hr running-mean daily maximum values for both the historical and future period. Comparisons of the average daily maximum wet-bulb temperature before and after bias correction for the 2000 land use historical simulations are shown below (Fig. 5-7 through 5-8), where the Multi Model Mean (MMM) is the average of the three GCM forced simulations.

The data shown for the 1900 Land Use simulations was bias corrected using the factors calculated for the 2000 Land Use simulations. This ensures that all differences shown between the two simulations are due to agricultural land use differences and not due to any differences in bias correction.

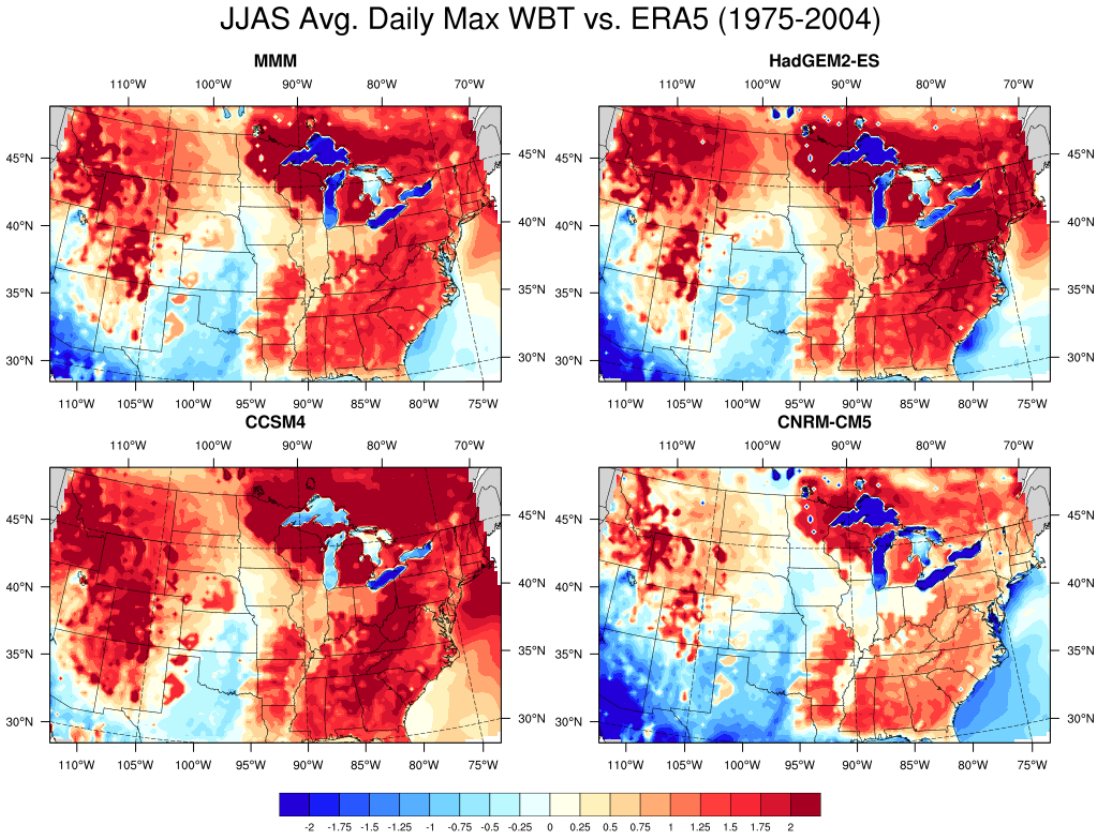

Figure 5-7: Bias (degrees C) in simulated 1975-2004 June-September average daily maximum wet-bulb temperatures versus ERA5 before bias correction

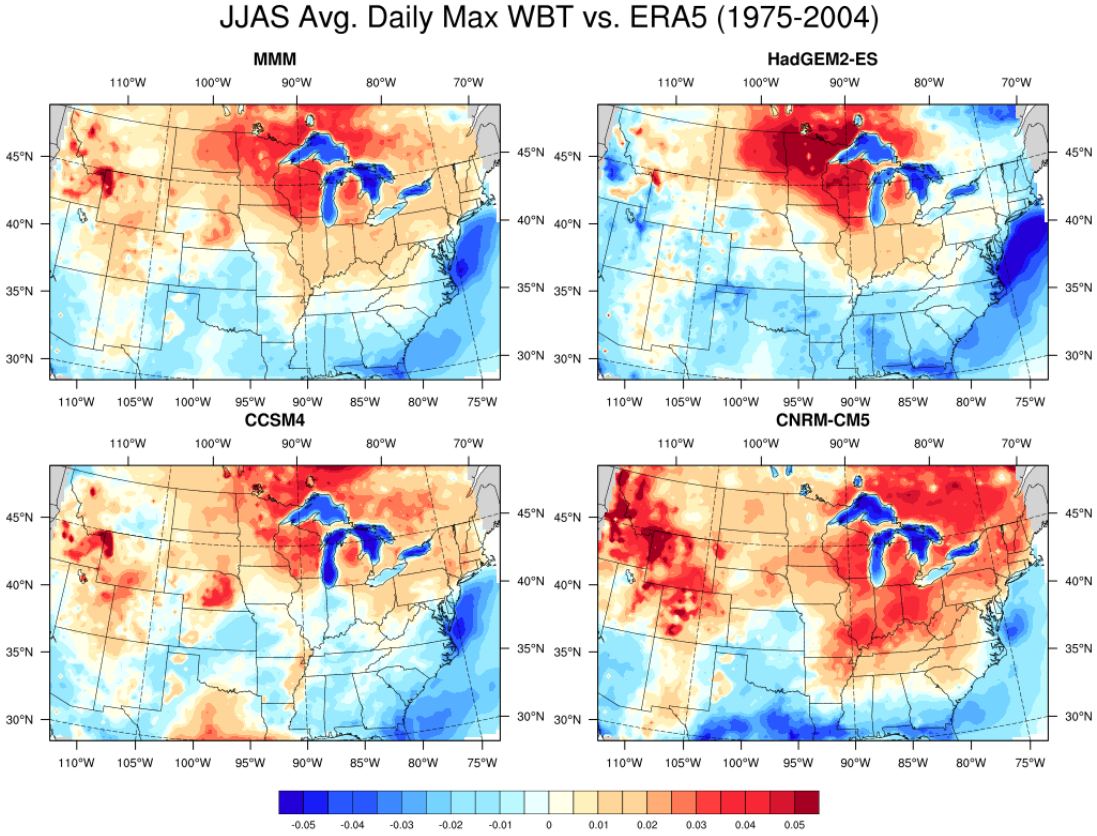

Figure 5-8: Bias (degrees C) in simulated 1975-2004 June-September average daily maximum wet-bulb temperatures versus ERA5 after bias correction

5.3.1 Representation of the Great Lakes

Evaporation over the Great Lakes has an inverted seasonal cycle relative to land evaporation, with a peak in the winter and minimum in the summer. This is due largely to the differential between the lake surface temperature being colder than the near surface air temperature in the summer and warmer in the winter [136]. In their original form, MRCM simulations forced from the original GCM inputs generated erroneous seasonal climatologies of ground temperature (used as a proxy for lake surface temperature(LST)) and evapotranspiration over the Great Lakes (Fig. 5-9). This is largely due to different prescription of land sea masks, and the heterogeneity in lake representation in the GCMs. Mallard et al. (2015) showed issues with dynamical downscaling over the Great Lakes where lake temperatures may be pulled from the nearest available SST data [149].

Previous literature has shown the importance of accurately representing lakes in climate modeling [79] [21] [284] [285]. Bennington et al. (2014) showed that modification of the 1D lake model in their simulations of the Great Lakes region with RegCM4 caused air temperatures over nearby land in the summer to decrease 1-2 °C, as well as modifying regional sea level pressure and 10-meter wind patterns [21].Hanrahan et al. (2021) also showed that lake temperature perturbations in their modeling study could significantly alter downstream precipitation [90]. Accurate representation of evapotranspiration and temperature changes is especially crucial in this study where both measures are important to wet-bulb temperature prediction.

In order to ensure accurate representation of the Great Lakes as a water body in the model, LSTs were inserted into the SST files for the purpose of creating initial and boundary conditions. In the absence of a fully coupled lake model in MRCM, the prescription of consistent lake temperatures in this study was a middle ground in addressing the problem. The state of the art representation of the Great Lakes is a fully coupled ocean-atmosphere model that accounts for ice dynamics and stratification [285].

To preserve the crucial temperature differential in the face of biases in air tem-

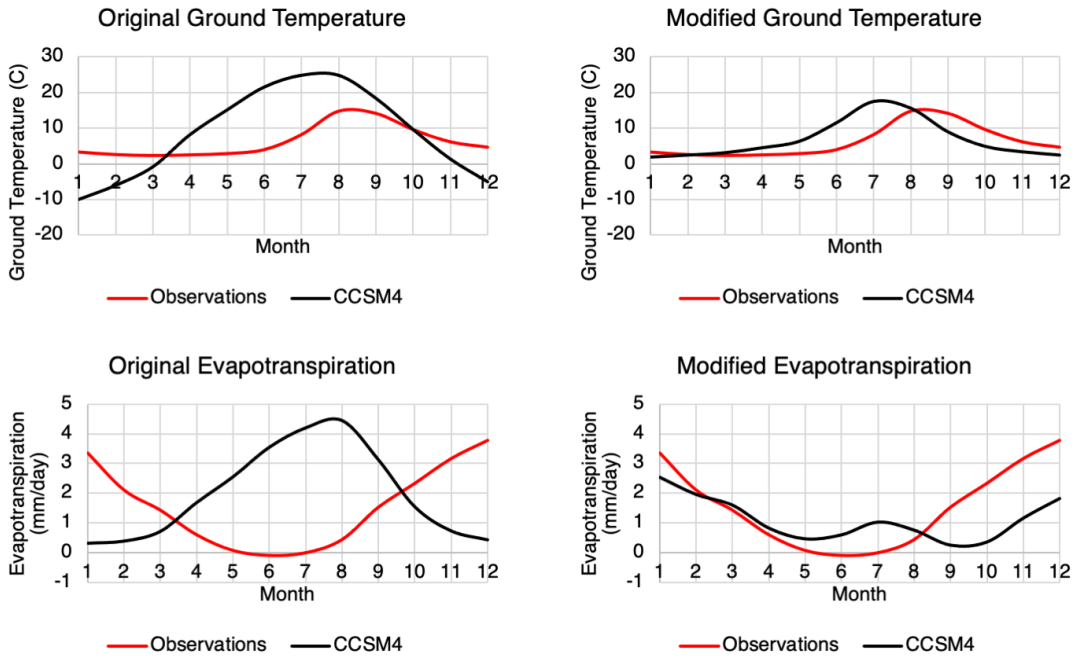

Figure 5-9: Comparisons between monthly mean ground temperature (degrees C) and evapotranspiration (mm/day) over Lake Superior from 1995-2004 in CCSM4-2000 and observations before and after modifications were made to LSTs. Observed Surface temperatures were obtained from GLSEA [186], and evapotranspiration observations were downloaded from GLHCD as output from the NOAA/GLERL Large Lake Thermodynamic Model [115].

perature in the forcing GCM data, model specific lake surface temperatures were generated at a daily time scale from the near surface air temperature GCM data and an empirical relationship between air temperature and LST presented in Tables 1 and 2 of Trumpickas et al. (2009) [253]. The same relationships were used to create LSTs for the historical (1975-2004) and future (2070-2099) period and the relationship for Lake Huron was applied to Lake Michigan due to its exclusion from the analysis in Trumpickas et al. (2009).

There are several important caveats to make in our use of the air temperature and LST in these modeling experiments. First, as mentioned previously, is the lack of a unique relationship for Lake Michigan. Second is the assumption that the relationship between lake surface temperature and air temperature will remain constant, which is unlikely as even in the historical period, the Lakes have been shown to be warming quicker then the surrounding area [283]. The relationships, in their simplicity also do not deal with icing, though they do address the crucial 4 degree Celsius threshold for stratification.

Regardless of the caveats and the oversimplification of the lake surface, this update of LSTs compares favorably to observed LSTs taken from GLSEA (Fig. 5-9). Increases in LST over the lakes in simulations are similar to those found in Trumpickas et al. (2009) with allowances for different model usage and the application of a different greenhouse gas forcing scenario. Under an A2 scenario, Trumpickas et al. (2009) forecast an increase in maximum seasonal LST of 4.8°C, 6.7°C, and 3.3°C from 1971-2000 to 2071-2100 in Lakes Ontario, Superior, and Erie respectively [253]. In our simulations the corresponding maximum temperature increases from the monthly climatology from 1985-2004 to 2080-2099 under the RCP8.5 scenario are 5.8°C, 9.5°C, and 4.2°C in CCSM4-2000 and 5.2°C, 10.0°C, and 4.1°C in CNRM-2000. Similarly, updated inclusion of the Great Lakes is shown to improve the historical simulation of 2m air temperature, relative humidity, and specific humidity over the lakes as compared to ERA5 reanalysis data (Figs. F-2 through F-5). Figures for historical to future changes in input LSTs in CCSM4-2000 and CNRM-2000 can be found in Figure F-1. Note that lake surface temperatures are constrained at a minimum of

4 degrees Celsius with the relationships in Trumpickas et al. (2009), however, this should not interfere with our July-September analysis and it is close to the average lake surface temperatures presented in the observations for comparison, as well as being a critical temperature threshold for seasonal mixing and stratification in the lakes [283].

Figures showing historical averages in simulations with all code updates, bias correction and lake adjustments incorporated in comparison to ERA5 reanalysis data can be found in figures F-6 through F-12.

5.4 Results

Future wet-bulb temperature patterns will increase across the United States with heterogeneity in the magnitude of the change, with the north of the domain seeing stronger increases. Simulations of wet-bulb temperature in the region under RCP8.5 averaged over June-September from 1975-2004 to 2070-2099 show increases in all metrics of wet-bulb temperature (average, 95th percentile, and period maximum) for both the daily minimum and daily maximum wet-bulb temperatures (Fig. 5-10). For both the daily maximum and daily minimum wet-bulb temperature metrics, the average values are increasing more than the extremes in the future, and daily minimum wet-bulb temperature is projected to increase more than daily maximum. While daily minimums are less deadly in isolation the high nighttime temperatures can contribute to increased mortality during heat stress events, as was the case in the 1995 heat wave [183]. Figures of the change in wet-bulb temperature metrics for all three GCM forced simulations can be found in figures F-13 through F-18

The changes shown in Fig. 5-10 are mechanistically consistent with changes in other surface variables, and align with the projected changes and connections presented in Chapters 3 and 4 as well as the previous presentation of moist static energy (Fig. 5-11). Future 2m air temperatures will rise over the entire region along with specific humidity, increasing moist static energy. While relative humidity will decrease over most of the domain, some areas such as the Great Lakes will see little to

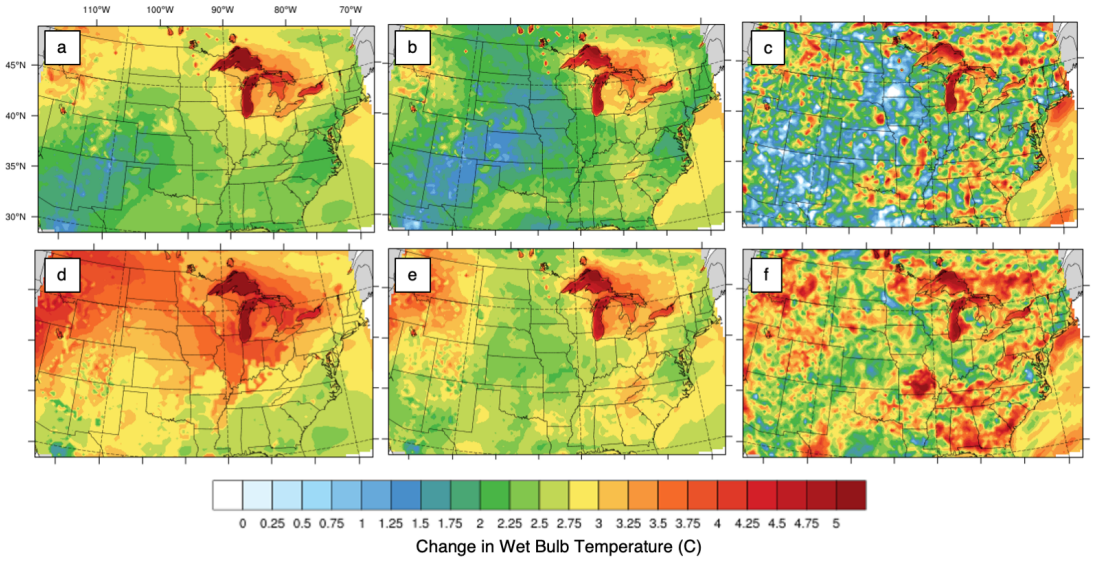

Figure 5-10: Change in JJAS average from 1975-2004 to 2070-2099 under RCP8.5 in CCSM4-2000 for a) average daily maximum wet-bulb temperature (degrees C) b) 95th percentile daily maximum wet-bulb temperature (degrees C) c) period maximum daily maximum wet-bulb temperature (degrees C) d) average daily minimum wet-bulb temperature (degrees C) e) 95th percentile daily minimum wet-bulb temperature (degrees C) f) period maximum daily minimum wet-bulb temperature (degrees C).

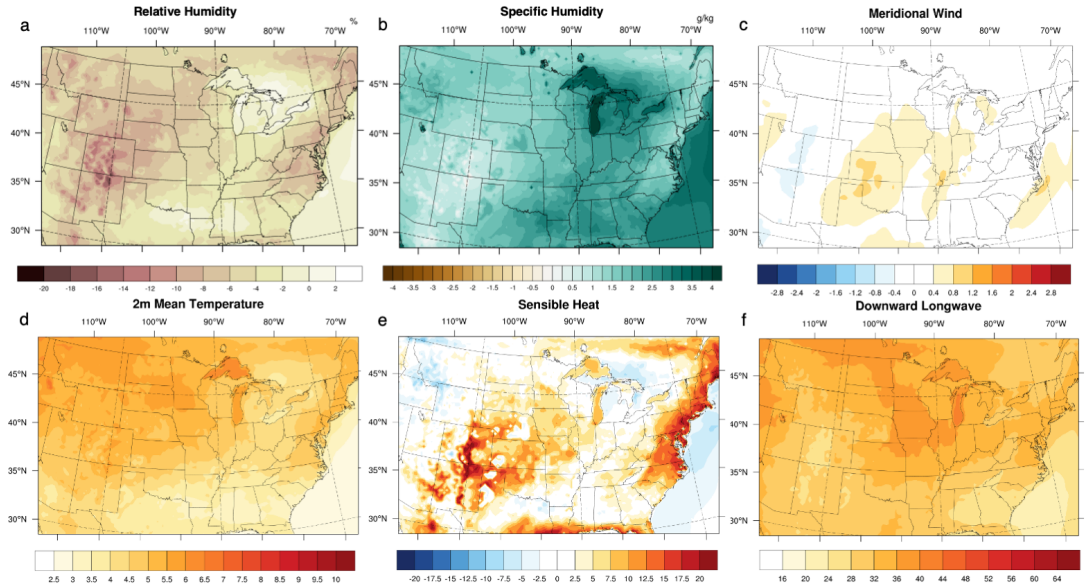

Figure 5-11: Change in JJAS Average from 1975-2004 to 2070-2099 under RCP8.5 in CCSM4-2000 for a) relative humidity (%) b) specific humidity (g/kg) c) meridional wind (m/s) d) 2-meter air temperature (degrees C) e) sensible heat flux (W/m^2) f) downward longwave radiation (W/m^2)

no change in relative humidity. Figures of the change in these surface variables for all three GCM forced simulations can be found in figures F-19 through F-22.

5.4.1 Impact of Land Use Change in the Historical Climate

First, we show that while bias exists in the original simulation results and in the bias corrected results, the inclusion of agricultural development in the simulations produces a more accurate picture of historical wet-bulb temperature patterns and reduces the existing cold bias in the Midwest (Fig. 5-12).

In order to investigate the impacts of agricultural development on wet-bulb temperature, two areas are chosen for analysis. An area from 40-43°N, 96.5-100°W in Nebraska as defined as irrigated area. Similarly an area from 39-41.5°N, 83.5-95.5°W is defined as non-irrigated area. These areas are marked out in green in Fig. 5-13 & 5-14, and results are shown for simulations using CCSM4.

Inclusion of non-irrigated (irrigated) agricultural development in the simulations increases average daily maximum wet-bulb temperature by 0.3 (0.7) °C in the historical period and by 0.3 (0.9) °C in the future period. Warming of wet-bulb temperature due to climate change under full agricultural development is 2.6°C from 20.2°C to 22.8°C in the central Midwest.

Similar patterns can be seen in the changes of 95th percentile daily maximum wet-bulb temperature. Inclusion of non-irrigated (irrigated) agricultural development in the simulations increases 95th percentile daily maximum wet-bulb temperature by 0.6 (0.5) °C in the historical period and by 0.5 (0.6) °C in the future period. Warming of wet-bulb temperature due to climate change under full agricultural development is 2.0°C from 24.6°C to 26.6°C.

Simulation results show that even despite the large projected increase in daily minimum wet-bulb temperatures, there is little difference in the impact of non-irrigated versus irrigated areas, and these areas even serve to dampen the daily maximum wet-bulb temperatures in their immediate area. Inclusion of non-irrigated (irrigated) agricultural development in the simulations decreases average daily minimum wet-bulb temperature by 0.1 (0.2) °C in the historical period and by 0.2 (0.2) °C in the

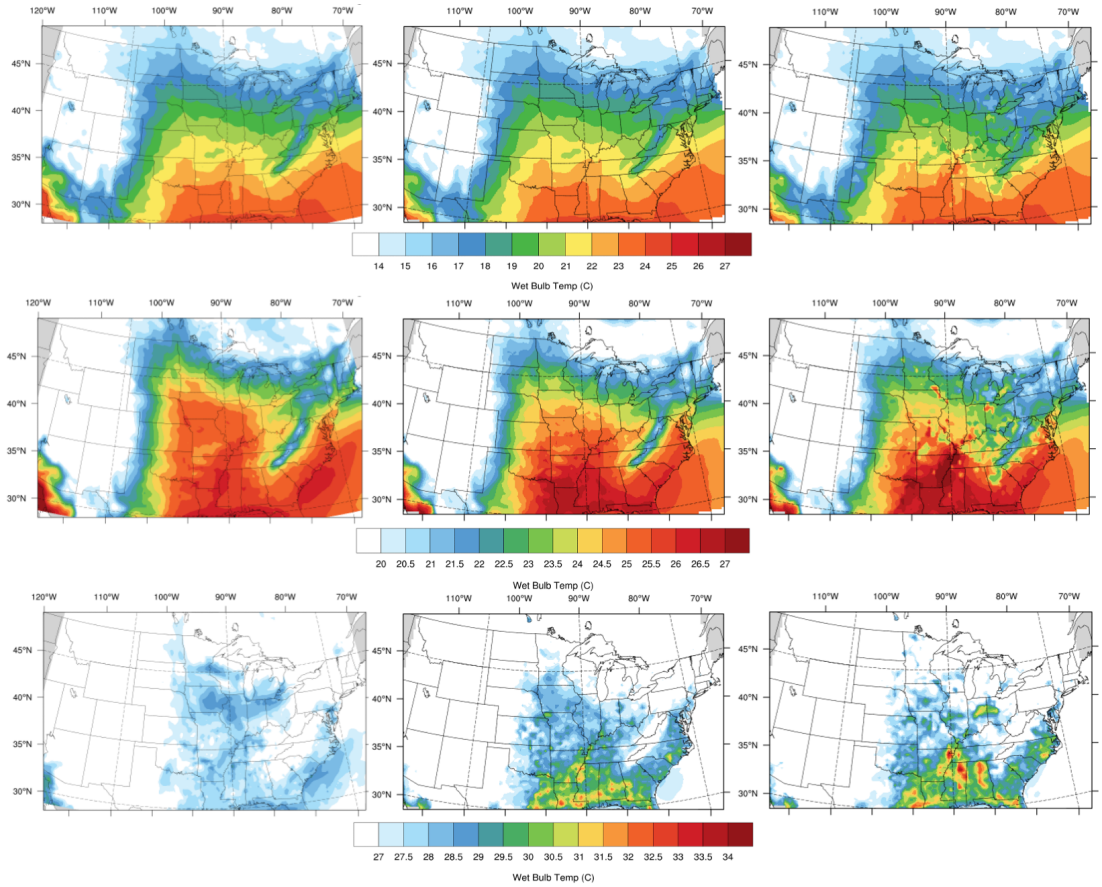

Figure 5-12: Comparison of JJAS average 1975-2004 bias corrected simulations of average daily maximum wet-bulb temperature (degrees C) (top row), 95th percentile daily maximum wet-bulb temperature (degrees C) (middle row) and period maximum daily maximum wet-bulb temperature (degrees C) (bottom row) between ERA5 data (left column), CCSM4-2000 bias corrected simulations (middle column), and CCSM4-1900 bias-corrected simulations (right column). Note that CCSM4-1900 simulations are bias-corrected using the same correction factor as the CCSM4-2000 simulation.

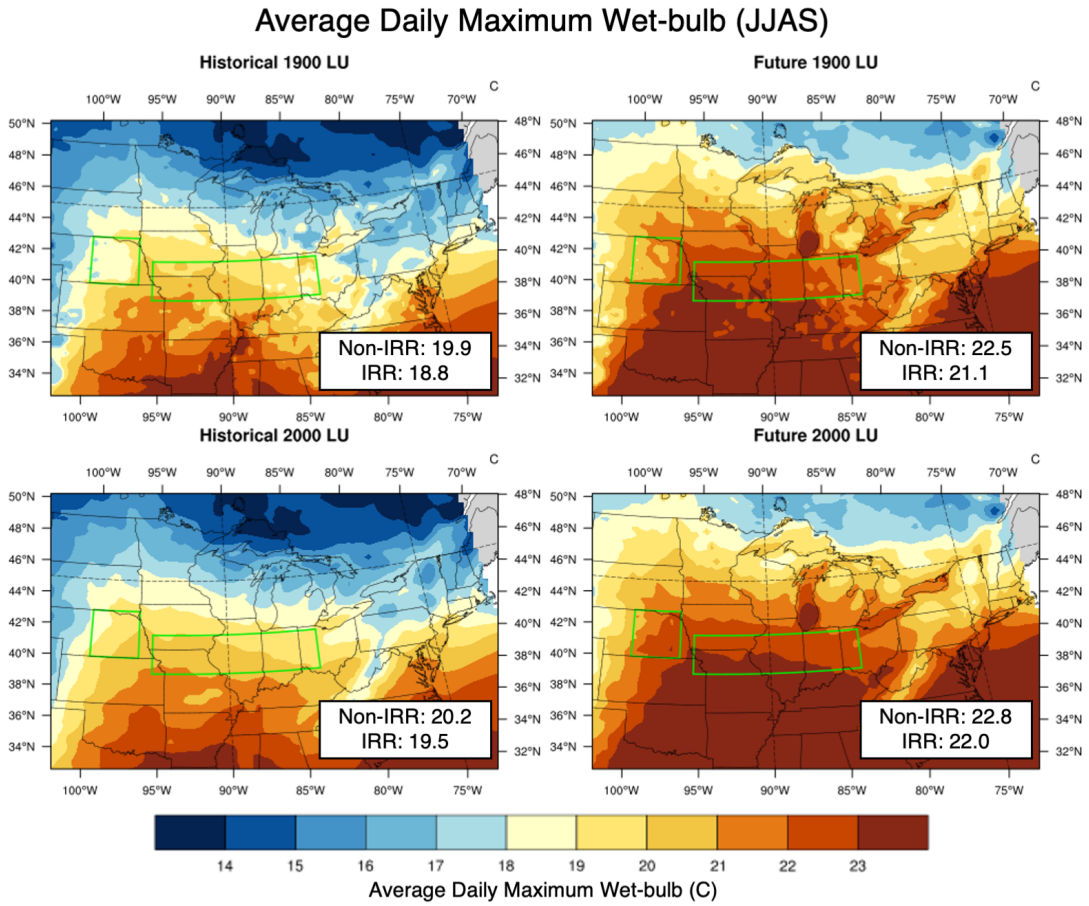

Figure 5-13: Maps of 30-year JJAS average daily maximum wet-bulb temperatures (degrees C) in historical (1975-2004) and future (2070-2099) simulations using CCSM4-1900 (top row) or CCSM4-2000 (bottom row). Irrigated and non-irrigated areas used for analysis and described in the text are outlined in green and area average wet-bulb temperatures are provided on the figure.

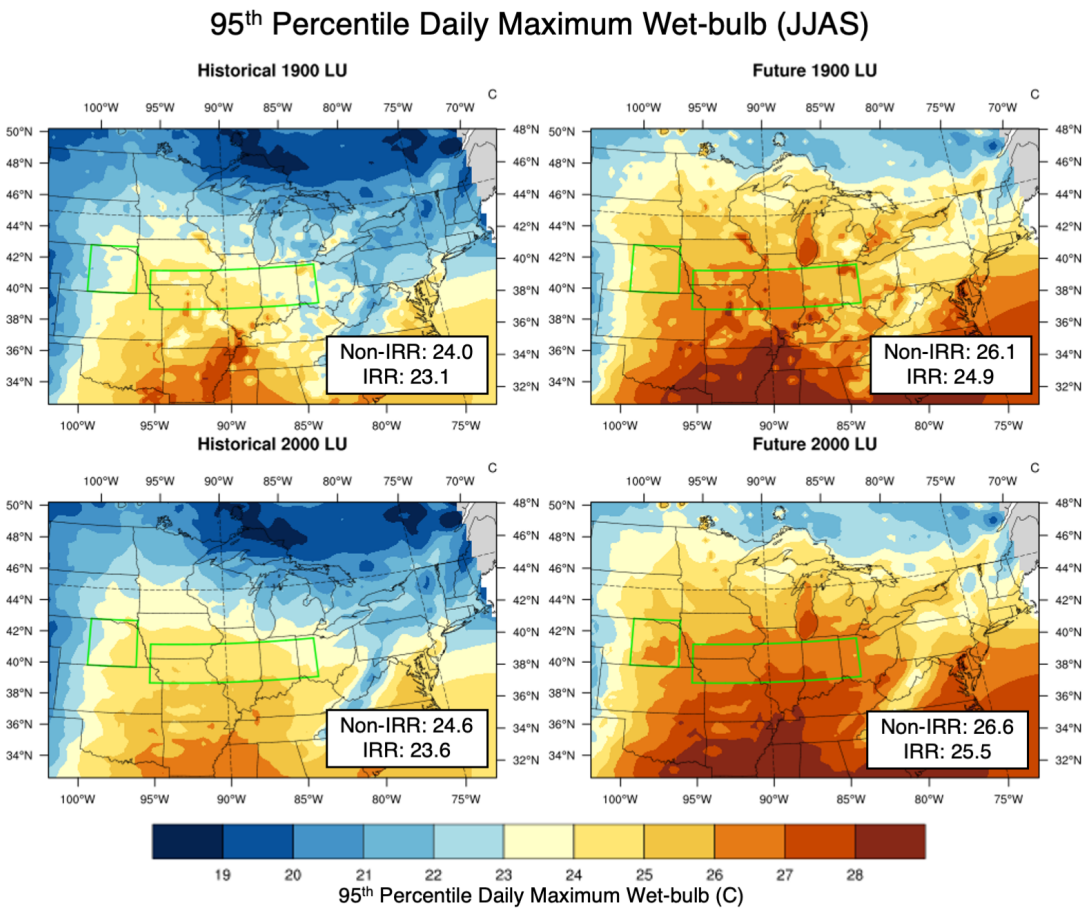

Figure 5-14: Maps of 30-year JJAS 95th percentile daily maximum wet-bulb temperatures (degrees C) in historical (1975-2004) and future (2070-2099) simulations using CCSM4-1900 (top row) or CCSM4-2000 (bottom row). Irrigated and non-irrigated areas used for analysis and described in the text are outlined in green and area average wet-bulb temperatures are provided on the figure.

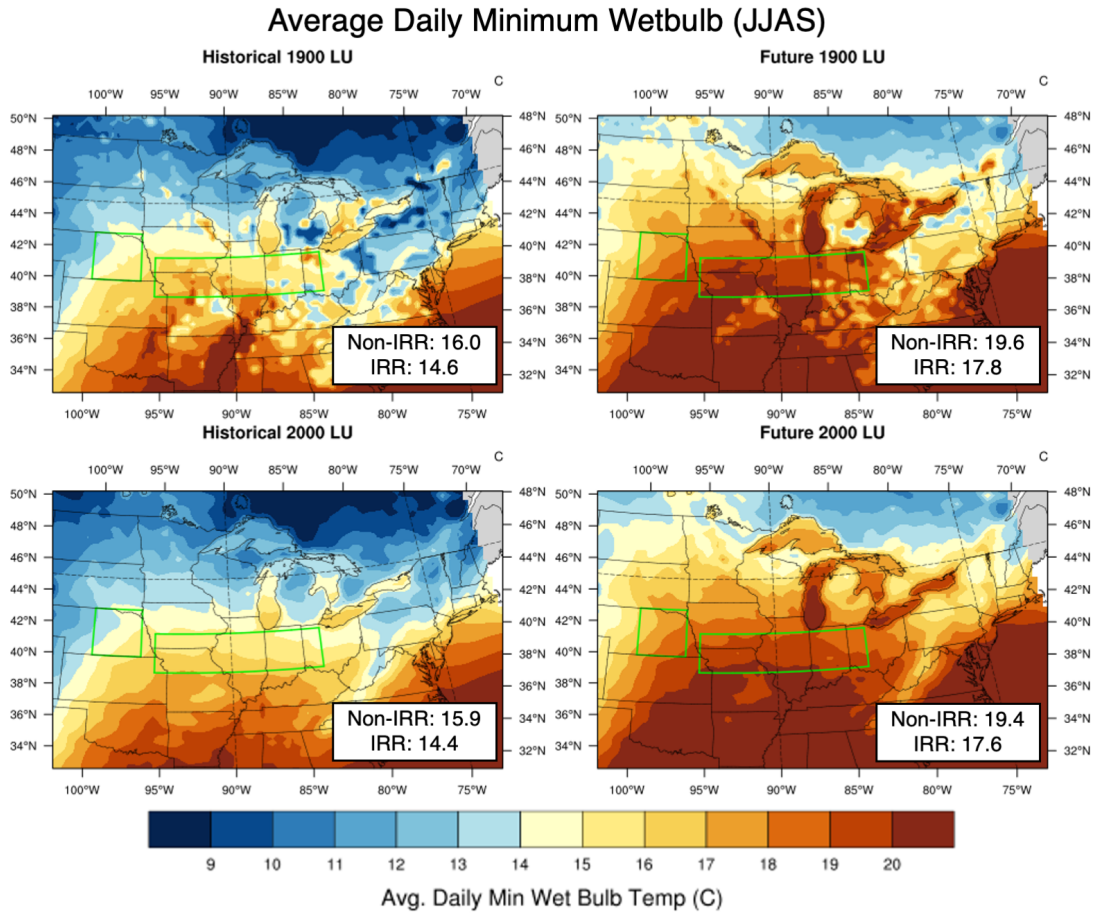

Figure 5-15: Maps of 30-year JJAS average daily minimum wet-bulb temperatures (degrees C) in historical (1975-2004) and future (2070-2099) simulations using CCSM4-1900 (top row) or CCSM4-2000 (bottom row). Irrigated and non-irrigated areas used for analysis and described in the text are outlined in green and area average wet-bulb temperatures are provided on the figure.

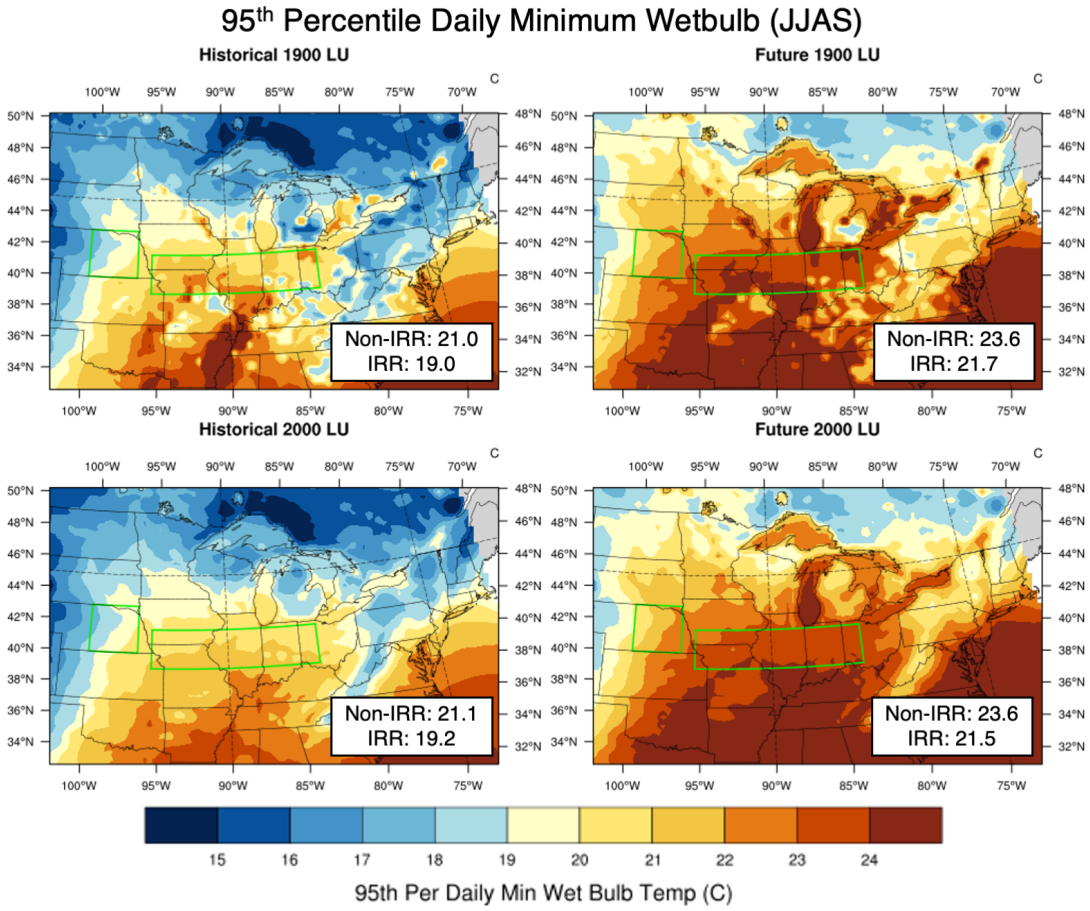

Figure 5-16: Maps of 30-year JJAS 95th percentile daily minimum wet-bulb temperatures (degrees C) in historical (1975-2004) and future (2070-2099) simulations using CCSM4-1900 (top row) or CCSM4-2000 (bottom row). Irrigated and non-irrigated areas used for analysis and described in the text are outlined in green and area average wet-bulb temperatures are provided on the figure.

future period (Fig. 5-15 & 5-16). Warming of daily minimum wet-bulb temperature due to climate change under full agricultural development is 3.5°C from 15.9°C to 19.4°C.

The 95th percentile of daily minimum temperatures do see a slight enhancement from agricultural development in the historical period. Inclusion of non-irrigated (irrigated) agricultural development in the simulations increases 95th percentile daily minimum wet-bulb temperature by 0.1 (0.2) °C in the historical period, but by 0 (-0.2) °C in the future period. Warming of 95th percentile daily minimum wet-bulb temperature due to climate change under full agricultural development is 2.5°C from 21.1°C to 23.6°C.

5.4.2 The Great Lakes

We have pointed out the Great Lakes as an area of interest in this study and a point of concern in correctly modeling surface temperature and moisture availability in the region. This is especially important in light of the Great Lakes region seemingly emerging as a hotspot of wet-bulb temperature change in the results as can be seen in Fig. 5-10. In CCSM4-2000 the JJAS average daily maximum wet-bulb temperature increase from the historical to future period is 3.3°C, 4.6°C, 3.9°C, and 4.9°C for Lakes Erie, Michigan, Ontario, and Superior respectively. These increase are larger, in some cases by a degree or more than the surrounding land area.

However, caution must be taken in the interpretation of these results, as future lake temperatures were estimated and may not reflect the future reality of lake surface temperature warming as mentioned previously. Despite this several patterns in the warming are consistent with other studies on the impact of climate change on the Great Lakes. Greater warming in the northern lakes, particularly Lake Superior is consistent with both a larger historical warming trend in these lakes [283] and studies showing that climate change will impact stratification and internal lake dynamics in evolving ways in deep water lakes like Lake Superior [286]. Additionally, the warming in wet-bulb temperature is consistent with the pattern of stronger dry-bulb temperature and specific humidity changes in the north of the domain.

Further research should be done to ensure that climate models are able to accurately recreate the seasonal cycle and trends in LST as well as the resultant changes in near surface air temperature and humidity. In the projections shown, the increase over the Great Lakes is likely driven by a water vapor feedback, similar to what may be occurring over irrigated areas. In these areas, temperature and specific humidity increases are more balanced, resulting in stable relative humidity levels in comparison to surrounding land areas. An increase in atmospheric water vapor content and net radiation (Fig. 5-11) enhances the wet-bulb temperature changes in these areas under climate change.

The enhanced warming over the Great Lakes even contributes to the initiation and propagation of high wet-bulb temperature heat events over the lakes themselves, a phenomena that we do not see in the historical period in the simulations. An example of such an event is seen in the future CCSM4-2000 simulation (Fig. 5-17)

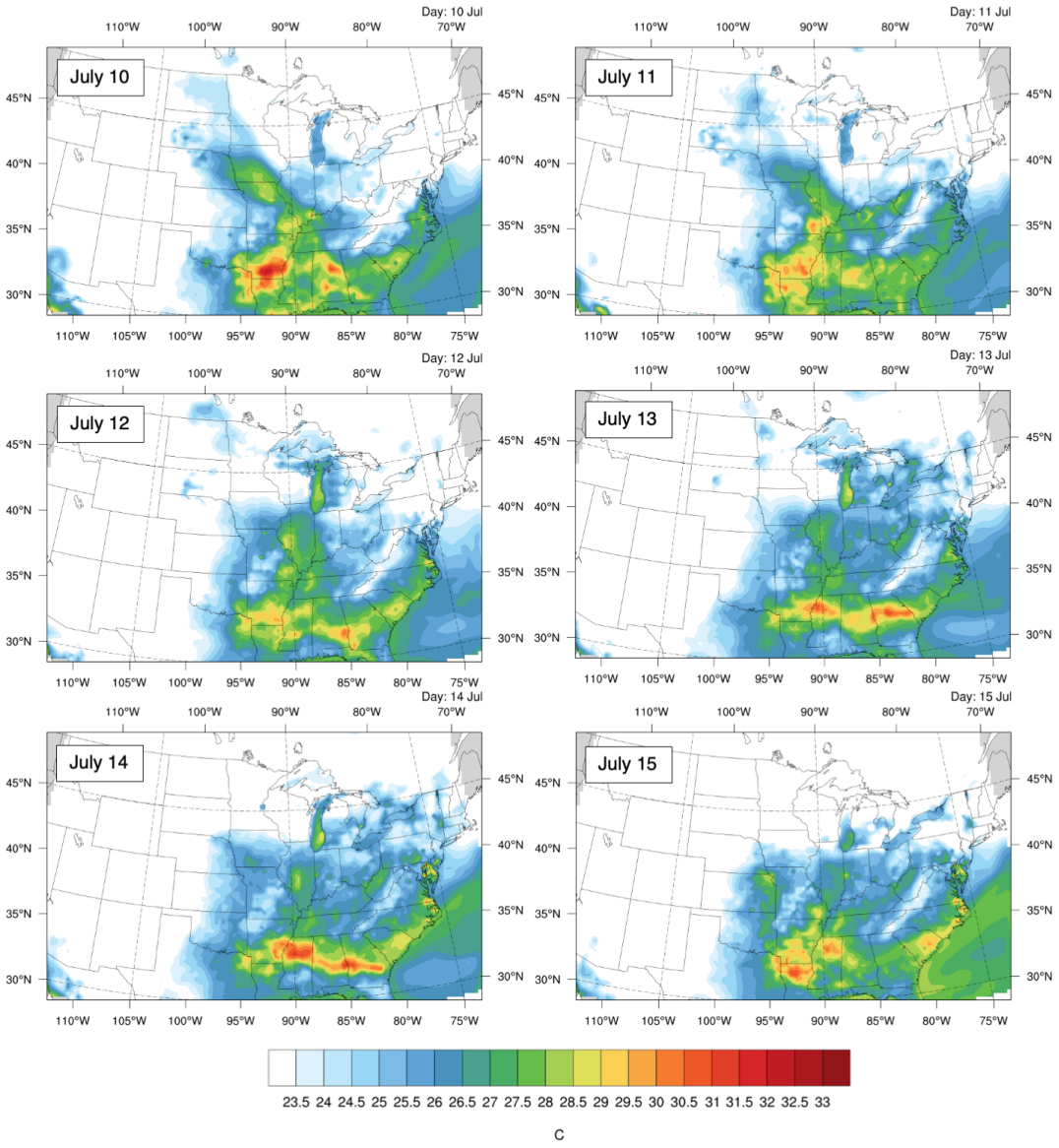

Figure 5-17: Maps showing the daily maximum wet-bulb temperature (degrees C) for a wet-bulb temperature event in the CCSM4-2000 simulation from July 10-15, 2082 that begins in the Great Lakes and propagates into the wider region.

5.4.3 Event Analysis

The shift in wet-bulb temperature climatology is important to understanding what new regions of the country may be at risk from humid heat stress. Because a prolonged exposure to elevated wet-bulb temperatures over several days is the cause of heat stress and mortality, we also analyze individual events here in order to understand how the threat of humid heat wave events will change in the future.

We use the thresholds laid out in Fig. 5-3 for wet-bulb temperatures, using 60% relative humidity as the average for the region of interest in the June-September season. Extreme caution events are those with maximum daily wet-bulb temperature exceeding 23.5°C, danger events exceed 26.5°C, and extreme danger events exceed 30.2°C. We also use a nighttime wet-bulb temperature threshold of 20.5°C. This aligns roughly with the National Weather Service nighttime risk temperature of 75 degrees [185]. In order to highlight events in our immediate region of interest, only grid cells between 37-48°N,81-100°W are considered in the identification process. In order to be considered a heat wave event, maximum and minimum temperatures must surpass the given thresholds on at least two consecutive days, with allowances of one day gaps in order to capture fluctuating but still coherent events. A heat wave day is marked when 10% of the grid cells (n = 216) surpass this threshold. Due to the strong signal in wet-bulb temperature over the Great Lakes, these areas are masked out for grid cell analysis, but still count in the total area considered. Event analysis is shown for the CCSM4 simulations (Figure 5-18), which were able to most closely match the event statistics in ERA5. No events were identified in either the historical or future simulations for the extreme danger level. Event statistics for CNRM-CM5 and HadGEM2-ES simulations can be found in Figures B-1 and B-2 respectively.

CCSM4-2000 simulations approach the average duration and anomaly for extreme caution heat waves in the ERA5 reanalysis (6.01 days versus 6.06 days, and 1.11°C versus 1.04°C respectively) but underestimate the total number of heat waves, finding only 575 heat wave event days versus 796 in the ERA5 reanalysis. The CCSM4-2000 simulations also approach the event statistics in ERA5 for danger level events although

Occurrence of Extreme Caution Days (+23.5 degrees) & Hot Nights (+20.5 degrees) Heat Wave Events

CCSM4 & 2000 LULC	Period Total Exceedance Days	Days in HW Events (days)	Average Length of HW Event (days)	Average HW Day TWmax Exceedance (C)
Historical (1975-2004)	601	575	6.01	1.11
Future (2070-2099)	2460	2444	22.5	1.42

CCSM4 & 1900 LULC	Period Total Exceedance Days	Days in HW Events (days)	Average Length of HW Event (days)	Average HW Day TWmax Exceedance (C)
Historical (1975-2004)	523	500	5.82	1.02
Future (2070-2099)	2389	2375	20.87	1.27

ERA5 - ExC	Period Total Exceedance Days	Days in HW Events (days)	Average Length of HW Event (days)	Average HW Day TWmax Exceedance (C)
Historical (1975-2004)	846	796	6.06	1.04

Occurrence of Danger Days (+26.5 degrees) & Hot Nights (+20.5 degrees) Heat Wave Events

CCSM4 & 2000 LULC	Period Total Exceedance Days	Days in HW Events (days)	Average Length of HW Event (days)	Average HW Day TWmax Exceedance (C)
Historical (1975-2004)	11	7	3.5	0.82
Future (2070-2099)	396	381	5.01	0.97

CCSM4 & 1900 LULC	Period Total Exceedance Days	Days in HW Events (days)	Average Length of HW Event (days)	Average HW Day TWmax Exceedance (C)
Historical (1975-2004)	0	0	~	~
Future (2070-2099)	162	154	4.66	0.95

ERA5 - D	Period Total Exceedance Days	Days in HW Events (days)	Average Length of HW Event (days)	Average HW Day TWmax Exceedance (C)
Historical (1975-2004)	13	10	2.5	0.74

Figure 5-18: Frequency, intensity, and duration statistics for events at the extreme caution and danger levels in CCSM4 simulations. Total exceedance days are the number of days that pass the area and threshold requirements regardless of if they are in a coherent heat wave event. Days in heat wave events notes the number of days contained in the heat wave events. The average heat wave day TWmax exceedance shows the average daily maximum wet-bulb temperature of heat wave event days beyond the prescribed threshold.

the smaller number of events identified makes comparison less reliable.

In the historical period, agricultural land use change increased the frequency and duration of heat wave events, although it had little to no impact on the average temperature anomaly (difference between the average daily maximum wet-bulb temperature on all heat wave days minus the threshold temperature). In CCSM4-2000 simulations for the historical period, the inclusion of agricultural development increased the frequency of extreme caution heat wave day occurrence by 75 days (15%), the average heat wave duration by 0.2 days (3%) and the temperature anomaly by 0.1°C (9%). No danger events were identified in the simulations with 1900 land use, while 7 days with an average heat wave length of 3.5 days and anomaly of 0.82°C were found in CCSM4-2000. A similar bump was seen in the future period; the inclusion of agricultural development increased the frequency of extreme caution heat wave day occurrence by 69 days (3%), the average heat wave duration by 1.6 days (8%) and the temperature anomaly by 0.15°C (12%). The inclusion of agricultural development has a much greater impact on the frequency of danger heat wave events in the future period, increasing them by 227 days (150%); a much more moderate impact was made on average heat wave duration and temperature anomaly - 0.35 days (8%) and 0.02°C (2%) respectively.

The impacts of climate change have a much more dramatic impact on the frequency, intensity, and duration of heat wave events under both the extreme caution and danger thresholds in both land use scenarios. In CCSM4-2000 simulations, climate change causes the frequency of extreme caution heat wave days to increase by 1,869 days (325%), the duration to increase by 16.5 days (275%) and the intensity by 0.31°C (28%). The frequency of danger events will increase by 374 days (from a historical frequency of 7 days), the duration by 1.5 days (43%) and the intensity by 0.15°C (18%). An example of this change in event occurrence can be seen through a time-series showing the percentage of the smaller domain that exceeds a given threshold in the past vs future period in the 3660 summer days considered in each period (Fig. 5-19).

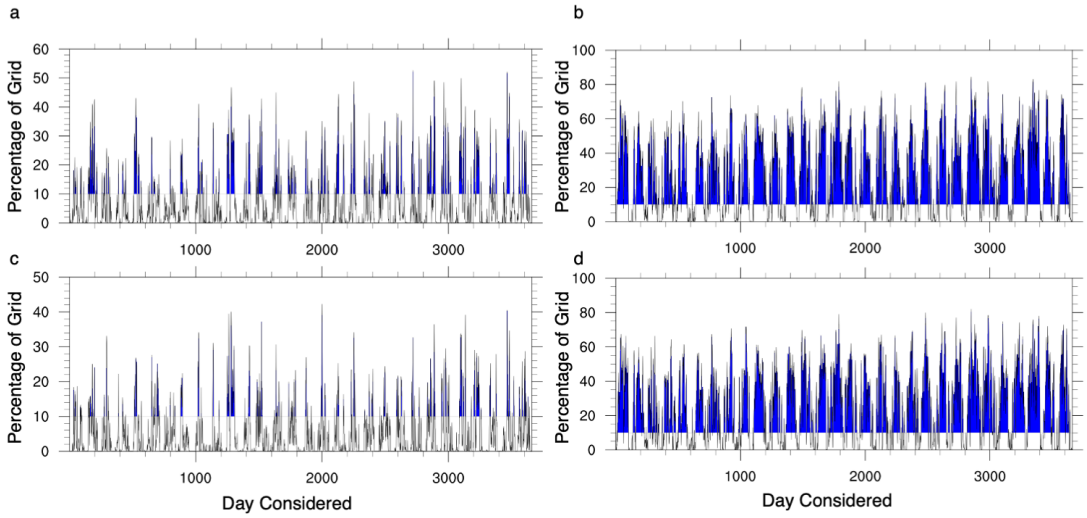

Figure 5-19: Timeseries showing the percent of the smaller domain where grid cells exceed the extreme caution thresholds for a) daily maximum threshold in the historical period (1975-2004) and c) daily minimum threshold in the historical period (1975-2004) in CCSM4-2000. Blue colors note days where greater than 10% of grid cells meet the requirement and are counted as heat wave days. b) same as (a) but for the future period (2070-2099) d) same as (c) but for the future period (2070-2099).

5.4.4 Associated Patterns

Extreme caution heat waves events in historical simulations with CCSM4-2000 show positive meridional wind anomalies (relative to the 1975-2004 JJAS average), positive anomalies in downward longwave and negative anomalies in sensible heat flux and increases in both 2m specific humidity and root zone soil moisture (Fig. 5-20). These changes all serve to increase the moist static energy and wet-bulb temperature in these humid heat events. The increase in meridional wind and the negative to positive, north to south surface pressure anomaly is also consistent with an increase in moisture advection – a pattern which has been found in other studies of Midwestern heat events [230] [251]. Additionally, the 1995 heat wave event discussed earlier was also associated with a southerly wind anomaly, especially at night (Fig. 5-4).

Raymond et al. (2017) showed that humid heat events in the Midwest are associated with similar specific humidity and meridional wind anomalies at the 850 mb level [211]. Ford and Schoof, 2017 also showed that "oppressive" heat wave events in Illinois are associated with both high temperature and high humidity, and occurred

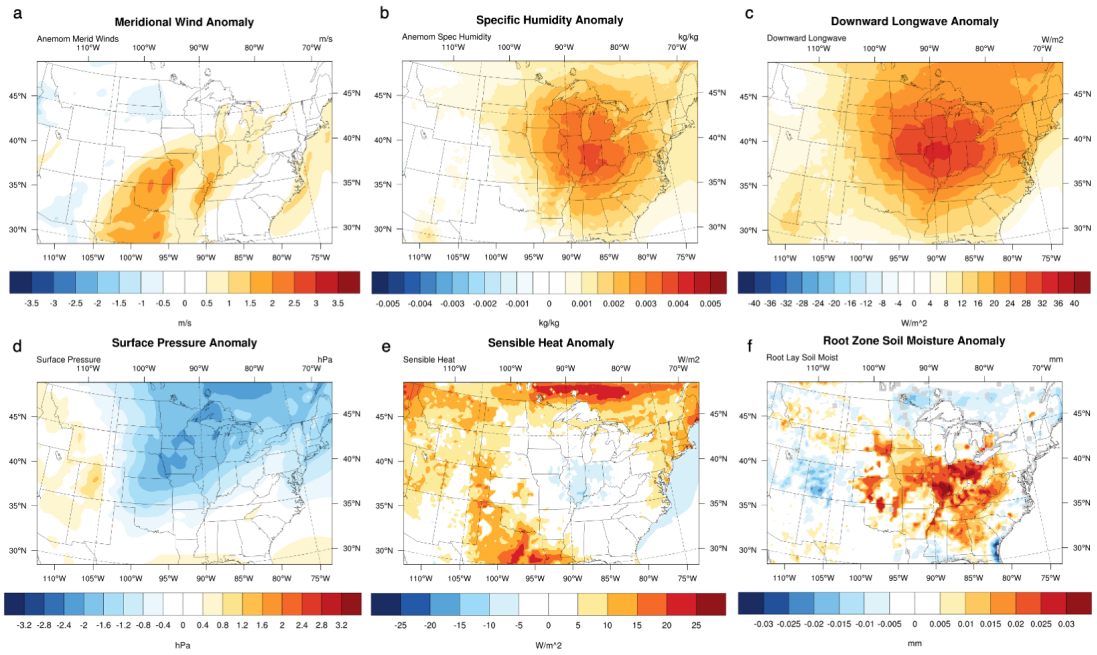

Figure 5-20: Average historical (1975-2004) JJAS anomalies relative to 1975-2004 JJAS averages for extreme caution exceedance days in the CCSM4-2000 for a) meridional wind (m/s) b) specific humidity (kg/kg) c) downward longwave radiation (W/m^2) d) surface pressure (hPa) e) sensible heat flux (W/m^2) f) root zone soil moisture (mm)

CCSM4 Extreme Caution & 2000 LULC & +VA Anomaly	Period Total Exceedance Days	Days in HW Events (days)	Average Length of HW Event (days)	Average HW Day TWmax Exceedance (C)
Historical (1975-2004)	414	389	4.89	1.10
Future (2070-2099)	1427	1377	6.43	1.43

CCSM4 Extreme Caution & 2000 LULC & 0/-VA Anomaly	Period Total Exceedance Days	Days in HW Events (days)	Average Length of HW Event (days)	Average HW Day TWmax Exceedance (C)
Historical (1975-2004)	187	136	2.82	1.16
Future (2070-2099)	1033	934	4.76	1.42

CCSM4 Extreme Caution & 1900 LULC & +VA Anomaly	Period Total Exceedance Days	Days in HW Events (days)	Average Length of HW Event (days)	Average HW Day TWmax Exceedance (C)
Historical (1975-2004)	347	323	4.51	1.00
Future (2070-2099)	1389	1335	6.51	1.28

CCSM4 Extreme Caution & 1900 LULC & 0/-VA Anomaly	Period Total Exceedance Days	Days in HW Events (days)	Average Length of HW Event (days)	Average HW Day TWmax Exceedance (C)
Historical (1975-2004)	176	123	3.0	1.08
Future (2070-2099)	1000	902	4.78	1.29

Figure 5-21: Frequency, intensity, and duration statistics for events at the extreme caution and danger levels in CCSM4 simulations. Events are shown for CCSM4-2000 (top row) and CCSM4-1900 (bottom row) and for days with positive meridional wind anomalies (left) and without (right). Total exceedance days are the number of days that pass the area and threshold requirements regardless of if they are in a coherent heat wave event. Days in heat wave events notes the number of days contained in the heat wave events. The average heat wave day TWmax exceedance shows the average daily maximum wet-bulb temperature of heat wave event days beyond the prescribed threshold.

both through local antecedent moisture conditions, and moisture transport [229]. An analysis of meridional wind anomalies in the Great Plains Lower Level Jet (GPLLJ) region (calculated as the anomaly in 36-42°N,95-100°W relative to the daily climatological average) shows that on average in the historical and future period 74% and 60% of extreme caution heat waves days are associated with positive meridional wind anomalies. This distribution is very slightly less in the 1900 land use simulations (72% and 60%) (Table 5-21). However, Schoof et al. (2019) found that future heat events are likely to be driven by warming rather than changes in associated circulation patterns [230]. The increase in meridional wind found in the future in our simulations (Fig. 5-11) coupled with the strong preference for heat waves with positive meridional anomalies in this region (Fig. 5-21), suggests that circulation may drive some of the increased future events. However, the partitioning of events with and without meridional wind anomalies shown in Fig. 5-21 remains relatively stable from the historical to future period, suggesting agreement that changes in circulation are unlikely to change heat wave patterns in the future.

5.4.5 Human Impact

Ultimately, these wet-bulb temperature and heat stress changes should be tied to their real impact on communities and public health. The thresholds chosen for heat event identification are related to the likelihood of heat disorders with prolonged exposure or strenuous activity [185].

While all populations regardless of demographics are in danger from very extreme wet-bulb temperatures, there have been many studies on the hazards posed by heat waves to different groups. Son et al. (2019) conducted a review of heat wave literature and while a wide range of factors were looked at across heat stress studies, the review only concluded that there was strong evidence of the increased heat risk for women and elderly populations [243]. Spangler and Wellenius (2020) found that heat index metrics are rising faster in socially vulnerable communities [244].

Here we use population projections at the county level in order to investigate the population that will be likely exposed to future wet-bulb temperature thresholds [100]. These projections are developed for the 5 Shared Socioeconomic Pathways (SSP) developed for use in CMIP6, and are given for breakdowns of age (5-year intervals), gender, and race. We use the population projections for SSP5, which assumes increasing development and globalization. This is the SSP linked to the high emission scenario in the CMIP6 projections and aligns most closely with our use of RCP8.5.

Illinois is used as an example here, but more state analysis for total and 60+ year-old population can be found in Figures F-23 through F-30. In Illinois, under historical conditions simulated in CCSM4-2000, currently (2020 population) 0% of the total population is exposed to average daily maximum wet-bulb temperatures that reach the extreme caution or danger levels (Fig. 5-22). Under future warming this will increase to 4.9% (0.7 million people) for the extreme caution threshold with populations taken for 2085. Similarly, currently 92% of the total population (12.2 million people) and 0% of the total population is exposed to 95th percentile daily maximum wet-bulb temperatures that reach the extreme caution or danger levels.

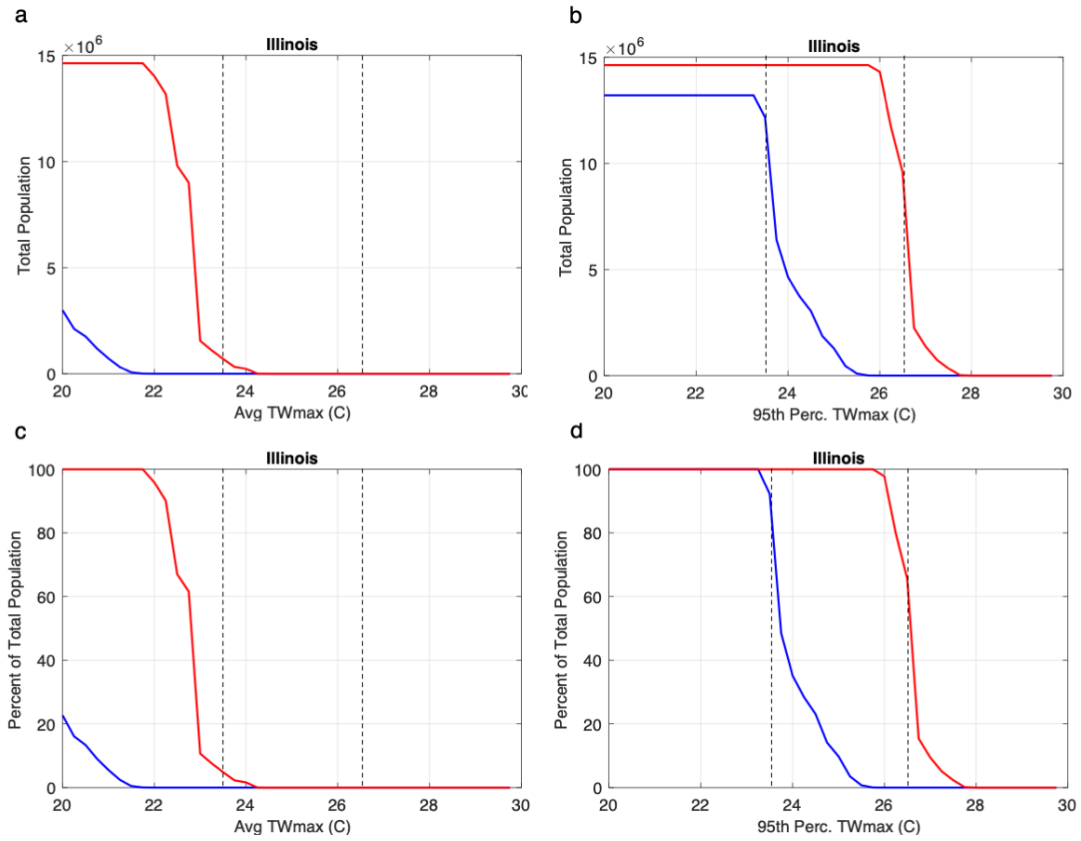

Figure 5-22: a) Total population living in a county with a given county average daily maximum wet-bulb temperature (degrees C) in JJAS in the historical (1975-2004) (blue) and future (2070-2099) (red) periods. b) same as (a) but for the 95th percentile of daily maximum wet-bulb temperature (degrees C) c) same as (a) but for percentage of the total population d) same as (b) but for percentage of the total population. Black dashed lines mark the extreme caution (23.5 degrees C) and danger (26.5 degrees C) thresholds.

Under future warming this will increase to 100% (14.6 million people) and 66% (9.6 million people) for extreme caution and danger thresholds.

This effect of shifting wet-bulb temperature can also be seen by examining distributions of daily maximum wet-bulb temperature in cities using the nearest simulation grid point from CCSM4-2000. While factors such as amplification from urban heat island effects are not taken into account here, this provides a reasonable projection for the general climate shift that residents of these cities will experience (Fig. 5-23). Distributions for more cities (written in black) can be found in Figure F-31. Additionally we see that while southern cities tend to have higher average daily maximum wet-bulb temperatures, their increase from the historical to future period is lower than for the Midwestern cities, especially relative to their historical mean (Table 5.2). Southern cities also tend to have smaller coefficients of variation (ratio of standard deviation to mean) than Midwestern cities, which tend to have a stronger leftward skew. We note that this skewness influences the coefficient as mean and standard deviation metrics are most appropriate for data with an approximately normal distribution.

The distributions shift rightward with time, with cities closer to the Great Lakes such as Milwaukee seeing larger shifts. Cities in the South and Southeast are included for comparison. In the future, the distributions of Milwaukee and Atlanta look similar while the future of Minneapolis/St. Paul looks like the historical distribution of cities like Atlanta or Nashville. Similarly the future distribution of Chicago looks more like the current distribution for Memphis, and the future distributions of Boston, Detroit, and Chicago are all similar as extreme wet-bulb temperature spreads farther up the East Coast at the same time as it moves northward into the Midwest.

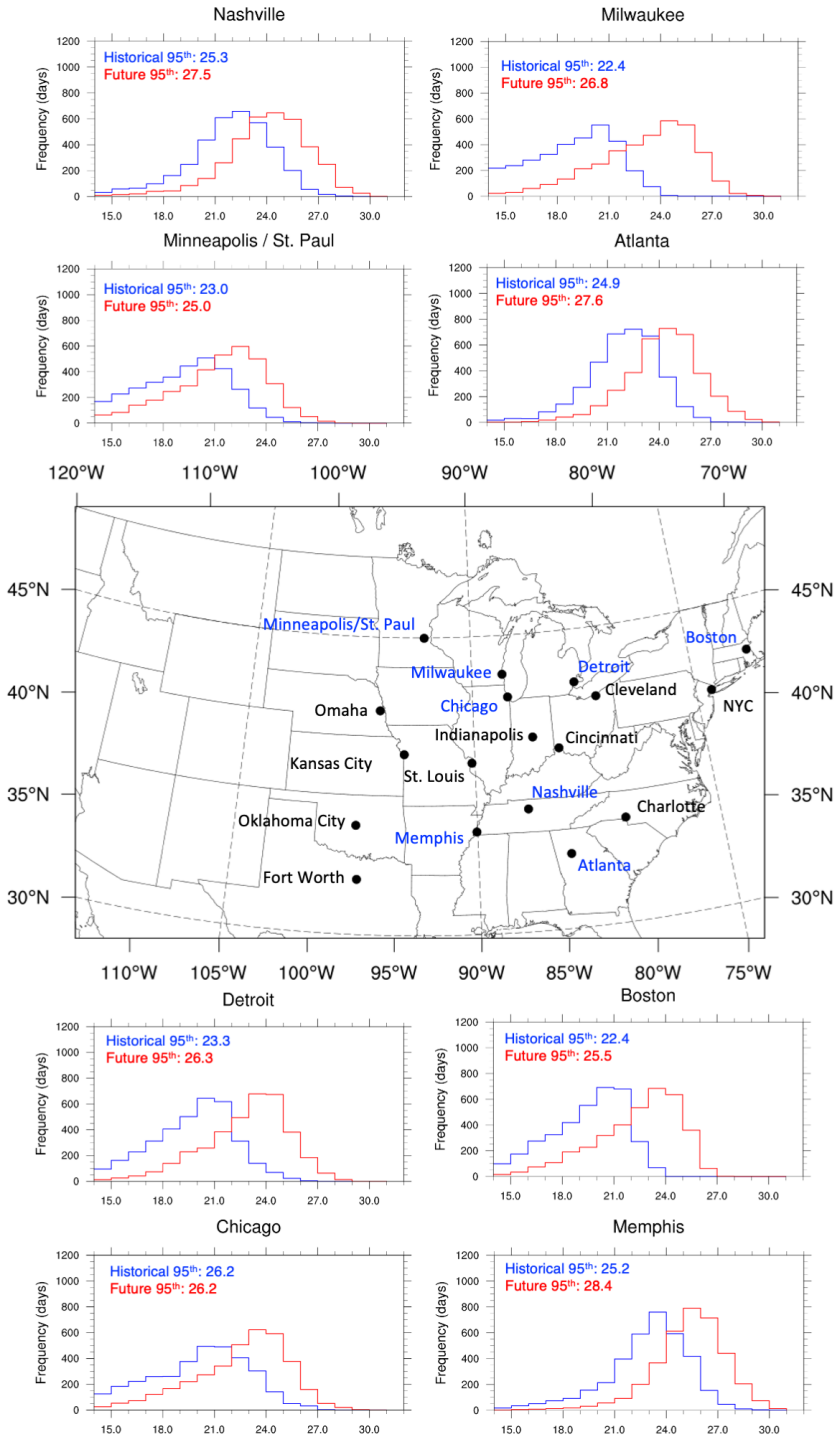

Figure 5-23: Distributions for the frequency of daily maximum wet-bulb temperatures (degrees C) in the CCSM4-2000 simulations from the historical (1975-2004) (blue) to the future (2070-2099) (red) periods. 95th percentile levels are shown in the individual plots for the historical and future period.

Table 5.2: Mean (μ), standard deviation (σ), and Coefficient of Variation (σ/μ) for daily maximum wet-bulb temperatures (degrees C) in the grid-cell nearest to selected cities for the historical (1975-2004) and future (2070-2099) period under RCP8.5

City	Hist μ	Hist σ	Future μ	Future σ	Hist. CV	Future CV
Minneapolis	18.23	20.99	13.55	9.78	0.74	0.47
Milwaukee	18.05	23.07	10.88	8.12	0.60	0.35
Chicago	19.47	22.37	12.79	9.01	0.66	0.40
Detroit	19.49	22.8	7.4	6.43	0.38	0.28
Kansas City	21.14	23.52	9.44	6.01	0.45	0.26
St. Louis	21.07	23.51	10.1	7.28	0.48	0.31
Indianapolis	20.18	22.84	10.6	9.14	0.53	0.40
Cincinnati	20.44	23	9.93	8.59	0.49	0.37
Cleveland	18.54	21.37	10.32	9.09	0.56	0.43
Omaha	20.36	22.78	11.39	7.32	0.56	0.32
Boston	19.33	22.33	5.6	6.18	0.29	0.28
NYC	20.02	22.94	6.13	6.5	0.31	0.28
Fort Worth	22.94	25.44	4.34	3.28	0.19	0.13
Oklahoma City	21.92	24.18	5.44	3.48	0.25	0.14
Memphis	22.78	25.33	7.07	4.77	0.31	0.19
Nashville	21.72	24.01	7.46	6.19	0.34	0.26
Atlanta	21.9	24.24	4.76	4.74	0.22	0.20
Charlotte	22.36	24.66	5.25	5.3	0.23	0.21

5.5 Discussion & Conclusions

Extreme wet-bulb temperatures pose a looming health risk for global communities, and previous research discussed here shows that dangerous and deadly conditions are likely to occur in the next century under climate change. The Midwest, while not an area that is accustomed to regular humid heat waves, will be forced to adapt to a future where elevated and extreme wet-bulb temperatures are a normal summer feature.

We have shown that while changes in agricultural development have modified the patterns of wet-bulb temperature in the past, under the current levels of development they will not exacerbate the wet-bulb temperature increases much more in the future. However, under a warming climate with increasing specific humidity, climate change will do a great deal to drive up wet-bulb temperatures on its own.

This work again shows the importance of a robust representation of agricultural development in climate studies, and highlights the importance of accurately representing land cover in general – as seen through the modification of the Great Lakes. Future work should explore this area further, and ensure that all models are able to accurately link the lakes and other large inland water bodies to the surrounding area.

While future changes in land cover and land use, as well as future increases in yield were beyond the scope of this study, this is an avenue for future study. Our simulations assume only past distributions of cropland and irrigation as well as yield levels, and these may change in the future. Further yield increases in the 21st century may potentially exacerbate wet-bulb temperatures in the future, especially if these yield increases correspond to a significant increase in evapotranspiration. Increased temperatures also pose a risk to agricultural areas as well as human health. A study by Schlenker and Roberts (2009) investigated the link between temperature and yields and found that the critical dry-bulb temperature for corn and soybean, the two most important summer crops in this area in terms of volume and economic value, is 29 degrees C and 30 degrees C respectively [228]. After this temperature, yields begin to decrease, which is problematic for a highly productive region that is a domestic and international supplier.

Finally, the changes seen in minimum wet-bulb temperature should also be pursued in further study especially given its historical depression due to agricultural development. While some studies have begun to separate out the occurrence of nighttime vs. day-time humid heat [251] [248], the direct connections between agricultural development and nighttime wet-bulb temperature have yet to be modeled.

Chapter 6

Summary & Conclusions

Through this thesis we have explored the Climate-Agriculture-Water nexus and how it can elucidate observed trends in the Central United States and Egypt. The findings described in these chapters add original contributions to the existing literature of the climate impacts of agricultural development on regional hydrology, the impact of agriculture on heat wave evolution, and the pressures that agriculture imposes on water availability at the edge of resource limits. The main original findings of each chapter are summarized below.

In Chapter 2, this thesis illustrates the vital link between agricultural development and water availability in Egypt, and how demand is tightly coupled to population and economic growth. While this connection is very clear in Egypt it is true for many areas at the local, regional, and global scales. We present an annual historical reconstruction of water demand and withdrawal from the Nile River down to the granularity of individual crop and animal products. We show that Egypt has been using the full available resources of the Nile since the late 1970's – starting from a surplus of about 20 km^3 per year in the 1960s leading to a deficit of about 40km^3 per year by the late 2010s. This deficit was managed by a massive increase in virtual water imports from 5 km^3 in the early 1970's to roughly 40 km^3 in the late 2010's. Our independent reconstruction of consumption and other water demands shows that the country is currently withdrawing on average 61.5 km^3 of water annually from the Nile, which is 11% greater than the 55.5 km^3 allocated through the 1959 agreement. By

developing a demand model that accurately recreates historical water demand, using relationships of water use to population and per-capita-GDP growth, this thesis is able to project water demand into the future and predict that in the early 2020's Egypt will be importing that same volume as virtual water embodied in agricultural products. Egypt's total water demand assuming increasing agricultural and municipal demand, stable industrial demand, and stable water reuse amounts, will be approximately 160 km^3 in 2030.

In Chapter 3, this thesis shows that the three components of agricultural development in the Central United States– expansion of cropland, intensification (yield increases), and irrigation development – have competing effects on shaping summer (July-August) regional climate, but collectively accounted for the observed temperature decreases (0.2-0.3 °C) from 1920-1949 to 1970-1999 and 30% of the precipitation increases (0.2-0.3 mm/day) depending on the region. Through a combined representation of the observed 400-500% crop yield increase, cropland expansion, and irrigation development, and the utilization of state-of-the-art long term reanalysis data sets, the 100-year simulations presented here show that agriculture has been the most significant anthropogenic driver of climate change in the 20th century. We demonstrate the importance of including all three components of agricultural development, as is seldom done in other studies, due to their competing climate effects. Expansion of cropland alone has a tendency to cause reductions in precipitation and evapotranspiration, with a mixed temperature effect. On the other hand, accurate representation of cropland intensification has a distinct cooling effect along with increases in precipitation and evapotranspiration, contrary to expected climate change impacts. Finally, the residual observed changes in the warming hole region in July-August from 1920-1949 to 1970-1999, not explained by agricultural development, are shown to be driven by changes in the sea surface temperature of the North Atlantic (cooling) and tropical Pacific (warming), which correlate to both colder and wetter conditions in the Central United States.

In Chapter 4, we show that the agriculturally driven cooling and wetting trends in the historical period have led to a modification of growing season (May-August)

water availability in the Heartland of the U.S., a core agricultural region we outline encompassing Iowa, Illinois, Indiana and Ohio. This water availability is represented here through Precipitation-Evapotranspiration (P-E), an analogue for the moisture convergence into this region. Analysis of observational data from gridded observations, outputs from the Variable Infiltration Capacity Model [140], and in-situ observations from Illinois show that from 1915-2005 evapotranspiration has increased (0.4 mm/yr), vapor pressure has increased (0.012 hPa/yr) and air temperature has been stable (0.001 C/yr). This has driven an increase in relative humidity (0.047 %/yr) and a resultant increase in precipitation (0.65 mm/yr). Ultimately, from 1915-1944 to 1975-2004 P-E increased approximately 17 mm in the Heartland. Future projections from the CMIP5 and CMIP6 multi-model ensembles forecast an enhancement of the seasonality of soil moisture in this region, with springs getting wetter and summers getting drier. In the future from 2006-2099, May-August temperature increases (0.062 C/yr in CMIP5) and associated reductions in relative humidity (-0.069 %/yr in CMIP5) are shown to lead to drying in the summertime, with a P-E reduction of 12 mm (36 mm) in CMIP5 (CMIP6). These changes will require adaptation in a system where spring drainage management is extensive but supplemental irrigation is limited. 40-50% of harvested cropland in Illinois was drained by subsurface tiles in 2017, while in 2007 only roughly 2% of cropland was irrigated. This allows ample room for future development and possibly a leveraging of the seasonal imbalance of water availability through runoff and rainfall management.

Finally, in Chapter 5 this thesis investigates the impact of agriculture on the climatology of heat waves in the Central U.S and their change from the historical (1975-2004) to future (2070-2099) period under RCP8.5 ('Business as Usual') forcing scenarios. Results show that while climate change will be the strongest driver of wet-bulb temperature changes, agricultural development has had a small but significant impact in the historical period. Simulations using MRCM are driven by carefully selected global climate models with modified representations of Great Lakes surface temperatures based on empirical relationships between lake and air temperatures. Results show that agricultural development has enhanced historical daily maximum

wet-bulb temperatures and depressed daily minimum wet-bulb temperatures in this region in both non-irrigated and irrigation areas; non-irrigated (irrigated) agriculture has increased June-September average daily maximum wet-bulb temperatures by 0.3 (0.7) °C in the historical period and has decreased average daily minimum wet-bulb temperatures by 0.1 (0.2) °C in the historical period. Irrigated areas also show a further enhancement effect on future daily maximum wet-bulb so that future irrigated agricultural areas will be 0.9 °C hotter than without development. Climate change will have a much greater impact on the change in extreme wet-bulb from the historical to the future period under current agricultural development levels, driving average daily maximum wet-bulb temperatures up by 2.6 °C across the central Midwest. Average daily minimum wet-bulb will see an even larger increase of 3.5°C. This is compared to a simulated 3.5°C to 5°C dry-bulb mean temperature increase in the same period and regions. Simulations of further wetbulb enhancement over the Great Lakes region are show as evidence of the importance of accurate representation of lake temperatures and fluxes over this region which is projected to warm significantly with little reduction in relative humidity. We present a corrected framework for approaching lake surface temperatures without a lake model, with strong caveats regarding model air temperature biases and the stability of the lake temperature trend under climate change. We also present an analysis of increases in humid heat wave events (2+ days beyond a given maximum and minimum wet-bulb threshold) over land in the region 37-48°N,81-100°W. While agricultural development increased the frequency of extreme caution (>23.5 degree) heat wave day occurrence by 75 days (15%), the average heat wave duration by 0.2 days (3%) and the temperature anomaly by 0.1°C (9%) in the historical period, climate change will increase these statistics by 1,869 days (325%), 16.5 days (275%) and 0.31°C (28%) respectively. These increases will force large new populations to adapt to historically unusual heat stress on a more regular basis, and the findings presented here show that plans must be made for this new heat stress normal to safeguard at risk communities and build resilience.

6.1 Broader Implications and Impacts

Although the results described in this thesis include novel contributions to the scientific literature in their areas, they will also have impact beyond the scientific community. An understanding of the impacts of agriculture on climate can improve our ability to model climate changes accurately, improving the quality of projections available for policy-making and improving public trust. Similarly, accurate projections of extreme events such as heat waves is key for adaptation planning and emergency management.

The connections between climate, agriculture, and water are particularly important in the Central U.S. and Egypt because they are vital suppliers of food both domestically and internationally. Changes in climate will potentially have far reaching complications and understanding how agriculture affects these systems can allow for more sustainable planning and careful adaptation.

6.2 Future Work

There are several areas of interest that emerged during this thesis that could not be included due to space and time. Many are already the subject of current study in the climate field, and the research being done on them can hopefully be improved and advanced by the work presented here:

Chapter 2 presents several policy proposals for managing future water demand in Egypt. Further quantification of these proposal's water savings would provide support for policy implementation. The reconstruction of historical water use presented here provides a good view of resource availability in order to guide future management decisions. Additionally, further research on the impacts of climate change is important for future planning and adaptation measures.

Chapter 3 presents the historical impact of agriculture on climate and future research should project what future changes, if any, on yield and cropland area will have concurrent with warming. Although production in the Central U.S. is necessarily

increasing to meet global demand, there is no consensus on how much yields will increase and what impact this may have on the climate.

In Chapter 4 we show that future summer drying in the Midwest – expressed through the balance of P-E – will likely move the area towards a previous climate state, and that the extensive management of the Cornbelt leaves ample room for adaptation. Further studies should examine the potential for supplementary irrigation in the summer, as well as the potential to harness an intensified seasonal cycle of moisture availability by using rainwater and runoff capture technology to use excess springtime moisture during dry summers.

In Chapter 5, we show the impact of agricultural development on the severity of heat wave events and wet-bulb temperature patterns. This area is on the forefront of climate research and therefore there are many avenues leading from the work presented here. Future work is needed on the impacts of any future development in cropland area and yield on further wet-bulb temperature enhancement, and the impacts that elevated wet-bulb temperature may have on crop yields and suitability. Continued work in the Great Lakes area is needed to confirm its position as a wet-bulb temperature hotspot and what impacts this will have on surrounding lake-side communities and wildlife. Finally, further exploration of the dominance of moisture versus temperature departures in extreme heat events in the future is needed, as well as an investigation of the changes in extreme daily minimum wet-bulb temperatures and how they are influenced by and may be beneficial to agricultural development.

Appendix A

CMIP5 and CMIP6 Multi-Model Ensemble

This appendix describes the CMIP5 and CMIP6 models used in Chapter 4 of this thesis, along with the reference papers and dataset references noted in the tables.

No.	Model	Modeling Center and Institution	Main Reference	Number of Ens. Used
1	ACCESS1.0	CSIRO (Commonwealth Scientific and Industrial Research Organisation, Australia), and BOM (Bureau of Meteorology, Australia) (CSIRO-BOM)	[1] Bi et al., 2013	1
2	ACCESS1.3			1
3	BCC-CSM1.1	Beijing Climate Center, China Meteorological Administration (BCC)	[2] Xin et al., 2013	1
4	BCC-CSM1.1(m)			1
5	BNU-ESM	College of Global Change and Earth System Science, Beijing Normal University (GCESS)	[3] Ji et al., 2014	1
6	CanESM2	Canadian Centre for Climate Modelling and Analysis (CCCma)	[4] Arora et al., 2011	5
7	CCSM4	National Center for Atmospheric Research (NCAR)	[5] Gent et al., 2011	6
8	CESM1(BGC)	National Science Foundation, Department of Energy, National Center for Atmospheric Research (NSF-DOE-NCAR)	[6] Neale et al., 2010	1
9	CESM1(CAM5)			3
10	CESM1(WACCM)			3
11	CMCC-CM	Centro Euro-Mediterraneo per I Cambiamenti Climatici (CMCC)	[7] Scoccimarro et al., 2011	1
12	CNRM-CM5	Centre National de Recherches Meteorologiques / Centre Europeen de Recherche et Formation Avancees en Calcul Scientifique (CNRM-CERFACS)	[8] Voldoire et al., 2013	5
13	CSIRO-Mk3.6.0	Commonwealth Scientific and Industrial Research Organisation in collaboration with the Queensland Climate Change Centre of Excellence (CSIRO-QCCCE)	[9] Rotstayn et al., 2013	10
14	FGOALS-g2	LASG, Institute of Atmospheric Physics, Chinese Academy of Sciences; and CESS, Tsinghua University (LASG-CESS)	[10] Li et al., 2013	1
15	FIO-ESM	The First Institute of Oceanography, SOA, China (FIO)	[11] Qiao et al., 2013	3
16	GFDL-CM3	Geophysical Fluid Dynamics Laboratory (NOAA-GFDL)	[12] Dunne et al., 2012	1
17	GFDL-ESM2G			1
18	GFDL-ESM2M			1
19	GISS-E2-H-CC	NASA Goddard Institute for Space Studies (NASA-GISS)	[13] Miller et al., 2014	1
20	GISS-E2-H			2
21	GISS-E2-R-CC			1
22	GISS-E2-R			2
23	HadGEM2-CC	Met Office Hadley Centre (additional HadGEM2-ES realizations contributed by Instituto Nacional de Pesquisas Espaciais) (MOHC)	[14] Collins et al., 2011	3
24	HadGEM2-ES			4
25	INM-CM4	Institute for Numerical Mathematics (INM)	[15] Volodin et al., 2010	1
26	IPSL-CM5A-LR	Institut Pierre-Simon Laplace (IPSL)	[16] Marti et al., 2010	4
27	IPSL-CM5A-MR			1
28	IPSL-CM5B-LR			1
29	MIROC5	Atmosphere and Ocean Research Institute (The University of Tokyo), National Institute for Environmental Studies, and Japan Agency for Marine-Earth Science and Technology (MIROC)	[17] Watanabe et al., 2010	3
30	MIROC-ESM-CHEM	Japan Agency for Marine-Earth Science and Technology, Atmosphere and Ocean Research Institute (The University of Tokyo), and National Institute for Environmental Studies (MIROC)		1
31	MIROC-ESM			1
32	MPI-ESM-LR	Max Planck Institute for Meteorology (MPI-M)	[18] Zanchettin et al., 2013	3
33	MPI-ESM-MR			1
34	MRI-CGCM3	Meteorological Research Institute (MRI)	[19] Yukimoto et al., 2012	1
35	NorESM1-ME	Norwegian Climate Centre (NCC)	[20] Bentsen et al., 2012	1
36	NorESM1-M			1

Figure A-1: CMIP5 Models used in Chapter 3

No.	Model	Modeling Group	Main Reference and Data Citations	Number of Ens. Used
1	ACCESS-CM2	Commonwealth Scientific and Industrial Research Organisation, Aspendale, Victoria 3195, Australia (CSIRO), Australian Research Council Centre of Excellence for Climate System Science (ARCCSS).	[21] Bi et al., 2020 [22] Dix et al., 2019a [23] Dix et al., 2019b	1
2	ACCESS-ESM1-5	Commonwealth Scientific and Industrial Research Organisation, Aspendale, Victoria 3195, Australia (CSIRO)	[24] Ziehn et al., 2020 [25] Ziehn et al., 2019a [26] Ziehn et al., 2019b	1
3	AWI-CM-1-1-MR	Alfred Wegener Institute, Helmholtz Centre for Polar and Marine Research, Am Handelshafen 12, 27570 Bremerhaven, Germany (AWI)	[27] Semmler et al., 2020 [28] Semmler et al., 2018 [29] Semmler et al., 2019	1
4	BCC-CSM2-MR	Beijing Climate Center, Beijing 100081, China (BCC)	[30] Wu et al., 2019 [31] Wu et al., 2018 [32] Xin et al., 2019	1
5	CAS-ESM2-0	Chinese Academy of Sciences, Beijing 100029, China (CAS)	[33] Dong et al., 2021 [34] Chai et al., 2020	1
6	CanESM5	Canadian Centre for Climate Modelling and Analysis, Environment and Climate Change Canada, Victoria, BC V8P 5C2, Canada (CCCma)	[35] Swart et al., 2019a [37] Swart et al., 2019b [38] Swart et al., 2019c	10
7	CESM2-WACCM	National Center for Atmospheric Research, Climate and Global Dynamics Laboratory, 1850 Table Mesa Drive, Boulder, CO 80305, USA (NCAR)	[39] Danabasoglu et al., 2020 [40] Danabasoglu, 2019a [41] Danabasoglu, 2019b	3
8	CMCC-CM2-SR5	Fondazione Centro Euro-Mediterraneo sui Cambiamenti Climatici, Lecce 73100, Italy (CMCC)	[42] Cherchi et al., 2019 [43] Lovato & Peano, 2020a [44] Lovato et al., 2021a [45] Lovato & Peano, 2020b [46] Lovato et al., 2021b	1
9	CMCC-ESM2			1
10	E3SM-1-1	Lawrence Livermore National Laboratory, Department of Energy (USA), Energy Exascale Earth System Model (E3SM) Project	[47] Golaz et al., 2019 [48] Bader et al., 2019 [49] Bader et al., 2020	1
11	EC-Earth3-CC	EC-Earth consortium, Rossby Center, Swedish Meteorological and Hydrological Institute/SMHI (Sweden)	[50] Doscher et al., 2021 [51] EC-Earth Consortium, 2020a [52] EC-Earth Consortium, 2019a [53] EC-Earth Consortium, 2020b [54] EC-Earth Consortium, 2019b	1
12	EC-Earth3			1
13	EC-Earth3-Veg-LR			1
14	EC-Earth3-Veg			1
15	FGOALS-f3-L	Chinese Academy of Sciences, Beijing 100029, China (CAS)	[55] He et al., 2019 [56] Yu, 2019a [57] Yu, 2019b	1
16	FGOALS-g3		[58] Pu et al., 2020 [59] Li, 2019a [60] Li, 2019b	1
17	FIO-ESM-2-0	First Institute of Oceanography, Ministry of Natural Resources, Qingdao 266061, China; Qingdao National Laboratory for Marine Science and Technology, Qingdao 266237, China (FIO-QLNM)	[61] Bao et al., 2020 [62] Song et al., 2019a [63] Song et al., 2019b	1
18	GFDL-CM4	National Oceanic and Atmospheric Administration, Geophysical Fluid Dynamics Laboratory, Princeton, NJ 08540, USA (NOAA-GFDL)	[64] Held et al., 2019 [65] Guo et al., 2018a [66] Guo et al., 2018b	1
19	GFDL-ESM4		[67] Dunne et al., 2020 [68] Krasting et al., 2018 [69] John et al., 2018	1
20	IITM-ESM	Centre for Climate Change Research, Indian Institute of Tropical Meteorology Pune, Maharashtra 411 008, India (CCCR-IITM)	[70] Krishnan et al., 2021 [71] Raghavan and Panickal, 2019 [72] Panickal and Narayanasetti, 2020	1
21	INM-CM4-8	Institute for Numerical Mathematics, Russian Academy of Science, Moscow 119991, Russia (INM)	[73] Volodin et al., 2018 [74] Volodin et al., 2019a [75] Volodin et al., 2019b	1
22	INM-CM5-0		[76] Volodin and Gritsun, 2018 [77] Volodin et al., 2019a [78] Volodin et al., 2019b	1
23	IPSL-CM6A-LR	Institut Pierre Simon Laplace, Paris 75252, France (IPSL)	[79] Boucher et al., 2020 [80] Boucher et al., 2018 [81] Boucher et al., 2019	3
24	KACE-1-0-G	National Institute of Meteorological Sciences/Korea Meteorological Administration, Climate Research Division, Seoho-bukro 33, Seogwipo-si, Jejudo 63568, Republic of Korea (NIMS-KMA)	[82] Lee et al., 2020 [83] Byun et al., 2019a [84] Byun et al., 2019b	1
25	MIROC6	Japan Agency for Marine-Earth Science and Technology (Japan)	[85] Tatebe et al., 2019 [86] Tatebe et al., 2018 [87] Shiogama et al., 2019	3
26	MPI-ESM1-2-HR	Max Planck Institute for Meteorology (Germany) (MPI)	[88] Muller et al., 2018 [89] Jungclaus et al., 2019 [90] Schupfner et al., 2019	1
27	MPI-ESM1-2-LR		[91] Mauritsen et al., 2019 [92] Wieners et al., 2019a [93] Wieners et al., 2019b	1
28	MRI-ESM2-0	Meteorological Research Institute, Japan, (MRI)	[94] Yukimoto et al., 2019a [95] Yukimoto et al., 2019b [96] Yukimoto et al., 2019c	1
29	NESM3	Nanjing University of Information Science and Technology (China)	[97] Cao et al., 2018 [98] Cao and Wang, 2019 [99] Cao, 2019	1
30	NorESM2-LM	Climate Modeling Consortium consisting of Center for International Climate and Environmental Research (Norway) (NCC)	[100] Seland et al., 2020 [101] Seland et al.,2019a [102] Bentsen et al., 2019a [103] Seland et al., 2019b [104] Bentsen et al., 2019b	1
31	NorESM2-MM			1
32	TaiESM1	Research Center for Environmental Changes, Academia Sinica Taiwan (AS-RCEC)	[105] Lee et al., 2020a [106] Lee et al., 2020b [107] Lee et al., 2020c	1

Figure A-2: CMIP6 Models used in Chapter 3

[1] Bi, D., Dix, M., Marsland, S. J., O'Farrell, S., Rashid, H. A., Uotila, P., Hirst, A. C., Kowalczyk, E., Golebiewski, M., Sullivan, A., Yan, H., Hannah, N., Franklin, C., Sun, Z., Vohralik, P., Watterson, I., Zhou, X., Fiedler, R., Collier, M., Ma, Y., Noonan, J., Stevens, L., Uhe, P., Zhu, H., Griffies, S. M., Hill, R., Harris, C., and Puri, K. (2013) The ACCESS coupled model: description, control climate and evaluation, Austr. Meteorol. Oceanogr. J. 63: 41–64.

[2] Xin, X., Wu, T., and Zhang, J. (2013) Introduction of CMIP5 experiments carried out with the climate system models of Beijing climate center, Adv. Clim. Change Res. 4: 41–49.

[3] Ji, D., Wang, L., Feng, J., Wu, Q., Cheng, H., Zhang, Q., Yang, J., Dong, W., Dai, Y., Gong, D., Zhang, R., Wang, X., Liu, J., Moore, J., Chen, D., and Zhou, M. (2014) Description and basic evaluation of Beijing Normal University earth system model (BNU-ESM) version 1, Geosci. Model Dev. 7(5): 2039–2064.

[4] Arora, V. K., Scinocca, J. F., Boer, G. J., Christian, J. R., Denman, K. L., Flato, G. M., Kharin, V. V., Lee, W. G.,and Merryfield, W. J. (2011) Carbon emission limits required to satisfy future representative concentration pathways of greenhouse gases, Geophys. Res. Lett. 38: L05805.

[5] Gent, P. R., Danabasoglu, G., Donner, L. J., Holland, M. M., Hunke, E. C., Jayne, S. R., Lawrence, D. M., Neale, R. B., Rasch, P. J., Vertenstein, M., Worley, P. H., Yang, Z., and Zhang, M. (2011) The Community Climate System Model Version 4, J. Clim. 24: 4973–4991.

[6] Neale, R. B., Richter, J. H., Conley, A. J., Park, S., Lauritzen, P. H., Gettelman, A., and Williamson, D. L. (2010) Description of the NCAR Community Atmosphere Model (CAM5.0), NCAR Tech. Rep. NCAR/TN-486+STR, 268 pp.

[7] Scoccimarro, E., Gualdi, S., Bellucci, A., Sanna, A., Giuseppe Fogli, P., Manzini, E., Vichi, M., Oddo, P., and Navarra, A. (2011) Effects of tropical cyclones on ocean heat transport in a high-resolution coupled general circulation model, J. Clim. 24(16): 4368–4384.

[8] Voldoire, A., Sanchez-Gomez, E., Salas y Mélia, D., Decharme, B., Cassou, C., Sénési, S., Valcke, S., Beau, I., Alias, A., Chevallier, M., Déqué, M., Deshayes, J., Douville, H., Fernandez, E., Madec, G., Maisonnave, E., Moine, M., Planton, S., Saint-Martin, D., Szopa, S., Tyteca, S., Alkama, R., Belamari, S., Braun, A., Coquart, L., and Chauvin, F. (2013) The CNRM-CM5.1 global climate model: description and basic evaluation, Clim. Dyn. 40: 2091–2121.

[9] Rotstayn, L. D., Collier, M. A., Dix, M. R., Feng, Y., Gordon, H., O'Farrell, S., Smith, I., and Syktus, J. (2010) Improved simulation of Australian climate and ENSO-related rainfall variability in a global climate model with an interactive aerosol treatment, Int. J. Climatol. 30: 1067–1088.

[10] Li, L., Lin, P., Yu, Y., Wang, B., Zhou, T., Liu, L., Liu, J., Bao, Q., Xu, S., Huang, W., Xia, K., Pu, Y., Dong, L., Shen, S., Liu, Y., Hu, N., Liu, M., Sun, W., Shi, X., Zheng, W., Wu, B., Song, M., Liu, H., Zhang, X., Wu, G., Xue, W., Huang, X., Yang, G., Song, Z., and Qiao, F. (2013) The flexible global ocean-atmosphere-land system model, grid-point version 2: FGOALS-g2, Adv. Atmos. Sci. 30(3): 543–560.

[11] Qiao, F., Z.Song, Y.Bao, Y.Song, Q.Shu, C.Huang and W.Zhao (2013), Development and evaluation of an Earth System Model with surface gravity waves, J. Geophys. Res. Oceans, 118, 4514–4524, doi:10.1002/jgrc.20327.

[12] Dunne, J., John, J., Adcroft, A., Griffies, S., Hallberg, R., Shevliakova, E., Stouffer, R., Cooke, W., Dunne, K., Harrison, M., Krasting, J., Malyshev, S., Milly, P., Phillips, P., Sentman, L., Samuels, B., Spelman, M., Winton, M., Wittenberg, A., and Zadeh, N. (2012) GFDL's ESM2 global coupled climate–carbon earth system models. Part I: physical formulation and baseline simulation characteristics, J. Clim. 25(19): 6646–6665.

[13] Miller, R., Schmidt, G., Nazarenko, L., Tausnev, N., Bauer, S., DelGenio, A., Kelley, M., Lo, K., Ruedy, R., Shindell, D., Aleinov, I., Bauer, M., Bleck, R., Canuto, V., Chen, Y., Cheng, Y., Clune, T., Faluvegi, G., Hansen, J., Healy, R., Kiang, N., Koch, D., Lacis, A., LeGrande, A., Lerner, J., Menon, S., Oinas, V., Pérez Garciía-Pando, C., Perlwitz, J., Puma, M., Rind, D., Romanou, A., Russell, G., Sato, M., Sun, S., Tsigaridis, K., Unger, N., Voulgarakis, A., Yao, M., and Zhang, J. (2014) CMIP5 historical simulations (1850-2012) with GISS Model E2, J. Adv. Model. Earth Syst. 6(2): 441–478.

[14] Collins, W. J., Bellouin, N., Doutriaux-Boucher, M., Gedney, N., Halloran, P., Hinton, T., Hughes, J., Jones, C. D., Joshi, M., Liddicoat, S., Martin, G., O'Connor, F., Rae, J., Senior, C., Sitch, S., Totterdell, I., Wiltshire, A., and Woodward, S. (2011) Development and evaluation of an earth-system model – HadGEM2, Geosci. Model Dev. 4: 1051–1075.

[15] Volodin, E. M., Diansky, N. A., and Gusev, A. V. (2010) Simulating present-day climate with the INMCM4.0 coupled model of the atmospheric and oceanic general circulations, Izvestiya Atmos. Ocean. Phys. 46: 414–431.

[16] Marti, O., Braconnot, P., Dufresne, J. L., Bellier, J., Benshila, R., Bony, S., Brockmann, P., Cadule, P., Caubel, A., Codron, F., de Noblet, N., Denvil, S., Fairhead, L., Fichefet, T., Foujols, M. A., Friedlingstein, P., Goosse, H., Grandpeix, J. Y., Guilyardi, E., Hourdin, F., Krinner, G., Lévy, C., Madec, G., Mignot, J., Musat, I., Swingedouw, D. J., and Talandier, C. (2010) Key features of the IPSL ocean atmosphere model and its sensitivity to atmospheric resolution. Clim. Dyn. 34: 1–26.

[17] Watanabe, M., Suzuki, T., O'ishi, R., Komuro, Y., Watanabe, S., Emori, S., Takemura, T., Chikira, M., Ogura, T., Sekiguchi, M., Takata, K., Yamazaki, D., Yokohata, T., Nozawa, T., Hasumi, H., Tatebe, H., and Kimoto, M. (2010) Improved climate simulation by MIROC5: mean states, variability, and climate sensitivity, J. Clim. 23: 6312–6335.

[18] Zanchettin, D., Rubino, A., Matei, D., Bothe, O., and Jungclaus, J. (2013) Multidecadal-to centennial SST variability in the MPI-ESM simulation ensemble for the last millennium, Clim. Dyn. 40: 1301–1318.

[19] Yukimoto, S., Adachi, Y., Hosaka, M., Sakami, T., Yoshimura, H., Hirabara, M., Tanaka,

T., Shindo, E., Tsujino, H., Deushi, M., Mizuta, R., Yabu, S., Obata, A., Nakano, H., Koshiro, T., and Ose, T. A. (2012) A new global climate model of the meteorological research institute: MRI–CGCM3 – model description and basic performance, J. Meteorol. Soc. Jpn. 90A: 23–64.

[20] Bentsen, M., Bethke, I., Debernard, J., Iversen, T., Kirkevag, A., Seland, O., Drange, H., Roelandt, C., Seierstad, I., Hoose, C., and Kristjaánsson, J. (2012), The Norwegian earth system model, NorESM1-M – Part 1: Description and basic evaluation, Geosci. Model Dev. Discus. 5(3): 2843–2931.

[21] Bi Daohua, Dix Martin, Marsland Simon, O'Farrell Siobhan, Sullivan Arnold, Bodman Roger, Law Rachel, Harman Ian, Srbinovsky Jhan, Rashid Harun A., Dobrohotoff Peter, Mackallah Chloe, Yan Hailin, Hirst Anthony, Savita Abhishek, Dias Fabio Boeira, Woodhouse Matthew, Fiedler Russell, Heerdegen Aidan (2020) Configuration and spin-up of ACCESS-CM2, the new generation Australian Community Climate and Earth System Simulator Coupled Model. Journal of Southern Hemisphere Earth Systems Science 70, 225-251. https://doi.org/10.1071/ES19040

[22] Dix, Martin; Bi, Doahua; Dobrohotoff, Peter; Fiedler, Russell; Harman, Ian; Law, Rachel; Mackallah, Chloe; Marsland, Simon; O'Farrell, Siobhan; Rashid, Harun; Srbinovsky, Jhan; Sullivan, Arnold; Trenham, Claire; Vohralik, Peter; Watterson, Ian; Williams, Gareth; Woodhouse, Matthew; Bodman, Roger; Dias, Fabio Boeira; Domingues, Catia; Hannah, Nicholas; Heerdegen, Aidan; Savita, Abhishek; Wales, Scott; Allen, Chris; Druken, Kelsey; Evans, Ben; Richards, Clare; Ridzwan, Syazwan Mohamed; Roberts, Dale; Smillie, Jon; Snow, Kate; Ward, Marshall; Yang, Rui (2019). CSIRO-ARCCSS ACCESS-CM2 model output prepared for CMIP6 CMIP historical. Earth System Grid Federation. doi:https://doi.org/10.22033/ESGF/CMIP6.4271

[23] Dix, Martin; Bi, Doahua; Dobrohotoff, Peter; Fiedler, Russell; Harman, Ian; Law, Rachel; Mackallah, Chloe; Marsland, Simon; O'Farrell, Siobhan; Rashid, Harun; Srbinovsky, Jhan; Sullivan, Arnold; Trenham, Claire; Vohralik, Peter; Watterson, Ian; Williams, Gareth; Woodhouse, Matthew; Bodman, Roger; Dias, Fabio Boeira; Domingues, Catia; Hannah, Nicholas; Heerdegen, Aidan; Savita, Abhishek; Wales, Scott; Allen, Chris; Druken, Kelsey; Evans, Ben; Richards, Clare; Ridzwan, Syazwan Mohamed; Roberts, Dale; Smillie, Jon; Snow, Kate; Ward, Marshall; Yang, Rui (2019). CSIRO-ARCCSS ACCESS-CM2 model output prepared for CMIP6 ScenarioMIP ssp585. Earth System Grid Federation. doi:https://doi.org/10.22033/ESGF/CMIP6.4332

[24] Ziehn Tilo, Chamberlain Matthew A., Law Rachel M., Lenton Andrew, Bodman Roger W., Dix Martin, Stevens Lauren, Wang Ying-Ping, Srbinovsky Jhan (2020) The Australian Earth System Model: ACCESS-ESM1.5. Journal of Southern Hemisphere Earth Systems Science 70, 193-214. https://doi.org/10.1071/ES19035

[25] Ziehn, Tilo; Chamberlain, Matthew; Lenton, Andrew; Law, Rachel; Bodman, Roger; Dix, Martin; Wang, Yingping; Dobrohotoff, Peter; Srbinovsky, Jhan; Stevens, Lauren; Vohralik, Peter; Mackallah, Chloe; Sullivan, Arnold; O'Farrell, Siobhan; Druken, Kelsey (2019). CSIRO ACCESS-

ESM1.5 model output prepared for CMIP6 CMIP historical. Earth System Grid Federation. doi: https://doi.org/10.22033/ESGF/CMIP6.4272.

[26] Ziehn, Tilo; Chamberlain, Matthew; Lenton, Andrew; Law, Rachel; Bodman, Roger; Dix, Martin; Wang, Yingping; Dobrohotoff, Peter; Srbinovsky, Jhan; Stevens, Lauren; Vohralik, Peter; Mackallah, Chloe; Sullivan, Arnold; O'Farrell, Siobhan; Druken, Kelsey (2019). CSIRO ACCESS-ESM1.5 model output prepared for CMIP6 ScenarioMIP ssp585. Earth System Grid Federation. oi:https://doi.org/10.22033/ESGF/CMIP6.4333

[27] Semmler, T., Danilov, S., Gierz, P., Goessling, H. F., Hegewald, J., Hinrichs, C., et al. (2020). Simulations for CMIP6 with the AWI climate model AWI-CM-1-1. Journal of Advances in Modeling Earth Systems, 12, e2019MS002009. https://doi.org/10.1029/2019MS002009

[28] Semmler, Tido; Danilov, Sergey; Rackow, Thomas; Sidorenko, Dmitry; Barbi, Dirk; Hegewald, Jan; Sein, Dmitri; Wang, Qiang; Jung, Thomas (2018). AWI AWI-CM1.1MR model output prepared for CMIP6 CMIP historical. Earth System Grid Federation. doi:https://doi.org/10.22033/ESGF/CMIP6.2686

[29] Semmler, Tido; Danilov, Sergey; Rackow, Thomas; Sidorenko, Dmitry; Barbi, Dirk; Hegewald, Jan; Pradhan, Himansu Kesari; Sein, Dmitri; Wang, Qiang; Jung, Thomas (2019). AWI AWI-CM1.1MR model output prepared for CMIP6 ScenarioMIP ssp585. Earth System Grid Federation. doi:https://doi.org/10.22033/ESGF/CMIP6.2817.

[30] Wu, T., Lu, Y., Fang, Y., Xin, X., Li, L., Li, W., Jie, W., Zhang, J., Liu, Y., Zhang, L. and Zhang, F., 2019. The Beijing Climate Center climate system model (BCC-CSM): The main progress from CMIP5 to CMIP6. Geoscientific Model Development, 12(4), pp.1573-1600.

[31] Wu, Tongwen; Chu, Min; Dong, Min; Fang, Yongjie; Jie, Weihua; Li, Jianglong; Li, Weiping; Liu, Qianxia; Shi, Xueli; Xin, Xiaoge; Yan, Jinghui; Zhang, Fang; Zhang, Jie; Zhang, Li; Zhang, Yanwu (2018). BCC BCC-CSM2MR model output prepared for CMIP6 CMIP historical. Earth System Grid Federation. doi:https://doi.org/10.22033/ESGF/CMIP6.2948

[32] Xin, Xiaoge; Wu, Tongwen; Shi, Xueli; Zhang, Fang; Li, Jianglong; Chu, Min; Liu, Qianxia; Yan, Jinghui; Ma, Qiang; Wei, Min (2019). BCC BCC-CSM2MR model output prepared for CMIP6 ScenarioMIP ssp585. Earth System Grid Federation. doi:https://doi.org/10.22033/ESGF/CMIP6.3050

[33] Dong, X., Jin, J., Liu, H., Zhang, H., Zhang, M., Lin, P., Zeng, Q., Zhou, G., Yu, Y., Song, M. and Lin, Z., 2021. CAS-ESM2. 0 Model Datasets for the CMIP6 Ocean Model Intercomparison Project Phase 1 (OMIP1). Advances in Atmospheric Sciences, 38(2), pp.307-316.

[34] Chai, Zhaoyang (2020). CAS CAS-ESM1.0 model output prepared for CMIP6 CMIP historical. Earth System Grid Federation. doi:https://doi.org/10.22033/ESGF/CMIP6.3353

[35] Swart, N. C., Cole, J. N. S., Kharin, V. V., Lazare, M., Scinocca, J. F., Gillett, N. P., Anstey, J., Arora, V., Christian, J. R., Hanna, S., Jiao, Y., Lee, W. G., Majaess, F., Saenko, O. A., Seiler,

C., Seinen, C., Shao, A., Sigmond, M., Solheim, L., von Salzen, K., Yang, D., & Winter, B. (2019a). The Canadian Earth System Model version 5 (CanESM5.0.3). Geoscientific Model Development, 12, 4823–4873. https://doi.org/10.5194/gmd-12-4823-2019

[37] Swart, Neil Cameron; Cole, Jason N.S.; Kharin, Viatcheslav V.; Lazare, Mike; Scinocca, John F.; Gillett, Nathan P.; Anstey, James; Arora, Vivek; Christian, James R.; Jiao, Yanjun; Lee, Warren G.; Majaess, Fouad; Saenko, Oleg A.; Seiler, Christian; Seinen, Clint; Shao, Andrew; Solheim, Larry; von Salzen, Knut; Yang, Duo; Winter, Barbara; Sigmond, Michael (2019). CCCma CanESM5 model output prepared for CMIP6 CMIP historical. Earth System Grid Federation. doi:https://doi.org/10.22033/ESGF/CMIP6.3610.

[38] Swart, Neil Cameron; Cole, Jason N.S.; Kharin, Viatcheslav V.; Lazare, Mike; Scinocca, John F.; Gillett, Nathan P.; Anstey, James; Arora, Vivek; Christian, James R.; Jiao, Yanjun; Lee, Warren G.; Majaess, Fouad; Saenko, Oleg A.; Seiler, Christian; Seinen, Clint; Shao, Andrew; Solheim, Larry; von Salzen, Knut; Yang, Duo; Winter, Barbara; Sigmond, Michael (2019). CCCma CanESM5 model output prepared for CMIP6 ScenarioMIP ssp585. Earth System Grid Federation. doi:https://doi.org/10.22033/ESGF/CMIP6.3696 .

[39] Danabasoglu, G., Lamarque, J.F., Bacmeister, J., Bailey, D.A., DuVivier, A.K., Edwards, J., Emmons, L.K., Fasullo, J., Garcia, R., Gettelman, A. and Hannay, C., 2020. The community earth system model version 2 (CESM2). Journal of Advances in Modeling Earth Systems, 12(2).

[40] Danabasoglu, Gokhan (2019). NCAR CESM2-WACCM model output prepared for CMIP6 CMIP historical. Earth System Grid Federation. doi:https://doi.org/10.22033/ESGF/CMIP6.10071

[41] Danabasoglu, Gokhan (2019). NCAR CESM2-WACCM model output prepared for CMIP6 ScenarioMIP ssp585. Earth System Grid Federation. doi:https://doi.org/10.22033/ESGF/CMIP6.10115

[42] Cherchi, A., Fogli, P.G., Lovato, T., Peano, D., Iovino, D., Gualdi, S., Masina, S., Scoccimarro, E., Materia, S., Bellucci, A. and Navarra, A., 2019. Global mean climate and main patterns of variability in the CMCC-CM2 coupled model. Journal of Advances in Modeling Earth Systems, 11(1), pp.185-209.

[43] Lovato, Tomas; Peano, Daniele (2020). CMCC CMCC-CM2-SR5 model output prepared for CMIP6 CMIP historical. Earth System Grid Federation. doi:https://doi.org/10.22033/ESGF/CMIP6.3825.

[44] Lovato, Tomas; Peano, Daniele; Butenschön, Momme (2021). CMCC CMCC-ESM2 model output prepared for CMIP6 CMIP historical. Earth System Grid Federation. doi:https://doi.org/10.22033/ESGF/CMIP6.13195

[45] Lovato, Tomas; Peano, Daniele (2020). CMCC CMCC-CM2-SR5 model output prepared for CMIP6 ScenarioMIP ssp585. Earth System Grid Federation. doi:https://doi.org/10.22033/ESGF/CMIP6.3896.

[46] Lovato, Tomas; Peano, Daniele; Butenschön, Momme (2021). CMCC CMCC-ESM2 model output prepared for CMIP6 ScenarioMIP ssp585. Earth System Grid Federation. doi:https://doi.org/10.22033/ESGF/CMIP6.13259

[47] Golaz, J.C., Caldwell, P.M., Van Roekel, L.P., Petersen, M.R., Tang, Q., Wolfe, J.D., Abeshu, G., Anantharaj, V., Asay-Davis, X.S., Bader, D.C. and Baldwin, S.A., 2019. The DOE E3SM coupled model version 1: Overview and evaluation at standard resolution. Journal of Advances in Modeling Earth Systems, 11(7), pp.2089-2129.

[48] Bader, David C.; Leung, Ruby; Taylor, Mark; McCoy, Renata B. (2019). E3SM-Project E3SM1.1 model output prepared for CMIP6 CMIP historical. Earth System Grid Federation. doi:https://doi.org/10.22033/ESGF/CMIP6.11485

[49] Bader, David C.; Leung, Ruby; Taylor, Mark; McCoy, Renata B. (2020). E3SM-Project E3SM1.1 model output prepared for CMIP6 ScenarioMIP ssp585. Earth System Grid Federation. doi:https://doi.org/10.22033/ESGF/CMIP6.15179

[50] Döscher, R., Acosta, M., Alessandri, A., Anthoni, P., Arneth, A., Arsouze, T., Bergmann, T., Bernadello, R., Bousetta, S., Caron, L.P. and Carver, G., 2021. The EC-earth3 Earth system model for the climate model intercomparison project 6. Geoscientific Model Development Discussions, pp.1-90.

[51] EC-Earth Consortium (EC-Earth) (2020). EC-Earth-Consortium EC-Earth-3-CC model output prepared for CMIP6 C4MIP. Earth System Grid Federation. doi:https://doi.org/10.22033/ESGF/CMIP6.650 .

[52] EC-Earth Consortium (EC-Earth) (2019). EC-Earth-Consortium EC-Earth3 model output prepared for CMIP6 CMIP. Earth System Grid Federation. doi:https://doi.org/10.22033/ESGF/CMIP6.181 .

[53] EC-Earth Consortium (EC-Earth) (2020). EC-Earth-Consortium EC-Earth3-Veg-LR model output prepared for CMIP6 CMIP. Earth System Grid Federation. doi:https://doi.org/10.22033/ESGF/CMIP6.643 .

[54] EC-Earth Consortium (EC-Earth) (2019). EC-Earth-Consortium EC-Earth3-Veg model output prepared for CMIP6 CMIP. Earth System Grid Federation. doi:https://doi.org/10.22033/ESGF/CMIP6.642 .

[55] He, B., Bao, Q., Wang, X., Zhou, L., Wu, X., Liu, Y., Wu, G., Chen, K., He, S., Hu, W. and Li, J., 2019. CAS FGOALS-f3-L model datasets for CMIP6 historical atmospheric model Intercomparison project simulation. Advances in Atmospheric Sciences, 36(8), pp.771-778.

[56] Yu, Yongqiang (2019). CAS FGOALS-f3-L model output prepared for CMIP6 CMIP historical. Earth System Grid Federation. doi:https://doi.org/10.22033/ESGF/CMIP6.3355

[57] Yu, Yongqiang (2019). CAS FGOALS-f3-L model output prepared for CMIP6 ScenarioMIP ssp585. Earth System Grid Federation. doi:https://doi.org/10.22033/ESGF/CMIP6.3502.

[58] Pu, Y., Liu, H., Yan, R., Yang, H., Xia, K., Li, Y., Dong, L., Li, L., Wang, H., Nie, Y. and Song, M., 2020. CAS FGOALS-g3 Model Datasets for the CMIP6 Scenario Model Intercomparison Project (ScenarioMIP). Advances in Atmospheric Sciences, 37(10), pp.1081-1092.

[59] Li, Lijuan (2019). CAS FGOALS-g3 model output prepared for CMIP6 CMIP historical. Earth System Grid Federation. doi:https://doi.org/10.22033/ESGF/CMIP6.3356

[60] Li, Lijuan (2019). CAS FGOALS-g3 model output prepared for CMIP6 ScenarioMIP ssp585. Earth System Grid Federation. doi:https://doi.org/10.22033/ESGF/CMIP6.3503 .

[61] Bao, Y., Song, Z. and Qiao, F., 2020. FIO-ESM version 2.0: Model description and evaluation. Journal of Geophysical Research: Oceans, 125(6), p.e2019JC016036.

[62] Song, Zhenya; Qiao, Fangli; Bao, Ying; Shu, Qi; Song, Yajuan; Yang, Xiaodan (2019). FIO-QLNM FIO-ESM2.0 model output prepared for CMIP6 CMIP historical. Earth System Grid Federation. doi:https://doi.org/10.22033/ESGF/CMIP6.9199

[63] Song, Zhenya; Qiao, Fangli; Bao, Ying; Shu, Qi; Song, Yajuan; Yang, Xiaodan (2019). FIO-QLNM FIO-ESM2.0 model output prepared for CMIP6 ScenarioMIP ssp585. Earth System Grid Federation. doi:https://doi.org/10.22033/ESGF/CMIP6.9214

[64] Held, I.M., Guo, H., Adcroft, A., Dunne, J.P., Horowitz, L.W., Krasting, J., Shevliakova, E., Winton, M., Zhao, M., Bushuk, M. and Wittenberg, A.T., 2019. Structure and performance of GFDL's CM4. 0 climate model. Journal of Advances in Modeling Earth Systems, 11(11), pp.3691-3727.

[65] Guo, Huan; John, Jasmin G; Blanton, Chris; McHugh, Colleen; Nikonov, Serguei; Radhakrishnan, Aparna; Rand, Kristopher; Zadeh, Niki T.; Balaji, V; Durachta, Jeff; Dupuis, Christopher; Menzel, Raymond; Robinson, Thomas; Underwood, Seth; Vahlenkamp, Hans; Bushuk, Mitchell; Dunne, Krista A.; Dussin, Raphael; Gauthier, Paul PG; Ginoux, Paul; Griffies, Stephen M.; Hallberg, Robert; Harrison, Matthew; Hurlin, William; Lin, Pu; Malyshev, Sergey; Naik, Vaishali; Paulot, Fabien; Paynter, David J; Ploshay, Jeffrey; Reichl, Brandon G; Schwarzkopf, Daniel M; Seman, Charles J; Shao, Andrew; Silvers, Levi; Wyman, Bruce; Yan, Xiaoqin; Zeng, Yujin; Adcroft, Alistair; Dunne, John P.; Held, Isaac M; Krasting, John P.; Horowitz, Larry W.; Milly, P.C.D; Shevliakova, Elena; Winton, Michael; Zhao, Ming; Zhang, Rong (2018). NOAA-GFDL GFDL-CM4 model output historical. Earth System Grid Federation. doi:https://doi.org/10.22033/ESGF/CMIP6.8594

[66] Guo, Huan; John, Jasmin G; Blanton, Chris; McHugh, Colleen; Nikonov, Serguei; Radhakrishnan, Aparna; Rand, Kristopher; Zadeh, Niki T.; Balaji, V; Durachta, Jeff; Dupuis, Christopher; Menzel, Raymond; Robinson, Thomas; Underwood, Seth; Vahlenkamp, Hans; Dunne, Krista A.; Gauthier, Paul PG; Ginoux, Paul; Griffies, Stephen M.; Hallberg, Robert; Harrison, Matthew; Hurlin, William; Lin, Pu; Malyshev, Sergey; Naik, Vaishali; Paulot, Fabien; Paynter, David J; Ploshay, Jeffrey; Schwarzkopf, Daniel M; Seman, Charles J; Shao, Andrew; Silvers, Levi; Wyman, Bruce; Yan, Xiaoqin; Zeng, Yujin; Adcroft, Alistair; Dunne, John P.; Held, Isaac M; Krasting, John

P.; Horowitz, Larry W.; Milly, Chris; Shevliakova, Elena; Winton, Michael; Zhao, Ming; Zhang, Rong (2018). NOAA-GFDL GFDL-CM4 model output prepared for CMIP6 ScenarioMIP ssp585. Earth System Grid Federation. doi:https://doi.org/10.22033/ESGF/CMIP6.9268 .

[67] Dunne, J.P., Horowitz, L.W., Adcroft, A.J., Ginoux, P., Held, I.M., John, J.G., Krasting, J.P., Malyshev, S., Naik, V., Paulot, F. and Shevliakova, E., 2020. The GFDL Earth System Model version 4.1 (GFDL-ESM 4.1): Overall coupled model description and simulation characteristics. Journal of Advances in Modeling Earth Systems, 12(11), p.e2019MS002015.

[68] Krasting, John P.; John, Jasmin G; Blanton, Chris; McHugh, Colleen; Nikonov, Serguei; Radhakrishnan, Aparna; Rand, Kristopher; Zadeh, Niki T.; Balaji, V; Durachta, Jeff; Dupuis, Christopher; Menzel, Raymond; Robinson, Thomas; Underwood, Seth; Vahlenkamp, Hans; Dunne, Krista A.; Gauthier, Paul PG; Ginoux, Paul; Griffies, Stephen M.; Hallberg, Robert; Harrison, Matthew; Hurlin, William; Malyshev, Sergey; Naik, Vaishali; Paulot, Fabien; Paynter, David J; Ploshay, Jeffrey; Reichl, Brandon G; Schwarzkopf, Daniel M; Seman, Charles J; Silvers, Levi; Wyman, Bruce; Zeng, Yujin; Adcroft, Alistair; Dunne, John P.; Dussin, Raphael; Guo, Huan; He, Jian; Held, Isaac M; Horowitz, Larry W.; Lin, Pu; Milly, P.C.D; Shevliakova, Elena; Stock, Charles; Winton, Michael; Wittenberg, Andrew T.; Xie, Yuanyu; Zhao, Ming (2018). NOAA-GFDL GFDL-ESM4 model output prepared for CMIP6 CMIP historical. Earth System Grid Federation. doi:https://doi.org/10.22033/ESGF/CMIP6.8597.

[69] John, Jasmin G; Blanton, Chris; McHugh, Colleen; Radhakrishnan, Aparna; Rand, Kristopher; Vahlenkamp, Hans; Wilson, Chandin; Zadeh, Niki T.; Dunne, John P.; Dussin, Raphael; Horowitz, Larry W.; Krasting, John P.; Lin, Pu; Malyshev, Sergey; Naik, Vaishali; Ploshay, Jeffrey; Shevliakova, Elena; Silvers, Levi; Stock, Charles; Winton, Michael; Zeng, Yujin (2018). NOAA-GFDL GFDL-ESM4 model output prepared for CMIP6 ScenarioMIP ssp585. Earth System Grid Federation. doi:https://doi.org/10.22033/ESGF/CMIP6.8706 .

[70] Krishnan, R., Swapna, P., Choudhury, A.D., Narayansetti, S., Prajeesh, A.G., Singh, M., Modi, A., Mathew, R., Vellore, R., Jyoti, J. and Sabin, T.P., 2021. The IITM Earth System Model (IITM ESM). arXiv preprint arXiv:2101.03410.

[71] Raghavan, Krishnan; Panickal, Swapna (2019). CCCR-IITM IITM-ESM model output prepared for CMIP6 CMIP historical. Earth System Grid Federation. doi:https://doi.org/10.22033/ESGF/CMIP6.3708 .

[72] Panickal, Swapna; Narayanasetti, Sandeep (2020). CCCR-IITM IITM-ESM model output prepared for CMIP6 ScenarioMIP ssp585. Earth System Grid Federation. doi:https://doi.org/10.22033/ESGF/CMIP6.14753

[73] Volodin, E.M., Mortikov, E.V., Kostrykin, S.V., Galin, V.Y., Lykossov, V.N., Gritsun, A.S., Diansky, N.A., Gusev, A.V., Iakovlev, N.G., Shestakova, A.A. and Emelina, S.V., 2018. Simulation of the modern climate using the INM-CM48 climate model. Russian Journal of Numerical Analysis

and Mathematical Modelling, 33(6), pp.367-374.

[74] Volodin, Evgeny; Mortikov, Evgeny; Gritsun, Andrey; Lykossov, Vasily; Galin, Vener; Diansky, Nikolay; Gusev, Anatoly; Kostrykin, Sergey; Iakovlev, Nikolay; Shestakova, Anna; Emelina, Svetlana (2019). INM INM-CM4-8 model output prepared for CMIP6 CMIP historical. Earth System Grid Federation. doi:https://doi.org/10.22033/ESGF/CMIP6.5069.

[75] Volodin, Evgeny; Mortikov, Evgeny; Gritsun, Andrey; Lykossov, Vasily; Galin, Vener; Diansky, Nikolay; Gusev, Anatoly; Kostrykin, Sergey; Iakovlev, Nikolay; Shestakova, Anna; Emelina, Svetlana (2019). INM INM-CM4-8 model output prepared for CMIP6 ScenarioMIP ssp585. Earth System Grid Federation. doi:https://doi.org/10.22033/ESGF/CMIP6.12337

[76] Volodin, E. and Gritsun, A., 2018. Simulation of observed climate changes in 1850–2014 with climate model INM-CM5. Earth System Dynamics, 9(4), pp.1235-1242.

[77] Volodin, Evgeny; Mortikov, Evgeny; Gritsun, Andrey; Lykossov, Vasily; Galin, Vener; Diansky, Nikolay; Gusev, Anatoly; Kostrykin, Sergey; Iakovlev, Nikolay; Shestakova, Anna; Emelina, Svetlana (2019). INM INM-CM5-0 model output prepared for CMIP6 CMIP historical. Earth System Grid Federation. doi:https://doi.org/10.22033/ESGF/CMIP6.5070 .

[78] Volodin, Evgeny; Mortikov, Evgeny; Gritsun, Andrey; Lykossov, Vasily; Galin, Vener; Diansky, Nikolay; Gusev, Anatoly; Kostrykin, Sergey; Iakovlev, Nikolay; Shestakova, Anna; Emelina, Svetlana (2019). INM INM-CM5-0 model output prepared for CMIP6 ScenarioMIP ssp585. Earth System Grid Federation. doi:https://doi.org/10.22033/ESGF/CMIP6.12338.

[79] Boucher, O., Servonnat, J., Albright, A.L., Aumont, O., Balkanski, Y., Bastrikov, V., Bekki, S., Bonnet, R., Bony, S., Bopp, L. and Braconnot, P., 2020. Presentation and evaluation of the IPSL-CM6A-LR climate model. Journal of Advances in Modeling Earth Systems, 12(7), p.e2019MS002010.

[80] Boucher, Olivier; Denvil, Sébastien; Levavasseur, Guillaume; Cozic, Anne; Caubel, Arnaud; Foujols, Marie-Alice; Meurdesoif, Yann; Cadule, Patricia; Devilliers, Marion; Ghattas, Josefine; Lebas, Nicolas; Lurton, Thibaut; Mellul, Lidia; Musat, Ionela; Mignot, Juliette; Cheruy, Frédérique (2018). IPSL IPSL-CM6A-LR model output prepared for CMIP6 CMIP historical. Earth System Grid Federation. doi:https://doi.org/10.22033/ESGF/CMIP6.5195 .

[81] Boucher, Olivier; Denvil, Sébastien; Levavasseur, Guillaume; Cozic, Anne; Caubel, Arnaud; Foujols, Marie-Alice; Meurdesoif, Yann; Cadule, Patricia; Devilliers, Marion; Dupont, Eliott; Lurton, Thibaut (2019). IPSL IPSL-CM6A-LR model output prepared for CMIP6 ScenarioMIP ssp585. Earth System Grid Federation. doi:https://doi.org/10.22033/ESGF/CMIP6.5271

[82] Lee, J., Kim, J., Sun, M.-A., Kim, B.-H., Moon, H., Sung, H. M., et al. (2020). Evaluation of the Korea meteorological administration advanced community earth-system model (K-ACE). Asia-Pacific Journal of Atmospheric Sciences, 56(3), 381–395. https://doi.org/10.1007/s13143-019-00144-7

[83] Byun, Young-Hwa; Lim, Yoon-Jin; Sung, Hyun Min; Kim, Jisun; Sun, Minah; Kim, Byeong-Hyeon (2019). NIMS-KMA KACE1.0-G model output prepared for CMIP6 CMIP historical. Earth System Grid Federation. doi:https://doi.org/10.22033/ESGF/CMIP6.8378

[84] Byun, Young-Hwa; Lim, Yoon-Jin; Shim, Sungbo; Sung, Hyun Min; Sun, Minah; Kim, Jisun; Kim, Byeong-Hyeon; Lee, Jae-Hee; Moon, Hyejin (2019). NIMS-KMA KACE1.0-G model output prepared for CMIP6 ScenarioMIP ssp585. Earth System Grid Federation. doi:https://doi.org/10.22033/ESGF/CMIP6.8456

[85] Tatebe, H., Ogura, T., Nitta, T., Komuro, Y., Ogochi, K., Takemura, T., et al. (2019). Description and basic evaluation of simulated mean state, internal variability, and climate sensitivity in MIROC6. Geoscientific Model Development, 12(7), 2727–2765. https://doi.org/10.5194/gmd-12-2727-2019

[86] Tatebe, Hiroaki; Watanabe, Masahiro (2018). MIROC MIROC6 model output prepared for CMIP6 CMIP historical. Earth System Grid Federation. doi:https://doi.org/10.22033/ESGF/CMIP6.5603.

[87] Shiogama, Hideo; Abe, Manabu; Tatebe, Hiroaki (2019). MIROC MIROC6 model output prepared for CMIP6 ScenarioMIP ssp585. Earth System Grid Federation. doi:https://doi.org/10.22033/ESGF/CMIP6.5771

[88] Müller, W. A., Jungclaus, J. H., Mauritsen, T., Baehr, J., Bittner, M., Budich, R., et al. (2018). A higher-resolution version of the Max Planck Institute Earth System Model (MPI-ESM1.2-HR). Journal of Advances in Modeling Earth Systems, 10, 1383–1413. https://doi.org/10.1029/2017MS001217

[89] Jungclaus, Johann; Bittner, Matthias; Wieners, Karl-Hermann; Wachsmann, Fabian; Schupfner, Martin; Legutke, Stephanie; Giorgetta, Marco; Reick, Christian; Gayler, Veronika; Haak, Helmuth; de Vrese, Philipp; Raddatz, Thomas; Esch, Monika; Mauritsen, Thorsten; von Storch, Jin-Song; Behrens, Jörg; Brovkin, Victor; Claussen, Martin; Crueger, Traute; Fast, Irina; Fiedler, Stephanie; Hagemann, Stefan; Hohenegger, Cathy; Jahns, Thomas; Kloster, Silvia; Kinne, Stefan; Lasslop, Gitta; Kornblueh, Luis; Marotzke, Jochem; Matei, Daniela; Meraner, Katharina; Mikolajewicz, Uwe; Modali, Kameswarrao; Müller, Wolfgang; Nabel, Julia; Notz, Dirk; Peters, Karsten; Pincus, Robert; Pohlmann, Holger; Pongratz, Julia; Rast, Sebastian; Schmidt, Hauke; Schnur, Reiner; Schulzweida, Uwe; Six, Katharina; Stevens, Bjorn; Voigt, Aiko; Roeckner, Erich (2019). MPI-M MPI-ESM1.2-HR model output prepared for CMIP6 CMIP historical. Earth System Grid Federation. doi:https://doi.org/10.22033/ESGF/CMIP6.6594 .

[90] Schupfner, Martin; Wieners, Karl-Hermann; Wachsmann, Fabian; Steger, Christian; Bittner, Matthias; Jungclaus, Johann; Früh, Barbara; Pankatz, Klaus; Giorgetta, Marco; Reick, Christian; Legutke, Stephanie; Esch, Monika; Gayler, Veronika; Haak, Helmuth; de Vrese, Philipp; Raddatz, Thomas; Mauritsen, Thorsten; von Storch, Jin-Song; Behrens, Jörg; Brovkin, Victor; Claussen,

Martin; Crueger, Traute; Fast, Irina; Fiedler, Stephanie; Hagemann, Stefan; Hohenegger, Cathy; Jahns, Thomas; Kloster, Silvia; Kinne, Stefan; Lasslop, Gitta; Kornblueh, Luis; Marotzke, Jochem; Matei, Daniela; Meraner, Katharina; Mikolajewicz, Uwe; Modali, Kameswarrao; Müller, Wolfgang; Nabel, Julia; Notz, Dirk; Peters, Karsten; Pincus, Robert; Pohlmann, Holger; Pongratz, Julia; Rast, Sebastian; Schmidt, Hauke; Schnur, Reiner; Schulzweida, Uwe; Six, Katharina; Stevens, Bjorn; Voigt, Aiko; Roeckner, Erich (2019). DKRZ MPI-ESM1.2-HR model output prepared for CMIP6 ScenarioMIP ssp585. Earth System Grid Federation. doi:https://doi.org/10.22033/ESGF/CMIP6.4403

[91] Mauritsen, T., Bader, J., Becker, T., Behrens, J., Bittner, M., Brokopf, R., et al. (2019). Developments in the MPI-M Earth System Model version 1.2 (MPI-ESM1.2) and its response to increasing CO2. Journal of Advances in Modeling Earth Systems, 11, 998–1038. https://doi.org/10.1029/2018MS001400

[92] Wieners, Karl-Hermann; Giorgetta, Marco; Jungclaus, Johann; Reick, Christian; Esch, Monika; Bittner, Matthias; Legutke, Stephanie; Schupfner, Martin; Wachsmann, Fabian; Gayler, Veronika; Haak, Helmuth; de Vrese, Philipp; Raddatz, Thomas; Mauritsen, Thorsten; von Storch, Jin-Song; Behrens, Jörg; Brovkin, Victor; Claussen, Martin; Crueger, Traute; Fast, Irina; Fiedler, Stephanie; Hagemann, Stefan; Hohenegger, Cathy; Jahns, Thomas; Kloster, Silvia; Kinne, Stefan; Lasslop, Gitta; Kornblueh, Luis; Marotzke, Jochem; Matei, Daniela; Meraner, Katharina; Mikolajewicz, Uwe; Modali, Kameswarrao; Müller, Wolfgang; Nabel, Julia; Notz, Dirk; Peters, Karsten; Pincus, Robert; Pohlmann, Holger; Pongratz, Julia; Rast, Sebastian; Schmidt, Hauke; Schnur, Reiner; Schulzweida, Uwe; Six, Katharina; Stevens, Bjorn; Voigt, Aiko; Roeckner, Erich (2019). MPI-M MPI-ESM1.2-LR model output prepared for CMIP6 CMIP historical. Earth System Grid Federation. doi:https://doi.org/10.22033/ESGF/CMIP6.6595.

[93] Wieners, Karl-Hermann; Giorgetta, Marco; Jungclaus, Johann; Reick, Christian; Esch, Monika; Bittner, Matthias; Gayler, Veronika; Haak, Helmuth; de Vrese, Philipp; Raddatz, Thomas; Mauritsen, Thorsten; von Storch, Jin-Song; Behrens, Jörg; Brovkin, Victor; Claussen, Martin; Crueger, Traute; Fast, Irina; Fiedler, Stephanie; Hagemann, Stefan; Hohenegger, Cathy; Jahns, Thomas; Kloster, Silvia; Kinne, Stefan; Lasslop, Gitta; Kornblueh, Luis; Marotzke, Jochem; Matei, Daniela; Meraner, Katharina; Mikolajewicz, Uwe; Modali, Kameswarrao; Müller, Wolfgang; Nabel, Julia; Notz, Dirk; Peters, Karsten; Pincus, Robert; Pohlmann, Holger; Pongratz, Julia; Rast, Sebastian; Schmidt, Hauke; Schnur, Reiner; Schulzweida, Uwe; Six, Katharina; Stevens, Bjorn; Voigt, Aiko; Roeckner, Erich (2019). MPI-M MPI-ESM1.2-LR model output prepared for CMIP6 ScenarioMIP ssp585. Earth System Grid Federation. doi:https://doi.org/10.22033/ESGF/CMIP6.6705

[94] Yukimoto, S., Kawai, H., Koshiro, T., Oshima, N., Yoshida, K., Urakawa, S., et al. (2019). The Meteorological Research Institute Earth System Model version 2.0, MRI-ESM2.0: Description and basic evaluation of the physical component. Journal of the Meteorological Society of Japan,

97(5), 931–965. https://doi.org/10.2151/jmsj.2019-051

[95] Yukimoto, Seiji; Koshiro, Tsuyoshi; Kawai, Hideaki; Oshima, Naga; Yoshida, Kohei; Urakawa, Shogo; Tsujino, Hiroyuki; Deushi, Makoto; Tanaka, Taichu; Hosaka, Masahiro; Yoshimura, Hiromasa; Shindo, Eiki; Mizuta, Ryo; Ishii, Masayoshi; Obata, Atsushi; Adachi, Yukimasa (2019). MRI MRI-ESM2.0 model output prepared for CMIP6 CMIP historical. Earth System Grid Federation. doi:https://doi.org/10.22033/ESGF/CMIP6.6842

[96] Yukimoto, Seiji; Koshiro, Tsuyoshi; Kawai, Hideaki; Oshima, Naga; Yoshida, Kohei; Urakawa, Shogo; Tsujino, Hiroyuki; Deushi, Makoto; Tanaka, Taichu; Hosaka, Masahiro; Yoshimura, Hiromasa; Shindo, Eiki; Mizuta, Ryo; Ishii, Masayoshi; Obata, Atsushi; Adachi, Yukimasa (2019). MRI MRI-ESM2.0 model output prepared for CMIP6 ScenarioMIP ssp585. Earth System Grid Federation. doi:https://doi.org/10.22033/ESGF/CMIP6.6929

[97] Cao, J., Wang, B., Yang, Y.-M., Ma, L., Li, J., Sun, B., et al. (2018). The NUIST Earth System Model (NESM) version 3: Description and preliminary evaluation. Geoscientific Model Development, 11(7), 2975–2993. https://doi.org/10.5194/gmd-11-2975-2018

[98] Cao, Jian; Wang, Bin (2019). NUIST NESMv3 model output prepared for CMIP6 CMIP historical. Earth System Grid Federation. doi:https://doi.org/10.22033/ESGF/CMIP6.8769

[99] Cao, Jian (2019). NUIST NESMv3 model output prepared for CMIP6 ScenarioMIP ssp585. Earth System Grid Federation. doi:https://doi.org/10.22033/ESGF/CMIP6.8790

[100] Seland, Ø., Bentsen, M., Olivié, D., Toniazzo, T., Gjermundsen, A., Graff, L. S., et al. (2020). Overview of the Norwegian Earth System Model (NorESM2) and key climate response of CMIP6 DECK, historical, and scenario simulations. Geoscientific Model Development, 13(12), 6165–6200. https://doi.org/10.5194/gmd-13-6165-2020

[101] Seland, Øyvind; Bentsen, Mats; Oliviè, Dirk Jan Leo; Toniazzo, Thomas; Gjermundsen, Ada; Graff, Lise Seland; Debernard, Jens Boldingh; Gupta, Alok Kumar; He, Yanchun; Kirkevåg, Alf; Schwinger, Jörg; Tjiputra, Jerry; Aas, Kjetil Schanke; Bethke, Ingo; Fan, Yuanchao; Griesfeller, Jan; Grini, Alf; Guo, Chuncheng; Ilicak, Mehmet; Karset, Inger Helene Hafsahl; Landgren, Oskar Andreas; Liakka, Johan; Moseid, Kine Onsum; Nummelin, Aleksi; Spensberger, Clemens; Tang, Hui; Zhang, Zhongshi; Heinze, Christoph; Iversen, Trond; Schulz, Michael (2019). NCC NorESM2-LM model output prepared for CMIP6 CMIP historical. Earth System Grid Federation. doi:https://doi.org/10.22033/ESGF/CMIP6.8036 .

[102] Seland, Øyvind; Bentsen, Mats; Oliviè, Dirk Jan Leo; Toniazzo, Thomas; Gjermundsen, Ada; Graff, Lise Seland; Debernard, Jens Boldingh; Gupta, Alok Kumar; He, Yanchun; Kirkevåg, Alf; Schwinger, Jörg; Tjiputra, Jerry; Aas, Kjetil Schanke; Bethke, Ingo; Fan, Yuanchao; Griesfeller, Jan; Grini, Alf; Guo, Chuncheng; Ilicak, Mehmet; Karset, Inger Helene Hafsahl; Landgren, Oskar Andreas; Liakka, Johan; Moseid, Kine Onsum; Nummelin, Aleksi; Spensberger, Clemens; Tang, Hui; Zhang, Zhongshi; Heinze, Christoph; Iversen, Trond; Schulz, Michael (2019). NCC

NorESM2-LM model output prepared for CMIP6 ScenarioMIP ssp585. Earth System Grid Federation. doi:https://doi.org/10.22033/ESGF/CMIP6.8319

[103] Bentsen, Mats; Oliviè, Dirk Jan Leo; Seland, Øyvind; Toniazzo, Thomas; Gjermundsen, Ada; Graff, Lise Seland; Debernard, Jens Boldingh; Gupta, Alok Kumar; He, Yanchun; Kirkevåg, Alf; Schwinger, Jörg; Tjiputra, Jerry; Aas, Kjetil Schanke; Bethke, Ingo; Fan, Yuanchao; Griesfeller, Jan; Grini, Alf; Guo, Chuncheng; Ilicak, Mehmet; Karset, Inger Helene Hafsahl; Landgren, Oskar Andreas; Liakka, Johan; Moseid, Kine Onsum; Nummelin, Aleksi; Spensberger, Clemens; Tang, Hui; Zhang, Zhongshi; Heinze, Christoph; Iversen, Trond; Schulz, Michael (2019). NCC NorESM2-MM model output prepared for CMIP6 CMIP historical. Earth System Grid Federation. doi:https://doi.org/10.22033/ESGF/CMIP6.8040

[104] Bentsen, Mats; Oliviè, Dirk Jan Leo; Seland, Øyvind; Toniazzo, Thomas; Gjermundsen, Ada; Graff, Lise Seland; Debernard, Jens Boldingh; Gupta, Alok Kumar; He, Yanchun; Kirkevåg, Alf; Schwinger, Jörg; Tjiputra, Jerry; Aas, Kjetil Schanke; Bethke, Ingo; Fan, Yuanchao; Griesfeller, Jan; Grini, Alf; Guo, Chuncheng; Ilicak, Mehmet; Karset, Inger Helene Hafsahl; Landgren, Oskar Andreas; Liakka, Johan; Moseid, Kine Onsum; Nummelin, Aleksi; Spensberger, Clemens; Tang, Hui; Zhang, Zhongshi; Heinze, Christoph; Iversen, Trond; Schulz, Michael (2019). NCC NorESM2-MM model output prepared for CMIP6 ScenarioMIP ssp585. Earth System Grid Federation. doi:https://doi.org/10.22033/ESGF/CMIP6.8321

[105] Lee, W.-L., Wang, Y.-C., Shiu, C.-J., Tsai, I., Tu, C.-Y., Lan, Y.-Y., et al. (2020). Taiwan Earth System Model: Description and evaluation of mean. Geoscientific Model Development, 13, 3887–3904. https://doi.org/10.5194/gmd-2019-377

[106] Lee, Wei-Liang; Liang, Hsin-Chien (2020). AS-RCEC TaiESM1.0 model output prepared for CMIP6 CMIP historical. Earth System Grid Federation. https://doi.org/10.22033/ESGF/CMIP6.9755

[107] Lee, Wei-Liang; Liang, Hsin-Chien (2020). AS-RCEC TaiESM1.0 model output prepared for CMIP6 ScenarioMIP ssp585. Earth System Grid Federation. doi:https://doi.org/10.22033/ESGF/CMIP6.9823 .

Appendix B

Supplementary Tables

This Appendix includes supplementary tables for content described in Chapter 2 and Chapter 5.

Table B.1: Data Sources and Download Links used in Chapter 2.

No.	Data	Source
1	Crop Water Requirements (Except Berseem, Tea, Palm Oil)	Mekonnen, M.M. and Hoekstra, A.Y. The green, blue and grey water footprint of crops and derived crop products, Value of Water Research Report Series No. 47, Volume II, Appendix II (UNESCO-IHE, Delft, the Netherlands., 2010) https://research.utwente.nl/files/59480760/Report47_WaterFootprintCrops_Vol2.pdf
2	Crop Water Requirements (Tea, Palm Oil)	Mekonnen, M.M. and Hoekstra, A.Y. National water footprint accounts: the green, blue and grey water footprint of production and consumption, Value of Water Research Report Series No. 50, Volume II, Appendix VI (UNESCO-IHE, Delft, the Netherlands, 2011) https://research.utwente.nl/files/5146139/Report50-NationalWaterFootprints-Vol2.pdf.pdf

No.	Data	Source
3	Animal Product Water Requirements	Mekonnen, M.M. and Hoekstra, A.Y. The green, blue and grey water footprint of farm animals and animal products, Value of Water Research Report Series No. 48, Volume II, Appendix V, Grazing Method (UNESCO-IHE, Delft, the Netherlands, 2010) https://research.utwente.nl/files/59481201/Report48_WaterFootprint_AnimalProducts_Vol2.pdf
4	Population	United Nations, Department of Economic and Social Affairs, Population Division. Total population (both sexes combined) by region, subregion and country, annually for 1950-2100 (thousands)). World Population Prospects 2019, Online Edition. Rev. 1. (File POP/1-1) (2019). Available Online at https://population.un.org/wpp/Download/Files/1_Indicators%20(Standard)/EXCEL_FILES/1_Population/WPP2019_POP_F01_1_TOTAL_POPULATION_BOTH_SEXES.xlsx; https://ourworldindata.org/grapher/absolute-increase-global-population; https://ourworldindata.org/grapher/population; https://ourworldindata.org/grapher/world-population-1750-2015-and-un-projection-until-2100
5	Fertility	United Nations, Department of Economic and Social Affairs, Population Division. Total fertility by region, subregion and country, 1950-2100 (live births per woman). World Population Prospects 2019, Online Edition. Rev. 1. (File FERT/4). (2019). https://population.un.org/wpp/Download/Files/1_Indicators%20(Standard)/EXCEL_FILES/2_Fertility/WPP2019_FERT_F04_TOTAL_FERTILITY.xlsx
6	Economic Data	http://www.fao.org/faostat/en/#data/MK
7	Production, Yield, Area Harvested	http://www.fao.org/faostat/en/#data/QC; http://www.fao.org/faostat/en/#data/QD; http://www.fao.org/faostat/en/#data/QA; http://www.fao.org/faostat/en/#data/QL; http://www.fao.org/faostat/en/#data/QP

No.	Data	Source
8	Berseem Production, Yield, Area Harvested	Dost, M., Bimal, M., El-Nahrawy, M., Khan, S., & Serkan, A. Egyptian Clover (Trifolium alexandrinum). King of Forage Crops. (Food and Agriculture Organization of the United Nations, Regional Office for the Near East and North Africa, Cairo, 2014) http://www.fao.org/3/a-i3500e.pdf
9	Animal Carcass Weights	http://www.fao.org/faostat/en/#data/QL
10	Feed & Food Supply	http://www.fao.org/faostat/en/#data/BC; http://www.fao.org/faostat/en/#data/BL; http://www.fao.org/faostat/en/#data/CC; http://www.fao.org/faostat/en/#data/CL; http://www.fao.org/faostat/en/#data/FBSH; http://www.fao.org/faostat/en/#data/FBS;
11	Import & Export Quantity & Value	http://www.fao.org/faostat/en/#data/TP; http://www.fao.org/faostat/en/#data/TA
12	Cereal Import Dependency Ratio	http://www.fao.org/faostat/en/#data/FS
13	Potential ET	CRU TS 4.04 https://crudata.uea.ac.uk/cru/data/hrg/cru_ts_4.04/ https://crudata.uea.ac.uk/cru/data/hrg/cru_ts_4.04/cruts.2004151855.v4.04/pet/
14	Dongola Monthly Inflow	Republic of Sudan Ministry of Irrigation and Water Resources (2020). Monthly Streamflow at Dongola (1963-2020). Processed and Compiled By Elzeinn, A. S.

No.	Data	Source
15	Height-Volume and Area-Volume Equations for Lake Nasser	Shafik, N. M. Updating the surface area and volume equations of Lake Nasser using multibeam system. Presented at 19th International Water Technology Conference (2016) [http://iwtc.info/wp-content/uploads/2016/05/41.pdf]
16	Egypt Water Withdrawals	Food and Agriculture Organization of the United Nations (FAO). AQUASTAT Main Database. (2016) http://www.fao.org/nr/water/aquastat/data/query/index.html?lang=en; Food and Agriculture Organization of the United Nations. AQUASTAT Country Profile – Egypt. Water Resources Factsheet. (Rome, Italy, 2016). Available Online at https://storage.googleapis.com/fao-aquastat.appspot.com/countries_regions/factsheets/water_resources/en/EGY-WRS.pdf; Food and Agriculture Organization of the United Nations (FAO). AQUASTAT Country Profile – Egypt. (Rome, Italy, 2016). Available Online at http://www.fao.org/3/i9729en/I9729EN.pdf
17	Lake Nasser Levels	Gammal, E. A. E., Salem, S.M., and Gammal, A. E. A. E. Change detection studies on the world's biggest artificial lake (Lake Nasser, Egypt). The Egyptian Journal of Remote Sensing and Space Science, 13 (2) 89-99, (2010). https://doi.org/10.1016/j.ejrs.2010.08.001.; NASA/USDA. G-REALM – Lake Nasser (0331) Height Variations from Altimetry https://ipad.fas.usda.gov/cropexplorer/global_reservoir/gr_regional_chart.aspx?regionid=metu&reservoir_name=Nasser
18	Irrigation Usage	FAO. 2016. AQUASTAT Main Database, Food and Agriculture Organization of the United Nations: Irrigation and Drainage Development. http://www.fao.org/aquastat/statistics/query/index.html?lang=en

No.	Data	Source
19	Storage Capacity	FAO. 2016. AQUASTAT Country Profile – Egypt. Food and Agriculture Organization of the United Nations (FAO). Rome, Italy https://storage.googleapis.com/fao-aquastat.appspot.com/Excel/dams/EGY-dams_eng.xlsx
20	Aswan Monthly Discharge	Vörösmarty, C.J., Fekete, B. M. & Tucker, B. A. River Discharge Database, Version 1.1 (RivDIS v1.0 supplement). Aswan Dam Egypt. Available through the Institute for the Study of Earth, Oceans, and Space / University of New Hampshire, Durham NH (USA). (1998) http://dx.doi.org/10.3334/ORNLDAAC/199

Table B.2: CURRENT VIRTUAL WATER TRADE BALANCE (VWTB) Monetary value, tonnage, and water equivalent of agricultural import and export in Egypt, using official trade values (2007-2011 average) (Source: FAOSTAT)

	Total Value (billion USD)	Total Water Consumed (km^3)	Total Trade Quantity (million tonnes)	Total Water Value (Million USD/km^3)
Imports	7.1	19.2	18.2	368.4 (a)
Exports	1.8	2.1	2.8	850.9 (b)
			VWTB (b/a)	**2.31**

Table B.3: CROP AND ANIMAL PRODUCT DATA Key crop and animal product figures and water usage estimates (2007-2011 average). * Indicates commodities where the 1996-2005 water consumption value was used in absence of yield and harvested area data for scaling. All total water use estimates are given in terms of consumption (without irrigation efficiency scaling). Import and Export Price/Quantity are computed individually for all years with official data and then averaged over the period. (Source: Import, Export and Production data from FAOSTAT; Crop water Requirement data from [a] except for Berseem where the water requirement is calculated using figures from [b], Animal Product water requirement from [c], and water requirement for tea and palm oil from [d]);[a] Mekonnen, M .M. & Hoekstra, A.Y. The green, blue and grey water footprint of crops and derived crop products, Value of Water Research Report Series No. 47, (UNESCO-IHE, Delft, the Netherlands, 2010). [b] Tyagi, N .K., Sharma, D. K. & Luthra, S. K. Determination of evapotranspiration for maize and berseem clover. Irrig Sci 21, 173–181 (2003). https://doi.org/10.1007/s00271-002-0061-3. [c] Mekonnen, M. M. & Hoekstra, A. Y. The green, blue and grey water footprint of farm animals and animal products, Value of Water Research Report Series No. 48, (UNESCO-IHE, Delft, the Netherlands, 2010). [d] Mekonnen, M. M. & Hoekstra, A. Y. National water footprint accounts: the green, blue and grey water footprint of production and consumption, Value of Water Research Report Series No. 50, (UNESCO-IHE, Delft, the Netherlands, 2011)

Crop	Water Req. (m^3/t)	Prod. Q. (t)	Imp. Q. (t)	Exp. Q. (t)	Imp. P/Q ($/t)	Exp. P/Q ($/t)	Imp. P. ($/$m^3$)	Exp. P. ($/$m^3$)	Prod. Water (km^3)	Imp. Water (km^3)	Exp. Water (km^3)
Maize	1062.1	7049659	5575547	7749	$309	$345	$0.29	$0.32	7.5	5.9	0
Wheat	901.3	7892700	9216803	2988	$326	$410	$0.36	$0.45	7.1	8.3	0
Rice	979.6	5931043	57490	563713	$432	$579	$0.44	$0.59	5.8	0.1	0.6
Sugarbeet	162.8	6250100		106		$710		$4.36	1		0
Sugar (Raw)	1124		965034	35836	$701	$613	$0.62	$0.55		1.1	0
Sugar (Refined)			90898	187028	$588	$599					
Soybean	1488.1	30068	1452998	388	$376	$1,560	$0.25	$1.05	0	2.2	0
Cotton Lint	8608	148000	45447	71361	$3,264	$3,725	$0.38	$0.43	1.3	0.4	0.6
Orange	472.6	2308800	177	645266	$850	$494	$1.80	$1.05	1.1	0	0.3
Tomato	141.6	8954400	1080	22976	$619	$448	$4.37	$3.16	1.3	0	0
Potato	273.6	3593700	98845	387742	$1,258	$449	$4.60	$1.64	1	0	0.1
Banana	428.9	1042300	10038	9322	$507	$591	$1.18	$1.38	0.4	0	0
Broad Beans	1502.8	250869	297605	11631	$748	$1,089	$0.50	$0.72	0.4	0.4	0
Barley	2150.1	143080	8163	6093	$378	$422	$0.18	$0.20	0.3	0	0

Crop	Water Req. (m^3/t)	Prod. Q. (t)	Imp. Q. (t)	Exp. Q. (t)	Imp. P/Q ($/t)	Exp. P/Q ($/t)	Imp. P. ($/$m^3$)	Exp. P. ($/$m^3$)	Prod. Water (km^3)	Imp. Water (km^3)	Exp. Water (km^3)
Groundnuts (In Shell)	1826.4	206780	2322	11234	$1,949	$1,062	$1.07	$0.58	0.4	0	0
Sorghum	500.8	806510	10358	4183	$501	$555	$1.00	$1.11	0.4	0	0
Olive	1340.5	457343	9	12797	$1,004	$987	$0.75	$0.74	0.6	0	0
Onion	205.5	2015147	381	287693	$615	$445	$2.99	$2.17	0.4	0	0.1
Beef*	11313	436310	1471	275	$3,509	$4,928	$0.31	$0.44	4.9	0	0
Chicken*	3680	708920	49375	1252	$2,029	$2,893	$0.55	$0.79	2.6	0.2	0
Berseem	100.2	48555000							4.9		
Beans, Dry	1858.1	75319	18647	52439	$845	$1,019	$0.45	$0.55	0.1	0	0.1
Chickpea	1176.4	7383	17475	4773	$1,097	$992	$0.93	$0.84	0	0	0
Lentil	4542.1	1648	88738	6379	$904	$1,080	$0.20	$0.24	0	0.4	0
Beans, Green	266.9	287240	1	16777	$1,000	$996	$3.75	$3.73	0.1	0	0
Lemons and Limes	557.5	315790	18	20460	$569	$606	$1.02	$1.09	0.2	0	0
Apple	623.3	513290	89951	155	$942	$830	$1.51	$1.33	0.3	0.1	0
Watermelon	92.1	1639600	17	10358	$907	$596	$9.85	$6.47	0.2	0	0

Crop	Water Req. (m^3/t)	Prod. Q. (t)	Imp. Q. (t)	Exp. Q. (t)	Imp. P/Q ($/t)	Exp. P/Q ($/t)	Imp. P. ($/$m^3$)	Exp. P. ($/$m^3$)	Prod. Water (km^3)	Imp. Water (km^3)	Exp. Water (km^3)
Mango	1777.8	527420		3715		$614		$0.35	0.9		0
Tea*	221		79562	2905	$2,380	$5,733	$10.77	$25.94		0	0
Molasses*	363	656000	5184	263920	$856	$537	$2.36	$1.48	0.2	0	0.1
Cottonseed Oil*	3738	31640	934	200	$597	$1,077	$0.16	$0.29	0.1	0	0
Maize Oil*	2226		30505	6541	$1,228	$1,229	$0.55	$0.55		0.1	0
Garlic	270	262082	5082	6112	$814	$883	$3.01	$3.27	0.1	0	0
Strawberry	282.4	219232	72	38076	$722	$878	$2.56	$3.11	0.1	0	0
Artichoke	771.2	195336	0	9872		$1,276		$1.65	0.2	0	0
Cabbage	202.6	662476	0	924		$703		$3.47	0.1	0	0
Carrot & Turnip	262.8	164128	0	347		$171		$0.65	0	0	0
Cauliflower & Broccoli	170.6	131772	3	1020	$2,867	$935	$16.80	$5.48	0	0	0
Chili Pepper Green	154.9	694868	0	5007		$901		$5.82	0.1	0	0

Crop	Water Req. (m^3/t)	Prod. Q. (t)	Imp. Q. (t)	Exp. Q. (t)	Imp. P/Q ($/t)	Exp. P/Q ($/t)	Imp. P. ($/$m^3$)	Exp. P. ($/$m^3$)	Prod. Water (km^3)	Imp. Water (km^3)	Exp. Water (km^3)
Cucumber	195.2	632741	0	521		$1,045		$5.35	0.1	0	0
Eggplant	270	1217940	0	270		$878		$3.25	0.3	0	0
Melon	168	957408	180	4452	$1,328	$672	$7.90	$4.00	0.2	0	0
Peaches & Nectarine	1152.8	358728	2104	6780	$797	$923	$0.69	$0.80	0.4	0	0
Pumpkin, Squash	182.7	659624		265		$403		$2.21	0.1		0
Sweet Potato	111	325130	0	9775		$529		$4.77	0	0	0
Tangerines, Mandarin, Clementine	574.6	794188	0	8647	$2,000	$657	$3.48	$1.14	0.5	0	0
Vegetable Leg Nes	2567.2	134140							0.3		
Vegetable Fresh Nes	192.7	577001	242	8559	$1,367	$734	$7.09	$3.81	0.1	0	0

	Maize	Wheat	Rice	Soybean	Broad Beans	Barley	Groundnuts (In Shell)	Sorghum	Beef *	Chicken *	Cottonseed Oil *	Maize Oil *
Maize	1.12	0.90	0.77	1.29	0.65	1.85	0.30	0.32	1.05	0.59	2.03	0.59
Wheat	1.56	1.26	1.08	1.80	0.91	2.59	0.43	0.45	1.47	0.83	2.85	0.82
Rice	2.23	1.79	1.54	2.57	1.30	3.69	0.61	0.65	2.09	1.18	4.07	1.18
Sugar beet	14.99	12.06	10.32	17.26	8.76	24.81	4.09	4.36	14.06	7.91	27.31	7.91
Sugar (Raw)	1.87	1.51	1.29	2.16	1.10	3.10	0.51	0.55	1.76	0.99	3.41	0.99
Soybean	3.60	2.90	2.48	4.15	2.11	5.96	0.98	1.05	3.38	1.90	6.56	1.90
Cotton Lint	1.49	1.20	1.02	1.71	0.87	2.46	0.41	0.43	1.40	0.78	2.71	0.78
Orange	3.59	2.89	2.47	4.14	2.10	5.95	0.98	1.04	3.37	1.90	6.54	1.89
Tomato	10.87	8.75	7.49	12.52	6.36	18.00	2.96	3.16	10.20	5.74	19.81	5.74
Potato	5.64	4.54	3.88	6.49	3.30	9.33	1.54	1.64	5.29	2.98	10.28	2.97
Banana	4.74	3.81	3.26	5.45	2.77	7.84	1.29	1.38	4.44	2.50	8.63	2.50
Broad Beans	2.49	2.00	1.71	2.87	1.46	4.12	0.68	0.72	2.34	1.31	4.54	1.31
Barley	0.67	0.54	0.46	0.78	0.39	1.12	0.18	0.20	0.63	0.36	1.23	0.36
Groundnuts (In Shell)	2.00	1.61	1.38	2.30	1.17	3.31	0.54	0.58	1.87	1.05	3.64	1.05
Sorghum	3.81	3.06	2.62	4.39	2.23	6.30	1.04	1.11	3.57	2.01	6.94	2.01
Olive	2.53	2.04	1.74	2.91	1.48	4.19	0.69	0.74	2.37	1.34	4.61	1.33
Onion	7.44	5.99	5.12	8.57	4.35	12.32	2.03	2.16	6.98	3.93	13.56	3.93
Beef *	1.50	1.20	1.03	1.72	0.88	2.48	0.41	0.44	1.40	0.79	2.73	0.79
Chicken *	2.70	2.17	1.86	3.11	1.58	4.47	0.74	0.79	2.53	1.43	4.92	1.43
Beans, Dry	1.89	1.52	1.30	2.17	1.10	3.12	0.51	0.55	1.77	0.99	3.43	0.99
Chickpea	2.90	2.33	2.00	3.34	1.69	4.80	0.79	0.84	2.72	1.53	5.28	1.53
Lentil	0.82	0.66	0.56	0.94	0.48	1.35	0.22	0.24	0.77	0.43	1.49	0.43
Beans, Green	12.83	10.32	8.83	14.77	7.50	21.23	3.50	3.73	12.03	6.77	23.37	6.76
Lemons and Limes	3.74	3.01	2.57	4.30	2.18	6.18	1.02	1.09	3.50	1.97	6.81	1.97
Apple	4.58	3.68	3.15	5.27	2.68	7.57	1.25	1.33	4.29	2.42	8.34	2.41
Watermelon	22.24	17.89	15.31	25.61	13.00	36.81	6.06	6.47	20.86	11.74	40.52	11.73
Mango	1.19	0.95	0.82	1.37	0.69	1.96	0.32	0.35	1.11	0.63	2.16	0.63
Molasses *	5.08	4.09	3.50	5.85	2.97	8.41	1.39	1.48	4.77	2.68	9.26	2.68
Cottonseed Oil *	0.99	0.80	0.68	1.14	0.58	1.64	0.27	0.29	0.93	0.52	1.80	0.52
Maize Oil *	1.90	1.53	1.31	2.19	1.11	3.14	0.52	0.55	1.78	1.00	3.46	1.00
Garlic	11.24	9.04	7.74	12.94	6.57	18.60	3.06	3.27	10.54	5.93	20.48	5.93
Strawberry	10.69	8.60	7.36	12.30	6.25	17.68	2.91	3.11	10.02	5.64	19.47	5.64
Artichoke	5.69	4.57	3.92	6.55	3.32	9.41	1.55	1.65	5.33	3.00	10.36	3.00
Cabbage	11.93	9.59	8.21	13.73	6.97	19.74	3.25	3.47	11.19	6.29	21.73	6.29
Carrot & Turnip	2.24	1.80	1.54	2.58	1.31	3.70	0.61	0.65	2.10	1.18	4.07	1.18
Cauliflower & Broccoli	18.84	15.15	12.97	21.69	11.01	31.17	5.14	5.48	17.67	9.94	34.32	9.93
Chili Pepper Green	19.99	16.08	13.76	23.02	11.69	33.09	5.45	5.81	18.75	10.55	36.42	10.54
Cucumber	18.40	14.80	12.67	21.19	10.76	30.45	5.02	5.35	17.26	9.71	33.52	9.70
Eggplant	11.18	8.99	7.69	12.87	6.53	18.50	3.05	3.25	10.48	5.90	20.36	5.89
Melon	13.75	11.06	9.46	15.83	8.04	22.75	3.75	4.00	12.90	7.25	25.05	7.25
Peaches & Nectarine	2.75	2.21	1.89	3.17	1.61	4.55	0.75	0.80	2.58	1.45	5.01	1.45
Pumpkin, Squash	7.58	6.10	5.22	8.73	4.43	12.55	2.07	2.20	7.11	4.00	13.81	4.00
Sweet Potato	16.38	13.18	11.28	18.86	9.57	27.11	4.47	4.76	15.36	8.64	29.84	8.64
Tangerines, Mandarin, Clementine	3.93	3.16	2.71	4.53	2.30	6.50	1.07	1.14	3.69	2.07	7.16	2.07
Vegetable Fresh Nes	13.09	10.53	9.01	15.08	7.65	21.67	3.57	3.81	12.28	6.91	23.85	6.90

Table B.5: VIRTUAL WATER TRADE BALANCE MATRIX Rows are exports and columns are imports. Irrigation efficiency not considered. Values used for calculation located in Table B.3

Table B.7: R^2 FOR PER CAPITA DEMAND RELATIONSHIPS (1975-2014 GDP PER CAPITA). Relationships for berseem, sugarcane, and seed cotton are done versus time instead of GDP per capita. * indicates significance at p = 0.05 ** indicates significance at p = 0.01

Commodity	**R^2**	**Commodity**	**R^2**
Maize	0.83 **	Bean (Dry)	0.13 *
Wheat	0.5 **	Chickpea	0.00

Commodity	**R^2**	**Commodity**	**R^2**
Rice	0.22 **	Lentil	0.22 **
Seed Cotton	0.89 **	Bean (Green)	0.00
Sugarcane	0	Lemon & Lime	0.1 *
Sugar beet	0.86 **	Apple	0.77 **
Banana	0.92 **	Mango	0.80 **
Barley	0.35 **	Date	0.77 **
Broad Bean	0.03	Watermelon	0.19 **
Berseem	0.84 **	Sunflower Seed	0.22 **
Grape	0.80 **	Garlic	0.04
Groundnut	0.67 **	Strawberry	0.90 **
Olive	0.87 **	Vegetable Leguminous n.e.s.	0.47 **
Onion, Dry	0.07	Artichoke	0.60 **
Orange	0.06	Cabbage	0.06
Potato	0.63 **	Carrot & Turnip	0.13 *
Tomato	0.77 **	Cauliflower & Broccoli	0.27 **
Sorghum	0.57 **	Chili Pepper (Green)	0.79 **
Soybean	0.69 **	Cucumber	0.22 **
Eggplant	0.79 **	Cotton Lint	0.50 **
Melon	0.41 **	Cottonseed Cake	0.05
Peach & Nectarines	0.54 **	Sugar (Raw Eq.)	0
Pumpkin & Squash	0.17 **	Molasses	0.14 *
Sweet Potato	0.62 **	Soybean Cake	0.36 **
Tangerine, Clementine, & Mandarin	0.89 **	Cottonseed Oil	0.75 **
Vegetables Fresh n.e.s.	0.04	Maize Oil	0.61 **
Beef	0.03	Palm Oil	0.43 **
Buffalo	0.02	Tea	0
Chicken	0.01	Sunflower Cake	0.45 **
Sheep	0.0	Milk (Whole)	0.49 **
Cheese	0.46 **	Milk (Skim)	0.38 **
Butter	0.00	Milk (Dried)	0.23 **
Eggs (Hen, In Shell)	0.17 **		

Crop to Increase	Additional Exports (thousand tonnes)	Export Price ($/m^3)	Money to Make (million $)	Water Needed (Mm^3)
Tomato	46.0	$3.16	20.6	6.5
Green Beans	33.6	$3.73	33.4	9.0
Watermelon	20.7	$6.47	12.3	1.9
Molasses	12.2	$3.27	6.6	6.6
Strawberry	76.2	$3.11	66.9	21.5
Cabbage	1.8	$3.47	1.3	0.4
Cauliflower & Broccoli	2.0	$5.48	1.9	0.3
Chili Pepper (Green)	10.0	$5.82	9.0	1.6
Cucumber	1.0	$5.35	1.1	0.2
Eggplant	0.5	$3.25	0.5	0.1
Melon	8.9	$4.00	6.0	1.5
Sweet Potato	19.6	$4.77	10.3	2.2
Totals	232.5		169.9	51.7

Crop to Reduce	Amount to Reduce (Mm^3)	Reduction in Production (thousand tonnes)	Money Needed to Import Replacement (Million $)
Wheat	62.5	69.4	22.6
Maize	65.8	62.0	19.1
Rice	51.1	52.1	22.5
Barley	2.7	1.3	0.5
Sorghum	3.6	7.1	3.6
Berseem	94.6	29.0 (Beef Reduction)	101.6
Totals	280.3	220.8	169.9
		Trade Balance	4.4

Table B.6: VIRTUAL WATER TRADE BALANCE POLICY PROPOSAL Policy Proposal for doubling exports. The principle for reduction is a proportional decrease based on the current amount of water currently used in Egypt to produce cereal crops. The principle for increase in export goods is a proportional increase in the amount of exports (i.e. increase the export of the selected goods by x%). Ultimately, a doubling of the export goods below produces enough revenue to buy cereal goods at a water share amplification of 4.4. (51.7 Mm^3 are consumed to buy cereal crops that would normally consume 280.3 Mm^3). Values used in calculation can be seen in Table B.2. Irrigation Method and efficiency are not considered.

Occurrence of Extreme Caution Days (+23.5 degrees) & Hot Nights (+20.5 degrees) Heat Wave Events

CNRM-CM5 & 2000 LULC	Period Total Exceedance Days	Days in HW Events (days)	Average Length of HW Event (days)	Average HW Day TWmax Exceedance (C)
Historical (1975-2004)	462	434	5.38	0.99
Future (2070-2099)	2257	2243	18.19	1.43

CNRM-CM5 & 1900 LULC	Period Total Exceedance Days	Days in HW Events (days)	Average Length of HW Event (days)	Average HW Day TWmax Exceedance (C)
Historical (1975-2004)	434	407	5.59	0.95
Future (2070-2099)	2196	2184	17.83	1.30

ERA5 - ExC	Period Total Exceedance Days	Days in HW Events (days)	Average Length of HW Event (days)	Average HW Day TWmax Exceedance (C)
Historical (1975-2004)	846	796	6.06	1.04

Occurrence of Danger Days (+26.5 degrees) & Hot Nights (+20.5 degrees) Heat Wave Events

CNRM-CM5 & 2000 LULC	Period Total Exceedance Days	Days in HW Events (days)	Average Length of HW Event (days)	Average HW Day TWmax Exceedance (C)
Historical (1975-2004)	0	0	~	~
Future (2070-2099)	417	390	5.86	0.97

CNRM-CM5 & 1900 LULC	Period Total Exceedance Days	Days in HW Events (days)	Average Length of HW Event (days)	Average HW Day TWmax Exceedance (C)
Historical (1975-2004)	0	0	~	~
Future (2070-2099)	242	214	5	0.94

ERA5 - D	Period Total Exceedance Days	Days in HW Events (days)	Average Length of HW Event (days)	Average HW Day TWmax Exceedance (C)
Historical (1975-2004)	13	10	2.5	0.74

Figure B-1: Heat wave statistics for CNRM-CM5 simulations

Occurrence of Extreme Caution Days (+23.5 degrees) & Hot Nights (+20.5 degrees) Heat Wave Events

HadGEM2-ES & 2000 LULC	Period Total Exceedance Days	Days in HW Events (days)	Average Length of HW Event (days)	Average HW Day TWmax Exceedance (C)
Historical (1975-2004)	250	229	4.61	0.86
Future (2070-2099)	2827	2818	34.2	1.58

HadGEM2-ES & 1900 LULC	Period Total Exceedance Days	Days in HW Events (days)	Average Length of HW Event (days)	Average HW Day TWmax Exceedance (C)
Historical (1975-2004)	229	213	4.29	0.85
Future (2070-2099)	2751	2743	32.14	1.41

ERA5 - ExC	Period Total Exceedance Days	Days in HW Events (days)	Average Length of HW Event (days)	Average HW Day TWmax Exceedance (C)
Historical (1975-2004)	846	796	6.06	1.04

Occurrence of Danger Days (+26.5 degrees) & Hot Nights (+20.5 degrees) Heat Wave Events

HadGEM2-ES & 2000 LULC	Period Total Exceedance Days	Days in HW Events (days)	Average Length of HW Event (days)	Average HW Day TWmax Exceedance (C)
Historical (1975-2004)	0	0	~	~
Future (2070-2099)	829	802	8.32	0.94

HadGEM2-ES & 1900 LULC	Period Total Exceedance Days	Days in HW Events (days)	Average Length of HW Event (days)	Average HW Day TWmax Exceedance (C)
Historical (1975-2004)	0	0	~	~
Future (2070-2099)	499	477	8.28	0.97

ERA5 - D	Period Total Exceedance Days	Days in HW Events (days)	Average Length of HW Event (days)	Average HW Day TWmax Exceedance (C)
Historical (1975-2004)	13	10	2.5	0.74

Figure B-2: Heat wave statistics for HadGEM2-ES simulations

Appendix C

Chapter 2 Supplementary Figures

This appendix provides supplementary figures described in the text of Chapter 2.

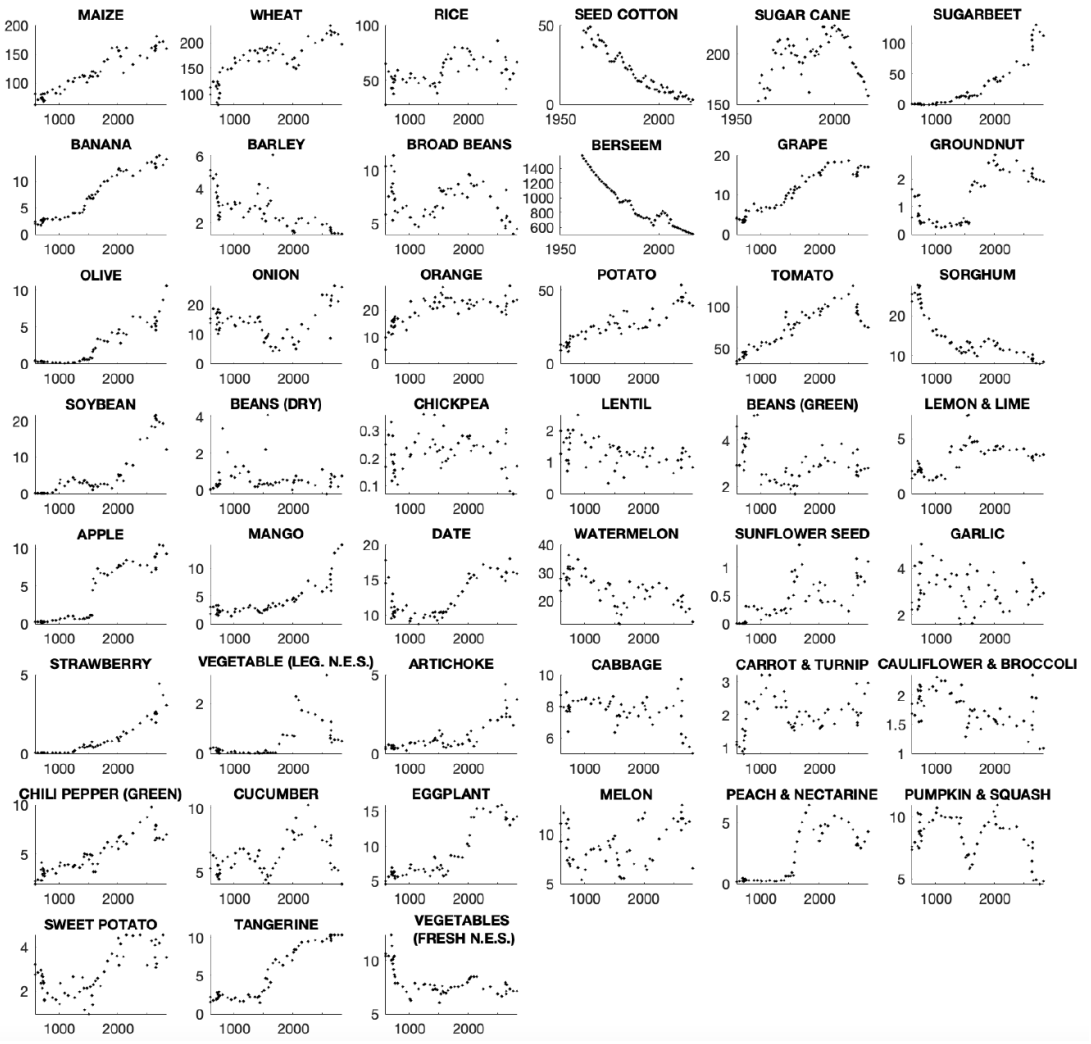

Figure C-1: Demand per capita (kg/capita/year) vs. GDP per capita (2010 USD/capita/year) relationships for individual crops (except sugarcane, berseem, and seed cotton which are time dependent relationships). Data Sources in Table B.1: (4) (6) (7) (8) (11)

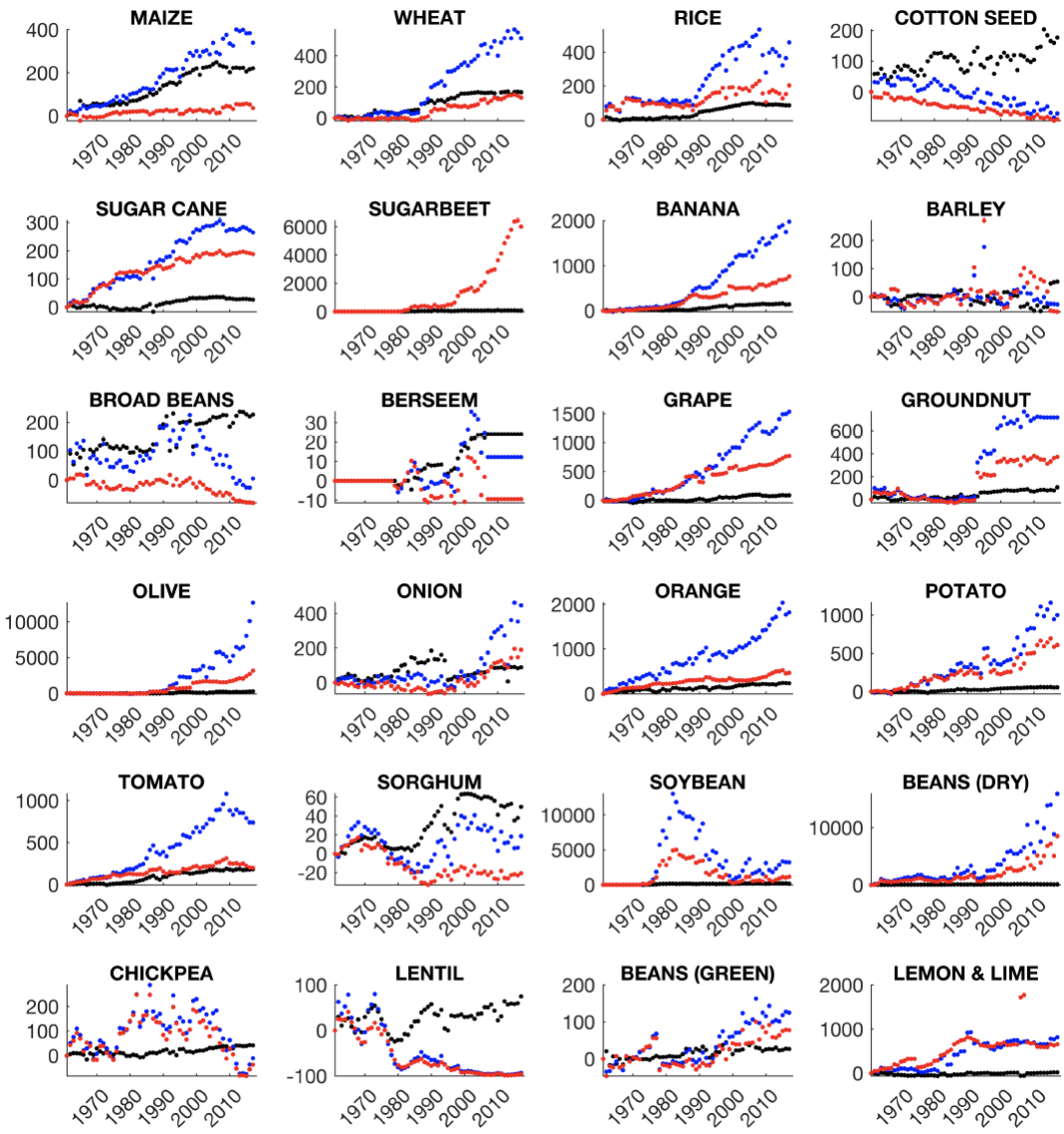

Figure C-2: Change relative to 1961 (%) of production (tonnes) [blue], yield (hg/ha) [black], and harvested area (ha) [red] of primary crops used in analysis. Data Sources in Table B.1: (7) (8)

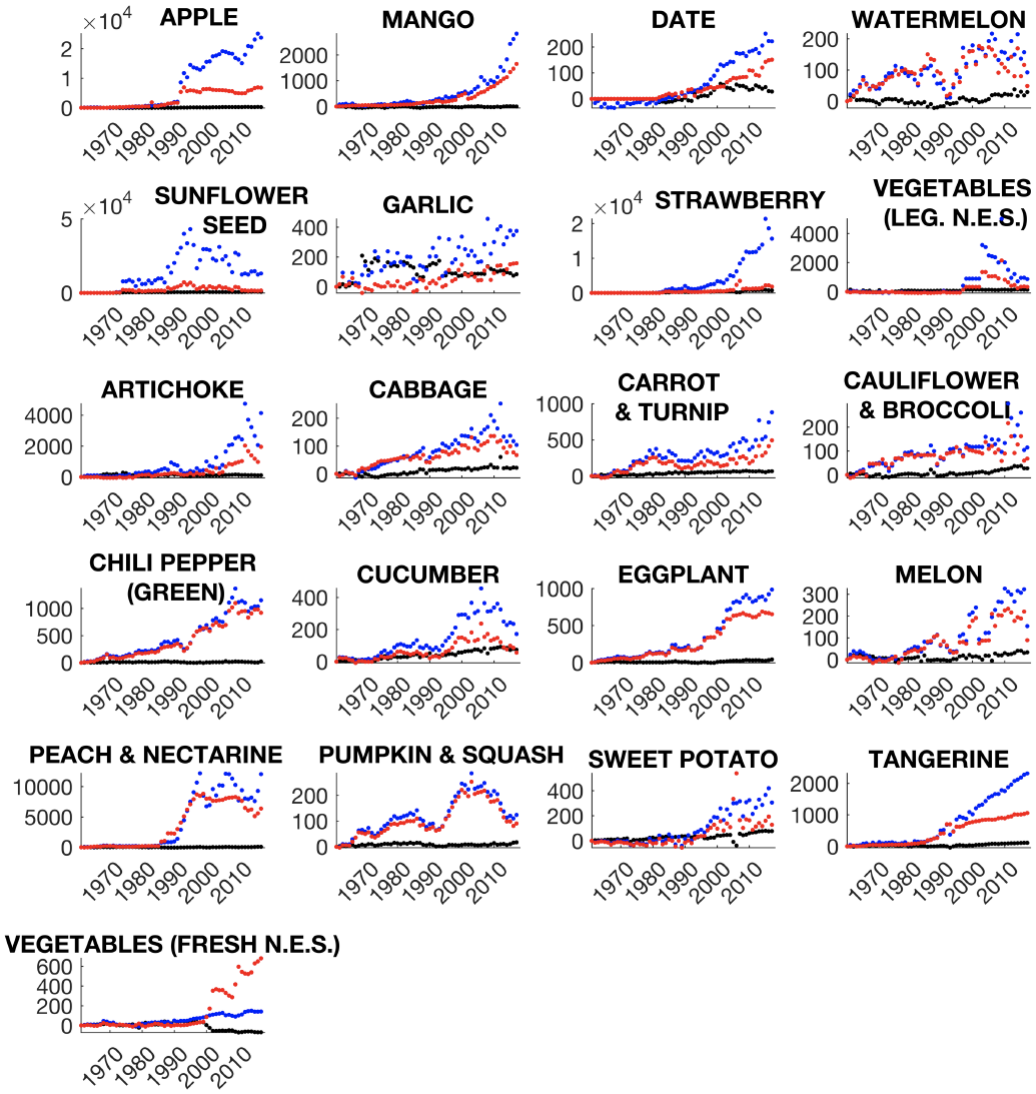

Figure C-3: Figure C-2 continued

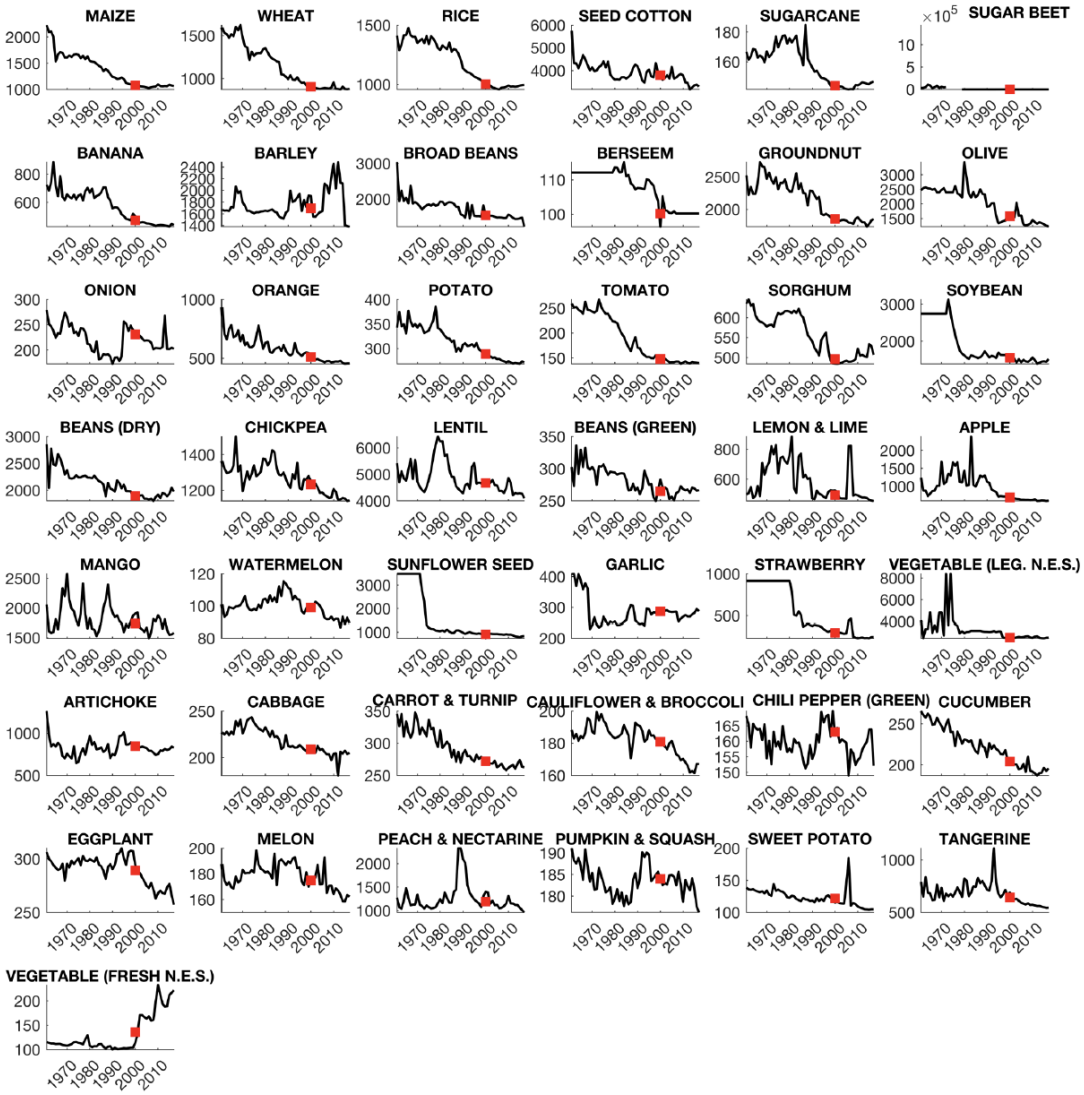

Figure C-4: Water consumption requirements for individual crops used in historical reconstruction (m^3/tonne). The red square indicates the base water consumption value from the literature [31] for the 1996-2005 period. Data Sources in Table B.1: (1) (7) (8)

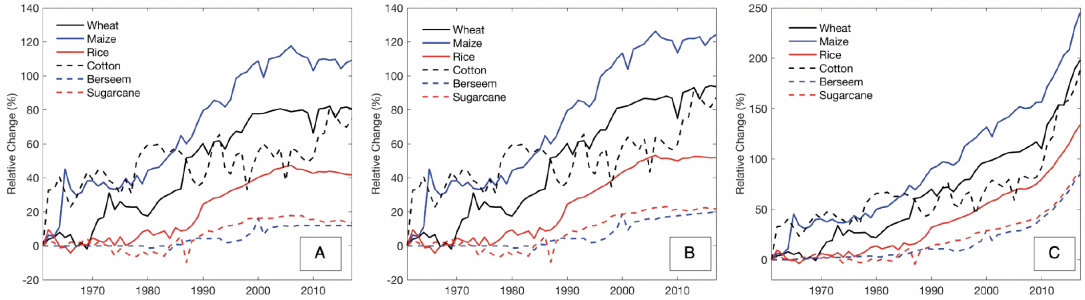

Figure C-5: (a) Water consumption requirement for major water consuming crops scaled using 1961 irrigation application efficiency (tonnes/m^3). 1961 values for wheat, maize, rice, cotton, berseem, and sugarcane are 0.0006, 0.0004, 0.0007, 0.0002, 0.0043, and 0.006 tonnes/m^3 respectively. (b) Evolving irrigation efficiency scaled water consumption requirement for major water consuming crops (tonnes/m^3). (c) Evolving irrigation efficiency scaled water consumption requirement for major water consuming crops also including proportion of reuse (tonnes/m^3). Data Sources in Table B.1: (1) (7) (8) (16) (18)

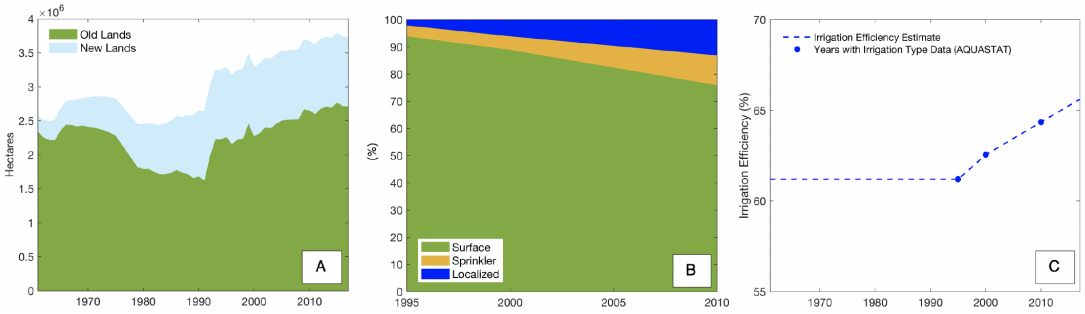

Figure C-6: Development of agricultural area in Egypt and use of irrigation technologies. (a) Old vs. New Land agricultural area (ha) in Egypt using total cropland data (FAO) and details on new land acquisition (Karajeh et al. (2013)) (b) Proportion of land using various irrigation technologies (%). Values are available for 1995, 2000, and 2010 and interpolated between (Data Source: (18)). (c) Estimate of country average irrigation efficiency (%) determined using the proportion of irrigation type in panel b and the FAO stated efficiency of the relative irrigation technologies. (Brouwer et al. (1989)); Karajeh, F., Oweis, T., Swelam, A., El-Gindy, A-G., El-Quosy, D. E. D., Khalifa, H., El-Kholy, M., El-Hafez, S. A. Water and Agriculture in Egypt. (Beirut, Lebanon: Food and Agriculture Organization of the United Nations (FAO), 2013) https://hdl.handle.net/20.500.11766/7872; Brouwer, C., Prins, K., & Heibloem, M. Annex 1: Irrigation Efficiencies. In Irrigation Water Management: Irrigation Scheduling: Training Manual 4. (1989) http://www.fao.org/3/t7202e/t7202e08.htm

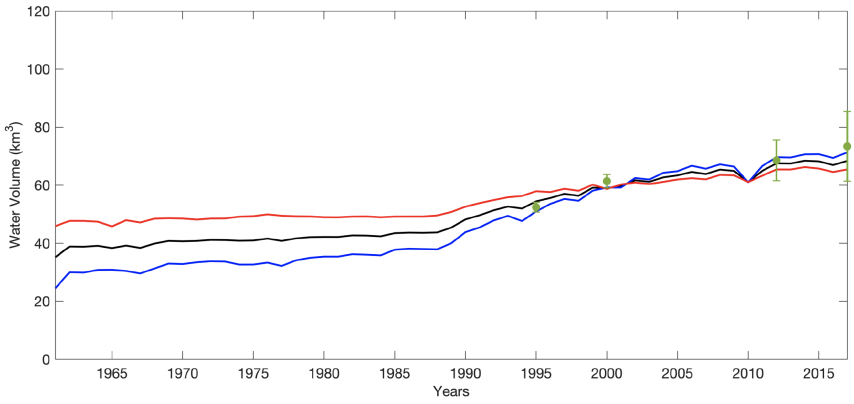

Figure C-7: Historical water use (km^3) for agriculture. Green data points show official data for Agricultural use. Error bars represent literature-derived estimates of agricultural drainage reuse, groundwater recharge reuse, and wastewater reuse with the assumption that all reuse is applied to agricultural purposes. The lines show bottom-up crop-data based estimates for agricultural use using three different crop water consumption assumptions: 1) constant tonnage water requirement (m^3/tonne) [blue] 2) constant area water requirement (m^3/ha) [red] 3) average of (1) and (2) (m^3/tonne) [black solid]. Data Sources in Table B.1: (1) (2) (7) (8) (16)

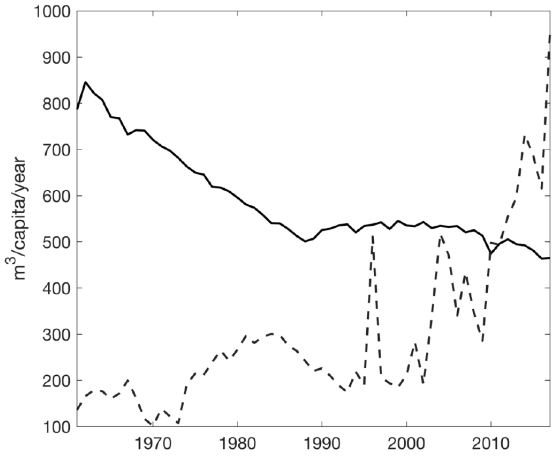

Figure C-8: a) Historical per capita water consumption (m^3/capita/year) for agricultural production [black solid] and historical per capita water embodied in primary and secondary crop imports (m^3/capita/year) [black dashed]. Data Source in Table B.1: (1) (2) (4) (7) (8) (11)

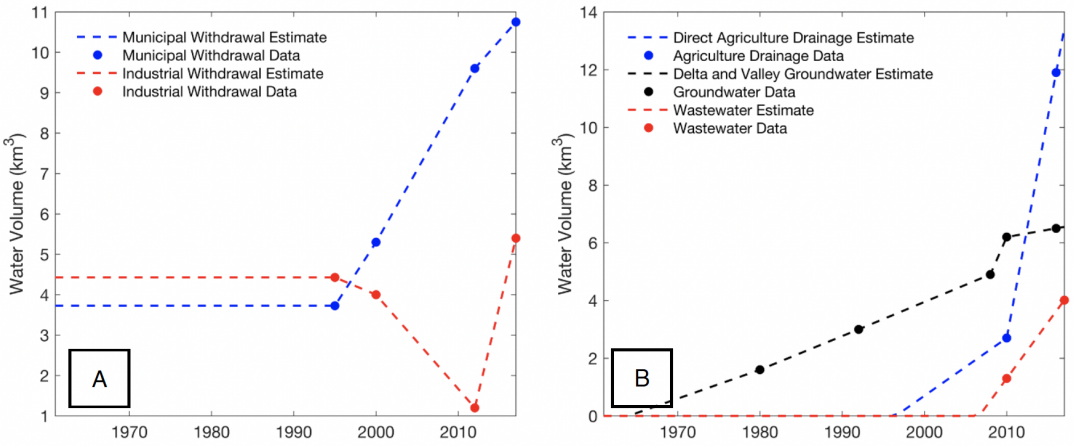

Figure C-9: Historical estimates for (a) municipal use (km^3) and industrial use (km^3) and (b) three components of reuse (km^3). Data Sources: (A) Municipal – (16); (A) Industrial – (16); (B) Direct Agricultural Drainage Reuse: 2010 (16); 2016 (16); (B) Wastewater Reuse: 2010 (16); 2017 (16); (B) Delta and Valley Groundwater Reuse: 1980 [226]); 1992 [171]; 2008 [171]; 2010 [148]; 2016 [69]

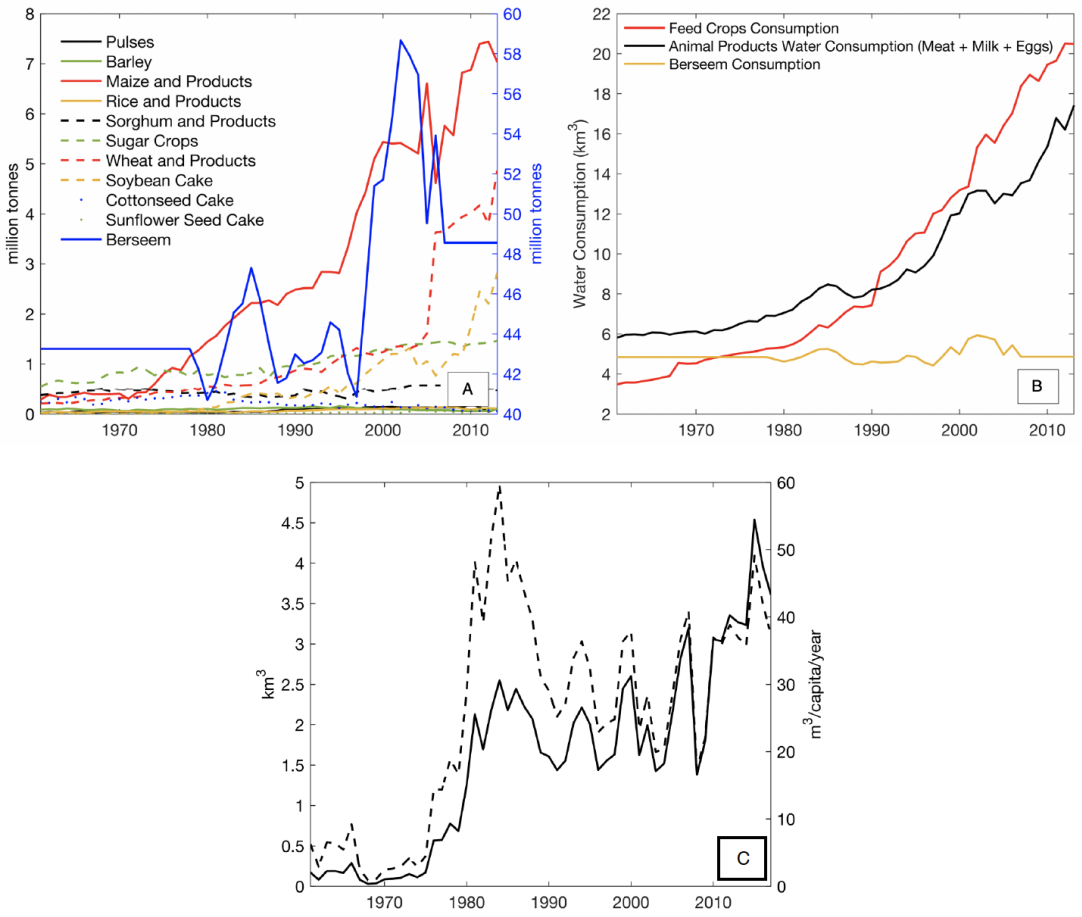

Figure C-10: (a) Feed products in Egypt (tonnes) (b) Estimates of water consumption (km^3) associated with feed products in panel (a) vs. consumption associated with animal product production in Egypt (meat, milk, and eggs) (c) Total virtual water import (km^3) (consumption equivalent) associated with animal products [black] and historical per capita water embodied in animal product imports (m^3/capita/year) [black dashed]. Data Source in Table B.1: (1) (3) (4) (7) (8) (9) (10) (11)

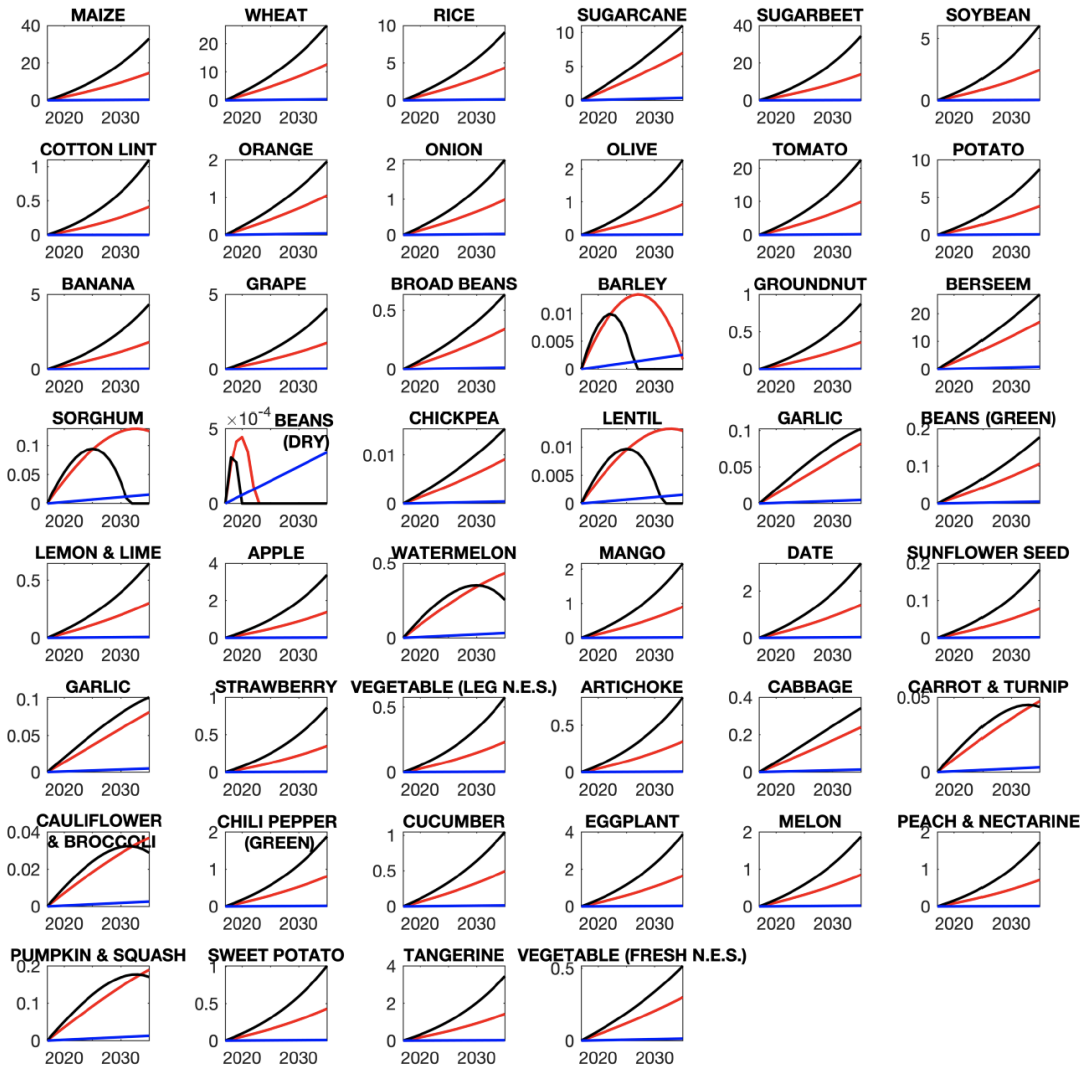

Figure C-11: Future additional demand (million tonnes) in a given year vs. 2017 for primary crops and cotton lint bounded by two scenarios: 4.5% GDP per capita growth and 2.5% population growth [black] and 0% GDP per capita growth and 0.1% population growth [blue]. The nominal growth scenario (2.3% GDP per capita growth and 1.7% population growth is shown in red. Data Source in Table B.1: (1) (2) (4) (6) (7) (8) (11)

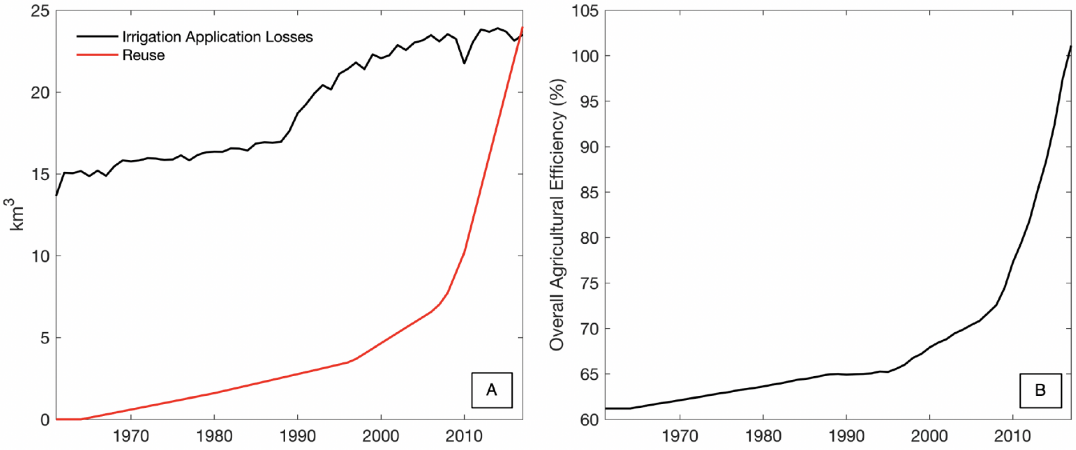

Figure C-12: (a) Volume of water withdrawn for agriculture but not used directly for crop evapotranspiration [black] and amount of reuse (treated municipal wastewater, direct use of agricultural drainage, use of local groundwater recharge) [red]. Note that the reuse exceeds the water surplus because a small amount of reuse is initially withdrawn for municipal purposes (treated municipal wastewater). (b) a measure of the true system efficiency by using net losses (application losses minus reuse).

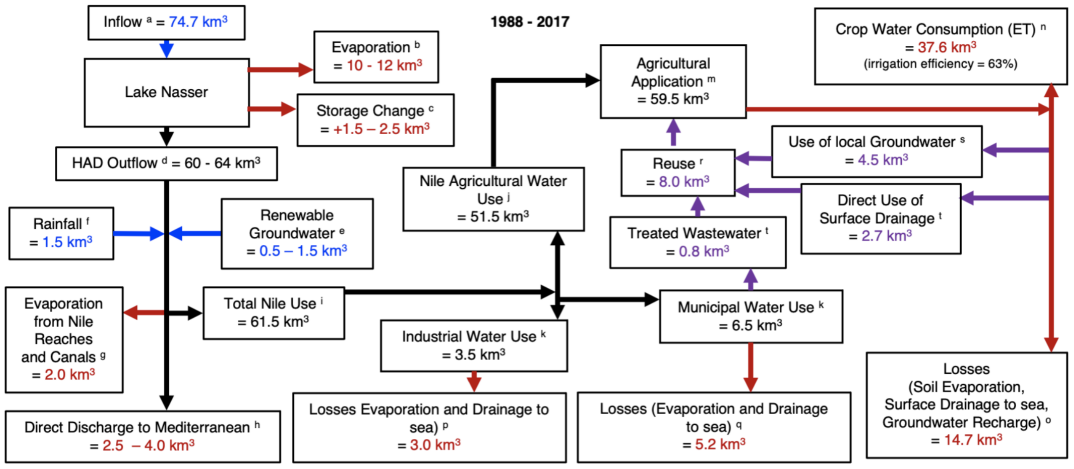

Figure C-13: Egyptian Nile Water System 1988-2017 average annual fluxes (km^3/yr). Red values are sinks, blue are sources, and purple indicates reuse. See Fig. 2-10 for Data Sources.

Appendix D

Chapter 3 Supplementary Material

The importance of SST teleconnections to regional climate in the Central U.S. is particularly well shown through the connection of the North Atlantic Subtropical High (NASH) and the Great Plains Lower-Level Jet (GPLLJ). As discussed in Chapter 3, there is a documented connection between a warm North Atlantic, cold Tropical Pacific, and hot and dry conditions in the Central U.S. and Great Plains. These same conditions – in particular in the North Atlantic – have been linked to complementary changes in the GPLLJ [274] [272].

One of the proposed connecting mechanisms between the North Atlantic SSTs and the Central U.S. is the modification of the NASH and through it the GPLLJ. The GPLLJ is a boundary layer and lower tropospheric feature that is defined by its high wind intensity aloft, vertical shear profile, and ability to transport moisture [103] [25]. In the United States, this feature is roughly 250 km wide and has a strong diurnal cycle with a nighttime peak and higher frequency of occurrence in the spring and summer [25]. It is formed through a proposed combination of inertial oscillation due to boundary layer decoupling and frictional effects [23] [43] and baroclinicity on sloping terrain [109]. This feature is consistent with strong moisture advection into the continental US, with 1/3 of moisture transport into the region being attributed to the structure [103].

MRCM can resolve the GPLLJ in its higher resolution as seen in Figure D-1 in a short simulation forced with ERA-Interim. The plot shows the time series of wind

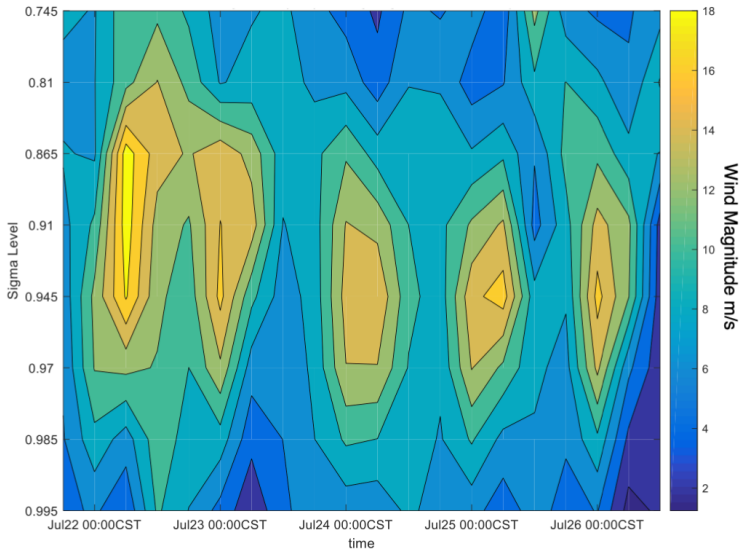

Figure D-1: Vertical profile of wind-speed (m/s) in lowest eight model sigma levels for the grid point 37N, 97W in a short term simulation in MRCM forced with ERA-Interim.

vector magnitude for the 8 lowest sigma levels and shows a peak wind speed of 18 m/s occurring just after midnight. The peak occurs just below the 850 mb pressure level at roughly 800 m, with the classic profile of vertical shear above and below the maximum, as well as an accurate representation of jet timing (Fig. D-2) with a peak at midnight.

While the connections between SST anomalies and the Great Plains Lower-Level Jet are still a topic of research, it has been proposed that the GPLJJ is impacted through a westward expansion of the NASH which is in turn modified by the North Atlantic Oscillation (NAO) and a proposed connection to the Atlantic Multi-decadal Oscillation (AMO) [274] [273] [34] [200] [177].

We can see this connection through maps of the average wind and pressure patterns associated with high and low SST anomalies in the two key regions (Fig. D-3). The figures show the upper and lower quartile of years for selected SST anomalies (9 years in each group) averaged over all years in the group relative to the full period average. SSTs are standardized detrended SST anomalies from ERSSTv5 and atmospheric data is obtained from ERA-Interim for 1979-2016 for a total of 38 years. Arrows show wind anomalies and shading shows the corresponding geopotential height

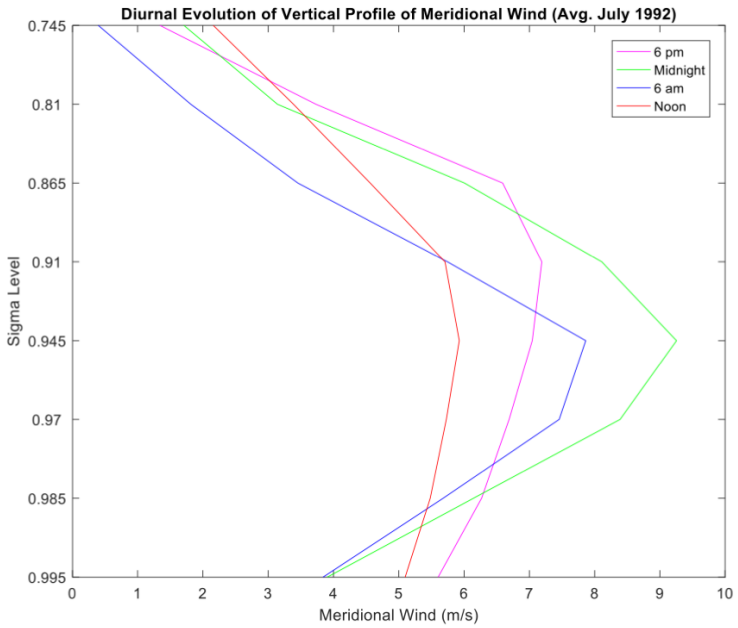

Figure D-2: Synoptic evolution of the vertical profile of meridional wind (m/s) averaged over July 1992 at the same grid point as Figure D-1

anomaly. During upper quartile years for the North Atlantic and lower quartile years for the Tropical Pacific, wind flow is northerly in the jet region. The opposite pattern exists for lower quartile North Atlantic SST and upper quartile Tropical Pacific SST.

This connection can also be explored through two contrasting hydroclimate events, the Dust Bowl drought of the 1930s and the Midwestern flood of 1993. In the 1930s the Midwest and Great Plains of the United States experienced the Dust Bowl - a large-scale, long-lasting meteorological drought event - with impacts of prolonged heat and dryness spreading far beyond the traditionally portrayed landscapes of the Oklahoma plains. While drought events are characterized primarily through precipitation deficits, the Dust Bowl emerges as a devastating event in the climate record due to its accompanying temperature anomalies (Fig. D-4). While there are several other major droughts in the regional record – particularly the 1950s drought – the extent, duration, and magnitude of the 1930s Dust Bowl's simultaneous precipitation and temperature anomalies as well as the widespread socio-economic impact mark it as the most significant summer event in this region during the observational period [31] [135] [52]. Studies have shown that the inception of the Dust Bowl was in large part

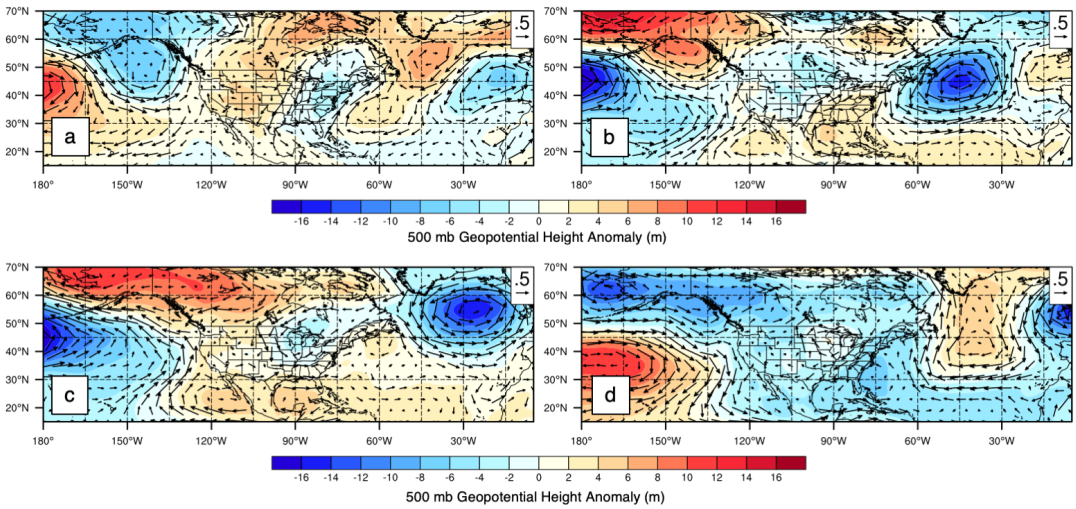

Figure D-3: a) Average July-August 850 mb wind anomaly for upper quartile North Atlantic SST anomaly years. Shading shows geopotential anomaly. b) same as (a) but for lower quartile of years. c) same as (a) but for Tropical Pacific SST. d) same as (b) but for Tropical Pacific SST.

due to sea surface temperature anomalies that have been linked to the occurrence of drought like conditions in the Southern and Central United States [232]; Further studies have shown that the extraordinary scope of the conditions may have been enhanced by a feedback loop of dust aerosols and vegetative loses [39] [37] as well as modifications in atmospheric structures and moisture transport mechanisms such as the GPLLJ [29] [38]. During the Dust Bowl period, anomalies in the North Atlantic were at their highest in the 20th century, and coincident with a negative tropical pacific pattern.

The 1993 flood is marked by negative anomalies in temperature and positive precipitation anomalies, as well as a strong southerly wind anomaly and opposite SST anomalies to the Dust Bowl Period (Fig. D-5). However, Patricola (2015) showed a linkage of the GPLLJ to the 1993 event but they concluded that this event was not closely linked to SST anomalies [199]. This demonstrates the added complexity in connecting low-frequency SST patterns to short extreme events versus long-term hydroclimate anomalies.

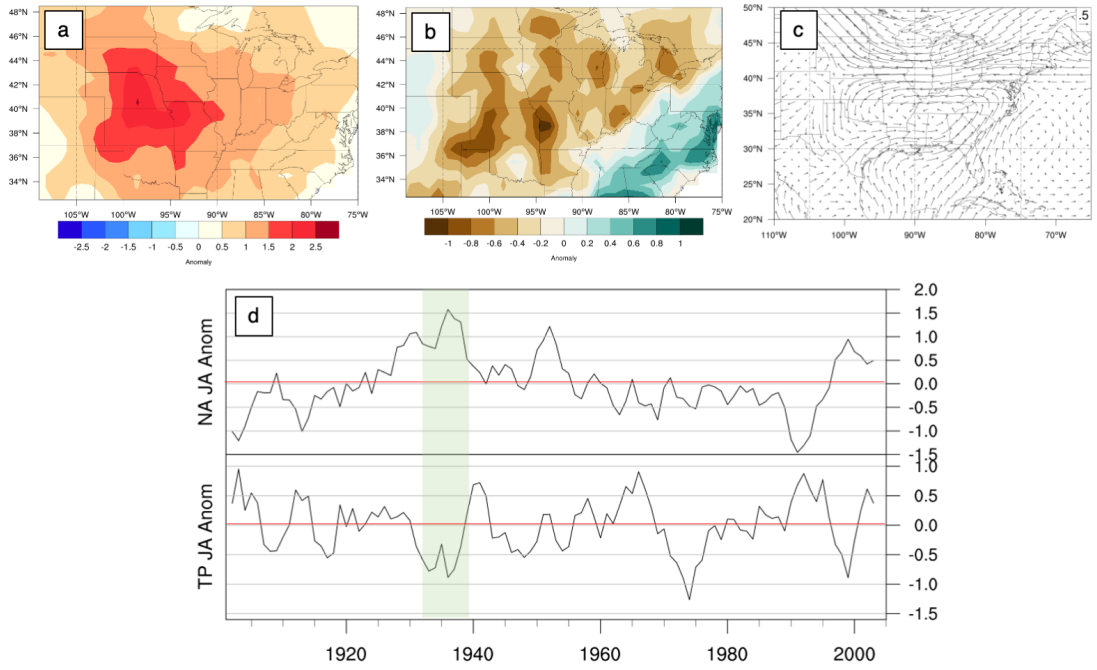

Figure D-4: July-August anomalies for 1932-1939 versus 1961-1990 in a) 2m air temperature (C) in CRUTS4.01 b) Precipitation (mm/day) in CRUTS4.01 c) 850 mb wind anomaly (m/s) in CERA20C and d) area averaged 4-year moving average SST anomaly in the North Atlantic (top) and Tropical Pacific (bottom)

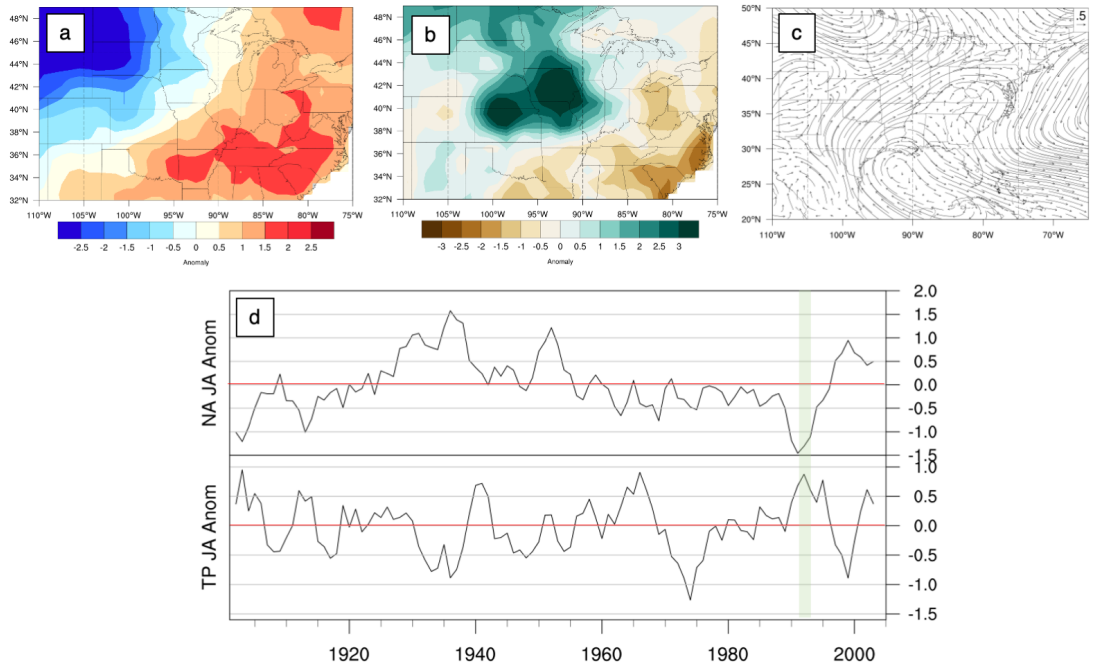

Figure D-5: July-August anomalies for 1993 versus 1961-1990 in a) 2m air temperature (C) in CRUTS4.01 b) Precipitation (mm/day) in CRUTS4.01 c) 850 mb wind anomaly (m/s) in CERA20C and d) area averaged 4-year moving average SST anomaly in the North Atlantic (top) and Tropical Pacific (bottom)

Appendix E

Chapter 4 Supplementary Figures

This appendix provides supplementary figures described in the text of Chapter 4.

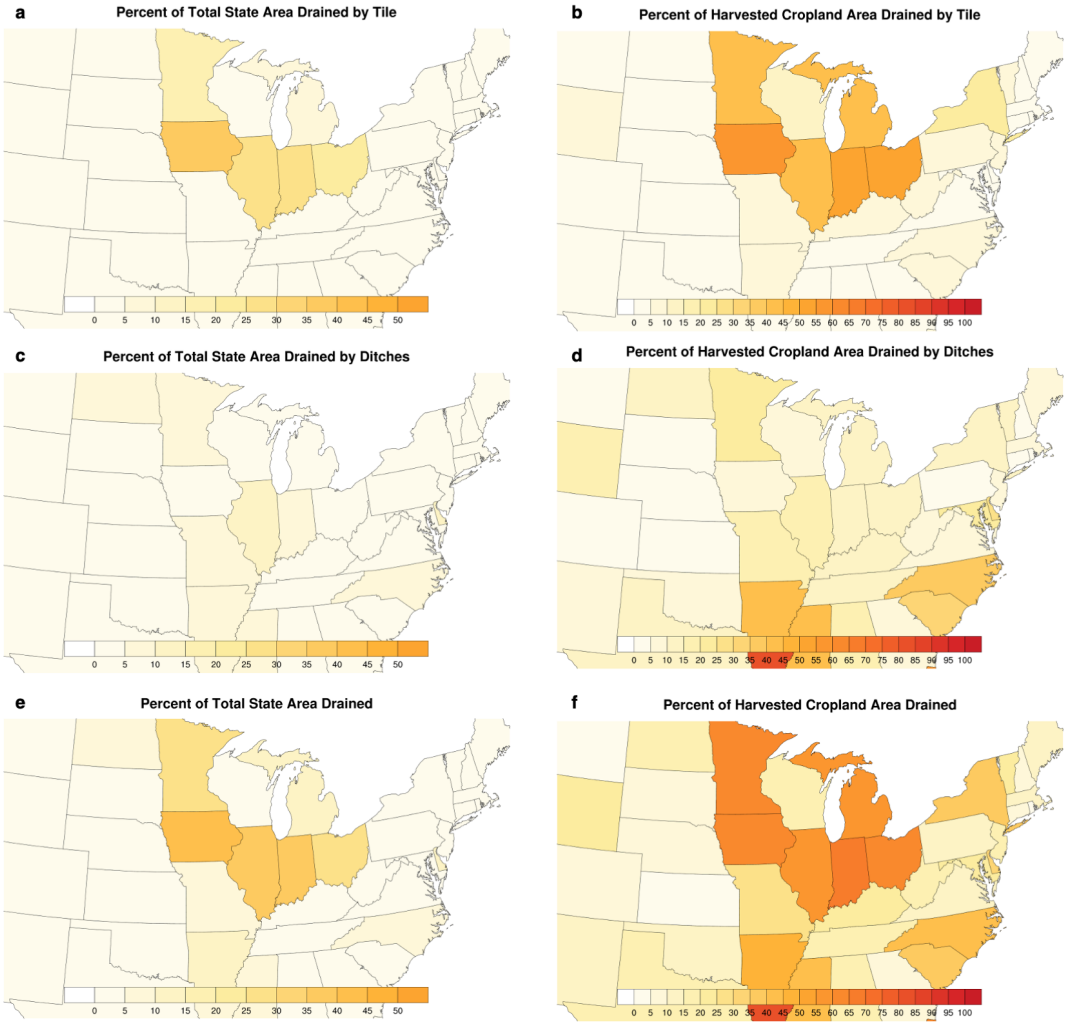

Figure E-1: Distribution of subsurface (tile) drainage area (ha) in the United States in 2017 as a percentage of (a) total area and (b) cropland area [261] (c-d) same as (a-b) for ditch drainage (e-f) same as (a-b) for total (tile + ditch) drainage.

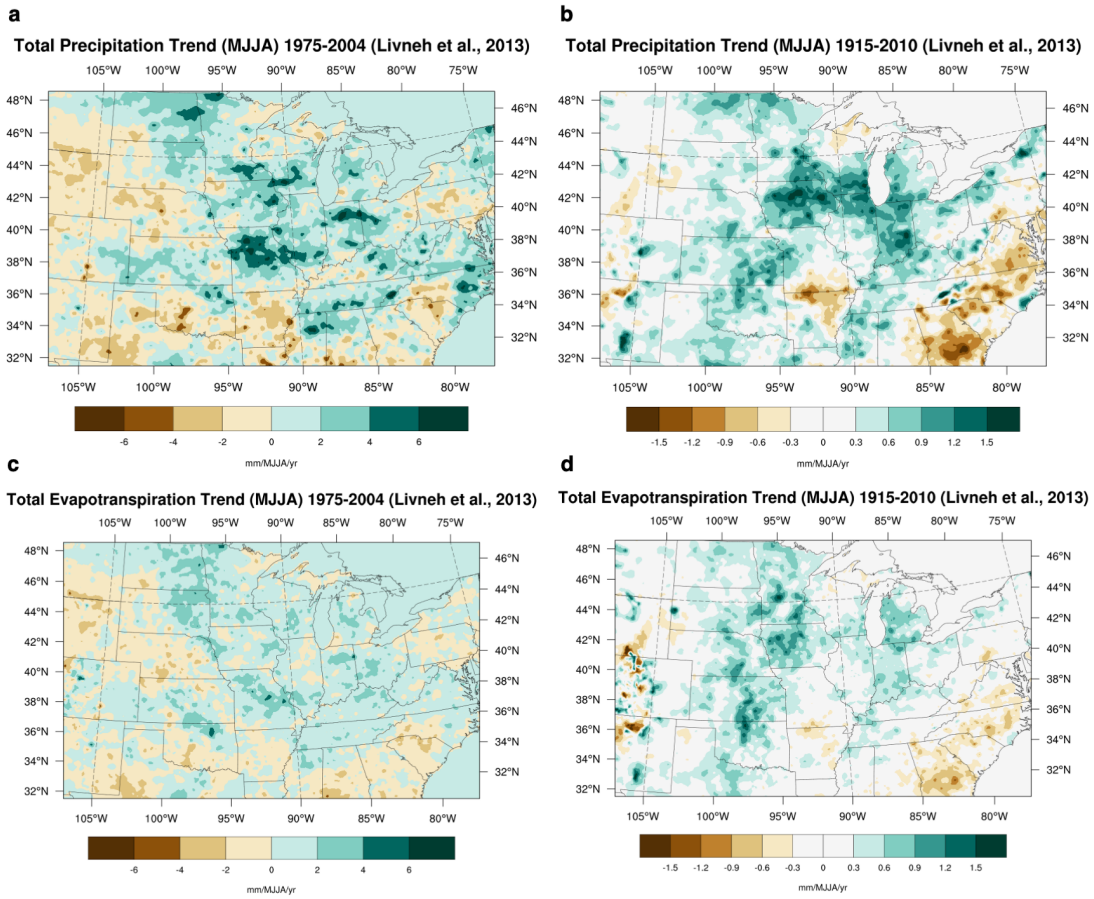

Figure E-2: Long term historical trends in observations for a) MJJA total precipitation from 1975-2004 (mm/MJJA) b) MJJA total precipitation from 1915-2010 (mm/MJJA) c) same as (a) but for evapotranspiration d) same as (b) but for evapotranspiration ([140]).

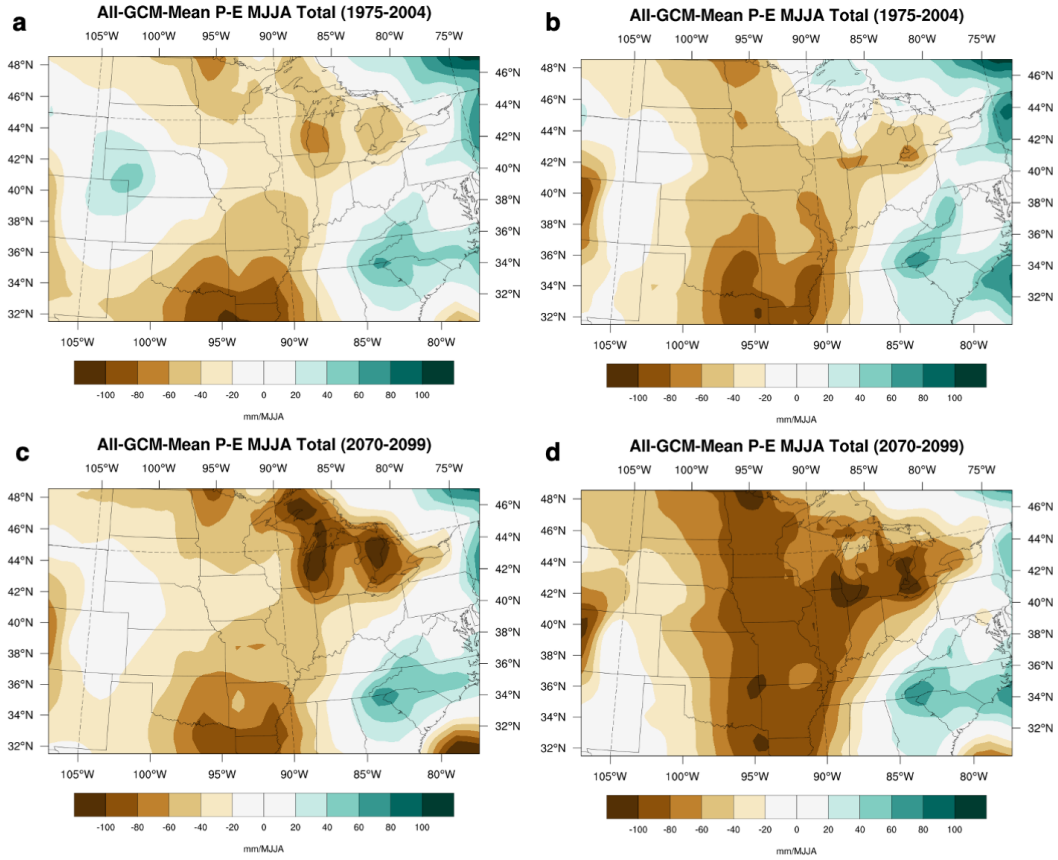

Figure E-3: Average MJJA total Multi-Model-Mean Precipitation-Evapotranspiration (mm/MJJA) for a) Historical period (1975-2004) in CMIP5 b) Historical period (1975-2004) in CMIP6 c) Future period (2070-2099) under RCP8.5 in CMIP5 d) Future period (2070-2099) under RCP8.5 in CMIP6

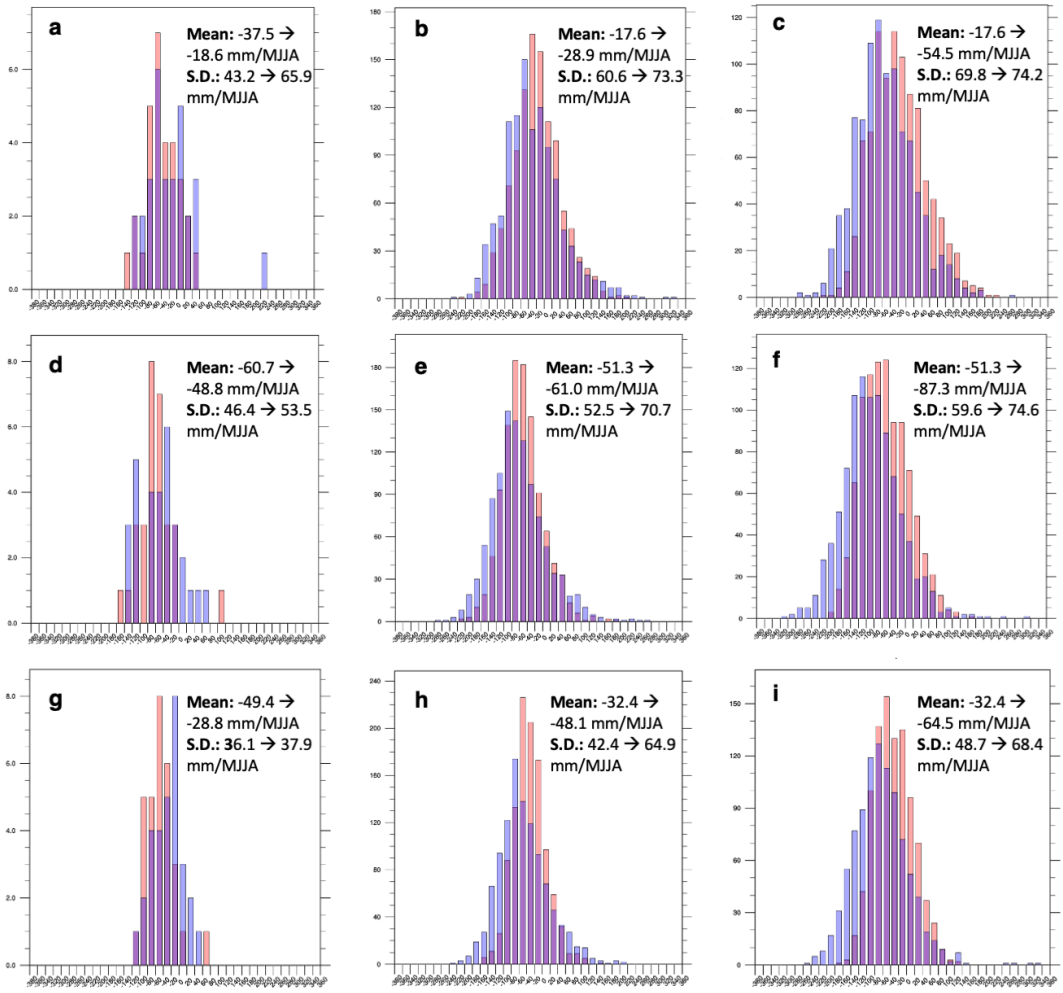

Figure E-4: a) Frequency of Region 1 (264.5-268.5°E,39.5-45.5°N) average May-August total P-E in the observations in early period (1915-1944) [red] and late period (1975-2004) [blue] b) Frequency of Region 1 bias-corrected average May-August Total P-E in all CMIP5 models in historical period (1975-2004) [red] and under RCP8.5 (2070-2099) [blue] c) same as (b) except for CMIP6 d-f) same as (a-c) for Region 2 (268.5-272.5°E,37.0-43.0°N) g-i) same as (a-c) for Region 3 (272.5-276.5°E,37.0-43.°N).

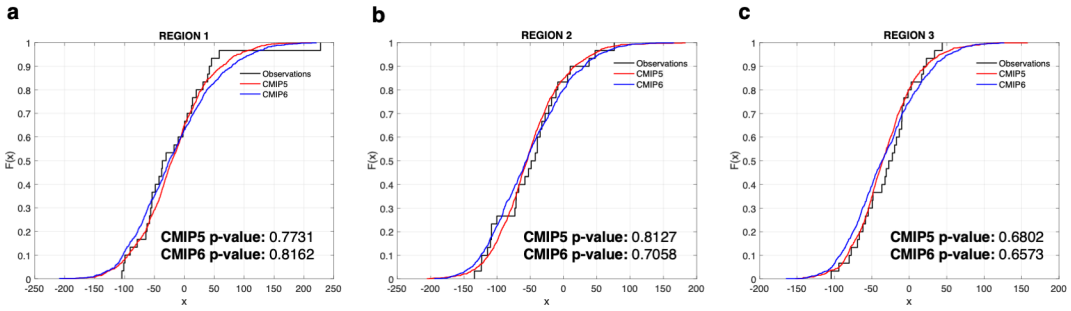

Figure E-5: Gaussian distribution quantile mapping bias-corrected CDF comparisons. KS-Test rejects null hypothesis at 5% significance if p-value < 0.05. If p-value > 0.05 then accept null hypothesis that data comes from the same distribution. (nobs = 30; nCMIP5 = 1080; nCMIP6 = 960) for a) Region 1 (264.5-268.5°E,39.5-45.5°N) b) Region 2 (268.5-272.5°E,37.0-43.0°N) and c) Region 3 (272.5-276.5°E,37.0-43.0°N).

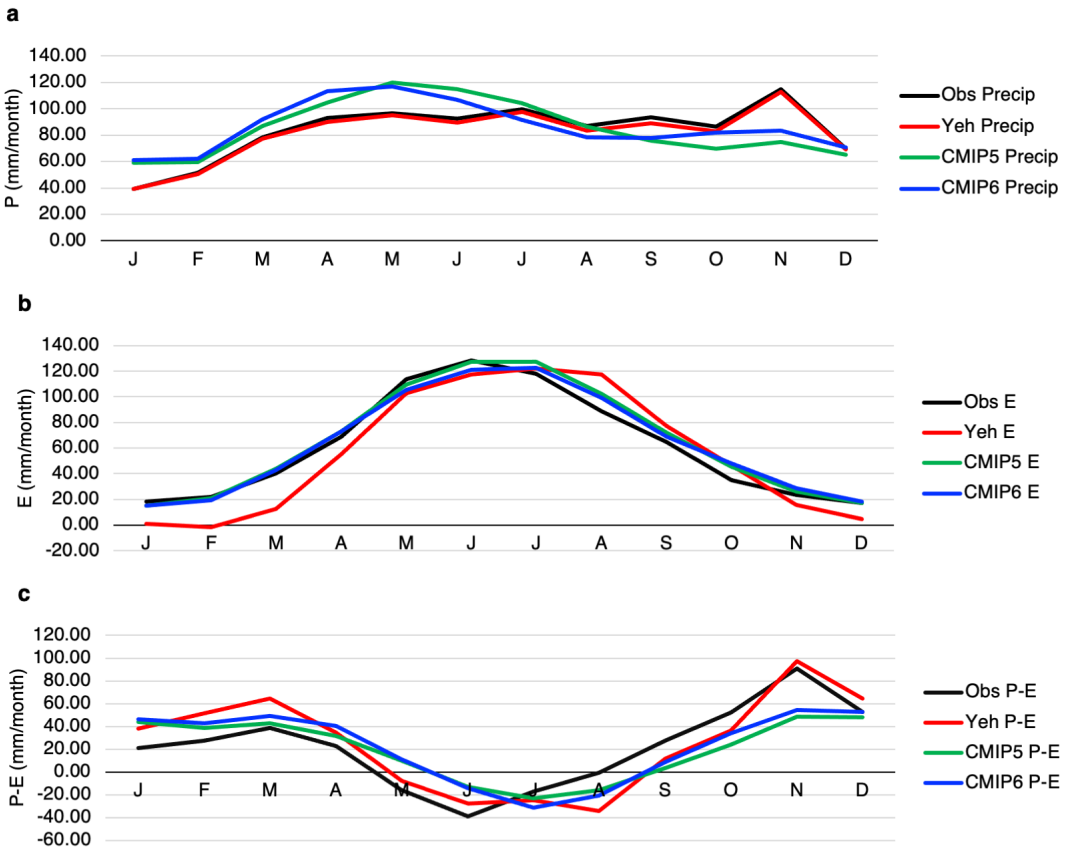

Figure E-6: 1983-1994 Average Climatology of a) Precipitation (mm/month) b) Evapotranspiration (mm/month) and c) Precipitation-Evapotranspiration (mm/month) for Illinois (268.5-272.5°E, 37.5-42.5°N). Observed data from [140] and Yeh data pulled from [287], CMIP5 and CMIP6 data is for the Multi-Model-Mean ensembles.

Appendix F

Chapter 5 Supplementary Figures

This appendix provides supplementary figures described in the text of Chapter 5.

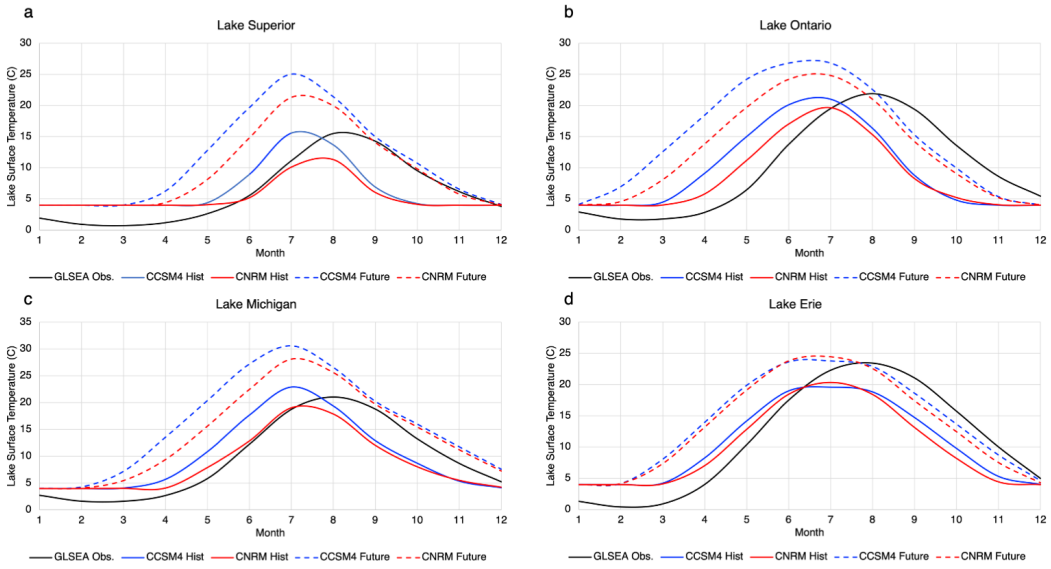

Figure F-1: Change in area average monthly climatology of lake surface temperatures (degrees C) from historical (1985-2004; solid lines) to future (2080-2099; dashed lines) for CCSM4-2000 (blue) and CNRM-CM5-2000 (red) for a) Lake Superior b) Lake Ontario c) Lake Michigan d) Lake Erie. Observations in the Historical period are from Great Lakes Surface Environmental Analysis (GLSEA) [186]

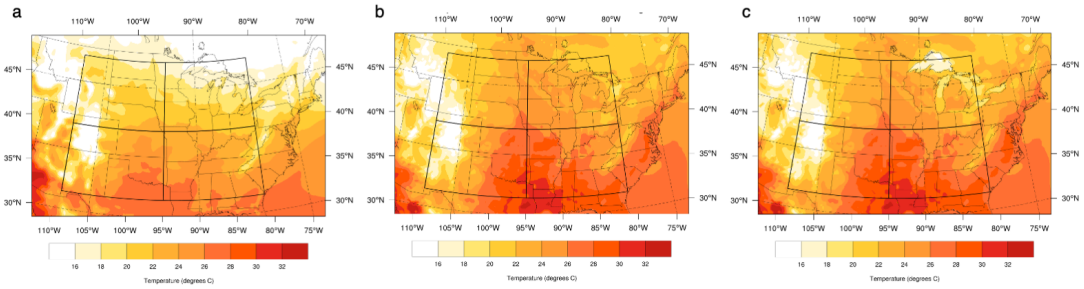

Figure F-2: a) 1975-2004 JJAS average of near surface air temperatures (degrees C) in ERA5 b) 1975-2004 JJAS average of near surface air temperatures (degrees C) in CCSM4-2000 without Lake Improvements c) 1975-2004 JJAS average of near surface air temperatures (degrees C) in CCSM4-2000 with Lake Improvements

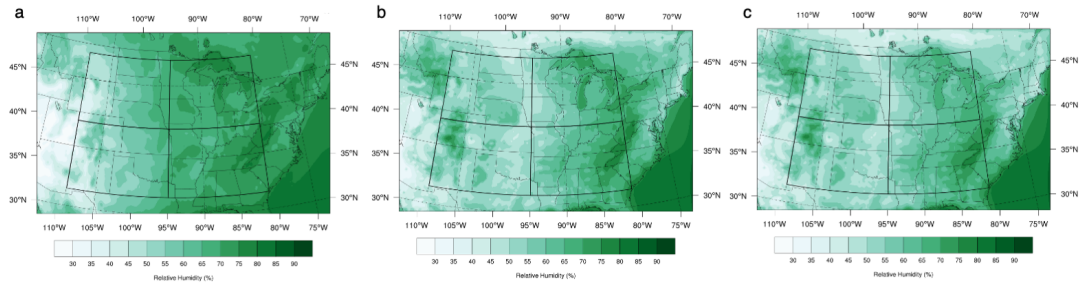

Figure F-3: a) 1975-2004 JJAS average of 2m relative humidity (%) in ERA5 b) 1975-2004 JJAS average of 2m relative humidity (%) in CCSM4-2000 without Lake Improvements c) 1975-2004 JJAS average of 2m relative humidity (%) in CCSM4-2000 with Lake Improvements

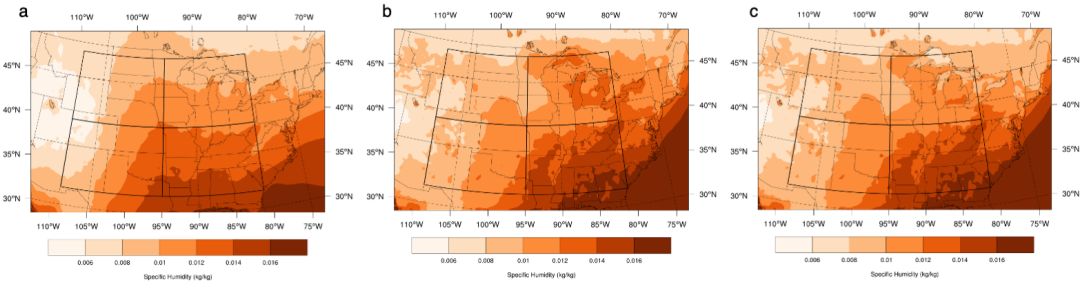

Figure F-4: a) 1975-2004 JJAS average of 2m specific humidity (kg/kg) in ERA5 b) 1975-2004 JJAS average of 2m specific humidity (kg/kg) in CCSM4-2000 without Lake Improvements c) 1975-2004 JJAS average of 2m specific humidity (kg/kg) in CCSM4-2000 with Lake Improvements

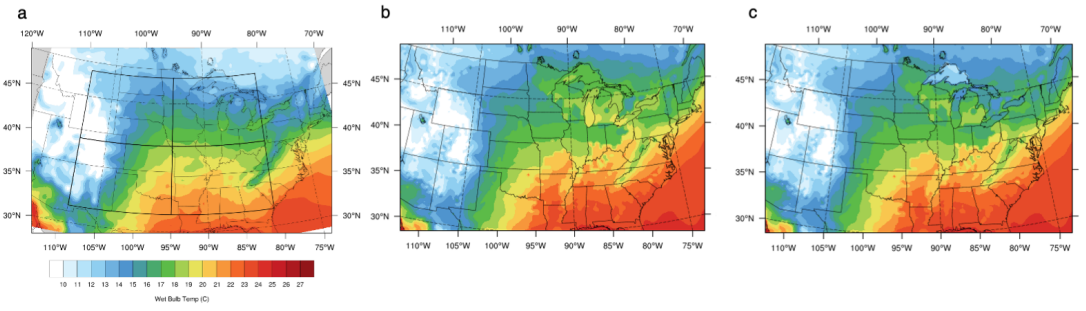

Figure F-5: a) 1975-2004 JJAS average of 2m average daily maximum wet-bulb temperature (degrees C) in ERA5 b) 1975-2004 JJAS average of 2m average daily maximum wet-bulb temperature (degrees C) in CCSM4-2000 without Lake Improvements or bias correction c) 1975-2004 JJAS average of 2m average daily maximum wet-bulb temperature (degrees C) in CCSM4-2000 with Lake Improvements without bias correction

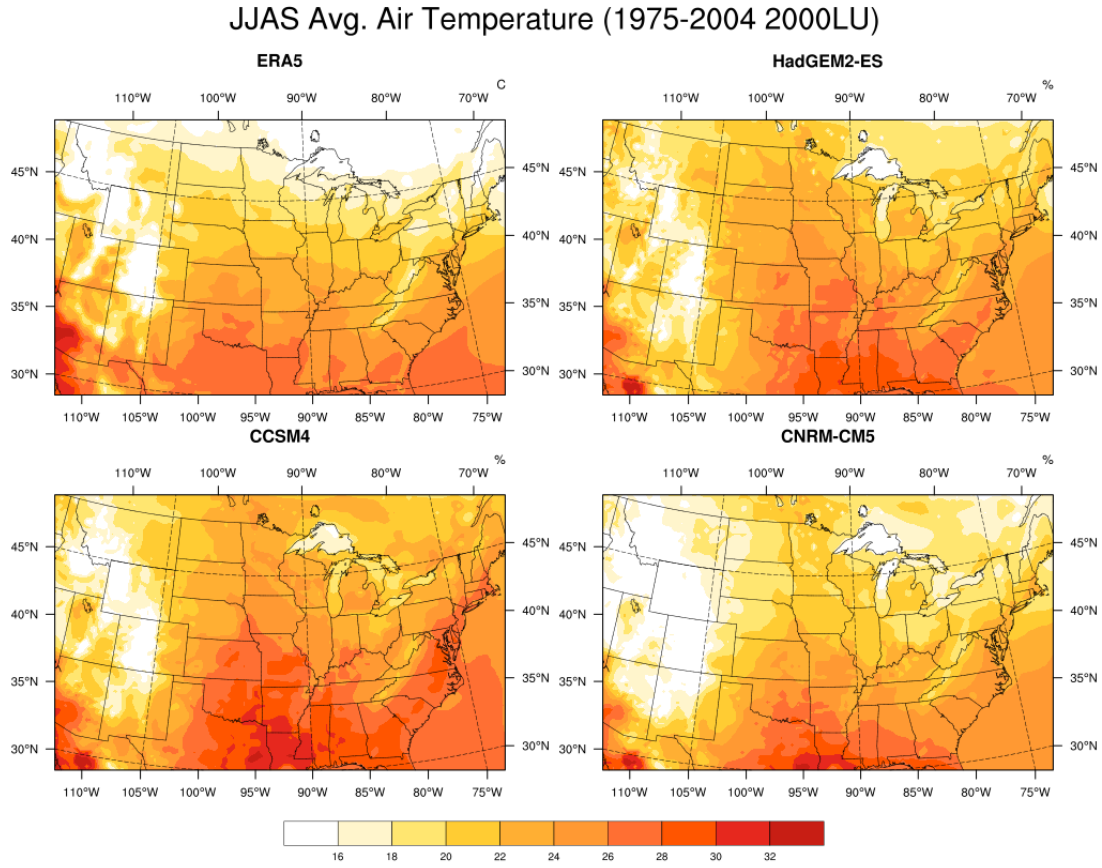

Figure F-6: June-September 1975-2004 average of 2m Air Temperature (degrees C) in ERA5 versus GCM forced simulations with 2000 Land Use and all code updates and lake adjustments.

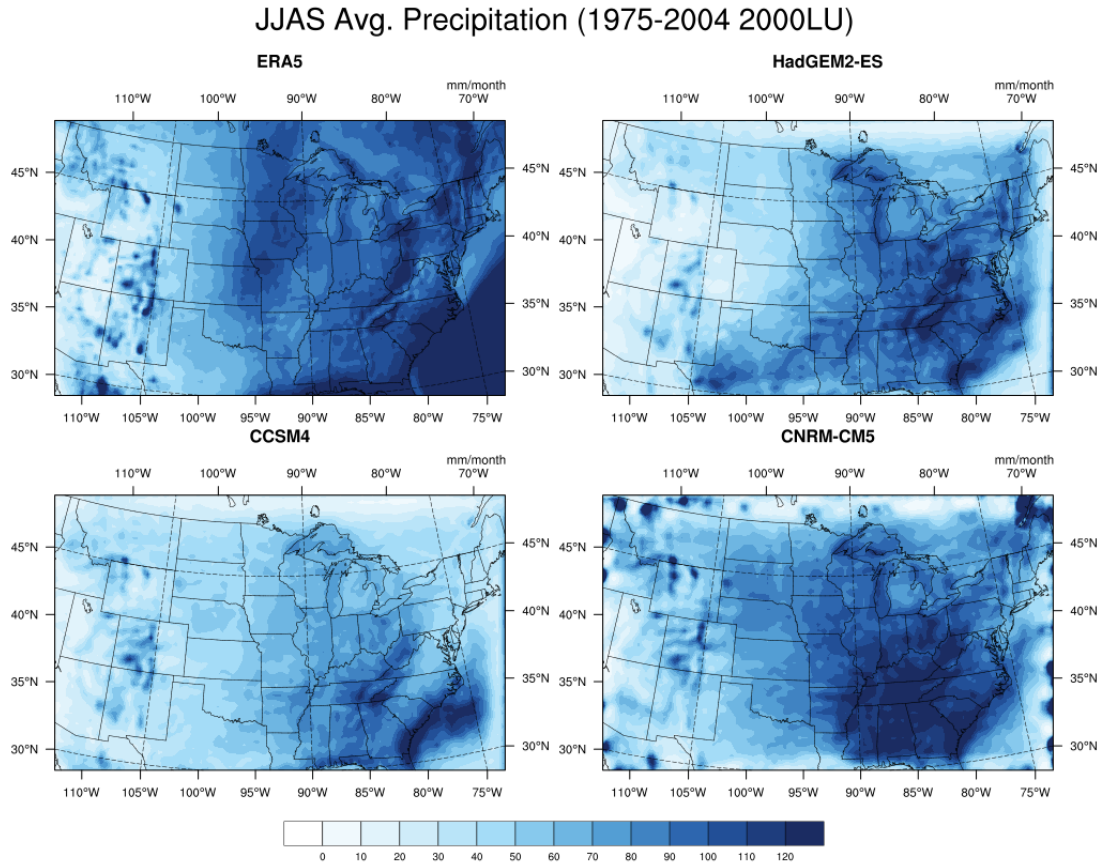

Figure F-7: June-September 1975-2004 average of Precipitation (mm/month) in ERA5 versus GCM forced simulations with 2000 Land Use and all code updates and lake adjustments.

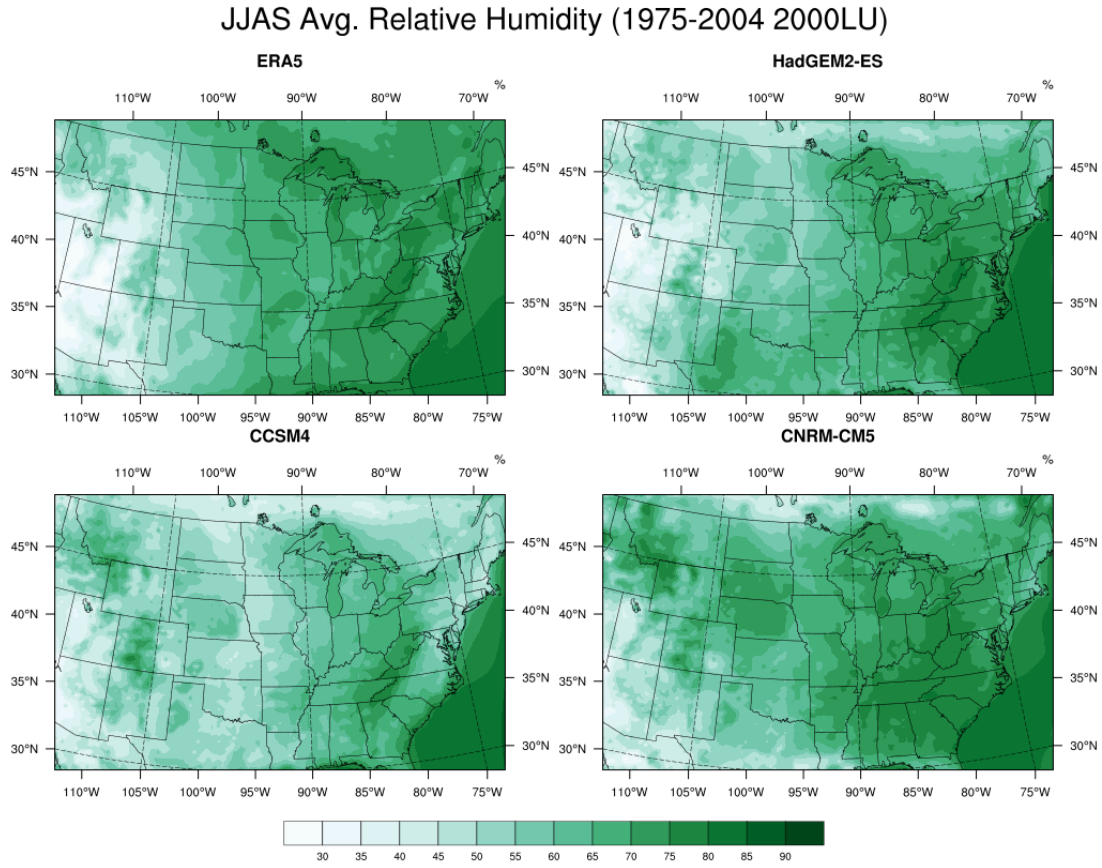

Figure F-8: June-September 1975-2004 average of Relative Humidity (%) in ERA5 (1000 mb) versus GCM forced simulations with 2000 Land Use and all code updates and lake adjustments (2m).

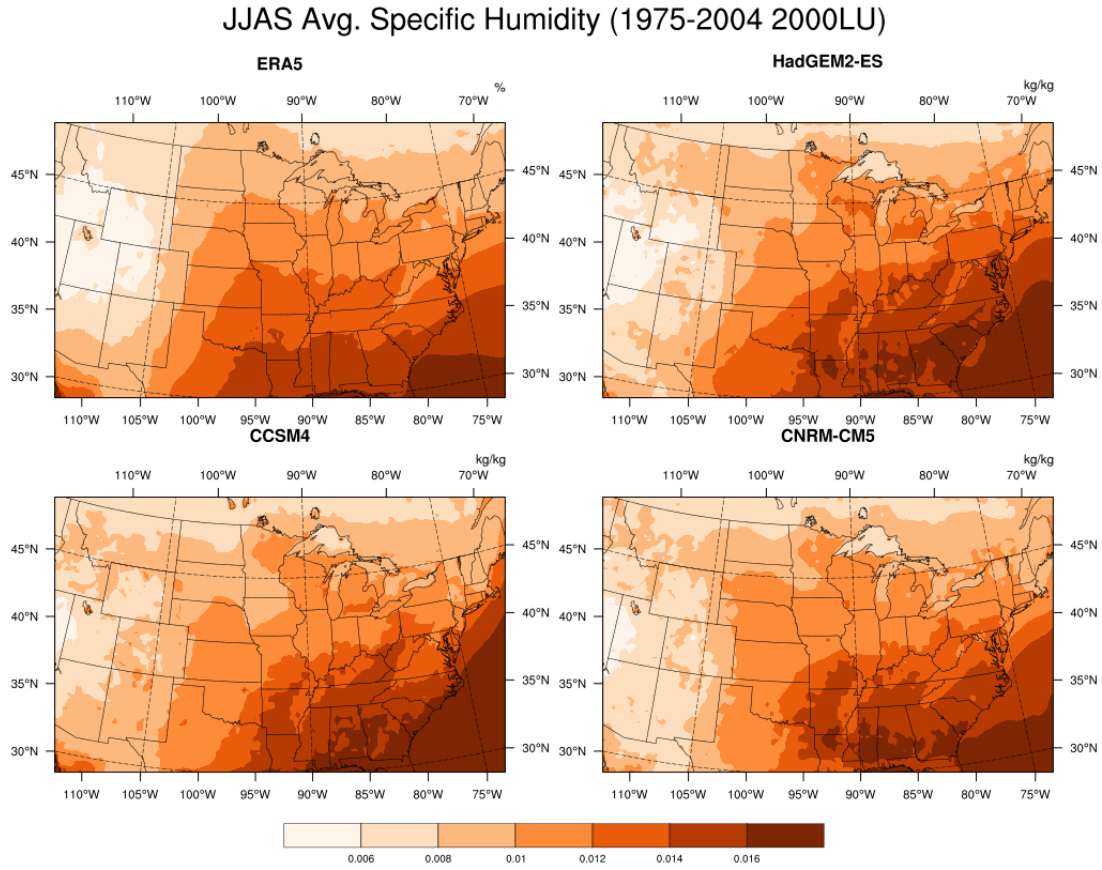

Figure F-9: June-September 1975-2004 average of Specific Humidity (kg/kg) in ERA5 (1000 mb) versus GCM forced simulations with 2000 Land Use and all code updates and lake adjustments (2m).

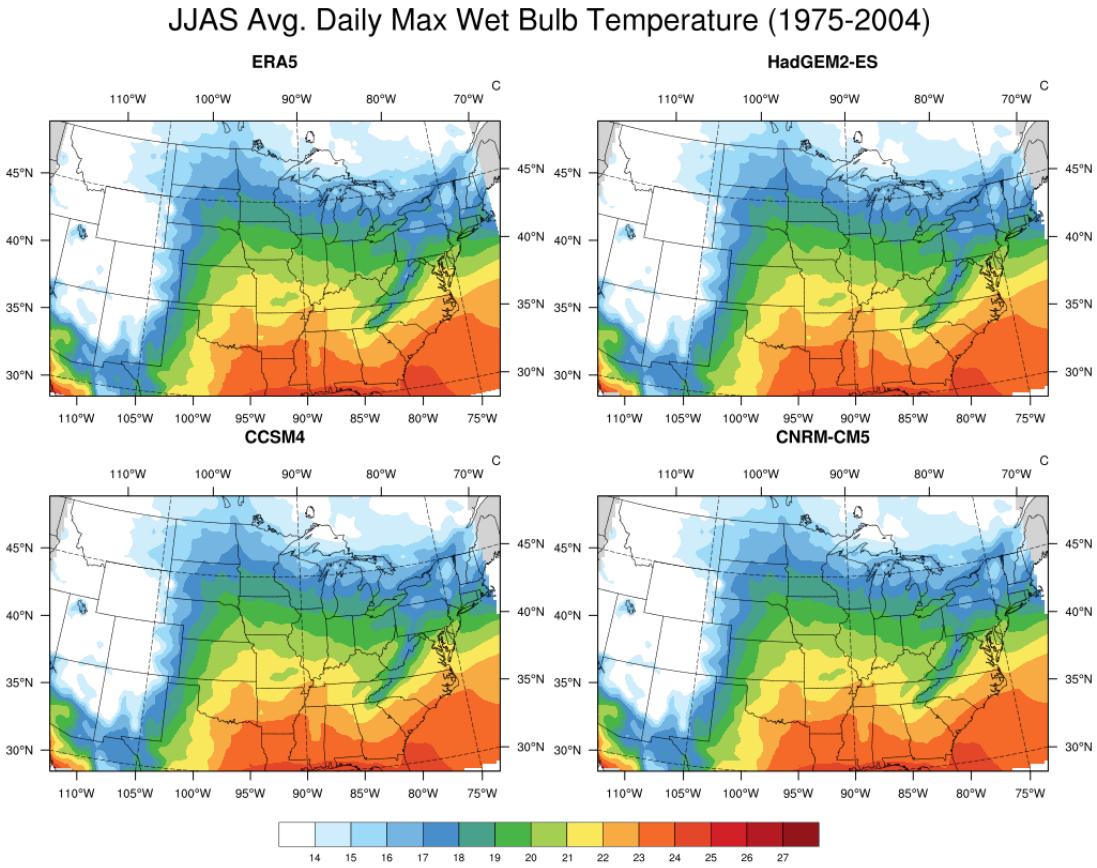

Figure F-10: June-September 1975-2004 average of 6hr-running mean average daily maximum wet-bulb temperature (degrees C) in ERA5 versus GCM forced simulations with 2000 Land Use and all code updates, bias correction, and lake adjustments.

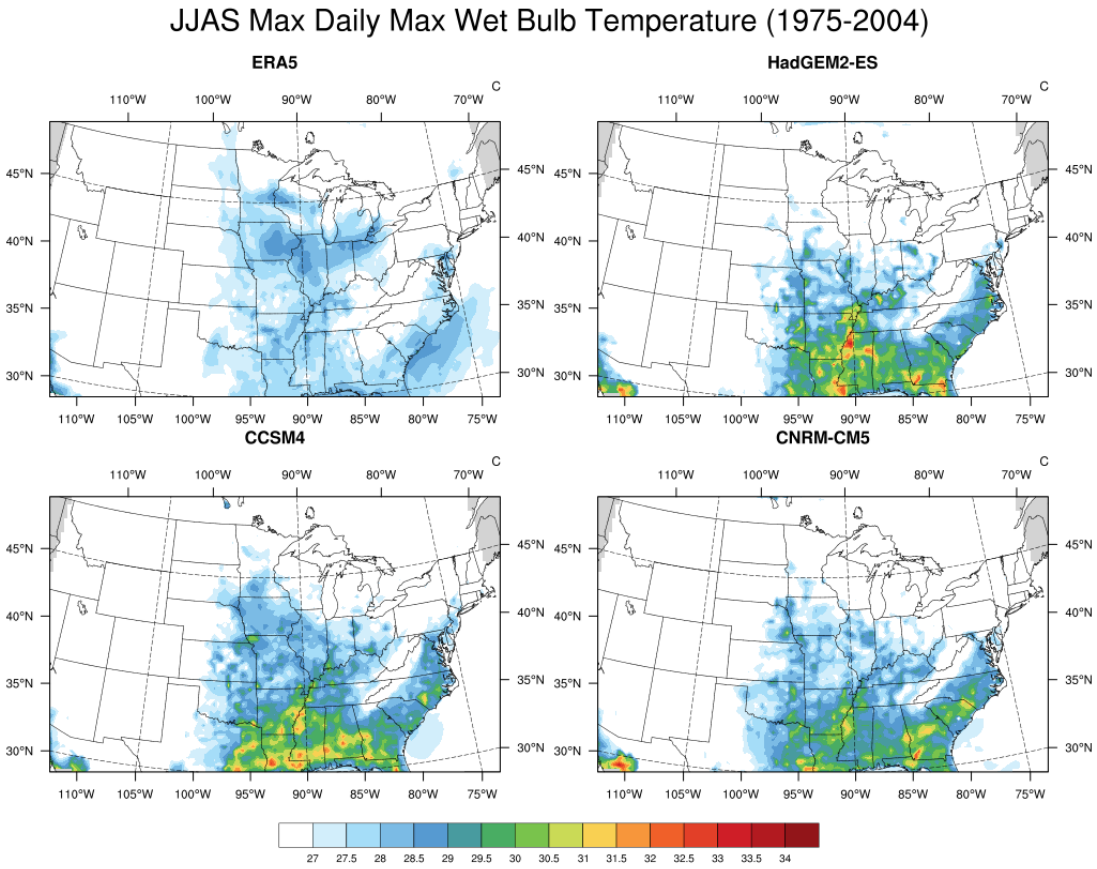

Figure F-11: June-September 1975-2004 6hr-running mean maximum daily maximum wet-bulb temperature (degrees C) in ERA5 versus GCM forced simulations with 2000 Land Use and all code updates, bias correction, and lake adjustments.

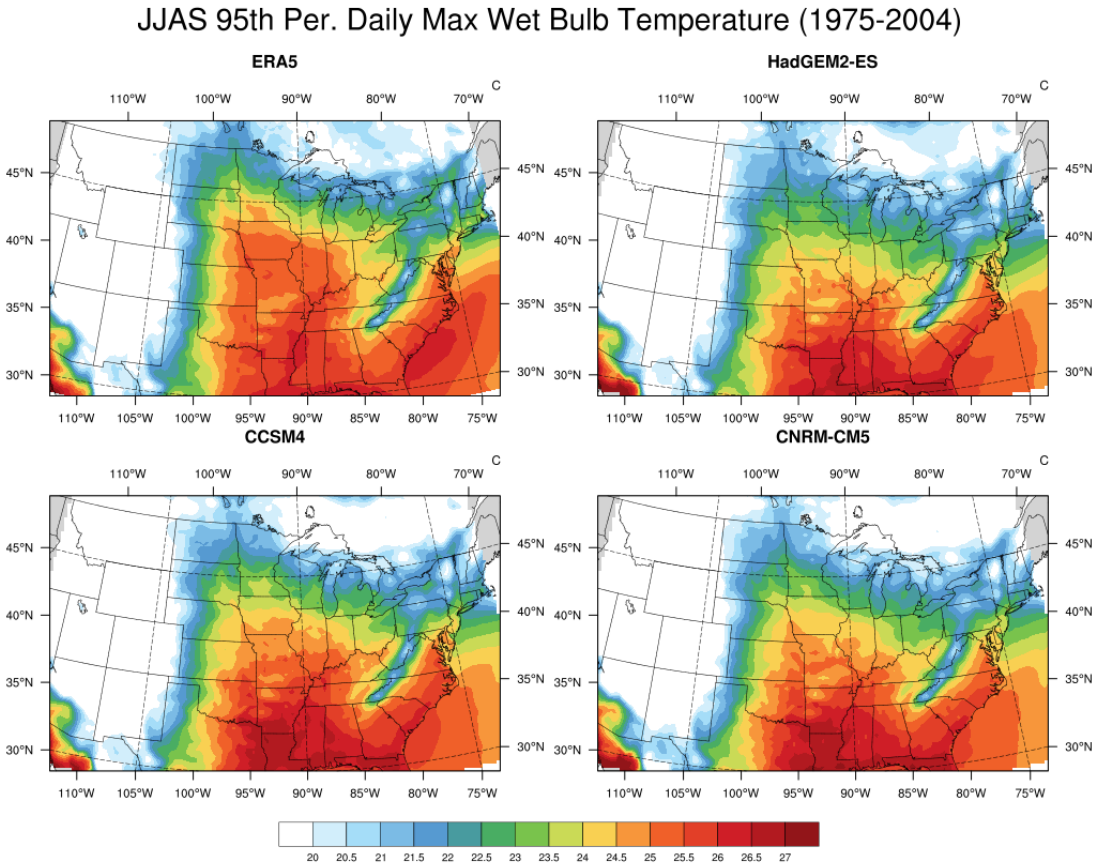

Figure F-12: June-September 1975-2004 average of 6hr-running mean 95th Percentile daily maximum wet-bulb temperature (degrees C) in ERA5 versus GCM forced simulations with 2000 Land Use and all code updates, bias correction, and lake adjustments.

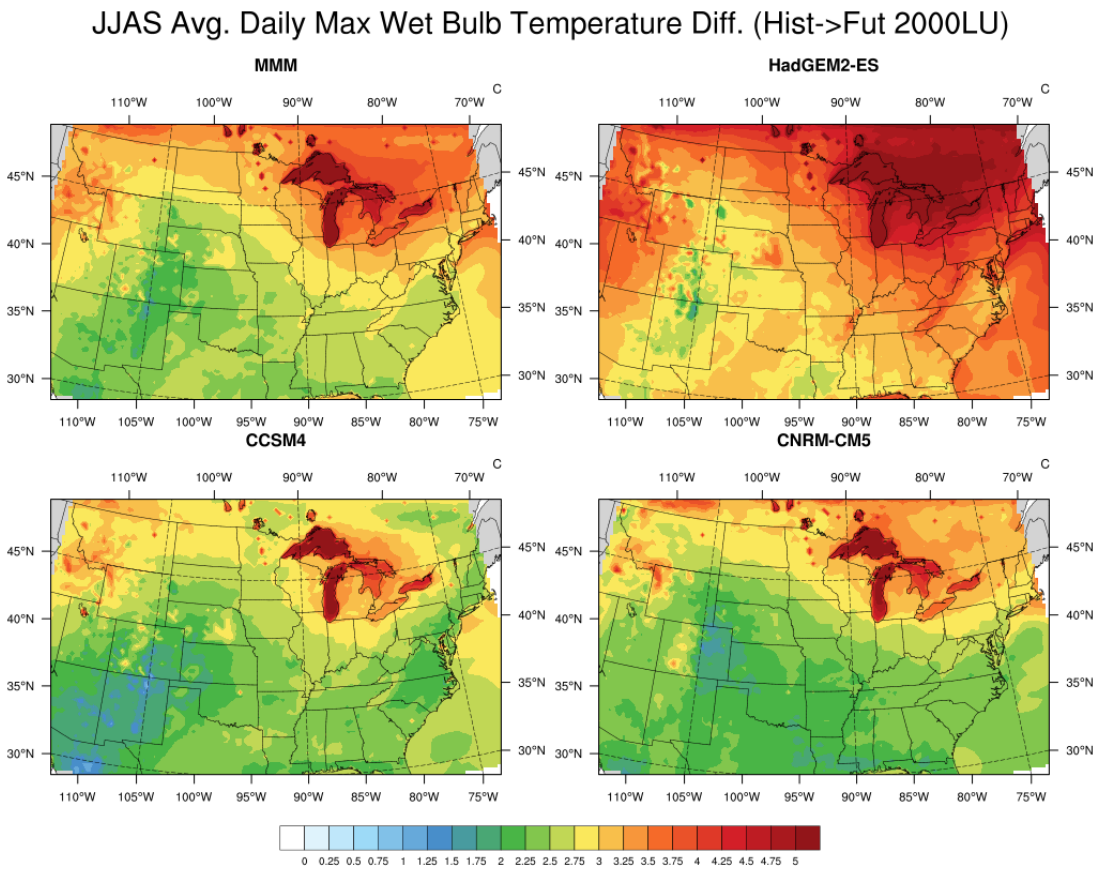

Figure F-13: Change in June-September average of 6hr-running mean average daily maximum wet-bulb temperature (degrees C) from the historical (1975-2004) to future (2070-2099) period under RCP8.5. Results are shown for individual GCM forced simulations with 2000 Land Use and all code updates, bias correction, and lake adjustments as well as the Multi-Model-Mean (MMM).

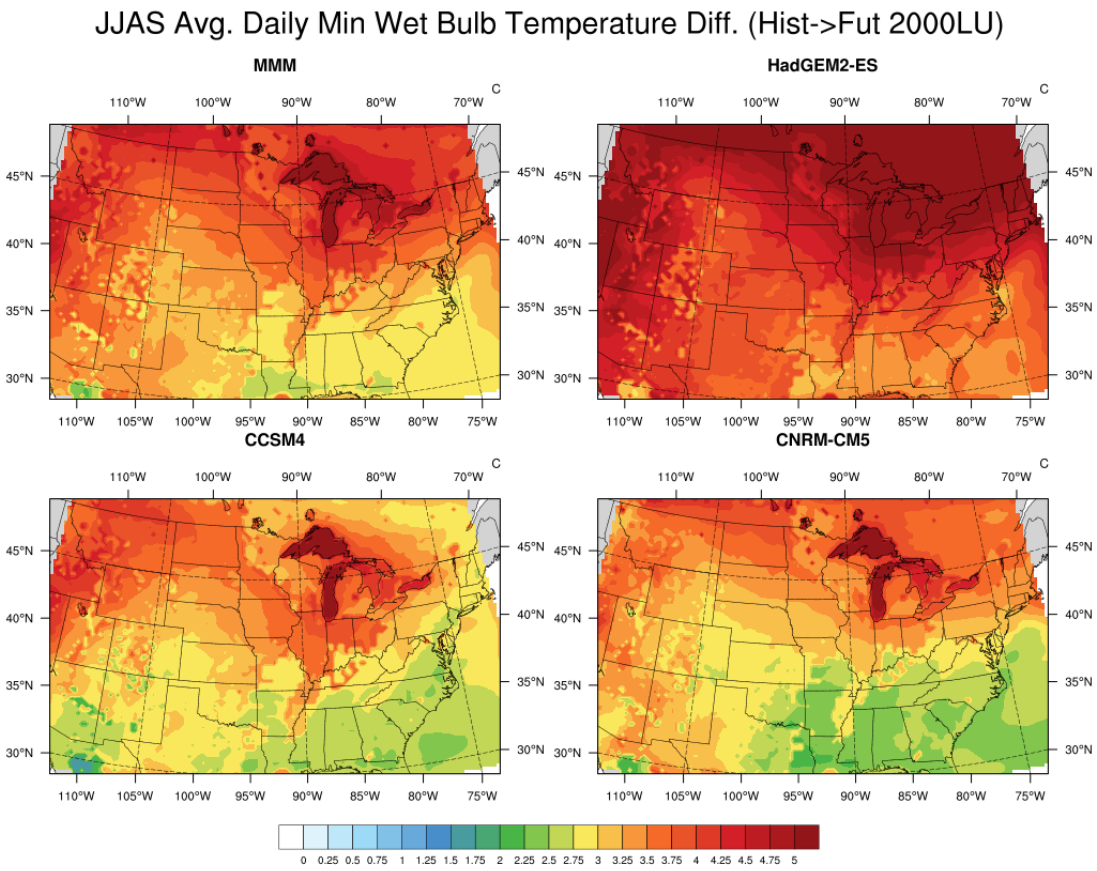

Figure F-14: Change in June-September average of 6hr-running mean average daily minimum wet-bulb temperature (degrees C) from the historical (1975-2004) to future (2070-2099) period under RCP8.5. Results are shown for individual GCM forced simulations with 2000 Land Use and all code updates, bias correction, and lake adjustments as well as the Multi-Model-Mean (MMM).

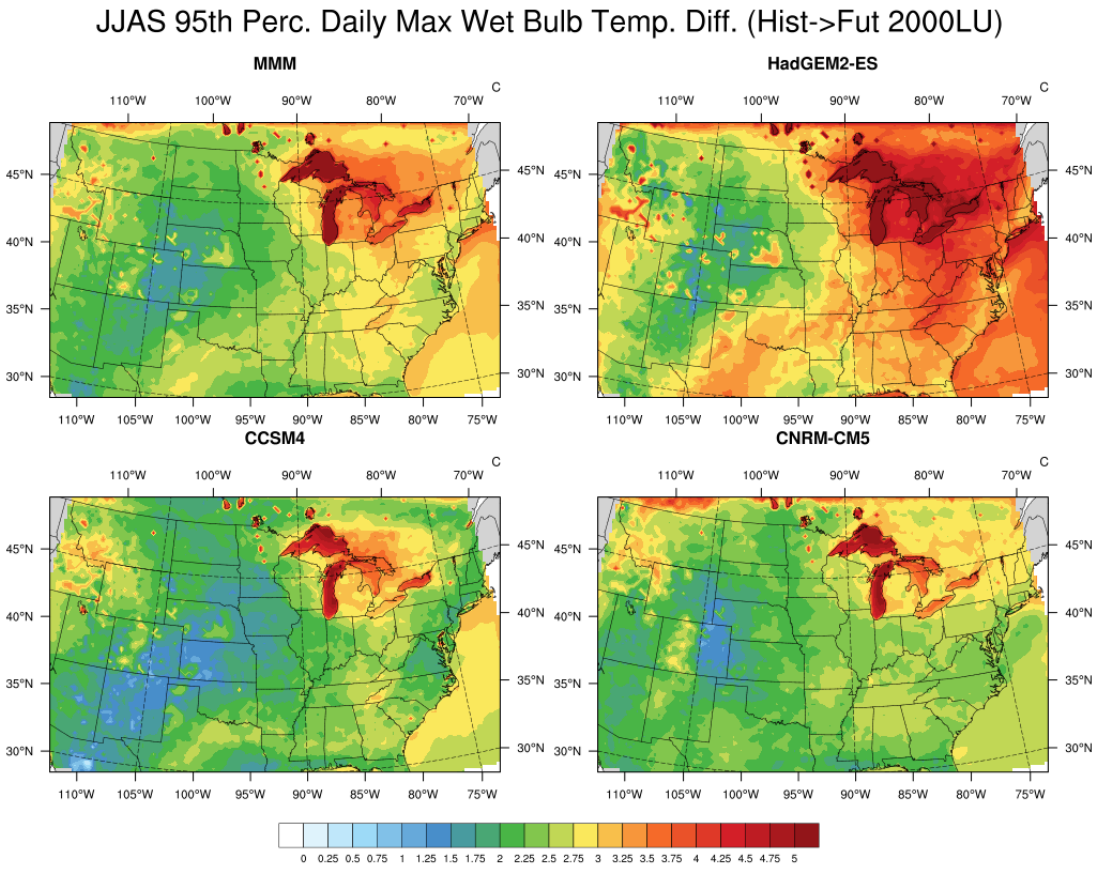

Figure F-15: Change in June-September average of 6hr-running mean 95th Percentile daily maximum wet-bulb temperature (degrees C) from the historical (1975-2004) to future (2070-2099) period under RCP8.5. Results are shown for individual GCM forced simulations with 2000 Land Use and all code updates, bias correction, and lake adjustments as well as the Multi-Model-Mean (MMM).

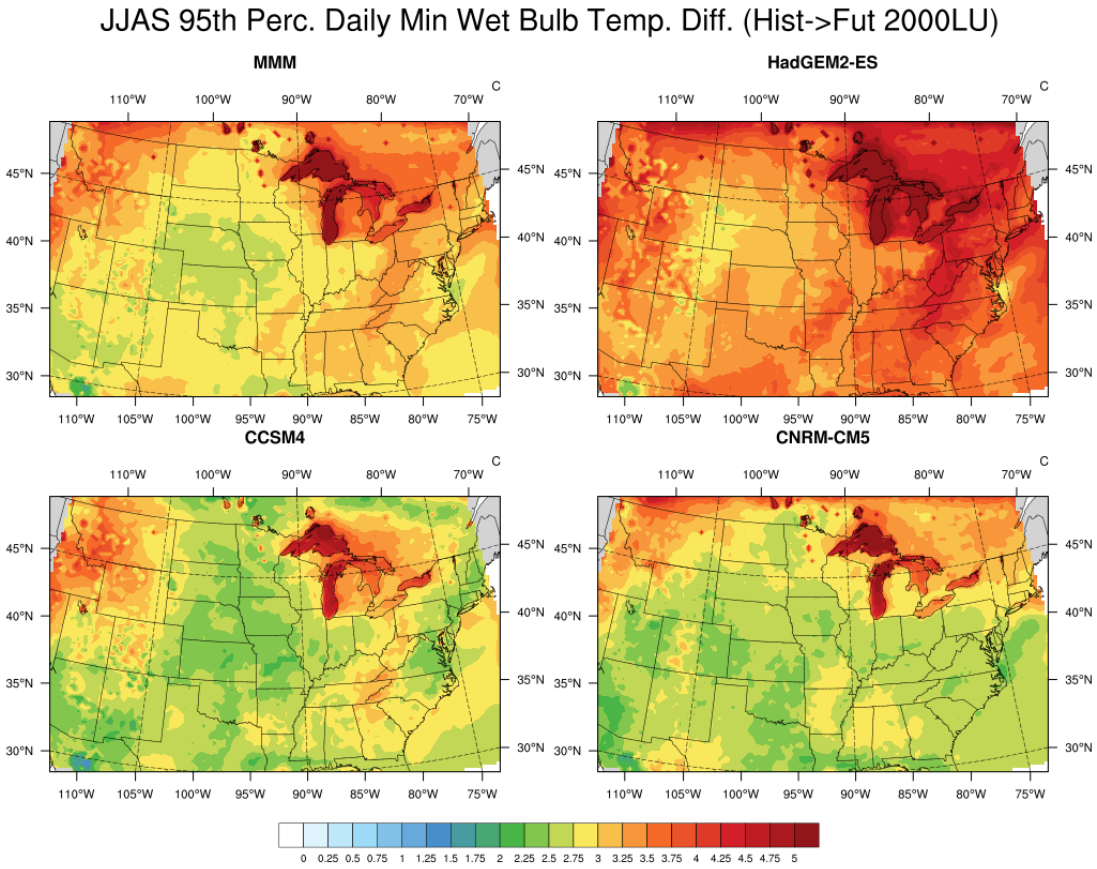

Figure F-16: Change in June-September average of 6hr-running mean 95th Percentile daily minimum wet-bulb temperature (degrees C) from the historical (1975-2004) to future (2070-2099) period under RCP8.5. Results are shown for individual GCM forced simulations with 2000 Land Use and all code updates, bias correction, and lake adjustments as well as the Multi-Model-Mean (MMM).

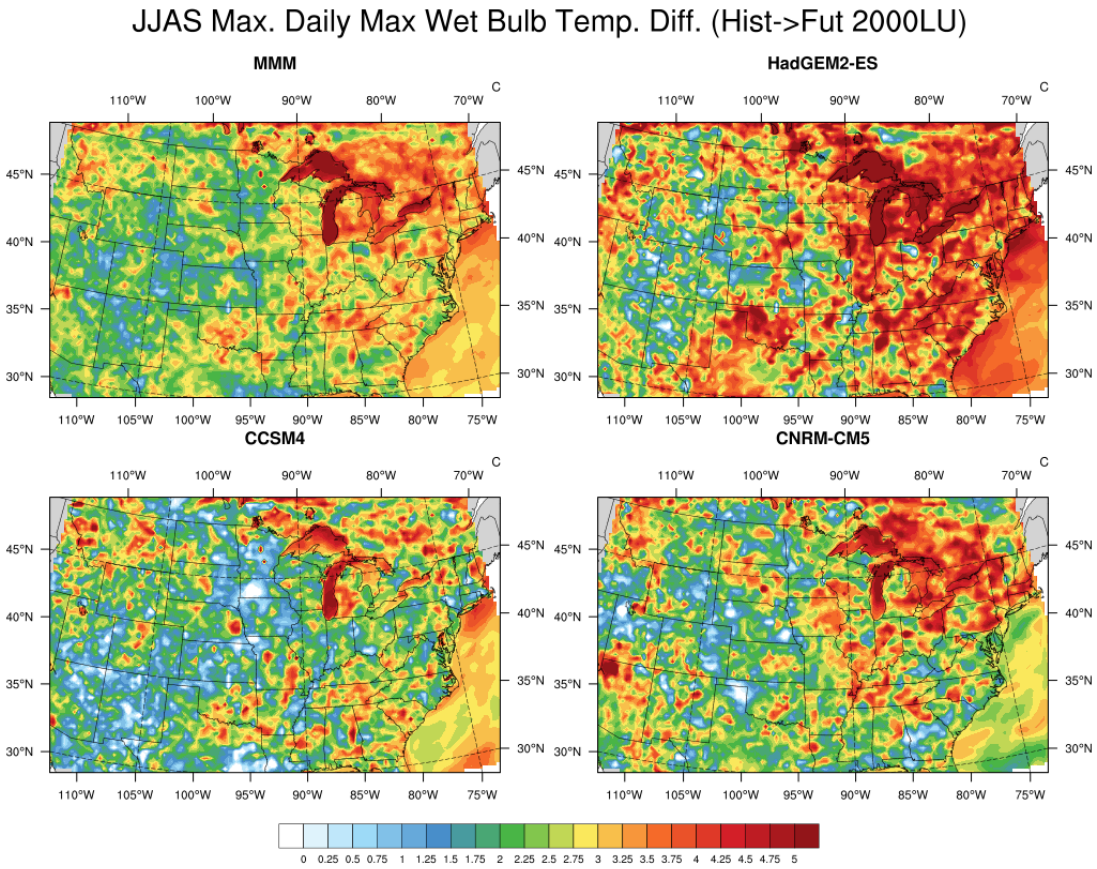

Figure F-17: Change in June-September average of 6hr-running mean maximum daily maximum wet-bulb temperature (degrees C) from the historical (1975-2004) to future (2070-2099) period under RCP8.5. Results are shown for individual GCM forced simulations with 2000 Land Use and all code updates, bias correction, and lake adjustments as well as the Multi-Model-Mean (MMM).

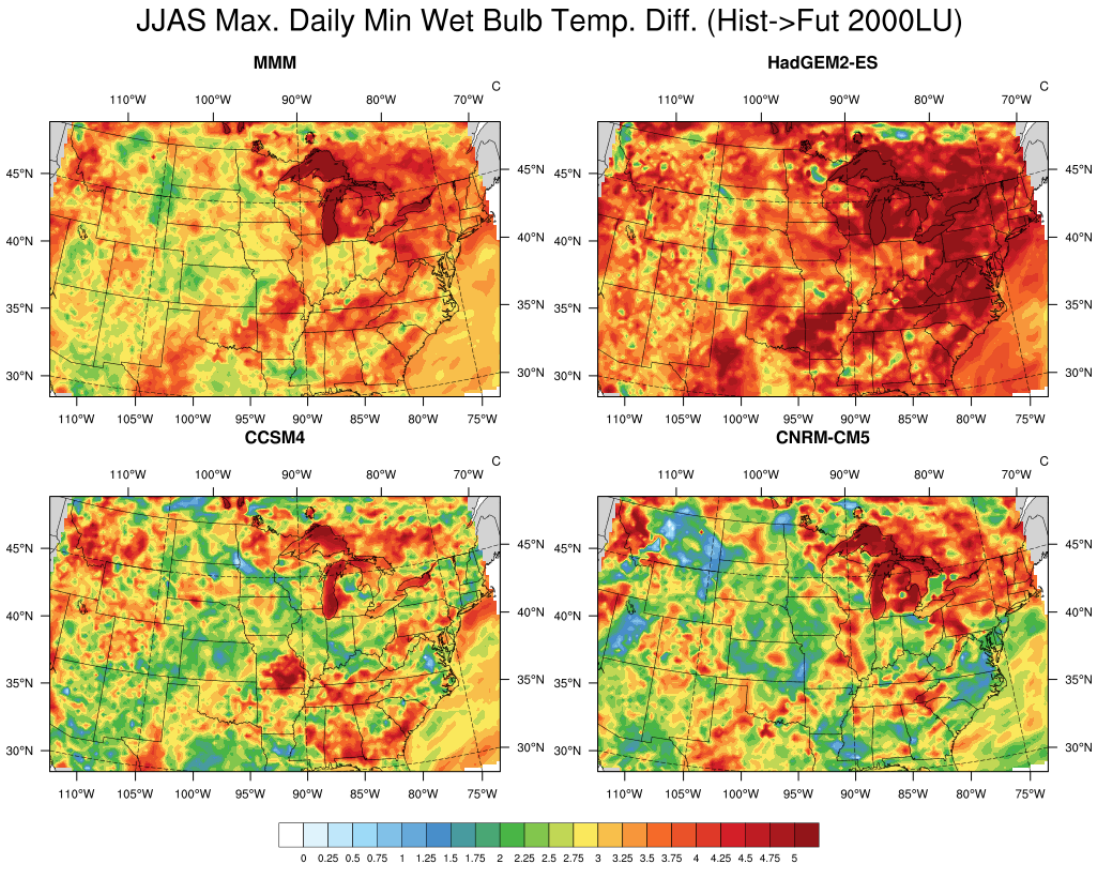

Figure F-18: Change in June-September average of 6hr-running mean maximum daily minimum wet-bulb temperature (degrees C) from the historical (1975-2004) to future (2070-2099) period under RCP8.5. Results are shown for individual GCM forced simulations with 2000 Land Use and all code updates, bias correction, and lake adjustments as well as the Multi-Model-Mean (MMM).

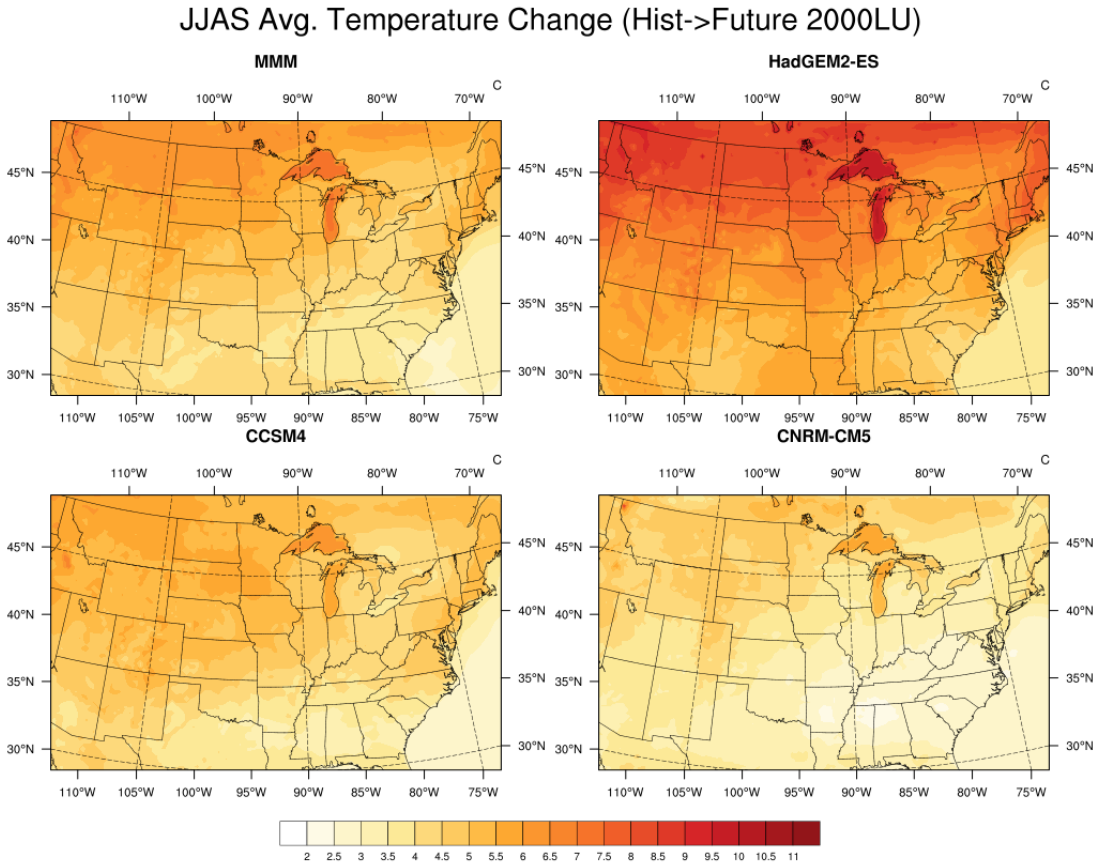

Figure F-19: Change in June-September average of 2m Air Temperature (degrees C) from the historical (1975-2004) to future (2070-2099) period under RCP8.5 in ERA5 versus GCM forced simulations with 2000 Land Use and all code updates and lake adjustments.

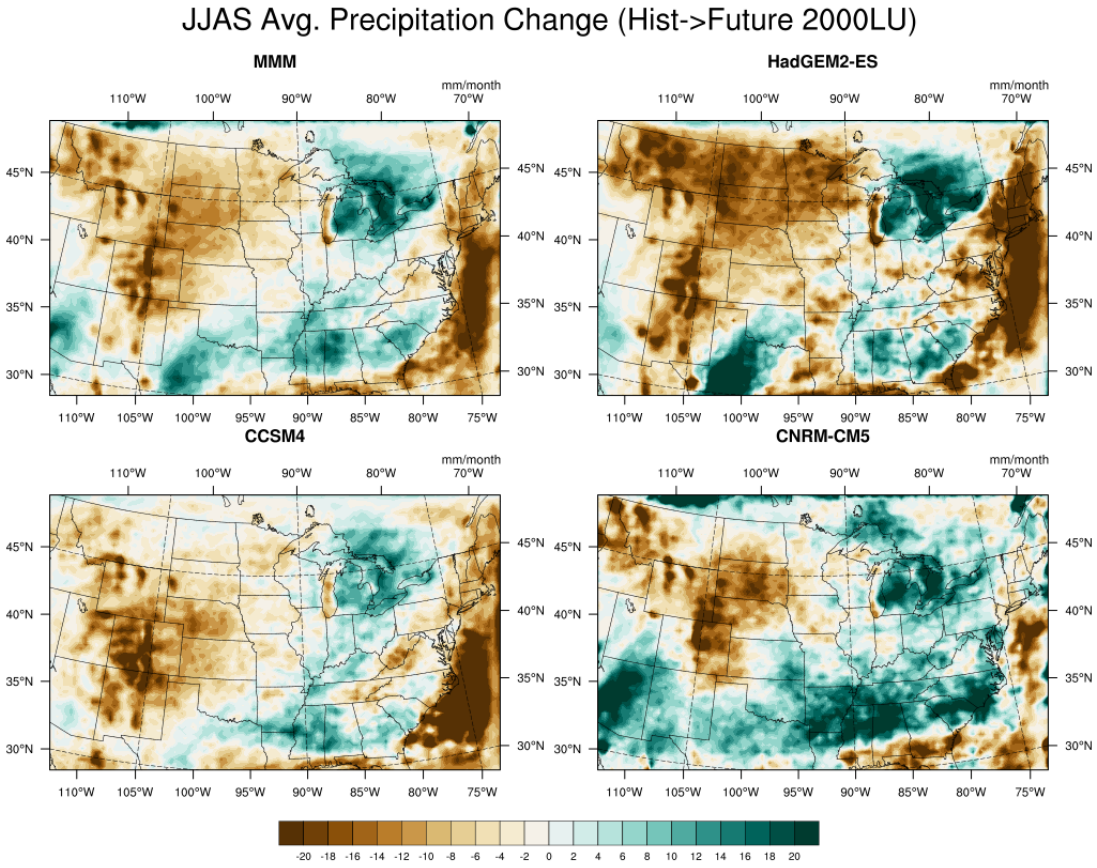

Figure F-20: Change in June-September average of Precipitation (mm/month) from the historical (1975-2004) to future (2070-2099) period under RCP8.5 in ERA5 versus GCM forced simulations with 2000 Land Use and all code updates and lake adjustments.

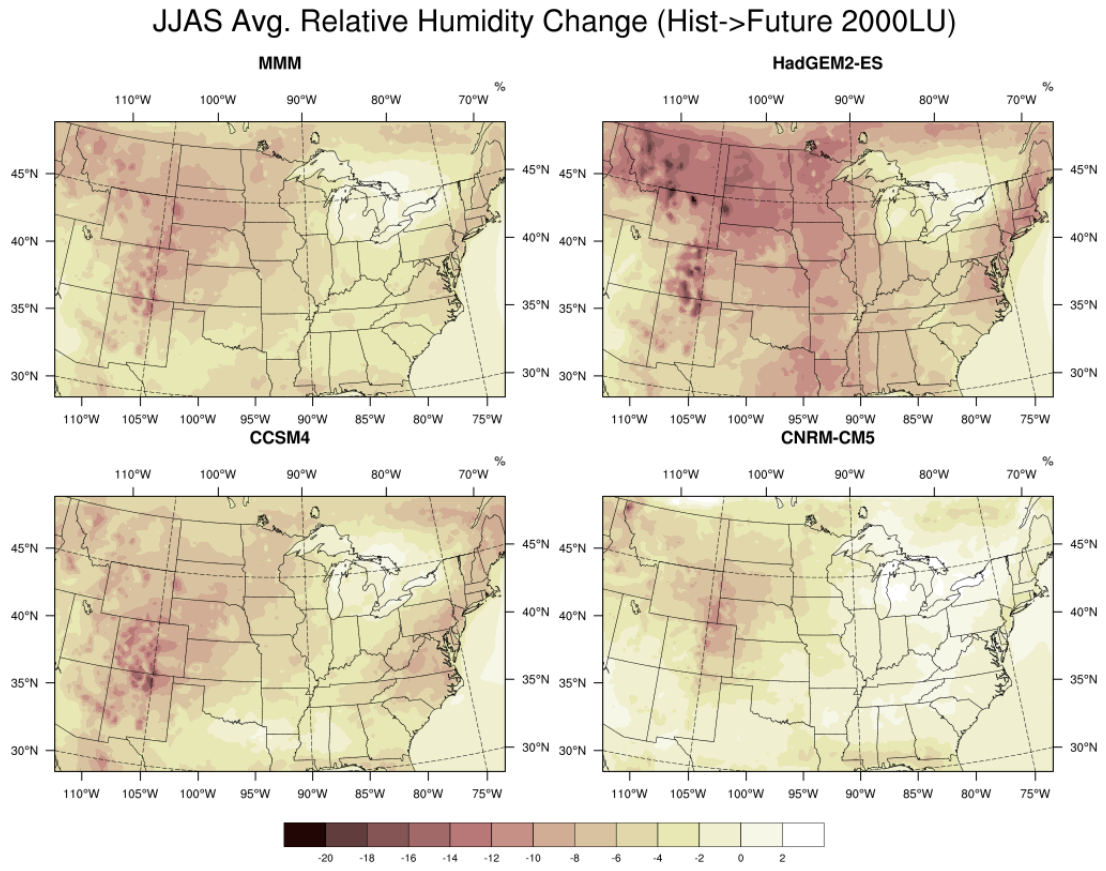

Figure F-21: Change in June-September average of Relative Humidity (%) from the historical (1975-2004) to future (2070-2099) period under RCP8.5 in ERA5 (1000 mb) versus GCM forced simulations with 2000 Land Use and all code updates and lake adjustments (2m).

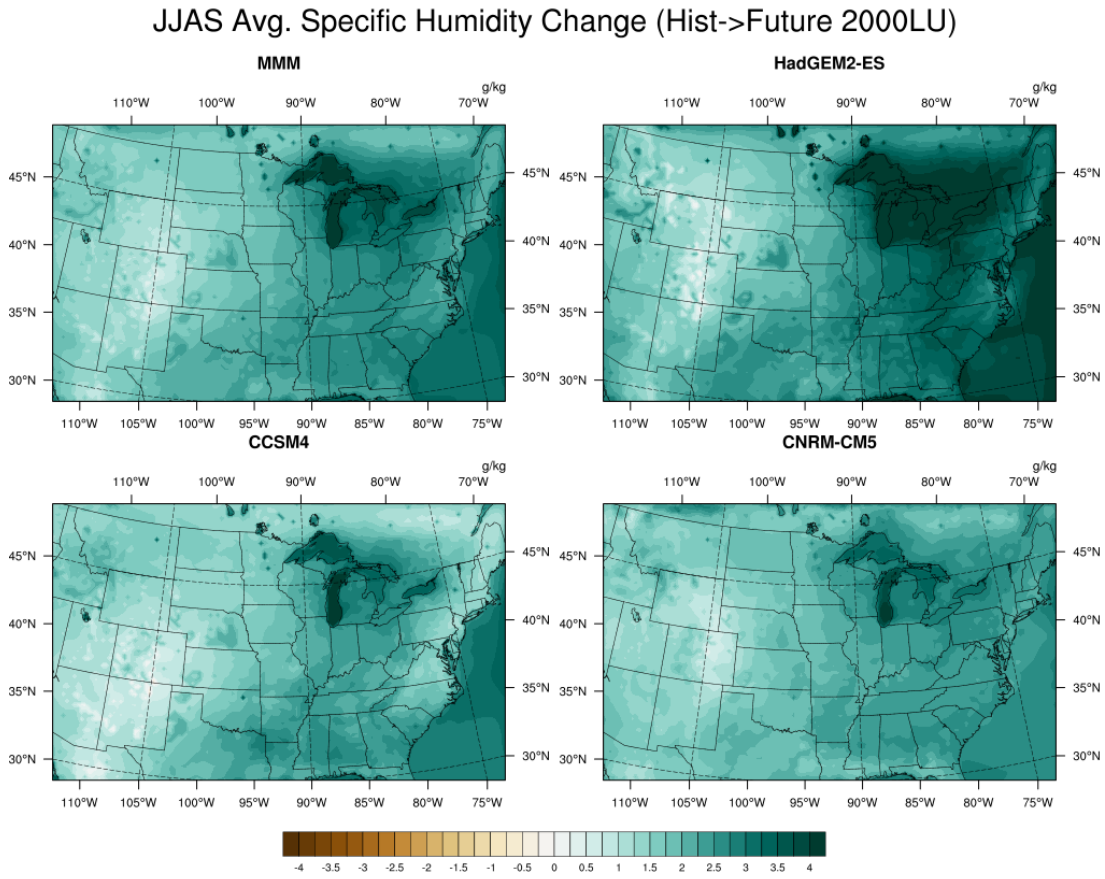

Figure F-22: Change in June-September average of Specific Humidity (g/kg) from the historical (1975-2004) to future (2070-2099) period under RCP8.5 in ERA5 (1000 mb) versus GCM forced simulations with 2000 Land Use and all code updates and lake adjustments (2m).

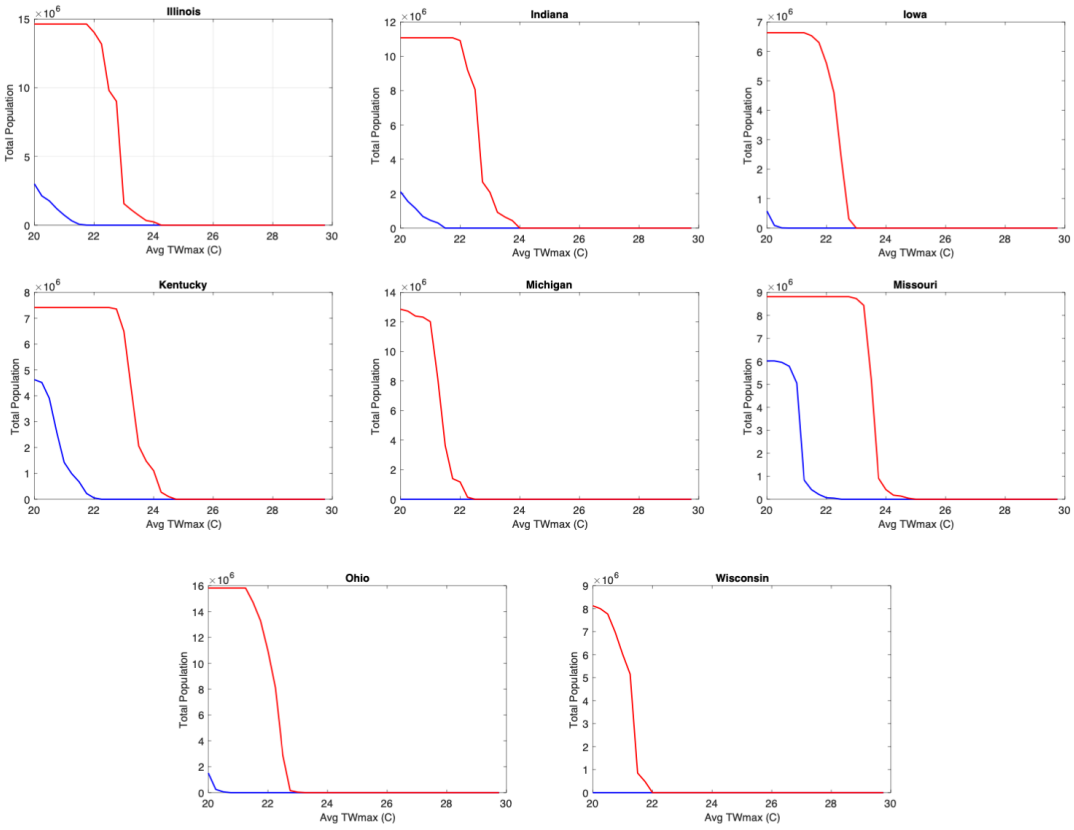

Figure F-23: Total population exposed to a given average daily maximum wet-bulb temperature (degrees C) on average in JJAS in the historical (1975-2004) (blue) and future (2070-2099) (red) periods for select states in CCSM4-2000.

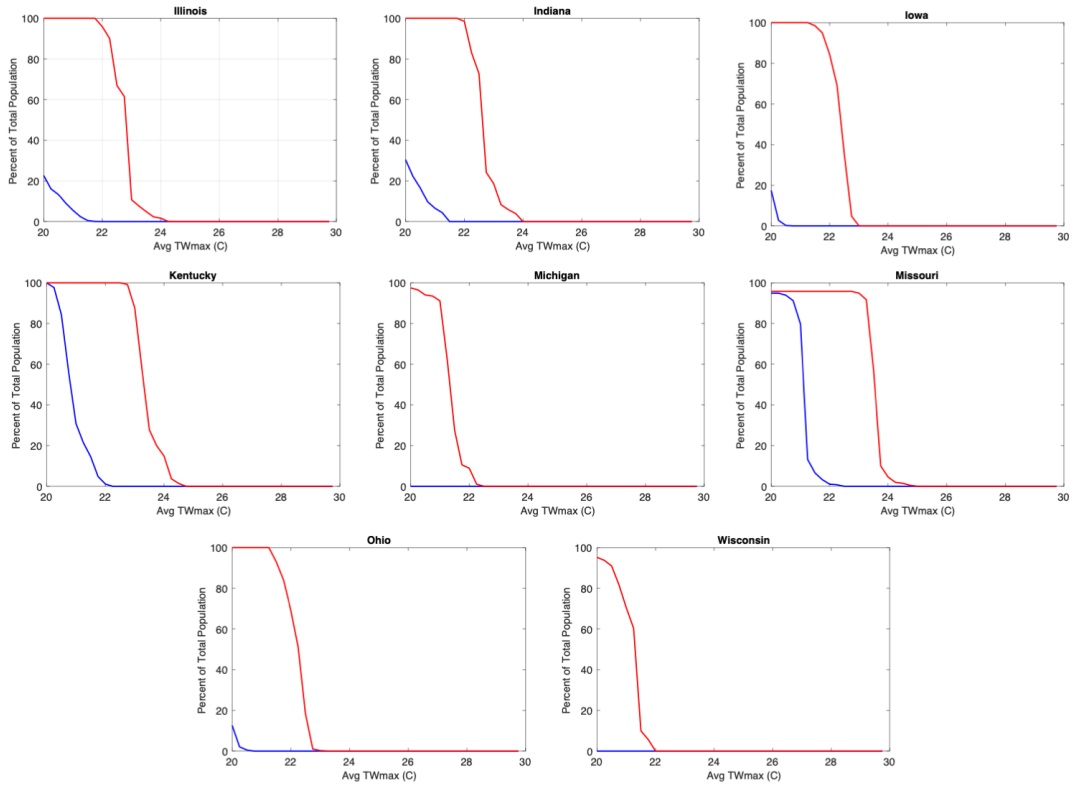

Figure F-24: Percentage of total population exposed to a given average daily maximum wet-bulb temperature (degrees C) on average in JJAS in the historical (1975-2004) (blue) and future (2070-2099) (red) periods for select states in CCSM4-2000.

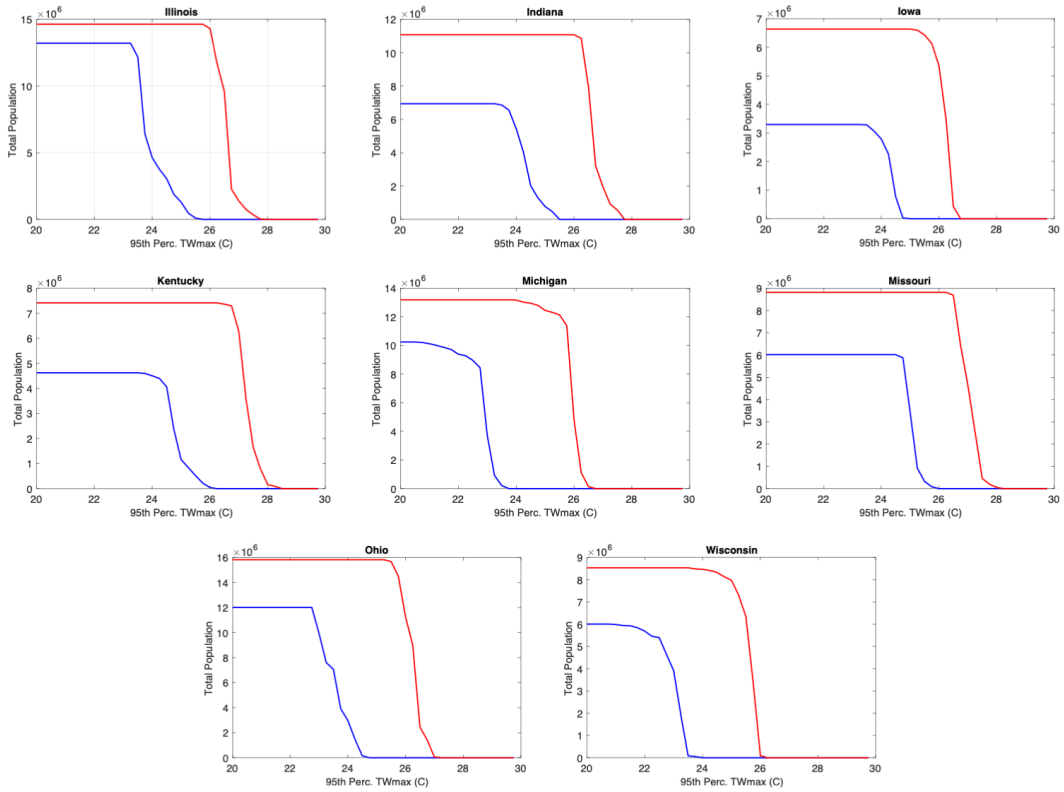

Figure F-25: Total population exposed to a given 95th percentile daily maximum wet-bulb temperature (degrees C) on average in JJAS in the historical (1975-2004) (blue) and future (2070-2099) (red) periods for select states in CCSM4-2000.

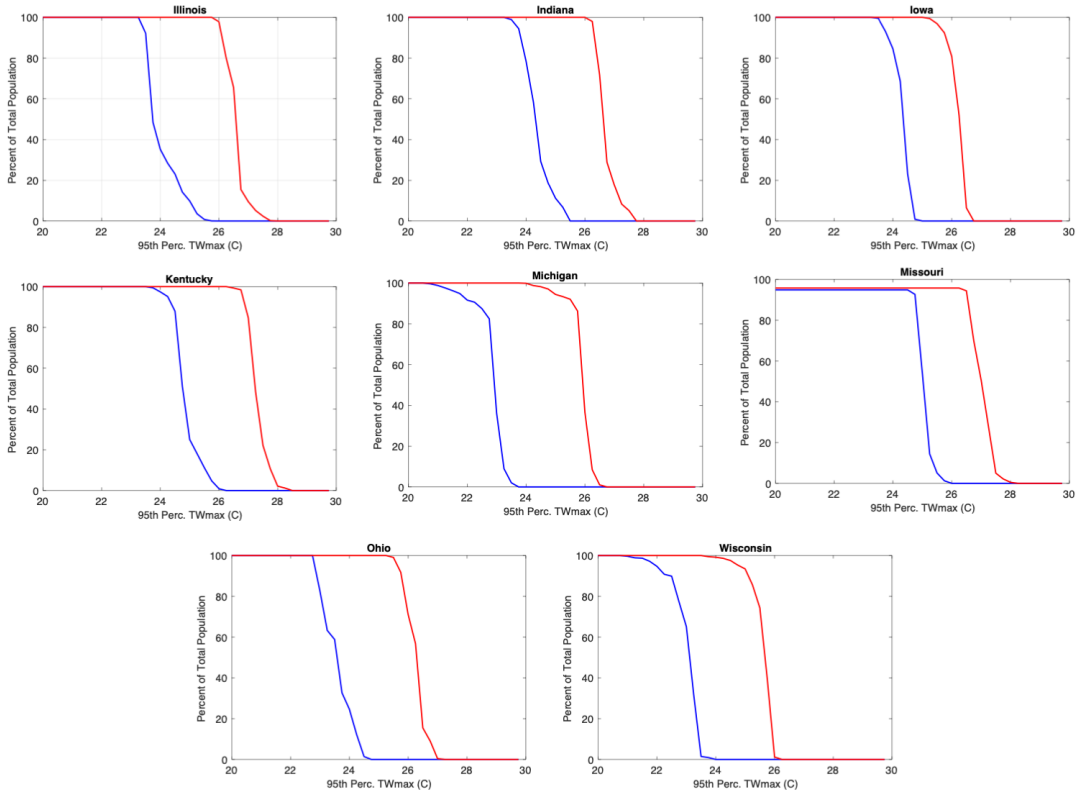

Figure F-26: Percentage of total population exposed to a given 95th percentile daily maximum wet-bulb temperature (degrees C) on average in JJAS in the historical (1975-2004) (blue) and future (2070-2099) (red) periods for select states in CCSM4-2000.

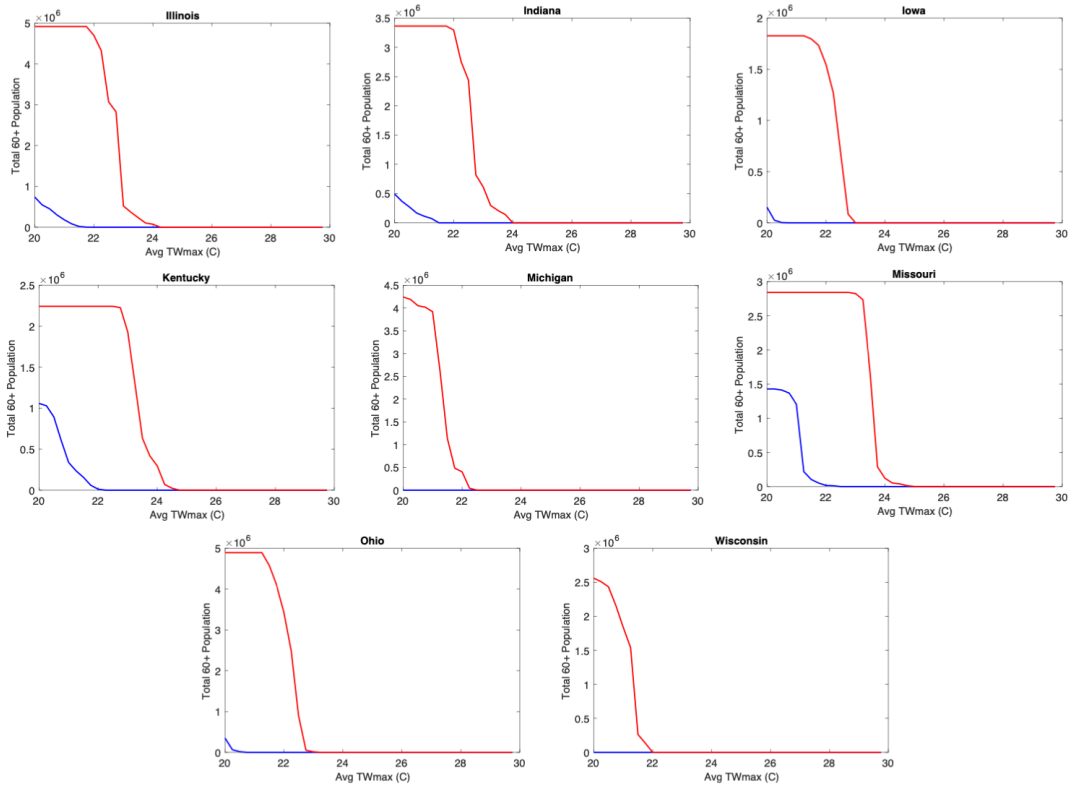

Figure F-27: Total 60+ years population exposed to a given average daily maximum wet-bulb temperature (degrees C) on average in JJAS in the historical (1975-2004) (blue) and future (2070-2099) (red) periods for select states in CCSM4-2000.

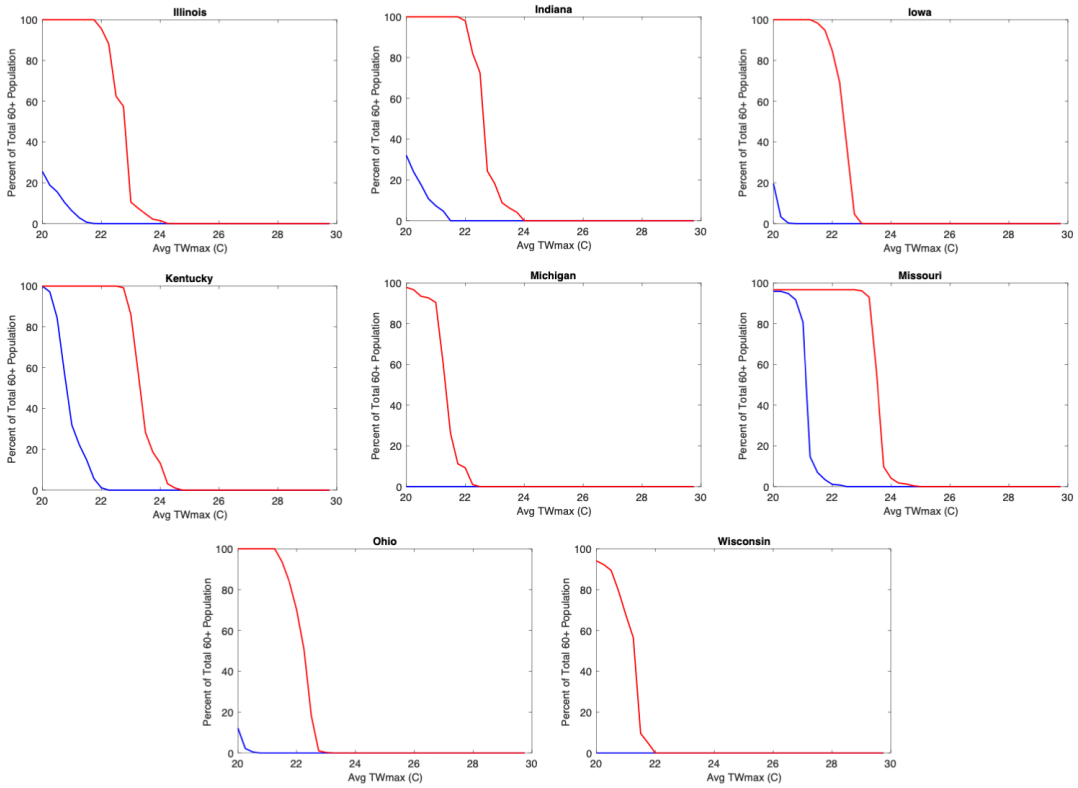

Figure F-28: Percentage of total 60+ years population exposed to a given average daily maximum wet-bulb temperature (degrees C) on average in JJAS in the historical (1975-2004) (blue) and future (2070-2099) (red) periods for select states in CCSM4-2000.

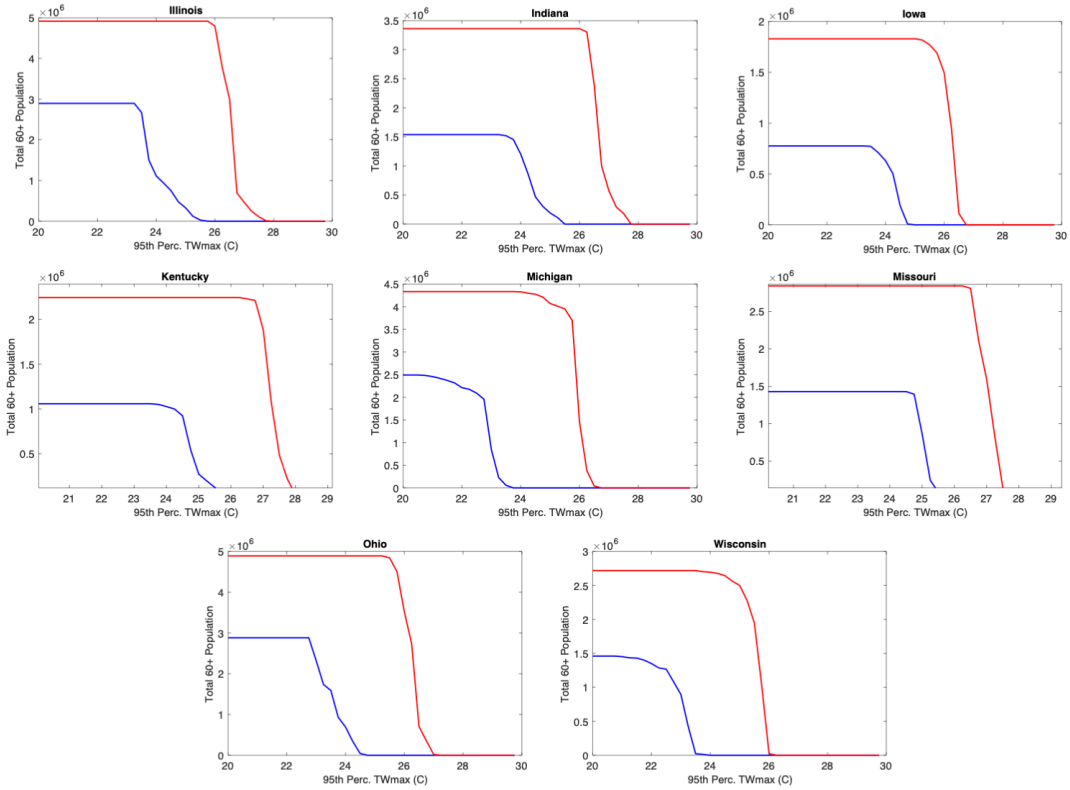

Figure F-29: Total 60+ years population exposed to a given 95th percentile daily maximum wet-bulb temperature (degrees C) on average in JJAS in the historical (1975-2004) (blue) and future (2070-2099) (red) periods for select states in CCSM4-2000.

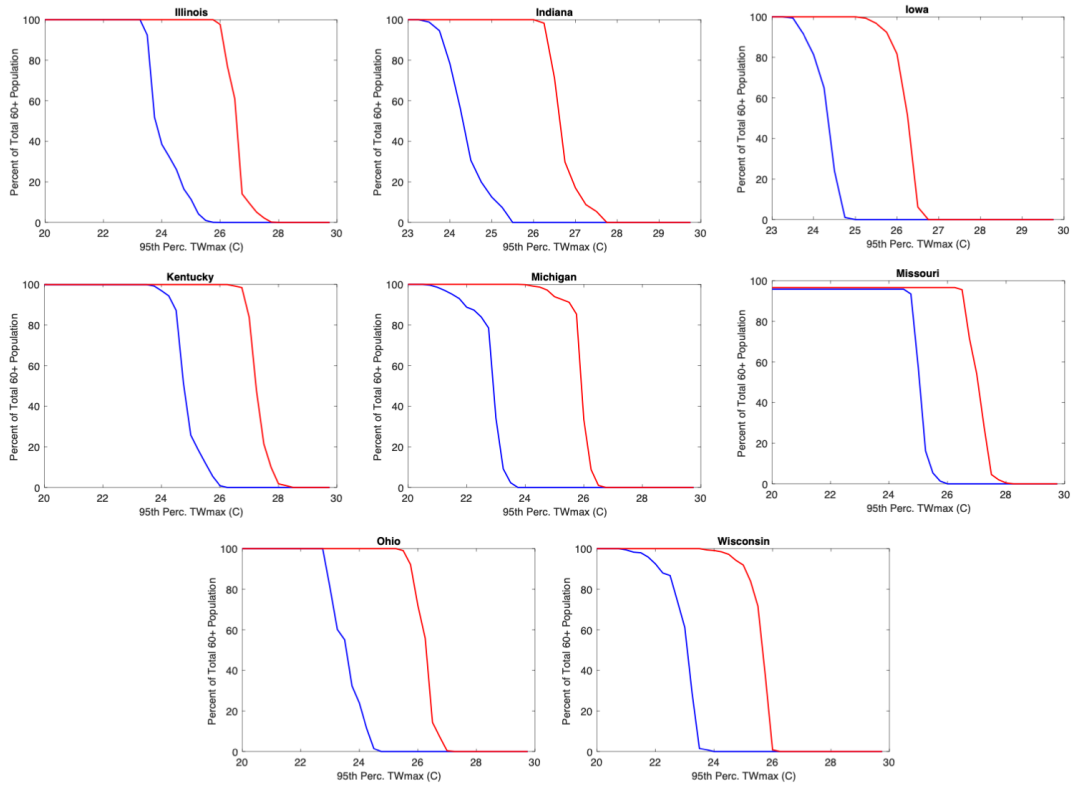

Figure F-30: Percentage of total 60+ years population exposed to a given 95th percentile daily maximum wet-bulb temperature (degrees C) on average in JJAS in the historical (1975-2004) (blue) and future (2070-2099) (red) periods for select states in CCSM4-2000.

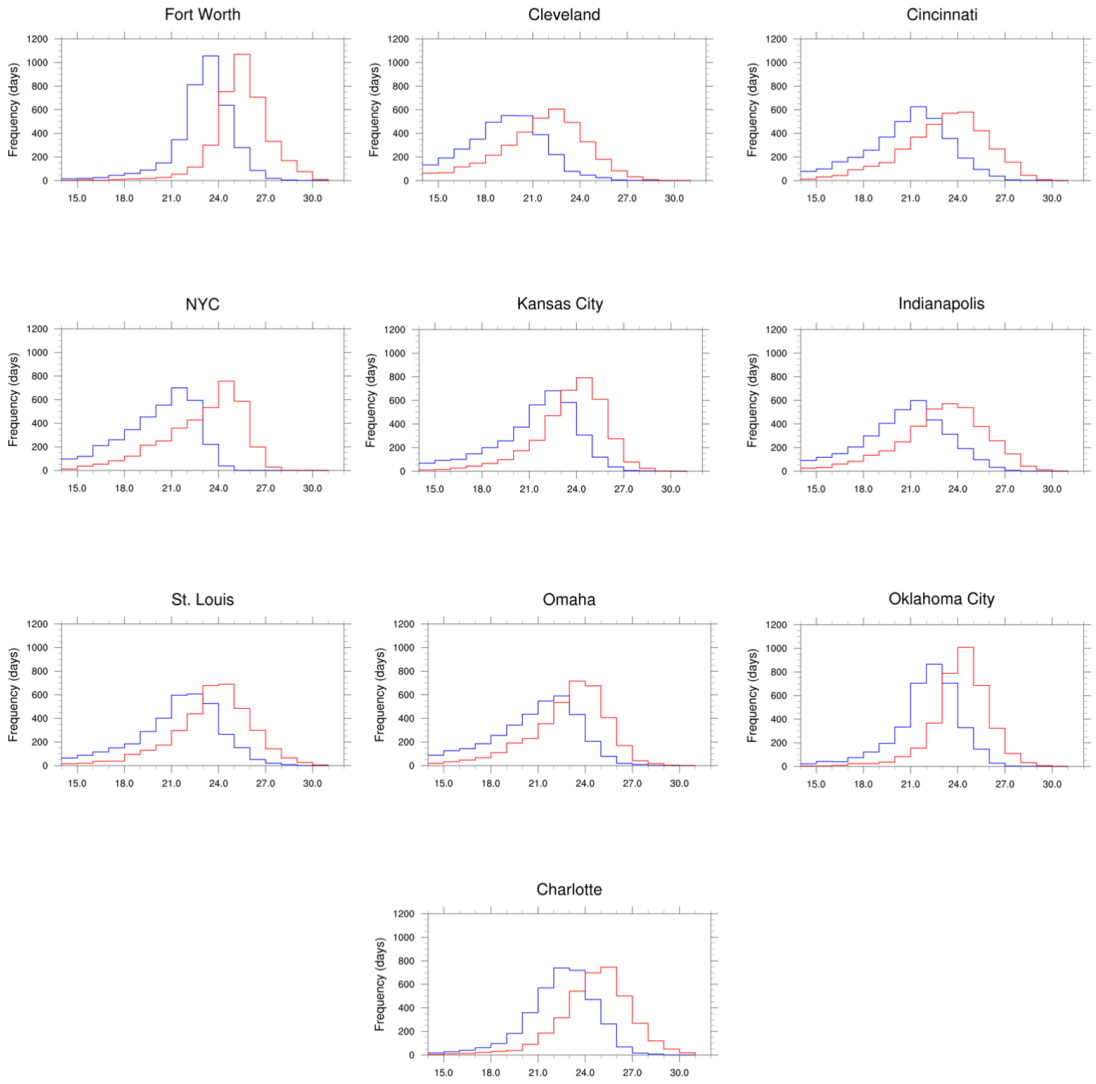

Figure F-31: Daily maximum wet-bulb temperature distributions (degrees C) for more cities in the CCSM4-2000 simulations from the historical (1975-2004) (blue) to the future (2070-2099) (red) periods.

Bibliography

[1] Abd-Elhamid, H., Javadi, A., and Abdelaty, I. Simulation of seawater intrusion in the Nile Delta aquifer under the conditions of climate change. *Hydrology Research 47*, 6 (2016).

[2] Abdel-Shafy, H., El-Saharty, A., Regelsberger, M., and Platzer, C. Rainwater in Egypt: Quantity, distribution and harvesting. *Mediterranean Marine Science 11*, 2 (2010).

[3] Abdelkader, A., Elshorbagy, A., Tuninetti, M., Laio, F., Ridolfi, L., Fahmy, H., and Hoekstra, A. Y. National water, food, and trade modeling framework: The case of Egypt. *Science of The Total Environment 639* (2018), 485–496.

[4] Abu Zeid, K. M. Existing and Recommended Water Policies in Egypt. Water Policies in MENA Countries. *Global Issues in Water Policy 23* (2020). S. Zekri (ed.).

[5] Adegoke, J. O., Pielke Sr., R. A., Eastman, J., Mahmood, R., and Hubbard, K. G. Impact of Irrigation on Midsummer Surface Fluxes and Temperature under Dry Synoptic Conditions: A Regional Atmospheric Model Study of the U. S. High Plains. *Monthly Weather Review 131*, 3 (2003), 556–564.

[6] Al-Shishini, A., and El-Bardisy, H. An econometric economical study for animal protein sources in Egypt. *Achives of Agriculture Sciences Journal 2*, 2 (2019). (G.T. Gilbert, Trans.).

[7] Alfaro, E. J., Gershunov, A., Cayan, D., Alfaro, E. J., Gershunov, A., and Cayan, D. Prediction of Summer Maximum and Minimum Temperature over the Central and Western United States: The Roles of Soil Moisture and Sea Surface Temperature. *Journal of Climate 19*, 8 (2006), 1407–1421.

[8] Allan, J. A. *Priorities for Water Resources Allocation and Management*. London: Overseas Development Administration, 1993.

[9] Alter, R. E., Douglas, H. C., Winter, J. M., and Eltahir, E. A. Twentieth century regional climate change during the summer in the central United States attributed to agricultural intensification. *Geophysical Research Letters 45* (2018), 770–777.

[10] Alter, R. E., Fan, Y., Lintner, B. R., and Weaver, C. P. Observational evidence that Great Plains irrigation has enhanced summer precipitation intensity and totals in the Midwestern United States. *Journal of Hydrometeorology 16*, 4 (2015), 1717–1735.

[11] Alter, R. E., Im, E.-S., and Eltahir, E. A. B. Rainfall consistently enhanced around the Gezira Scheme in East Africa due to irrigation. *Nature Geoscience Letters 8* (2015), 763 – 767.

[12] Antonelli, M., and Tamea, S. Food-water security and virtual water trade in the Middle East and North Africa. *International Journal of Water Resources Development 31*, 3 (2015).

[13] Arab Republic of Egypt Ministry of Water Resources and Irrigation (MWRI). Water for the Future: National Water Resources Plan 2017. Tech. rep., Arab Republic of Egypt, Ministry of Water Resources and Irrigation (MWRI), 2005. Available Online at http://gis.nacse.org/rewab/docs/National_Water_Resources_Plan_2017_en.pdf.

[14] Arakawa, A., and Schubert, W. H. Interaction of a cumulus cloud ensemble with the large-scale environment, Part I. *Journal of the Atmospheric Sciences 31*, 3 (1974), 674–701.

[15] Bandaru, V., West, T. O., Ricciuto, D. M., and Izaurralde, R. C. Estimating crop net primary production using national inventory data and MODIS-derived parameters. *ISPRS Journal of Photogrammetry and Remote Sensing 80* (2013), 61–71.

[16] Banerjee, A., Polvani, L. M., and Fyfe, J. C. The United States "Warming Hole": Quantifying the forced aerosol response given large internal variability. *Geophysical Research Letters 44*, 4 (2017), 1928–1937.

[17] Barriopedro, D., Fischer, E. M., Luterbacher, J., Trigo, R. M., and Garcia-Herrera, R. The hot summer of 2010: Redrawing the temperature record map of Europe. *Science 332*, 6026 (2011), 220–224.

[18] Basheer, M., Wheeler, K. G., Ribbe, L., Majdalawi, M., G., A., and Zagona, E. A. Quantifying and evaluating the impacts of cooperation in transboundary river basins on the Water-Energy-Food nexus: The Blue Nile Basin. *Science of The Total Environment 630* (2018), 1309–1323.

[19] Basso, B., Martinez-Ferra, R. A., Rill, L., and Ritchie, J. T. Contrasting Long-Term Temperature Trends Reveal Minor Changes in Projected Potential Evapotranspiration in the U.S. Midwest. *Nature Communications 12*, 1476 (2021).

[20] Ben-Ari, T., and Makowski, D. Decomposing global crop yield variability. *Environmental Research Letters 9*, 114011 (2014).

[21] Bennington, V., Notaro, M., and Holman, K. D. Improving climate sensitivity of deep lakes within a regional climate model and its impact on simulated climate. *Journal of Climate 27*, 8 (2014), 2886 – 2911.

[22] Bhatia, A., and Choi-Schagrin, W. Why record-breaking overnight temperatures are so concerning. *The New York Times, Upshot* (2021). Published July 9, 2021; Updated Sept. 15, 2021. Available online at urlhttps://www.nytimes.com/2021/07/09/upshot/record-breaking-hot-weather-at-night-deaths.html.

[23] Blackadar, A. K. Boundary layer wind maxima and their significance for the growth of nocturnal inversions. *Bull. Amer. Meteor. Soc. 38* (1957), 283–290.

[24] Bonfils, C., and Lobell, D. Empirical evidence for a recent slowdown in irrigation-induced cooling. *Proceedings of the National Academy of Sciences of the United States of America 104*, 34 (2007), 13582–13587.

[25] Bonner, W. D. Climatology of the Low Level Jet. *Mon. Weather Review 96* (1968), 833–850.

[26] Brooks, C. E. P. Periodicities in the Nile Floods. *Mem. R. Meteorol. Soc. 11* (1927), 9–26.

[27] Brouwer, C., Prins, K., and Heibloem, M. *In Irrigation Water Management: Irrigation Scheduling: Training Manual 4.* http://www.fao.org/3/t7202e/t7202e08.htm, 1989.

[28] Brown, P. J., and Degaetano, A. T. Trends in U.S. surface humidity, 1930-2010. *Journal of Applied Meteorology and Climatology 52*, 1 (2013), 147–163.

[29] Brönnimann, S., Stickler, A., Griesser, T., Ewen, T., Grant, A. N., Fischer, A. M., Schraner, M., Peter, T., Rozanov, E., and Ross, T. Exceptional atmospheric circulation during the "Dust Bowl". *Geophysical Research Letters 36*, 8 (2009).

[30] Burgman, R. J., and Jang, Y. Simulated U.S. drought response to interannual and decadal Pacific SST variability. *Journal of Climate 28*, 12 (2015), 4688–4705.

[31] Burnette, D. J., and Stahle, D. W. Historical perspective on the dust bowl drought in the central United States. *Climatic Change 116*, 3 (2013), 479–494.

[32] Centers for Disease Control and Prevention National Center for Health Statistics. Compressed Mortality File 1979-1998. CDC WONDER On-line Database, compiled from Compressed Mortality File CMF 1968-1988, Series 20, No. 2A, 2000 and CMF. 1989-1998, Series 20, No. 2E, 2003. Accessed at http://wonder.cdc.gov/cmf-icd9.html on Sep 12, 2018 1:30:48 PM.

[33] Chini, L., Hurtt, G., and Frolking, S. Harmonized global land use for years 1500 – 2100, v1. Dataset. Available on-line [http://daac.ornl.gov] from Oak Ridge National Laboratory Distributed Active Archive Center, Oak Ridge, Tennessee, USA, 2014. http://dx.doi.org/10.3334/ORNLDAAC/1248.

[34] Clement, A., Bellomo, K., Murphy, L. N., Cane, M. A., Mauritsen, T., Rädel, G., and Stevens, B. The Atlantic Multidecadal Oscillation without a role for ocean circulation. *Science 350*, 6258 (2015), 320–324.

[35] Compo, G. P., Whitaker, J. S., Sardeshmukh, P. D., Matsui, N., Allan, R. J., Yin, X., and et al. Review article: The twentieth century reanalysis project. *Quarterly Journal of the Royal Meteorological Society 137*, 654 (2011), 1–28. 20th Century Reanalysis V2c data provided by the NOAA/OAR/ESRL PSD, Boulder, Colorado, USA, from their web site at https://www.esrl.noaa.gov/psd/.

[36] Cook, B. I., Ault, T. R., and Smerdon, J. E. Unprecedented 21st century drought risk in the American Southwest and Central Plains. *Science Advances 1*, 1 (2015).

[37] Cook, B. I., Miller, R. L., and Seager, R. Amplification of the North American Dust Bowl drought through human-induced land degradation. *Proceedings of the National Academy of Sciences 106*, 13 (2009), 4997–5001.

[38] Cook, B. I., Seager, R., and Miller, R. L. Atmospheric circulation anomalies during two persistent North American droughts: 1932-1939 and 1948-1957. *Climate Dynamics 36*, 11-12 (2011), 2339–2355.

[39] Cook, K. H., Vizy, E. K., Launer, Z. S., and Patricola, C. M. Springtime Intensification of the Great Plains Low-Level Jet and Midwest Precipitation in GCM Simulations of the Twenty-First Century. *Journal of Climate 21*, 23 (2008), 6321 – 6340.

[40] Cornish, G., Bosworth, B., Perry, C., and Burke, J. Annex 1: Water charging for irrigation – data from the literature. In Water Charging in Irrigated Agriculture: An analysis of international experience. Available online at http://www.fao.org/3/y5690e/y5690e0b.htm, 2004.

[41] Dahl, T. E., and Allord, G. J. Water-Supply Paper 2425: History of Wetlands in the Coterminous United States In National Water Summary – Wetland Resources: Technical Aspects of Wetlands. Tech. rep., U.S. Geological Survey, 1997.

[42] Davies-Jones, R. An efficient and accurate method for computing the wet-bulb temperature along pseudoadiabats. *Monthly Weather Review 136*, 7 (2008), 2764 – 2785.

[43] de Wiel, B. J. H. V., Moene, A. F., Steeneveld, G. J., Baas, P., Bosveld, F. C., and Holtslag, A. A. M. A Conceptual View on Inertial Oscillations and Nocturnal Low-Level Jets. *Journal of the Atmospheric Sciences 67*, 8 (2010), 2679 – 2689.

[44] DeAngelis, A., Dominguez, F., Fan, Y., Robock, A., Kustu, M. D., and Robinson, D. Evidence of enhanced precipitation due to irrigation over the Great Plains of the United States. *Journal of Geophysical Research Atmospheres 115* (2010), D15115.

[45] Delaney, F., and Milner, G. The State of Climate Modeling in the Great Lakes Basin - A Synthesis in Support of a Workshop held on June 27, 2019 in Ann Arbor, MI. Toronto, Canada. Tech. rep., Ontario Climate Consortium, 2019.

[46] Delaney, F., and Milner, G. Water and Atmospheric Resources Monitoring Program. Illinois Climate Network. . Tech. rep., Illinois State Water Survey, 2204 Griffith Drive, Champaign, IL 61820-7495., 2021. https://dx.doi.org/10.13012/J8MW2F2Q.

[47] Deser, C., Knutti, R., Solomon, S., and Phillips, A. S. Communication of the role of natural variability in future North American climate. *Nature Climate Change 2*, 11 (2012), 775–779.

[48] Diffenbaugh, N. S. Influence of modern land cover on the climate of the United States. *Climate Dynamics 33* (2009), 945–958.

[49] Diffenbaugh, N. S., and Ashfaq, M. Intensification of hot extremes in the United States. *Geophysical Research Letters 37*, L15701 (2010).

[50] Diffenbaugh, N. S., Pal, J. S., Giorgi, F., and Gao, X. Heat stress intensification in the Mediterranean climate change hotspot. *Geophysical Research Letters 34*, L11706 (2007).

[51] Diffenbaugh, N. S., Pal, J. S., Trapp, R. J., and Giorgi, F. Fine-scale processes regulate the response of extreme events to global climate change. *Proceedings of the National Academy of Sciences 102*, 44 (2005), 15774–15778.

[52] Donat, M. G., King, A. D., Overpeck, J. T., Alexander, L. V., Durre, I., and Karoly, D. J. Extraordinary heat during the 1930s US Dust Bowl and associated large-scale conditions. *Climate Dynamics 46*, 1-2 (2016), 413–426.

[53] Dost, M., Bimal, M., El-Nahrawy, M., Khan, S., and Serkan, A. Egyptian clover (trifolium alexandrinum). king of forage crops. (Food and Agriculture Organization of the United Nations, Regional Office for the Near East and North Africa, Cairo). Available online at http://www.fao.org/3/a-i3500e.pdf, 2014.

[54] Douglas, H. *Observational analysis of twentieth century summer climate over North America.* (Masters Thesis), Retrieved from DSpace@MIT. (http://hdl.handle.net/1721.1/104191). Cambridge, MA: Massachusetts Institute of Technology, 2016.

[55] Dunne, J. P., Stouffer, R. J., and John, J. G. Reductions in labour capacity from heat stress under climate warming. *Nature Climate Change 3*, SI (2013), 563–566.

[56] Duvick, D. N. The contribution of breeding to yield advances in maize (Zea mays L.). *Advances in Agronomy 86* (2005), 83–145.

[57] ECMWF. Reanalysis Datasets: CERA-20C. Retrieved from https://www.ecmwf.int/en/forecasts/datasets/reanalysis-datasets/cera-20c, 2017.

[58] Eltahir, E. A. B. A Soil Moisture-Rainfall Feedback Mechanism: 1. Theory and observations. *Water Resources Research 34*, 4 (apr 1998), 765–776.

[59] Elzein, A. S. Monthly Streamflow at Dongola (1890-2020). Republic of Sudan Ministry of Irrigation and Water Resources, 2020.

[60] Enfield, D. B., Mestas-Nuñez, A. M., and Trimble, P. J. The Atlantic Multidecadal Oscillation and its relation to rainfall and river flows in the continental U.S. *Geophys. Res. Lett. 28*, 10 (2001), 2077–2080.

[61] Eyring, V., Bony, S., Meehl, G. A., Senior, C. A., Stevens, B., Stouffer, R. J., and Taylor, K. E. Overview of the Coupled Model Intercomparison Project Phase 6 (CMIP6) experimental design and organization. *Geosci. Model Dev. 9* (2016), 1937–1958.

[62] Falkenmark, M., Lundquist, J., and Widstrand, C. Macro-scale Water Scarcity Requires Micro-scale Approaches: Aspects of Vulnerability in Semi-arid Development. *Natural Resources Forum 13*, 4 (1989).

[63] FAO. Crop water information. Available Online at http://www.fao.org/land-water/databases-and-software/crop-information/en/ [Accessed March 2020].

[64] FAO. Food supply – livestock and fish primary equivalent. FAOSTAT Statistical Database. Available Online at http://www.fao.org/faostat/en/#data/CL. Accessed April 2020., 1997.

[65] FAO. Macro indicators. FAOSTAT Statistical Database. Available Online at http://www.fao.org/faostat/en/#data/MK. Accessed April 2020., 1997.

[66] FAO. Suite of food security indicators. FAOSTAT Statistical Database. Available Online at http://www.fao.org/faostat/en/#data/FS. Accessed April 2020., 1997.

[67] FAO. Egypt country programming framework. Available Online at http://www.fao.org/publications/card/en/c/0603d9fd-85c9-4557-8772-eb40602666a6, 2013.

[68] FAO. AQUASTAT Country Profile – Egypt. Food and Agriculture Organization of the United Nation, Rome. Available Online at http://www.fao.org/3/i9729en/I9729EN.pdf, 2016.

[69] FAO. AQUASTAT Country Profile – Egypt. Country Factsheet. Food and Agriculture Organization of the United Nations (FAO), Rome, Italy. Available Online at https://storage.googleapis.com/fao-aquastat.appspot.com/countries_regions/factsheets/summary_statistics/en/EGY-CF.pdf, 2016.

[70] FAO. Aquastat country profile – egypt. water resources factsheet. Available Online at https://storage.googleapis.com/fao-aquastat.appspot.com/countries_regions/factsheets/water_resources/en/EGY-WRS.pdf. Accessed April 2020., 2016.

[71] FAO. AQUASTAT Country Profile – Sudan. Food and Agriculture Organization of the United Nation, Rome. Available Online at http://www.fao.org/3/i9808en/I9808EN.pdf, 2016.

[72] FAO. Aquastat main database. Available Online at http://www.fao.org/nr/water/aquastat/data/query/index.html?lang=en. Accessed April 2020., 2016.

[73] FAO. AQUASTAT Main Database, Water Resources: Exploitable Water Resources and Dam Capacity, Egypt, 2016.

[74] FAO. Maize: Water Supply and Crop Yield. Food and Agriculture Organization of the United Nation, Rome. Available at http://www.fao.org/land-water/databases-and-software/crop-information/maize/en/, 2018.

[75] FAO. Suite of food security indicators: Cereal import dependency ratio (percent) (3yr average). FAOSTAT Statistical Database. Accessed April 2020., 2020.

[76] Findell, K. L., and Delworth, T. L. Impact of common sea surface temperature anomalies on global drought and pluvial frequency. *Journal of Climate 23*, 3 (2010), 485–503.

[77] Fischer, E. M., and Knutti, R. Robust projections of combined humidity and temperature extremes. *Nature Climate Change 3*, 2 (2013), 126–130.

[78] Fischer, E. M., and Schar, C. Consistent geographical patterns of changes in high-impact European heatwaves. *Nature Geoscience 3* (2010), 398–403.

[79] Gao, Y., Fu, J. S., Drake, J. B., Liu, Y., and Lamarque, J.-F. Projected changes of extreme weather events in the eastern United States based on a high-resolution climate modeling system. *Environmental Research Letters 7*, 044025 (2012).

[80] Gaulier, G., and Zignago, S. Baci: International trade database at the product-level. the 1994-2007 version. CEPII Working Paper 2010-23, CEPII., 2010.

[81] Gianotti, R. L., and Eltahir, E. A. B. Regional climate modeling over the Maritime Continent. Part I: New parameterization for convective cloud fraction. *Journal of Climate 27*, 4 (2014), 1488–1503.

[82] Gianotti, R. L., and Eltahir, E. A. B. Regional climate modeling over the Maritime Continent. Part II: New parameterization for autoconversion of convective rainfall. *Journal of Climate 27*, 4 (2014), 1504–1523.

[83] Gianotti, R. L., Zhang, D., and Eltahir, E. A. B. Assessment of the Regional Climate Model version 3 over the Maritime Continent using different cumulus parameterization and land surface schemes. *Journal of Climate 25*, 2 (jan 2012), 638–656.

[84] Global Water Intelligence. Egypt to slash subsidies in water and wastewater. Available Online at https://www.globalwaterintel.com/news/2017/31/egypt-to-slash-subsidies-in-water-and-wastewater?dm_i=36G3,IGWK,2MX9NG,1XJV0,1.

[85] Goldman, A., and Smith, J. Agricultural Transformations in India and Northern Nigeria: Exploring the nature of Green Revolutions. *World Development 23*, 2 (1995), 243–263.

[86] Grafton, R., Williams, J., Perry, C. J., and et al. The paradox of irrigation efficiency. *Science 361*, 6404 (2018).

[87] Grell, G. A. Prognostic evaluation of assumptions used by cumulus parameterizations. *Monthly Weather Review 121*, 3 (1993), 764–787.

[88] Halder, S., Saha, S. K., Dirmeyer, P. A., Chase, T. N., and Goswami, B. N. Investigating the impact of land-use land-cover change on Indian summer monsoon daily rainfall and temperature during 1951-2005 using a regional climate model. *Hydrology and Earth System Sciences 20* (2016), 1765–1784.

[89] Hamza, W. *P. Wangersky (ed), Estuaries; Handbook of Environmental Chemistry, V5.* Springer Verlag, Heidelberg,, 2006.

[90] Hanrahan, J., Langlois, J., Cornell, L., Huang, H., Winter, J. M., Clemins, P. J., Beckage, B., and Bruyère, C. Examining the impacts of great lakes temperature perturbations on simulated precipitation in the northeastern united states. *Journal of Applied Meteorology and Climatology 60*, 7 (2021), 935 – 949.

[91] Hansen, J., Sato, M., Ruedy, R., Kharecha, P., Lacis, A., Miller, R. L., Nazarenko, L., Lo, K., Schmidt, G. A., Russell, G., Aleinov,

I., Bauer, S., Baum, E., Cairns, B., Canuto, V., Chandler, M., Cheng, Y., Cohen, A., Del Genio, A., Faluvegi, G., Fleming, E., Friend, A., Hall, T., Jackman, C., Jonas, J., Kelley, M., Kiang, N. Y., Koch, D., Labow, G., Lerner, J., Menon, S., Novakov, T., Oinas, V., Perlwitz, J. P., Perlwitz, J., Rind, D., Romanou, A., Schmunk, R., Shindell, D., Stone, P., Sun, S., Streets, D., Tausnev, N., Thresher, D., Unger, N., Yao, M., and Zhang, S. Climate simulations for 1880-2003 with giss modele. *Clim. Dyn. 29* (2007), 661–696.

[92] Harding, K. J., and Snyder, P. K. Modeling the atmospheric response to irrigation in the Great Plains. Part I: General impacts on precipitation and the energy budget. *Journal of Hydrometeorology 13* (2012), 1667–1686.

[93] Harris, I., Jones, P. D., Osborn, T. J., and Lister, D. H. Updated high-resolution grids of monthly climatic observations - the CRU TS3.10 dataset. *International Journal of Climatology 34*, 3 (2014), 623–642. Data retrieved from https://crudata.uea.ac.uk/cru/data/hrg/.

[94] Harris, I. C., and Jones, P. D. CRU TS4.01: Climatic Research Unit (CRU) Time-Series (TS) version 4.01 of high-resolution gridded data of month-by-month variation in climate (Jan. 1901- Dec. 2016). University of East Anglia Climatic Research Unit, Centre for Environmental Data Analysis., 2017.

[95] Harris, I. C., Jones, P. D., and Osborn, T. CRU TS4.04: Climatic Research Unit (CRU) Time-Series (TS) version 4.04 of high-resolution gridded data of month-by-month variation in climate (Jan. 1901- Dec. 2019). University of East Anglia Climatic Research Unit, Centre for Environmental Data Analysis., 2020.

[96] Hassan, E. Egypt to plant 100 million olive trees across the country by 2022. Aldiplomasy. Available Online at https://www.aldiplomasy.com/en/?p=17158;, 2019.

[97] Hassan, F. A. Historical Nile Floods and their Implications for Climatic Change. *Science 212*, 4499 (1981).

[98] Hatfield, J. Agriculture in the Midwest. Tech. rep., In U.S. National Climate Assessment Midwest Technical Input Report. J. Winkler, J. Andresen, J. Hatfield, D. Bidwell, and D. Brown, coordinators. Available from Great Lakes Integrated Sciences and Assessments (GLISA) Center, http://glisa.umich.edu/media/files/NCA/MTIT_Agriculture.pdf, 2012.

[99] Hatfield, J. L. Climate Impacts on Agriculture: Implications for Crop Production. *Agronomy Journal 103*, 2 (2011).

[100] Hauer, M. Population projections for U.S. counties by age, sex, and race controlled to shared socioeconomic pathway. *Sci. Data 6*, 190005 (2019).

[101] Hayhoe, K., Wuebbles, D. J., Easterling, D. R., Fahey, D. W., Doherty, S., Kossin, J., Sweet, W., Vose, R., and Wehner, M. *Impacts, Risks, and Adaptation in the United States: Fourth National Climate Assessment, Volume II [Reidmiller, D.R., C.W. Avery, D.R. Easterling, K.E. Kunkel, K.L.M. Lewis, T.K. Maycock, and B.C. Stewart (eds.)].* U.S. Global Change Research Program, Washington, DC, USA, 2018.

[102] Heckert, N., and Filliben, J. J. NIST handbook 148: DATAPLOT reference manual, Volume I: Commands. Tech. rep., National Institute of Standards and Technology Handbook Series, June 2003, http://www.itl.nist.gov/div898/software/dataplot/refman1/auxillar/ks2samp.htm, 6 2003.

[103] Helfand, H. M., and Schubert, S. D. Climatology of the Simulated Great Plains Low-Level Jet and Its Contribution to the Continental Moisture Budget of the United States. *Journal of Climate 8*, 4 (1995), 784 – 806.

[104] Hereher, M. E. Vulnerability of the Nile Delta to sea level rise: an assessment using remote sensing. *Geomatics, Natural Hazards and Risk 1*, 4 (2010).

[105] Herodotus. An account of Egypt by Herodotus, being the second book of his histories called Euterpe. (G. C. Macaulay, Trans.) https://www.gutenberg.org/files/2131/2131-h/2131-h.htm, 2006.

[106] Hersbach, H., Bell, B., Berrisford, P., Hirahara, S., Horányi, A., Muñoz-Sabater, J., Nicolas, J., Peubey, C., Radu, R., Schepers, D., Simmons, A., Soci, C., Abdalla, S., Abellan, X., Balsamo, G., Bechtold, P., Biavati, G., Bidlot, J., Bonavita, M., Chiara, G. D., Dahlgren, P., Dee, D., Diamantakis, M., Dragani, R., Flemming, J., Forbes, R., Fuentes, M., Geer, A., Haimberger, L., Healy, S., Hogan, R. J., Hólm, E., Janisková, M., Keeley, S., Laloyaux, P., Lopez, P., Lupu, C., Radnoti, G., de Rosnay, P., Rozum, I., Vamborg, F., Villaume, S., and Thépaut, J.-N. The ERA5 global reanalysis. *Quarterly Journal of the Royal Meteorological Society 146*, 730 (2020), 1999–2049.

[107] Hicke, J. A., and Lobell, D. B. Spatiotemporal patterns of cropland area and net primary production in the central United States estimated from USDA agricultural information. *Geophysical Research Letters 31*, 20 (2004), 1–5.

[108] Hollinger, S. E., and Isard, S. A. A Soil Moisture Climatology of Illinois. *Journal of Climate 7*, 5 (1994), 822–833.

[109] Holton, J. R. The diurnal boundary layer wind oscillation above sloping terrain. *Tellus 19* (1967), 199–205.

[110] Hopwood, D., Goldschmidt, A. E., and et al. Egypt: Agriculture and Fishing. *The Encyclopedia Britannica* (2020).

[111] Hu, Q., Feng, S., and Oglesby, R. J. Variations in North American summer precipitation driven by the Atlantic Multidecadal Oscillation. *Journal of Climate 24*, 21 (2011), 5555–5570.

[112] Huang, B., Thorne, P. W., Banzon, V. F., Boyer, T., Chepurin, G., Lawrimore, J. H., Menne, M. J., Smith, T. M., Vose, R. S., and Zhang, H.-M. Extended reconstructed sea surface temperature, version 5 (ERSSTv5): Upgrades, validations, and intercomparisons. *Journal of Climate 30*, 20 (2017), 8179–8205.

[113] Huber, D. B., Mechem, D. B., and Brunsell, N. A. The effects of Great Plains irrigation on the surface energy balance, regional circulation, and precipitation. *Climate 2* (2014), 103–128.

[114] Hudson, J. C. *Making the Corn Belt: A Geographical History of Middle-Western Agriculture.* Indiana University Press, 1994.

[115] Hunter, T. S., Clites, A. H., Gronewold, A. D., and Campbell., K. B. Development and application of a North American Great Lakes hydrometeorological database - Part I: Precipitation, evaporation, runoff, and air temperature. *Journal of Great Lakes Research 41*, 1 (2015), 65–77.

[116] Huntington, T. G. Evidence for intensification of the global water cycle: Review and synthesis. *Journal of Hydrology 319* (2006), 83–95.

[117] Hurtt, G. C., Chini, L., Sahajpal, R., Frolking, S., Bodirsky, B. L., Calvin, K., Doelman, J., Fisk, J., Fujimori, S., Goldewijk, K. K., Hasegawa, T., Havlik, P., Heinimann, A., Humpenöder, F., Jungclaus, J., Kaplan, J., Krisztin, T., Lawrence, D., Lawrence, P., Mertz, O., Pongratz, J., Popp, A., Riahi, K., Shevliakova, E., Stehfest, E., Thornton, P., van Vuuren, D., and Zhang, X. Harmonization of Global Land Use Change and Management for the Period 850-2015. Version 20190529. Earth System Grid Federation. https://doi.org/10.22033/ESGF/input4MIPs.10454, 2019.

[118] Hurtt, G. C., Chini, L. P., Frolking, S., Betts, R. A., Feddema, J., Fischer, G., Fisk, J. P., Hibbard, K., Houghton, R. A., Janetos, A., Jones, C. D., Kindermann, G., Kinoshita, T., Klein Goldewijk, K., Riahi, K., Shevliakova, E., Smith, S., Stehfest, E., Thomson, A., Thornton, P., van Vuuren, D. P., and Wang, Y. P. Harmonization of land-use scenarios for the period 1500-2100: 600 years of global gridded annual land-use transitions, wood harvest, and resulting secondary lands. *Climatic Change 109*, 1 (2011), 117–161.

[119] Im, E.-S., and Eltahir, E. A. B. Enhancement of rainfall and runoff upstream from irrigation location in a climate model of West Africa. *Water Resources Research 50* (2014), 8651–8674.

[120] Im, E.-S., Gianotti, R., and Eltahir, E. A. B. Improving the Simulation of the West African Monsoon Using the MIT Regional Climate Model. *Journal of Climate 27* (2014), 2209–2229.

[121] Im, E.-S., Marcella, M. P., and Eltahir, E. A. B. Impact of potential large-scale irrigation on the West African monsoon and its dependence on location of irrigated area. *Journal of Climate 27*, 3 (2014), 994–1009.

[122] Im, E.-S., Pal, J. S., and Eltahir, E. A. B. Deadly heat waves projected in the densely populated agricultural regions of South Asia. *Science Advances 3*, e1603322 (2017).

[123] Jaafar, H. H., and Ahmad, F. A. Crop yield prediction from remotely sensed vegetation indices and primary productivity in arid and semi-arid lands. *International Journal of Remote Sensing 36*, 18 (2015), 4570–4589.

[124] Jia, L., Vecchi, G. A., Yang, X., Gudgel, R. G., Delworth, T. L., Stern, W. F., Paffendorf, K., Underwood, S. D., and Zeng, F. The roles of radiative forcing, sea surface temperatures, and atmospheric and land initial conditions in U.S. summer warming episodes. *Journal of Climate 29*, 11 (2016), 4121–4135.

[125] Jin, J., and Miller, N. L. Regional simulations to quantify land use change and irrigation impacts on hydroclimate in the California Central Valley. *Theoretical Applied Climatology 104* (2011), 429–442.

[126] Kang, S., and Eltahir, E. A. B. North China Plain threatened by deadly heatwaves due to climate change and irrigation. *Nature Communications 9*, 1 (2018), 1–9.

[127] Knight, J. R., Folland, C. K., and Scaife, A. A. Climate impacts of the Atlantic Multidecadal Oscillation. *Geophysical Research Letters 33*, 17 (2006), 2–5.

[128] Koster, R. D., Wang, H., Schubert, S. D., Suarez, M. J., and Mahanama, S. Drought-induced warming in the continental United States under different SST regimes. *Journal of Climate 22*, 20 (2009), 5385–5400.

[129] Krakauer, N. Y., Cook, B. I., and Puma, M. J. Effect of irrigation on humid heat extremes. *Environmental Research Letters 15* (2020).

[130] Kucharik, C. J., and Ramankutty, N. Trends and variability in U.S. corn yields over the twentieth century. *Earth Interactions 9*, 1 (2005), 1–29.

[131] Kueppers, L. M., Snyder, M. A., and Sloan, L. C. Irrigation cooling effect: Regional climate forcing by land-use change. *Geophysical Research Letters 34* (2007), L03703.

[132] Kumar, S., Dirmeyer, P. A., Merwade, V., DelSole, T., Adams, J. M., and D., N. Land use/cover change impacts in CMIP5 climate simulations: A new methodology and 21st century challenges. *Journal of Geophys. Res. Atmos. 118* (2013), 6337–6353.

[133] Kunkel, K. E., Liang, X.-Z., Zhu, J., and Lin, Y. Can CGCMs simulate the twentieth-century warming hole in the central United States? *Journal of Climate 19* (2006), 4137–4153.

[134] Laloyaux, P. The Climate Data Guide: CERA-20C: ECMWF's Coupled Ocean-Atmosphere Reanalysis of the 20th Century. National Center for Atmospheric Research Staff (Eds.). Retrieved from https://climatedataguide.ucar.edu/climate-data/cera-20c-ecmwfs-coupled-ocean-atmosphere-reanalysis-20th-century., 2017.

[135] Lee, J. A., and Gill, T. E. Multiple causes of wind erosion in the Dust Bowl. *Aeolian Research 19* (2015), 15–36.

[136] Lenters, J. D., Anderton, J. B., Blanken, P., Spence, C., and Suyker, A. E. Assessing the impacts of climate variability and change on great lakes evaporation. In: 2011 Project Reports. D. Brown, D. Bidwell, and L. Briley, eds. Available from the Great Lakes Integrated Sciences and Assessments (GLISA) Center: http://glisaclimate.org/media/GLISA_Lake_Evaporation.pdf, 2013.

[137] Lev-Yadun, S., Gopher, A., and Abbo, S. The Cradle of Agriculture. *Science 288*, 5471 (2000), 1602–1603.

[138] Li, T., Horton, R. M., and Kinney, P. L. Projections of seasonal patterns in temperature- related deaths for Manhattan, New York. *Nature Climate Change 3*, 8 (2013), 717–721.

[139] Li, Z., Liu, S., Tan, Z., Bliss, N. B., Young, C. J., West, T. O., and Ogle, S. M. Comparing cropland net primary production estimates from inventory, a satellite-based model, and a process-based model in the Midwest of the United States. *Ecological Modelling 277* (2014), 1–12.

[140] Livneh, B., Rosenberg, E. A., Lin, C., Nijssen, B., Mishra, V., Andreadis, K. M., Maurer, E. P., and Lettenmaier, D. P. A long-term hydrologically based dataset of land surface fluxes and states for the conterminous United States: Update and extensions. *Journal of Climate 26*, 23 (2013), 9384–9392.

[141] Lixia, H., Wallace, E. T., Rachid, D., and Gamal, S. Policy Options to Improve Water Allocation Efficiency: Analysis on Egypt and Morocco. *Water International 31*, 3 (2006).

[142] Lo, M.-H., and Famiglietti, J. S. Irrigation in California's Central Valley strengthens the southwestern U.S. water cycle. *Geophysical Research Letters 40*, 2 (2013), 301–306.

[143] Lobell, D., Bala, G., Mirin, A., Phillips, T., Maxwell, R., and Rotman, D. Regional differences in the influence of irrigation on climate. *Journal of Climate 22*, 8 (2009), 2248–2255.

[144] Lobell, D. B., Bonfils, C. J., Kueppers, L. M., and Snyder, M. A. Irrigation cooling effect on temperature and heat index extremes. *Geophysical Research Letters 35*, 9 (2008), L09705.

[145] Lu, Y., Harding, K., and Kueppers, L. Irrigation Effects on Land-Atmosphere Coupling Strength in the United States. *Journal of Climate 30* (2017), 3671–3685.

[146] Luber, G., and McGeehin, M. Climate change and extreme heat events. *American Journal of Preventative Medicine 35*, 5 (2008).

[147] Lutsko, N. J. The relative contributions of temperature and moisture to heat stress changes under warming. *Journal of Climate 34*, 3 (2021), 901 – 917.

[148] Mahmoud, M. A., and Negm, A. M. Groundwater in the Nile Delta. *Hdb Env Chem 73* (2019), 141–158.

[149] Mallard, M. S., Nolte, C. G., Spero, T. L., Bullock, O. R., Alapaty, K., Herwehe, J. A., Gula, J., and Bowden, J. H. Technical challenges and solutions in representing lakes when using WRF in downscaling applications. *Geosci. Model Dev. 8* (2015), 1085–1096.

[150] Maloney, E. D., Camargo, S. J., Chang, E., Colle, B., Fu, R., Geil, K. L., Hu, Q., Jiang, X., Johnson, N., Karnauskas, K. B., Kinter, J., Kirtman, B., Kumar, S., Langenbrunner, B., Lombardo, K., Long, L. N., Mariotti, A., Meyerson, J. E., Mo, K. C., Neelin, J. D., Pan, Z., Seager, R., Serra, Y., Seth, A., Sheffield, J., Stroeve, J., Thibeault, J., Xie, S.-P., Wang, C., Wyman, B., and Zhao, M. North American Climate in CMIP5 Experiments: Part III: Assessment of Twenty-First-Century Projections. *Journal of Climate 27*, 6 (2014), 2230 – 2270.

[151] Marcella, M. P. *Biosphere-atmosphere interactions over semi-arid regions: Modeling the role of mineral aerosols and irrigation in the regional climate system.* (doctoral dissertation), Retrieved from DSpace@MIT. (http://hdl.handle.net/1721.1/79490). Cambridge, MA: Massachusetts Institute of Technology, 2013.

[152] Marcella, M. P., and Eltahir, E. A. B. Effects of mineral aerosols on the summertime climate of southwest Asia: Incorporating subgrid variability in a dust emission scheme. *Journal of Geophysical Research 115* (2010), D18203.

[153] Marcella, M. P., and Eltahir, E. A. B. Modeling the summertime climate of Southwest Asia: The role of land surface processes in shaping the climate of semiarid regions. *Journal of Climate 25* (2012), 704–719.

[154] Mascioli, N. R., Previdi, M., Fiore, A. M., and Ting, M. Timing and seasonality of the United States 'warming hole'. *Environmental Research Letters 12*, 034008 (2017).

[155] McConnell, M. Feedgrains sector at a glance. Accessed online on June 28, 2021 at https://www.ers.usda.gov/topics/crops/corn-and-other-feedgrains/feedgrains-sector-at-a-glance/, 2021.

[156] McCorvie, M. R., and Lant, C. L. Drainage District Formation and the Loss of Midwestern Wetlands, 1850-1930. *Agricultural History 67*, 4 (1993).

[157] Meehl, G. A., Arblaster, J. M., and Branstator, G. Mechanisms Contributing to the Warming Hole and the Consequent U.S. East-West Differential of Heat Extremes. *Journal of Climate 25*, 18 (2012).

[158] Meehl, G. A., and Tebaldi, C. More Intense, More Frequent, and Longer Lasting Heat Waves in the 21st Century. *Science 305* (2004), 994–997.

[159] Mei, R., and Wang, G. Impact of sea surface temperature and soil moisture on summer precipitation in the United States based on observational data. *Journal of Hydrometeorology 12*, 5 (2011), 1086–1099.

[160] Meinshausen, M., Smith, S. J., Calvin, K., Daniel, J. S., Kainuma, M. L., Lamarque, J.-F., Matsumoto, K., Montzka, S. A., Raper, S. C. B., Riahi, K., Thomson, A., Velders, G. J. M., and van Vuuren, D. P. P. The RCP greenhouse gas concentrations and their extensions from 1765 to 2300. *Climatic Change 109* (2011), 213–241. Data Retrieved from http://www.pik-potsdam.de/ mmalte/rcps/.

[161] Mekonnen, M. M., and Hoekstra, A. Y. *The green, blue and grey water footprint of crops and derived crop products. Value of Water Research Report Series No. 47, Vol. I.* UNESCO-IHE, Delft, the Netherlands, 2010. Available at https://research.utwente.nl/en/publications/the-green-blue-and-grey-water-footprint-of-crops-and-derived-crop-3.

[162] Mekonnen, M. M., and Hoekstra, A. Y. *The green, blue and grey water footprint of crops and derived crop products, Value of Water Research Report Series No. 47, Vol. II, App. II.* UNESCO-IHE, Delft, the Netherlands, 2010. Available at https://research.utwente.nl/files/59480760/Report47_WaterFootprintCrops_Vol2.pdf.

[163] Mekonnen, M. M., and Hoekstra, A. Y. *The green, blue and grey water footprint of crops and derived crop products. Value of Water Research Report Series No. 47, Vol. II, App. II.* UNESCO-IHE, Delft, the

Netherlands, 2010. Available at https://research.utwente.nl/files/59480760/Report47_WaterFootprintCrops_Vol2.pdf.

[164] Mekonnen, M. M., and Hoekstra, A. Y. *The green, blue and grey water footprint of farm animals and animal products (grazing method). Value of Water Research Report Series No. 48, Vol. II, App. V.* UNESCO-IHE, Delft, the Netherlands, 2010. Available at https://research.utwente.nl/files/59481201/Report48_WaterFootprint_AnimalProducts_Vol2.pdf.

[165] Mekonnen, M. M., and Hoekstra, A. Y. *National water footprint accounts: the green, blue and grey water footprint of production and consumption. Value of Water Research Report Series No. 50, Vol. II, App. VI.* UNESCO-IHE, Delft, the Netherlands, 2011. Available at https://research.utwente.nl/files/5146139/Report50-NationalWaterFootprints-Vol2.pdf.

[166] Mekonnen, M. M., and Hoekstra, A. Y. TA Global Assessment of the Water Footprint of Farm Animal Products. *Ecosystems 15* (2012), 401–415.

[167] Mekonnen, M. M., and Hoekstra, A. Y. The green, blue and grey water footprint of crops and derived crop products. *Hydrol. Earth Syst. Sci. 15* (2019), 1577–1600.

[168] Mishra, V., Ambika, A. K., Asoka, A., Aadhar, S., Buzan, J., Kumar, R., and Huber, M. Moist heat stress extremes in india enhanced by irrigation. *Nature Geoscience 13*, 11 (2020), 722–728.

[169] Monfreda, C., Ramankutty, N., and Foley, J. A. Farming the planet: 2. Geographic distribution of crop areas, yields, physiological types, and net primary production in the year 2000. *Global Biogeochemical Cycles 22* (2008), GB1022.

[170] Mora, C., Dousset, B., Caldwell, I. R., Powell, F. E., Geronimo, R. C., Bielecki, C. R., Counsell, C. W., Dietrich, B. S., Johnston, E. T., Louis, L. V., Lucas, M. P., Mckenzie, M. M., Shea, A. G., Tseng, H., Giambelluca, T. W., Leon, L. R., Hawkins, E., and Trauernicht, C. Global risk of deadly heat. *Nature Climate Change 7* (2017).

[171] Morsy, W. S. *Environmental management of groundwater resources for Nile Delta region.* (Doctoral Thesis), Cairo University, Egypt, 2009.

[172] Mueller, N. D., Butler, E. E., McKinnon, K. A., Rhines, A., Tingley, M., Holbrook, N. M., and Huybers, P. Cooling of US Midwest summer temperature extremes from cropland intensification. *Nature Climate Change 6*, 3 (2015), 317–322.

[173] Mukherjee, S., Mishra, A. K., Mann, M. E., and Raymond, C. Anthropogenic Warming and Population Growth May Double US Heat Stress by the Late 21st Century. *Earth's Future 9*, 5 (2021).

[174] NASS. Farm and Ranch Irrigation Survey (2008). 2007 Census of Agriculture, Volume 3, Special Studies, Part 1. Tech. rep., National Agricultural Statistics Service (NASS), US Department of Agriculture, 2010. http://www.agcensus.usda.gov/Publications/2007/Online_Highlights/Farm_and_Ranch_Irrigation_Survey/index.asp,01/02/2011.

[175] Nassar, A. Comparison of micro irrigation systems for olive trees. *Misr J. Ag. Eng. 26*, 1 (2009).

[176] Negm, A. M. e. Conventional Water Resources and Agriculture in Egypt. *Handbook Env Chem 74* (2019), 471—488.

[177] Nigam, S., Guan, B., and Ruiz-Barradas, A. Key role of the Atlantic Multidecadal Oscillation in 20th century drought and wet periods over the Great Plains. *Geophysical Research Letters 38*, 16 (2011), 1–6.

[178] Nikiel, C. Regional Summer Climate Variability and Change over North America in the 20th Century. Master's thesis, Massachusetts Institute of Technology, Cambridge, Massachusetts, 2018.

[179] Nikiel, C., and Eltahir, E. A. B. *A Path Forward for Sharing the Nile Water: Sustainable, Smart, Equitable, Incremental.* Agricultural Technology in the Nile Basin: Current Use and Potential Expansion; Ed. Stephanie McPherson. Published by the Author, Cambridge, MA, 2019.

[180] Nikiel, C., and Eltahir, E. A. B. Summer Climate Change in the Midwest and Great Plains due to Agricultural Development during the Twentieth Century. *Journal of Climate 32* (2019), 5583–5599.

[181] Nikiel, C., and Eltahir, E. A. B. Past and future trends of Egypt's water consumption and its sources. *Nature Communications 12*, 4508 (2021).

[182] Nile Basin Initiative (NBI). *The Nile Basin Water Resources Atlas.* Available online at http://atlas.nilebasin.org/treatise/water-withdrawal-for-irrigation-in-the-nile-basin/, 2016.

[183] NOAA. July 1995 heat wave. natural disaster survey report. Available from https://www.weather.gov/media/publications/assessments/heat95.pdf, 1995.

[184] NOAA, N. Glossary - heat wave. Available from http://w1.weather.gov/glossary/index.php?letter=h, 2018.

[185] NOAA, N. Heat watch vs. warning. heat safety tools. Available from https://www.weather.gov/safety/heat-ww, 2021.

[186] NOAA CoastWatch Great Lakes. Great Lakes Statistics (Surface Temperatures). Accessed at https://coastwatch.glerl.noaa.gov/statistic/statistic.html.

[187] Oki, T., and Kanae, S. Global hydrological cycles and world water resources. *Science 313* (2006).

[188] Omar, M. E. D. M., and Moussa, A. M. A. Water management in Egypt for facing the future challenges. *Journal of Advanced Research 7*, 3 (2016).

[189] Omer, A. M. Water resources and freshwater ecosystems in Sudan. *Renewable and Sustainable Energy Reviews 12*, 8 (2008).

[190] Ozdogan, M., Rodell, M., Beaudoing, H. K., and Toll, D. L. Simulating the effects of irrigation over the United States in a land surface model based on satellite-derived agricultural data. *Journal of Hydrometeorology 11* (2010), 171–184.

[191] O'Neill, B. C., and et al. The Scenario Model Intercomparison Project (ScenarioMIP) for CMIP6. *Geoscientific Model Development 9* (2016), 3461–3482.

[192] Pal, J. S., and Eltahir, E. A. B. Teleconnections of soil moisture and rainfall during the 1993 midwest summer flood. *Geophysical Research Letters 29*, 18 (2002), 12–1 – 12–4.

[193] Pal, J. S., and Eltahir, E. A. B. Future temperature in southwest Asia projected to exceed a threshold for human adaptability. *Nature Climate Change 18203* (2015), 1–4.

[194] Pan, Z., Arritt, R. W., Takle, E. S., Gutowski Jr., W. J., Anderson, C. J., and Segal, M. Altered hydrologic feedback in a warming climate introduces a "warming hole". *Geophysical Research Letters 31*, 17 (2004).

[195] Pan, Z., Shi, C., Kumar, S., and Gao, Z. North Pacific SST forcing on the Central United States "Warming Hole" as simulated in CMIP5 coupled historical and uncoupled AMIP experiments. *Atmosphere-Ocean 55*, 1 (2017), 57–77.

[196] Parsons, K. Heat stress standard ISO 7243 and its global application. *Industrial Health 44* (2006), 368–379.

[197] Partridge, T. F., Winter, J. M., Liu, L., Kendall, A. D., Basso, B., and W., H. D. Mid-20th century warming hole boosts U.S. maize yields. *Environmental Research Letters 14*, 11 (2019).

[198] Partridge, T. F., Winter, J. M., Osterberg, E. C., Hyndman, D. W., Kendall, A. D., and Magilligan, F. J. Spatially distinct seasonal patterns and forcings of the U.S. Warming Hole. *Geophysical Research Letters 45*, 4 (2018), 2055–2063.

[199] Patricola, C. M., Chang, P., and Saravanan, R. Impact of Atlantic SST and high frequency atmospheric variability on the 1993 and 2008 Midwest floods: Regional climate model simulations of extreme climate events. *Climatic Change 129*, 3 (2015), 397–411.

[200] Patricola, C. M., and Cook, K. H. Mid-twenty-first century climate change in the Central United States. Part 2: Climate Change Processes. *Climate Dynamics 40* (2013), 569–583.

[201] Patricola, C. M., and Cook, K. H. Mid-twenty-first century warm season climate change in the Central United States. Part 1: Regional and global model predictions. *Climate Dynamics 40* (2013), 551–568.

[202] Pielke Sr., R. A., Mahmood, R., and McAlpine, C. Land's complex role in climate change. *Physics Today 69*, 11 (2016), 40–46.

[203] Pielke Sr., R. A., Pitman, A., Niyogi, D., Mahmood, R., Mcalpine, C., Hossain, F., Goldewijk, K. K., Nair, U., Betts, R., Fall, S., Reichstein, M., Kabat, P., and de Noblet, N. Land use / land cover changes and climate: Modeling analysis and observational evidence. *WIREs Climate Change 2* (2011), 828–850.

[204] Poli, P., Hersbach, H., Dee, D. P., Berrisford, P., Simmons, A. J., Vitart, F., and et al. ERA-20C: An atmospheric reanalysis of the twentieth century. *Journal of Climate 29*, 11 (2016), 4083–4097.

[205] Prince, S. D., Haskett, J., Steininger, M., Strand, H., and Wright, R. Net primary production of U.S. Midwest croplands from agricultural harvest yield data. *Ecological Applications 11*, 4 (2001), 1194–1205.

[206] Qian, Y., Huang, M., Yang, B., and Berg, L. K. A Modeling Study of Irrigation Effects on Surface Fluxes and Land-Air-Cloud Interactions in the Southern Great Plains. *Journal of Hydrometeorology 14* (2013), 700–721.

[207] Ramankutty, N., and Foley, J. A. Estimating historical changes in global land cover: Croplands from 1700 to 1992. *Global Biogeochemical Cycles 13*, 4 (1999), 997–1027.

[208] Ramankutty, N., Foley, J. A., and Olejniczak, N. J. People on the Land: changes in global population and croplands during the 20th century. *Ambio 31*, 3 (2002), 251–257.

[209] Rastogi, D., Lehner, F., and Ashfaq, M. Revisiting Recent U.S. Heat Waves in a Warmer and More Humid Climate. *Geophysical Research Letters 47*, 9 (2020), e2019GL086736.

[210] Ray, D. K., Ramankutty, N., Mueller, N. D., West, P. C., and Foley, J. A. Recent patterns of crop yield growth and stagnation. *Nature Communications 3*, 1293 (2012).

[211] Raymond, C., Singh, D., and Horton, R. Spatiotemporal patterns and synoptics of extreme wet-bulb temperature in the contiguous United States. *J. Geophys. Res. Atmos. 122*, 24 (2017), 13108–13124.

[212] Rayner, N. A., Parker, D. E., Horton, E. B., Folland, C. K., Alexander, L. V., Rowell, D. P., Kent, E. C., and Kaplan, A. Global analyses of sea surface temperature, sea ice, and night marine air temperature since the late nineteenth century. *Journal of Geophysical Research 108*, D14 (2003). Data Retrieved from https://www.metoffice.gov.uk/hadobs/hadisst/data/download.html.

[213] RFE/RL. Russia cuts off wheat, other grain exports. In Radio Free Europe/Radio Liberty. Available Online at https://www.rferl.org/a/russia-cuts-off-wheat-other-grain-exports/30577633.html, 2020.

[214] Ritchie, H. Meat and Dairy Production: Meat Consumption vs. GDP per Capita, 2017. Our World in Data. (2017; Accessed August 2020) [https://ourworldindata.org/grapher/meat-consumption-vs-gdp-per-capita], 2017.

[215] Ritchie, H., and Roser, M. Crop yields. Published online at OurWorldInData.org at https://ourworldindata.org/crop-yields, 2013.

[216] Ritchie, H., and Roser, M. Land use. Published online at OurWorldInData.org at https://ourworldindata.org/land-use, 2013.

[217] Robinson, P. J. On the definition of a heat wave. *Journal of Applied Meteorology 40*, 4 (2001), 762–775.

[218] Rogers, R. R., and Yau, M. K. *A Short Course in Cloud Physics, 3rd Edition*. Butterworth-Heinemann, Elsevier, 1989.

[219] Roser, M., and Ritchie, H. Food supply. Our World in Data. (2013; Accessed August 2020) [https://ourworldindata.org/grapher/daily-per-capita-supply-of-calories-vs-gdp-per-capita?time=latest], 2013.

[220] Roser, M., Ritchie, H., and Ortiz-Ospina, E. World population growth. Published online at OurWorldInData.org at https://ourworldindata.org/world-population-growth, 2013.

[221] Roxburgh, S. H., Berry, S. L., Buckley, T. N., Barnes, B., and Roderick, M. L. What is NPP? Inconsistent accounting of respiratory fluxes in the definition of net primary production. *Functional Ecology 19*, 3 (2005), 378–382.

[222] Ruiz-Barradas, A., and Nigam, S. Great Plains precipitation and its SST links in twentieth-century climate simulations, and twenty-first-and twenty-second-century climate projections. *Journal of Climate 23* (2010), 6409–6429.

[223] Russo, S., Sillmann, J., and Sterl, A. Humid heat waves at different warming levels. *Scientific Reports 7*, 7477 (2017).

[224] Sacks, W. J., and Kucharik, C. J. Crop management and phenology trends in the U.S. Corn Belt: Impacts on yields, evapotranspiration and energy balance. *Agricultural and Forest Meteorology 151*, 7 (2011), 882–894.

[225] Said, R. *The River Nile*. Pergamon, 1993.

[226] Sallam, O. M. Vision for Future Management of Groundwater in the Nile Delta of Egypt After Construction of the Ethiopian Dams. *Hydrol Current Res. 9*, 302 (2018).

[227] Salman, M. S. The new state of South Sudan and the hydro-politics of the Nile Basin. *Water International 36*, 2 (2011).

[228] Schlenker, W., and Roberts, M. J. Do nonlinear temperature effects indicate severe damages to U.S. crop yields under climate change? *Proc. Natl. Acad. Sci. U. S. A. 106*, 155 (2009), 94–98.

[229] Schoof, J. T., Ford, T. W., and Pryor, S. C. Recent Changes in U.S. Regional Heat Wave Characteristics in Observations and Reanalyses. *Journal of Applied Meteorology and Climatology 56*, 9 (2017), 2621 – 2636.

[230] Schoof, J. T., Pryor, S. C., and Ford, T. W. Projected Changes in United States Regional Extreme Heat Days Derived From Bivariate Quantile Mapping of CMIP5 Simulations. *Journal of Geophysical Research: Atmospheres 124*, 10 (2019), 5214–5232.

[231] Schubert, S., Gutzler, D., Wang, H., Dai, A., Delworth, T., Deser, C., Findell, K., Fu, R., Higgins, W., Hoerling, M., Kirtman, B., Koster, R., Kumar, A., Legler, D., Lettenmaier, D., Lyon, B., Magana, V., Mo, K., Nigam, S., Pegion, P., Phillips, A., Pulwarty, R., Rind, D., Ruiz-Barradas, A., Schemm, J., Seager, R., Stewart, R., Suarez, M., Syktus, J., Ting, M., Wang, C., Weaver, S., and Zeng, N. A U.S. Clivar project to assess and compare the responses of global climate models to drought-related SST forcing patterns: Overview and results. *Journal of Climate 22*, 19 (2009), 5251–5272.

[232] Schubert, S. D., Suarez, M. J., Pegion, P. J., Koster, R. D., and Bacmeister, T. On the Cause of the 1930s Dust Bowl. *Science 303*, 5665 (2004), 1855–1859.

[233] Seager, R., and Hoerling, M. Atmosphere and ocean origins of North American droughts. *Journal of Climate 27*, 12 (2014), 4581–4606.

[234] Seager, R., Kushnir, Y., Ting, M., Cane, M., Naik, N., and Miller, J. Would advance knowledge of 1930s SSTs have allowed prediction of the dust bowl drought? *Journal of Climate 21*, 13 (2008), 3261–3281.

[235] Seneviratne, S. I., Pal, J. S., Eltahir, E. A. B., and C., S. Summer dryness in a warmer climate: A process study with a regional climate model. *Climate Dynamics 20* (2002), 69–85.

[236] Sherwood, S. C., and Huber, M. An adaptability limit to climate change due to heat stress. *Proceedings of the National Academy of Sciences 107*, 21 (2010), 9552 – 9555.

[237] Sheskin, D. J. *Handbook of parametric and nonparametric statistical procedures*. (Fourth Ed.). Boca Raton, FL: Chapman & Hall/CRC, 2007.

[238] Siam, M., and Eltahir, E. A. B. Climate change enhances interannual variability of the Nile River flow. *Nature Climate Change 7* (2017), 350–354.

[239] Siebert, S., Kummu, M., Porkka, M., Döll, P., Ramankutty, N., and Scanlon, B. R. A global data set of the extent of irrigated land from 1900 to 2005. *Hydrology and Earth System Sciences 19* (2015), 1521–1545.

[240] Simoes, A. Observatory of Economic Complexity: Which Countries Export Corn (2016). Available at http://atlas.media.mit.edu/en/visualize/tree_map/hs92/export/show/all/1005/2016/, (Accessed 10/08/2018), 2016.

[241] Simoes, A. Observatory of Economic Complexity: Which Countries Export Soybean (2016). Available at http://atlas.media.mit.edu/en/visualize/tree_map/hs92/export/show/all/1201/2016/, (Accessed 10/08/2018), 2016.

[242] Smith, S. C., and Massey, D. T. Miscellaneous Publication Number 1455: Farm Drainage in the United States: History. Status, and Prospects. Tech. rep., United States Department of Agriculture, Economic Research Service, 1997.

[243] Son, J.-Y., Liu, J. C., and Bell, M. L. Temperature-related mortality: A systematic review and investigation of effect modifiers. *Environmental Research Letters 14*, 7 (2019).

[244] Spangler, K. R., and Wellenius, G. A. Spatial patterns of recent us summertime heat trends: Implications for heat sensitivity and health adaptations. *Environmental Research Communications 2* (2020).

[245] Steduto, P., Hsiao, T. C., Fereres, E., and Raes, D. FAO Irrigation and Drainage Paper 66: Crop yield response to water. Tech. rep., Food and Agriculture organization of the United States, 2012. Available online at http://www.fao.org/3/i2800e/i2800e.pdf.

[246] Sterling, S. M., Ducharne, A., and Polcher, J. The impact of global land-cover change on the terrestrial water cycle. *Nature Climate Change 3*, 4 (2012), 385–390.

[247] Takouleu, J. M. Egypt: Lining irrigation canals to save 5 billion m^3 of water. Afrik21. Available Online at https://www.afrik21.africa/en/egypt-lining-irrigation-canals-to-save-5-billion-m%C2%B3-of-water/, 2020.

[248] Tavakol, A., Rahmani, V., and Harrington Jr, J. Changes in the frequency of hot, humid days and nights in the Mississippi River Basin. *International Journal of Climatology 40*, 11 (2020), 4715–4730.

[249] Taylor, K. E., Stouffer, R. J., and Meehl, G. A. An Overview of CMIP5 and the experiment design. *Bulletin of the American Meteorological Society 93* (2012), 485–498.

[250] Teng, H., Branstator, G., Meehl, G. A., and Washington, W. M. Projected intensification of subseasonal temperature variability and heat waves in the Great Plains. *Geophysical Research Letters 43* (2016), 2165–2173.

[251] Thomas, N. P., Bosilovich, M. G., Marquardt Collow, A. B., Koster, R. D., Schubert, S. D., Dezfuli, A., and Mahanama, S. P. Mechanisms associated with daytime and nighttime heat waves over the contiguous united states. *Journal of Applied Meteorology and Climatology 59* (2020), 1865–1882.

[252] Ting, M., and Wang, H. Summertime US precipitation variability and its relation to Pacific sea surface temperature. *Journal of Climate 10*, 8 (1997), 1853–1873.

[253] Trumpickas, J., Shuter, B. J., and Minns, C. K. Forecasting impacts of climate change on Great Lakes surface water temperatures. *Journal of Great Lakes Research 35*, 3 (2009), 454–463.

[254] Tsur, Y. Economic Aspects of Irrigation Water Pricing. *Canadian Water Resources Journal 30*, 1 (2005), 31–46.

[255] Twine, T. E., Kucharik, C. J., and Foley, J. A. Effects of land cover change on the energy and water balance of the Mississippi River Basin. *Journal of Hydrometeorology 5* (2004), 640–655.

[256] Tyagi, N. K., Sharma, D. K., and Luthra, S. K. Determination of evapotranspiration for maize and berseem clover. *Irrig. Sci. 21* (2003).

[257] United Nations. Agreement between the Republic of the Sudan and the United Arab Republic for the full utilization of the Nile waters signed at Cairo. Treaty Series, 453, 51. [https://treaties.un.org/doc/Publication/UNTS/Volume%20453/volume-453-I-6519-English.pdf], 1963.

[258] United Nations. Department of economic and social affairs, population division. total fertility by region, subregion and country, 1950-2100 (live births per woman). world population prospects 2019, online edition. rev. 1. (file

fert/4). Available Online at https://population.un.org/wpp/Download/Files/1_Indicators%20(Standard)/EXCEL_FILES/2_Fertility/WPP2019_FERT_F04_TOTAL_FERTILITY.xlsx, 2019.

[259] United Nations. Department of economic and social affairs, population division. total population (both sexes combined) by region, subregion and country, annually for 1950-2100 (thousands)). world population prospects 2019, online edition. rev. 1. (file pop/1-1). Available Online at https://population.un.org/wpp/Download/Files/1_Indicators%20(Standard)/EXCEL_FILES/1_Population/WPP2019_POP_F01_1_TOTAL_POPULATION_BOTH_SEXES.xlsx, 2019.

[260] U.S. Census Bureau. U.S. and World Population Clock. Available at https://www.census.gov/popclock/, 2017.

[261] USDA. 2017 Census of Agriculture. Tech. rep., U.S. Department of Agriculture, Complete data available at www.nass.usda.gov/AgCensus.

[262] USDA-NASS. Quick Stats. U.S. Department of Agriculture National Agricultural Statistics Service (USDA NASS). Retrieved from https://quickstats.nass.usda.gov/., 2016.

[263] USGCRP. Impacts, Risks, and Adaptation in the United States: Fourth National Climate Assessment, Volume II [Reidmiller, D.R., C.W. Avery, D.R. Easterling, K.E. Kunkel, K.L.M. Lewis, T.K. Maycock, and B.C. Stewart (eds.)]. U.S. Global Change Research Program, Washington, DC, USA, 1515 pp. doi: 10.7930/NCA4.2018, 2018.

[264] Valayamkunnath, P., Barlage, M., Chen, F., Gochis, D. J., and J., F. K. Mapping of 30-meter resolution tile-drained croplands using a geospatial modeling approach. *Nature Scientific Data 7*, 257 (2020).

[265] Vörösmarty, C. J., Fekete, B. M., and Tucker, B. A. River Discharge Database, Version 1.1 (RivDIS v1.0 supplement). Aswan Dam Egypt. Available through the Institute for the Study of Earth, Oceans, and Space / University of New Hampshire, Durham NH (USA) at http://dx.doi.org/10.3334/ORNLDAAC/199, 1998.

[266] Wang, H., and Schubert, S. The precipitation response over the continental United States to cold tropical Pacific sea surface temperatures. *Journal of Climate 27*, 13 (2014), 5036–5055.

[267] Wang, H., Schubert, S., Suarez, M., Chen, J., Hoerling, M., Kumar, A., and Pegion, P. Attribution of the seasonality and regionality in climate trends over the United States during 1950-2000. *Journal of Climate 22*, 10 (2009), 2571–2590.

[268] Wang, H., Schubert, S., Suarez, M., and Koster, R. The physical mechanisms by which the leading patterns of SST variability impact U.S. precipitation. *Journal of Climate 23*, 7 (2010), 1815–1836.

[269] Wang, P., Leung, R. L., Lu, J., Song, F., and Tang, J. Extreme Wet-Bulb Temperatures in China: The Significant Role of Moisture. *Journal of Geophysical Research: Atmospheres 124*, 11 (2019), 944–960.

[270] Wang, P., Yang, Y., Tang, J., Leung, L. R., and Liao, H. Intensified humid heat events under global warming. *Geophysical Research Letters 48*, 2 (2021).

[271] Warntz, W. A Historical Consideration of the Terms "Corn" and "Corn Belt" in the United States. *Agricultural History 31*, 1 (1957).

[272] Weaver, S. J. Factors Associated with Decadal Variability in Great Plains Summertime Surface Temperatures. *Journal of Climate 26*, 1 (2013), 343 – 350.

[273] Weaver, S. J., and Nigam, S. Variability of the Great Plains Low-Level Jet: Large-scale circulation context and hydroclimate impacts. *Journal of Climate 21*, 7 (2008), 1532–1551.

[274] Weaver, S. J., Schubert, S., and Wang, H. Warm season variations in the low-level circulation and precipitation over the central United States in observations, AMIP simulations, and Idealized SST experiments. *Journal of Climate 22*, 20 (2009), 5401–5420.

[275] West, T. O., Brandt, C. C., Baskaran, L. M., Hellwinckel, C. M., Mueller, R., Bernacchi, C. J., Bandaru, V., Yang, B., Wilson, B. S., Marland, G., Nelson, R. G., De La Torre Ugarte, D. G., and Post, W. M. Cropland carbon fluxes in the United States: Increasing geospatial resolution of inventory-based carbon accounting. *Ecological Applications 20*, 4 (2010), 1074–1086.

[276] Wetherald, R., and S., M. The Mechanisms of Summer Dryness Induced by Greenhouse Warming. *Journal of Climate 8* (1995), 3096–3108.

[277] Wheeler, K., Jeuland, M., Hall, J. W., and et al. Understanding and managing new risks on the Nile with the Grand Ethiopian Renaissance Dam. *Nature Communications 11*, 5222 (2020).

[278] Winter, J. M. *Coupling of Integrated BIosphere Simulator to Regional Climate Model version 3.* (masters thesis), Retrieved from DSpace@MIT. (http://hdl.handle.net/1721.1/34272). Cambridge, MA: Massachusetts Institute of Technology, 2006.

[279] Winter, J. M., and Eltahir, E. A. B. Modeling the hydroclimatology of the Midwestern United States. Part 1: Current climate. *Climate Dynamics 38* (2012), 573–593.

[280] Winter, J. M., and Eltahir, E. A. B. Modeling the hydroclimatology of the Midwestern United States. Part 2: Future climate. *Climate Dynamics 38* (2012), 595–611.

[281] Winter, J. M., Yeh, P. J.-F., Fu, X., and Eltahir, E. A. B. Uncertainty in modeled and observed climate change impacts on American Midwest hydrology. *Water Resources Research 50* (2015).

[282] World Bank. Employment in Agriculture (%) of total Employment. (modeled ILO estimate) – Egypt, Arab Rep. Data from International Labour Organization, ILOSTAT database. [Retrieved January 11, 2021]. Available Online at https://data.worldbank.org/indicator/SL.AGR.EMPL.ZS?locations=EG, 2020.

[283] Wuebbbles, D., Cardinale, B., Cherkauer, K., Davidson-Arnott, R., Hellmann, J., Infante, D., Johnson, L., de Loe, R., Lofgren, B., Packman, A., Seglenieks, F., Sharma, A., Sohngen, B., Tiboris, M., Vimont, D., Wilson, R., Kunkel, K., and Ballinger, K. An Assessment of the Impacts of Climate Change on the Great Lakes. Tech. rep., Environmental Law and Policy Center and the Chicago Council on Global Affairs. Available at https://elpc.org/wp-content/uploads/2020/04/2019-ELPCPublication-Great-Lakes-Climate-Change-Report.pdf, 2019.

[284] Xue, P., and Eltahir, E. A. B. Estimation of the Heat and Water Budgets of the Persian (Arabian) Gulf Using a Regional Climate Model. *Journal of Climate 28* (2015), 5041–5062.

[285] Xue, P., Pal, J. S., Ye, X., Lenters, J. D., Huang, C., and Chu, P. Y. Improving the Simulation of Large Lakes in Regional Climate Modeling: Two-Way Lake-Atmopshere Coupling with a 3D Hydrodynamic Model of the Great Lakes. *Journal of Climate 30* (2017), 1605–1627.

[286] Ye, X., Anderson, E. J., Chu, P. Y., Huang, C., and Xue, P. Impact of water mixing and ice formation on the warming of lake superior: A model-guided mechanism study. *Limnology and Oceanography 64*, 2 (2019), 558–574.

[287] Yeh, P. J.-F., Irizarry, M., and Eltahir, E. A. B. Hydroclimatology of Illinois: A comparison of monthly evaporation estimates based on atmospheric water balance and soil water balance. *Journal of Geophysical Research 103*, D16 (1998).

[288] Yeh, P. J.-F., and Wu, C. Recent acceleration of the terrestrial hydrologic cycle in the U.S. Midwest. *Journal of Geophys. Res. Atmos. 123* (2018).

[289] Zeitoun, M., Allan, J. A., and Mohieldeen, Y. Virtual water 'flows' of the Nile Basin, 1998–2004: A first approximation and implications for water security. *Global Environmental Change 20*, 2 (2010).

[290] Zhang, Y., Gao, Z., Pan, Z., Li, D., and Wan, B. Record-breaking temperatures in China during the warming and recent hiatus periods. *Journal of Geophysical Research Atmospheres 121* (2016), 241–258.